Diss. ETH No. 24364

A SUPERSOLID OF MATTER AND LIGHT

A thesis submitted to attain the degree of

DOCTOR OF SCIENCES of ETH ZURICH

(Dr. sc. ETH Zurich)

presented by

JULIAN LÉONARD

M. Sc., Université Pierre et Marie Curie, Paris

born on 15.01.1989

in Viernheim, Germany

accepted on the recommendation of

Prof. Dr. Tilman Esslinger, examiner

Prof. Dr. Jonathan Home, co-examiner

2017

JULIAN LÉONARD
A supersolid of matter and light,
Diss. ETH No. 24364 © May 2017

Digital Object Identifier DOI:10.3929/ethz-b-000262194

To my family.

ABSTRACT

A supersolid is a quantum phase of matter that demonstrates both solid and superfluid properties. In combination with gaseous and liquid superfluids it forms the triad of quantum phases analogous to the classical states of matter: solid, liquid and gas. Despite efforts in a number of systems—most prominently helium—experimental verification of supersolidity has remained elusive.

We report on the realization and characterization of a supersolid. A phase transition from a gaseous Bose-Einstein condensate to the supersolid crystal is induced by photon-mediated interactions among the atoms that are a result of symmetric coupling with the modes of two optical cavities. At the critical point, continuous translational symmetry is broken along one direction and a periodic density pattern with a coherent wave function forms. We verify both the structure formation and superfluidity by performing matter-wave interference of the many-body wavefunction.

The phase transition from the superfluid to the supersolid is marked by the onset of light fields in both optical cavities, whose amplitudes are equivalent to the real and imaginary part of the continuous symmetry. This unique real-time observable permits extensive studies of the supersolid state and the phase transition. We demonstrate a high ground-state degeneracy and observe the associated Higgs and Goldstone modes across the critical point. Their dynamics are visible as amplitude and phase oscillation in the cavity fields, facilitating studies on their decay and response. Approaching the phase transition, we examine the critical fluctuations of the density distribution in the vicinity of the critical point by permanently measuring the photon occupation of both cavities.

The continuous symmetry is the result of symmetry enhancement from two competing order parameters with underlying discrete symmetries. In order to explore the crossover region between continuous and discrete symmetry breaking, we study the vicinity of the symmetry-enhanced region by creating a slight asymmetry in the two coupling strengths. We observe an increasing anisotropy in the distribution of the broken symmetry, accompanied by a rising mass of the Goldstone mode.

The experiments were performed with a new apparatus that was constructed in the context of this thesis. The setup is optimized for a fast, robust preparation sequence of the quantum gas. We introduce a new method to transport ultracold atoms with focus-tunable lenses, which is superior to previously established methods in terms of flexibility, stability, costs and space requirements. Furthermore, the vacuum system features a conceptually new design including a transfer system that permits one to readily exchange the cavity setup. This establishes our experiment as a versatile quantum simulator to engineer atom-light interactions in various optical cavity environments.

ZUSAMMENFASSUNG

Ein Suprasolid ist ein Quantenzustand der gleichzeitig feste und flüssige Eigenschaften aufweist. Gemeinsam mit gasförmigen und flüssigen Suprafluiden bildet er eine Dreiheit an Quantenzuständen in Analogie zu den klassischen Aggregatzuständen Gas, Flüssigkeit und Festkörper. Trotz Bestrebungen in verschiedenen Systemen – allen voran Helium – konnte ein Suprasolid noch nicht experimentell nachgewiesen werden.

In dieser Arbeit wird die erste Herstellung und Charakterisierung eines solchen Suprasolids vorgestellt. Der Phasenübergang von einem gasförmigen Bose-Einstein-Kondensat zu dem suprasoliden Kristall wird von einer atomaren Wechselwirkung verursacht, die von Photonen aus zwei optischen Resonatoren getragen wird. Am kritischen Punkt bildet sich ein periodisches Dichtemuster in der kohärenten atomaren Wellenfunktion, das die kontinuierliche Translationssymmetrie des Kondensats entlang einer Richtung bricht. Wir weisen sowohl die Strukturbildung als auch die Suprafluidität durch Materiewellen-Interferenz der Vielteilchen-Wellenfunktion nach.

Der Phasenübergang vom Suprafluid zum Suprasolid ist durch die Enstehung von Lichtfeldern in beiden Resonatoren gekennzeichnet, deren Amplituden dem realen und imaginären Teil der kontinuierlichen Symmetrie entsprechen. Diese einzigartige Echtzeit-Observable lässt weitreichende Studien des suprasoliden Zustands und des Phasenübergangs zu. Wir weisen eine hohe Entartung des Grundzustands nach und beobachten die entsprechenden Higgs- und Goldstone-Moden über den kritischen Punkt hinweg. Ihre Dynamik ist in den Resonatormoden als Amplituden- und Phasenoszillation sichtbar, was Studien zu ihrem Zerfall und Antwortverhalten ermöglicht. Nah am Phasenübergang untersuchen wir die kritischen Fluktuationen der Dichtemodulation, indem wir die Photonenbesetzung beider Resonatoren messen.

Die kontinuierliche Symmetrie ist das Ergebnis einer Symmetrie-Erweiterung aus zwei konkurrierenden Ordnungsparametern mit zugrundeliegenden diskreten Symmetrien. Um den Übergang von der kontinuierlichen zur diskreten Symmetrie zu erforschen, studieren wir die Umgebung der symmetrie-erweiterten Region indem wir eine geringfügige Asymmetrie in die Kopplungsstärken einführen. Wir beobachten eine zunehmende Anisotropie in der Verteilung der gebrochenen Symmetrie, begleitet von einer ansteigenden Masse der Goldstone-Mode.

Die Experimente wurden mit einer neuen Apparatur durchgeführt, die im Rahmen dieser Arbeit errichtet wurde. Der Aufbau ist auf eine schnelle und robuste Präparationssequenz des Quantengases ausgerichtet. Wir führen eine neue Transportmethode für ultrakalte Atome ein, die auf Linsen mit verstellbarer Brennweite basiert und bisherigen Methoden bezüglich Flexibilität, Stabilität, Kosten und Platzanforderungen überlegen ist. Ferner zeichnet sich das Vakuumsystem durch einen konzeptionell neuen Ansatz mit einem Transfersystem aus, das es erlaubt den Resonator-Aufbau ohne Weiteres auszutauschen. Unser Experiment schafft dadurch einen vielseitigen Quantensimulator für konstruierte Atom-Licht-Wechselwirkungen in verschiedenen Resonator-Umgebungen.

CONTENTS

Detailed tables of contents can be found at the beginning of each chapter.

1 INTRODUCTION

Together, solids and fluids dominate our surrounding in everyday life, yet their behaviour is opposite in many respects: solid materials are characterized by structural rigidity and resistance to changes of shape, and thus they form the basis of most created objects. Fluids (including gases), quite the contrary, adapt their shape to their container and continuously flow under applied shear stress. In the presence of a force such as gravity, this property makes them an ideal transport medium, which is central to processes such as blood circulation, the hydrological cycle, heat conduction or water transport. On the microscopic level, solids and fluids differ by the arrangement of the constituent particles. The atoms, molecules or ions a solid is composed of are mostly arranged in a repeating pattern. Knowledge of the position of one particle and its distance to the adjacent one is in principle sufficient to predict the position of all others. Fluids do not possess this order and their particles are equally likely to be found at every position.

Solids and fluids behave differently

Whether a material is solid, liquid or gaseous (or even plasmonic, with the electrons stripped off the nuclei) depends on the strength of the interactions among the particles compared to their motional energy. The forces in a solid are strong enough for the particles to retain their position, whereas thermal motion in a fluid can overcome these bonds and allow the particles to move freely. The point where interaction and motion are equally strong marks the phase transition between a solid and a liquid. An additional state in between, which would manifest both properties simultaneously, does not exist: they are mutually exclusive.

Phase transitions driven by thermal...

Phase transitions can also occur at absolute zero temperature, where thermal motion is absent. If allowed by quantum statistics, all particles occupy the motional ground state and share a common wave function with a well-defined phase. The lack of a finite temperature also results in the absence of friction. The quantum fluctuations associated with the zero-point energy persist and their interplay with the interactions among the particles can drive transitions between different quantum phases , much like thermal fluctuations and interactions for classical phases [1]. Yet, the passage from classical to quantum phases presents an exception in the context of phase transitions, because it is not interaction driven but a purely quantum statistical effect [2].

...and by quantum fluctuations

The discovery of superfluid helium in 1938 [3, 4] led to the first identification of such a quantum phase [5, 6]. It can be created by cooling liquid helium below 2.17 K, the so-called λ point. The substance indeed behaves much like a classical liquid, except that it flows without friction on all surfaces. Microscopically this effect can be ascribed to the phase coherence of the atoms sharing one common ground state. Superfluid helium presents a *quantum liquid*, where quantum fluctuations instead of thermal fluctuations dominate over the interactions among the atoms. Its finding triggered the search for quantum analogs for the other states of matter. This was soon successful for a plasma-type phase, when BCS theory identified the previously discovered superconductors as a *quantum plasma*, where phase coherence among electron pairs leads to dissipation-free charge transport in a metal [7, 8]. A *quantum gas* had been predicted by Bose and Einstein before [2], and

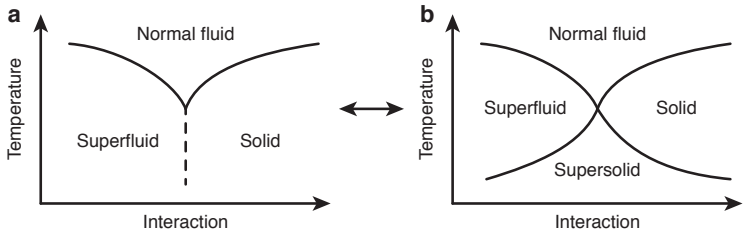

Figure 1.1: *Phase diagram for crystalline order vs. phase coherence.* Whether a supersolid state exists at low temperature depends on the microscopic details of the interactions, which are often unknown. **a,** Scenario without a supersolid. When lowering the temperature of a material, it can become either solid or superfluid, depending on the interaction strength among the particles. **b,** Scenario with a supersolid phase at low temperatures. It appears as a fourth phase between the superfluid and the solid phase and combines phase coherence and solid order.

was finally discovered in 1995 with weakly interacting ultracold atoms [9, 10].

The concept of a supersolid is paradoxical

Yet, the remaining quantum state of matter, a *quantum solid*—or supersolid— remained elusive. In analogy to a classical solid, its constituents were expected to arrange on a periodic pattern, but at the same time, they would occupy a common ground-state wave function and therefore exhibit flow without friction [11, 12]. A supersolid therefore combines structural rigidity and frictionless flow, two properties that we normally conceive of as mutually exclusive. This behaviour makes the supersolid probably the most paradoxical state among the four fundamental quantum phases. Early discussions on supersolidity indeed considered the existence of such a state so absurd that they tried to proof its impossibility, for instance O. Penrose and L. Onsager [13].

Crystalline order vs. phase coherence

Conceptually, a supersolid can be interpreted in terms of the coexistence of two different kinds of order: phase coherence and periodic density order. Their interplay is illustrated in Fig. 1.1 with two phase diagrams, whose topology is generic for the situation of two order parameters. When lowering the temperature of a material, it can become either solid or superfluid, depending on the interaction strength among the particles. One possibility is that the phase coherence of a superfluid and the crystalline order of a solid mutually exclude one another. The other possibility includes a supersolid state with both orders present. It is expected to exist at low temperature with interactions strong enough to form a crystal, but weak enough to maintain phase coherence. Whether the former or the latter scenario applies in a system depends on the microscopic properties of the material, which are often unknown.

Supersolidity and zero-point motion

The speculations on the existence of a supersolid state started with fundamental work by D. J. Thouless [11], A. F. Andreev and I. M. Lifshitz [12], and G. V. Chester [14] describing the various possibilities of a supersolid state [15]. They concluded that a prerequisite to maintain coherence in a crystalline material is a large zero-point motion of the particles around their lattice sites. Two concepts seemed plausible as mechanisms for the formation of a supersolid [15]:

- Quantum fluctuations allow particles to tunnel and to restore phase coherence
- Vacancies or impurities are sufficiently mobile to undergo Bose-Einstein condensation

The search for supersolids hence focussed on materials with large quantum fluctuations. In a crystal they can be quantified with the dimensionless de-Boer parameter [16–18][1]:

$$\Lambda = \frac{1}{2\pi}\frac{\lambda_{dB}}{\sigma} \tag{1.1}$$

It compares the interparticle distance σ with the de-Broglie wavelength $\lambda_{dB} = \hbar/p$, where $\hbar$ is the Planck constant and p the particle momentum. Among all elements, the de-Boer parameter distinguishes helium as most promising candidate for a supersolid state with $\Lambda_{^4He} = 0.30$, followed by hydrogen $\Lambda_{H_2} = 0.19$ and deuterium $\Lambda_{D_2} = 0.14$ [15]. The number of experiments investigating the possibility of supersolidity in helium increased rapidly [19, 20] with different approaches including thermodynamic measurements [21–25], ultrasound studies [26–28], plastic flow [29–31] and mass flow [32], albeit with negative results.

Quest for supersolid helium

The most promising route proved to be torsional oscillator experiments, originating on a proposal by A. Leggett [33]. He considered a sample of solid helium that is placed in a cylindrical bucket under high pressure. The resonant oscillation frequency of the bucket in the presence of a drive depends on its moment of inertia. If the sample exhibited frictionless flow, it would not contribute to the rotation, resulting in a decreasing moment of inertia and a reduced oscillation frequency. Despite several attempts with negative results [34–36], the method ultimately seemed successful with the experiments of Kim and Chan [37, 38]. Their results were confirmed by other groups soon after [39–43], and further characterizations of the specific heat capacity [44, 45] and mass transport [46, 47] supported the interpretation. However, the enthusiasm was lessened when the number of observed anomalous effects increased [48–50]. A controversial debate on the existence of a supersolid began, which culminated in the measurement of the shear modulus of helium [51]. Its temperature dependence was identical to the moment of inertia and suggested crystal dislocations as the origin of the reduced rotational inertia. Indeed, when repeating the torsional oscillator experiments with a new apparatus that avoided the formation of crystal dislocations, Chan found the moment of inertia to remain constant [52] and the existence of supersolidity in helium again remained elusive.

Quantum gases might seem an unusual supersolid candidate at first sight, showing much weaker interactions than liquid superfluids such as helium [9, 10]. Their advantage is, however, the large coherence length paired with a number of tools to engineer the interaction strength and range. Whilst contact interactions can be readily adjusted with Feshbach resonances, their short range compared to the interparticle distance is not sufficient to develop a density pattern [53]. The challenge for supersolid formation amounts to finding a system offering suitable interactions to break the translational symmetry of the quantum gas while maintaining its phase coherence. As a consequence, engineering long-range interactions has become an important objective for experiments with quantum gases, with researchers utilizing a number of different approaches.

Engineering long-range interactions with quantum gases

One route employs atomic species with large magnetic dipole moments, for example chromium [54], dysprosium [55] or erbium [56], which show dipolar interactions over larger length scales. Interaction effects have been

1 We use the definition introduced in [18], which differs from de Boer's original definition by a factor $(2\pi\sqrt{2})^{-1}$.

observed in free space [57] and in optical lattices [58]. The observation of quantum droplets has proven the interactions to be strong enough to break the translational symmetry [59–61], however, this comes at the cost of lost phase coherence among the droplets.

Another approach uses heteronuclear molecules, which show strong electric dipole moments instead [62]. They have been produced in the quantum regime by preparing the constituents separately and then coherently transferring them to the rovibrational ground state, both for bosonic [63–65] and fermionic [66, 67] combinations as well as in optical lattices [68]. Their interaction strength can even be superior to magnetic dipolar interactions, but experiments have not yet shown evidence for translational symmetry breaking [62].

Rydberg atoms present a further path to long-range interacting quantum systems, which even allows to adjust the strength by the choice of Rydberg state [69]. Spatial structures of up to five atoms have been observed [70, 71], but at the absence of phase coherence among the atoms and at timescales too short to observe pattern formation from motional interaction. This can possibly be overcome in the future with Rydberg-dressed atoms, where the dominant contribution comes from the trapped electronic ground state and the long-range interactions originate from a weak admixture of the Rydberg state to the ground state [72, 73].

Atom-light interactions

A complementary route to creating long-range interactions employs atom-light interactions. In its most simple form, a cold atomic cloud is illuminated by a laser beam with a wavelength $\lambda_p = 2\pi/k_p$ far off-resonance from the internal atomic transitions [74]. This induces electric dipole moments in the atoms that can interact with each other with an interaction potential $\propto \sin(k_p r)/r^2$, where r is the distance between the atoms. However, due to incoherent scattering the heating rate is too large to induce a structural phase transition, independent of the laser frequency.

Enhanced dipole interactions with optical cavities

The coherent scattering can be enhanced compared to incoherent processes by placing the atomic cloud inside an optical cavity. While the strength of the interactions can be increased with such an approach, their range extends over the entire cloud, since all atoms couple equally to the cavity mode. A single-mode cavity has been observed to break discrete translational symmetry on the lattice structure predefined by the cavity mode [75], and presents a realization of the otherwise only theoretically studied lattice supersolids [76]. A different approach is based on the Talbot effect and has shown translational symmetry breaking for a thermal cloud [77], yet the quantum regime was not reached. Further proposals for supersolid formation with light-matter coupling exist both in free space [78] and for multimode cavities [79].

Here we show how a combination of two optical cavities can break the continuous translational symmetry of a quantum gas while maintaining its phase coherence. The strength of the induced photon-mediated interactions can be tuned over a broad range that allows to create self-organized structures emerging at arbitrary positions with a lattice constant determined by the optical wavelength. In analogy to the solid-state scenario, the de-Boer parameter for our supersolid is typically $\Lambda \sim 1$. We characterize the supersolid in terms of the zero-temperature phase diagram, the elementary excitations and its critical behaviour at the phase transition. Furthermore, we go beyond supersolidity and control the quality of the translational symmetry that is broken at the phase transition, giving insight into the crossover between discrete and continuous symmetries.

A transfer system with exchangeable science platform

The experiments were performed with an apparatus that was constructed in the course of this thesis. Its vacuum system is conceptually different from established quantum gas experiments as it includes a transfer system that allows one to exchange the cavity setup. The vacuum system with the transfer mechanism is presented in Chap. 2. A load-lock chamber is connected to the main chamber with a gate valve, through which a new setup can be inserted without compromising the vacuum of the main chamber. The science platform is equipped with diverse electrical and thermal contacts that increase the flexibility to setups that also involve solid-state devices other than optical cavities. This enables a rapid exchange of the setup and the prospect to work with a variety of platforms.

Preparation of a Bose-Einstein condensate

The starting point of the experiments is a BEC of ^{87}Rb atoms. We generate a new sample in a preparation sequence lasting several seconds, which is followed by the actual experiment. The atoms are captured and then cooled to quantum degeneracy in a combination of different techniques involving laser beams, magnetic fields and RF fields. The preparation sequence including all relevant experimental setups is described in Chap. 3. A unique feature of the apparatus is the method to transport the cold atoms into the cavity setup. We steer the focal length of a focus-tunable lens by applying a variable current, which displaces the position of an attractive dipole potential [80]. This allows us to transport the atomic cloud from the preparation chamber into the cavity setup over 28 cm. We choose an optical scheme that displaces the focus position at constant beam radius, providing uniform trapping conditions over the full transport length.

Optical transport with focus-tunable lenses

Two crossed cavities

Our approach to generate a supersolid state is based on the dispersive interaction of a BEC with two cavity modes crossing at an angle of 60°. The science platform with the cavity setup that was employed in this thesis is presented in Chap. 4. The mounts for the cavity mirrors are built in a way to minimize mode displacement during the bakeout and to ensure overlapping cavity modes. In addition to the cavities, the platform includes mirrors to reflect the cavity modes onto the optical viewports of the vacuum chamber. The cavity length (an hence the resonance frequency) can be steered with piezo components that are included into the mount of each mirror. The probing and the length stabilization are achieved with laser beams at frequencies with and without a significant effect on the atoms, respectively. We obtain full control over all probe and stabilization fields with a laser system that allows us to steer the frequency of each beam individually.

Self-organization in a rectangular lattice geometry

Experiments on self-organization with a single optical cavity so far have been limited to density modulations with a chequerboard geometry, since the system geometry only allowed for an orthogonal angle between the transverse pump and the cavity axis [81]. Instead, we have studied single-mode self-organization with a non-orthogonal transverse pump by coupling to one of the two cavities with a transverse pump at an angle of 60° with respect to the cavity axis. This gives rise to a density modulation with rectangular lattice geometry and leads to new effects thanks to its reduced symmetry compared to a square lattice. Our generalized system requires an extension of the theoretical framework for self-organization. We study further phenomena that go beyond the conventional description of self-organization in optical cavities, such as finite temperature and the interplay and competition of self-organization and spin transitions. Furthermore, the decay rates of the two cavity fields differs by approximately a factor five, which makes it possible to demonstrate the influence of dissipation on the shape of the phase diagram. The corresponding experiments are discussed in Chap. 5.

Competing order with two cavities

Coupling the atoms to both cavities simultaneously leads to a situation of competing orders, where two self-organization processes compete with each other. This situation is investigated in Chap. 6. It is reminiscent of the schematic phase diagrams illustrated in Fig. 1.1, but with each order parameter representing only a discrete symmetry. The competition is driven by the coupling to each cavity, which we adjust with the detuning of each cavity resonance from the the transverse pump frequency. We study the phase diagram and draw comparison to a theoretical model that presents a two-cavity extension from the previously employed single-cavity description. Our parameter range sets the phase diagram to the limiting scenario, where simultaneous presence of both orders is neither inhibited nor supported. The result is a narrow, yet stable region between the two organized phases in the phase diagram.

Supersolid formation in a quantum gas

This insight forms the basis of Chap. 7. The limiting scenario leads to a situation of symmetry enhancement, if the couplings to both cavities are identical. The two order parameters with discrete symmetries form a single one representing a continuous symmetry. When entering the ordered phase, the position of the atomic density modulation reflects this symmetry and hence breaks translational invariance of the superfluid quantum gas. This is the signature of a supersolid state. We study the ground-state degeneracy and its transition from continuous to discrete symmetry by applying a mismatch to the couplings.

Most phase transitions are characterized by a critical behaviour of the thermodynamic quantities [1]. This includes a critical slowing down of the system timescales and fluctuations at diverging time and length scales. One signature of critical behaviour is a softening of the lowest excitation at the phase transition. We first restrict the discussion to a single cavity and study the elementary excitations across the self-organization phase transition, as presented in Chap. 8. The excitation spectrum shows the frequency softening of a roton mode and a diverging susceptibility upon approaching the critical point. We present three methods for probing the excitation frequencies, all giving coinciding results while offering a complementary view on the intricate atom-photon dynamics in the system. All methods are based on cavity-enhanced Bragg spectroscopy, where the Bragg beams are formed by the transverse pump beam and a probe beam on the cavity axis. If their relative detuning matches the resonance condition, processes that create or annihilate collective excitations in the system are enhanced.

Frequency softening of the roton mode

Extending the system to two cavities, we investigate the excitation spectrum at the superfluid-supersolid phase transition. These results are discussed in Chap. 9. The broken continuous symmetry gives rise to two different types of excitations: a Higgs mode with amplitude fluctuations and a Goldstone mode with phase fluctuations. Since the fields form a U(1)-symmetric order parameter that can be modulated and monitored along both quadratures in real time, the two excitation types can be distinguished by correlations and anticorrelations in the light fields. We make use of this unique access and verify the amplitude and the phase character of the excitations, and observe the dynamics from an impulse response.

Higgs and Goldstone modes in the supersolid

We further characterize the critical behaviour by investigating the fluctuations of the order parameter in the vicinity of the critical point. The fluctuations can be accessed in real-time access by detecting the photons leaking from the cavity. The influence of dissipation on the critical exponent has been subject to a debate with theoretical and experimental studies. Our system not only allows to measure the critical behaviour at the superfluid-

Fluctuations at the superfluid-supersolid phase transition

supersolid phase transition, but also study the influence of dissipation on the critical exponent by performing measurements with the different decay rate of the two cavities. The results suggest a similar influence of both dissipation rates. We observe increasing fluctuations when matching the couplings to both cavities resulting in a larger critical exponent at the superfluid-supersolid phase transition compared to the single-mode self-organization.

Outlook

The presented results set the grounds for further studies of the supersolid state. The extension to self-organization with multiple cavity modes provides a route for creating and studying glassy many-body systems with controllably lifted ground-state degeneracies, such as supersolids in the presence of disorder. Beyond supersolidity, our set-up can be interpreted as identical two-level systems coupled with two quantized light fields, thus providing access to a new class of quantum optical models that break a continuous symmetry. Even more possible systems could be studied by exchanging the science platform with the transfer system, for instance Rydberg excitations in optical cavities [82], local perturbation of the self-organized cloud or cavities with sub-recoil linewidths [83].

The work presented in this thesis has been carried out in collaboration with Tobias Donner, Moonjoo Lee, Andrea Morales, Philip Zupancic and Tilman Esslinger.

Part I

EXPERIMENTAL SETUP

2

A VACUUM SYSTEM WITH EXCHANGEABLE SCIENCE PLATFORM

The vacuum system lies at the heart of any quantum gas experiment. It allows to isolate the trapped atomic cloud from the environment. The vacuum system presented here is exceptional, as it combines the properties of conventional quantum gas experiments with a load-lock system, where a science platform can be exchanged. After a brief overview of the design and construction of the vacuum system, each of its elements is adressed in more detail. We close with a description of the applied vacuum procedures.

CHAPTER CONTENTS

Hybrid quantum systems

The development of hybrid quantum systems, which combine two experimental platforms, is driven by the goal of harnessing the advantages and strengths of both systems [84–86]. This has been motivated in particular by the fields of quantum information and quantum technology, which rely on interfaces of a quantum emitter with a coherent electromagnetic field. Examples for successful implementations include Rydberg atoms in MW cavities [87], single atoms coupled to optical cavities [88] or optical nanofibers [89], and superconducting circuits [90]. Atoms and membranes that are coupled to the field of an optical or MW were used to perform sympathetic cooling [83, 91–93].

Lack of flexibility for the experimental setup

While the studied systems are very different in their properties, these experiments have in common that they are not very versatile and the vacuum part usually is rather rebuilt than modified. Interfaces with cold atoms require an UHV environment to inhibit collisions with thermal particles, yielding hardly modifiable vacuum chambers that are surrounded by optics to cool and manipulate the atoms. However, an experimental setup where different systems can be brought into the vauum chamber would be desirable.

2.1 CONCEPT OF THE VACUUM SYSTEM

The vacuum system aims at providing the possibility to rapidly exchange the setup that is under investigation. The principle is shown in Fig. 2.1[1]. All

1 Our convention for the laboratory coordinate system is different from the physics coordinate system, in which we will describe the experiments. In the following we identify the laboratory coordinate system with (x_L, y_L, z_L) and the physics coordinate system with (x, y, z).

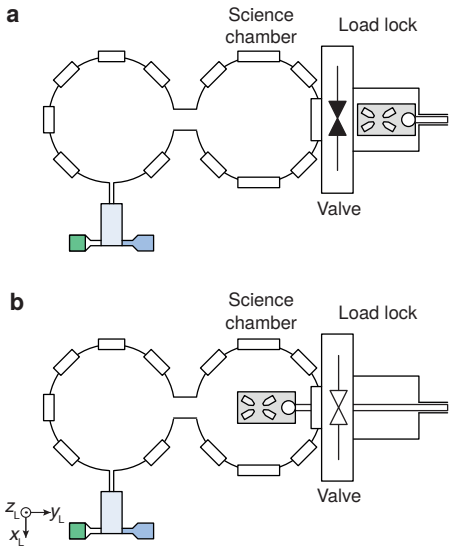

Figure 2.1: *Concept of the vacuum system.* An exchangeable science platform containing a setup with optical or electronic devices (e. g. optical cavities) can be exchanged through a load-lock chamber, which is separated from the science chamber by a gate valve. **a,** The platform is inserted into the load-lock chamber, which is subsequently evacuated and baked until UHV conditions are established. **b,** Once the pressure in the load-lock chamber and the science chamber are comparable, the gate valve can be opened and the platform can be translated with a sample manipulator. The vacuum in the science chamber is not harmed at any time during the exchange procedure.

An exchangeable platform to house the science setup

relevant parts of the setup are included in a science platform that can be exchanged through a second chamber, the *load-lock*, which is separated by a gate valve from the science chamber, where the experiment takes place. The mechanism is inspired by MBE experiments, where samples are exchanged on a regular basis through a load-lock chamber without compromising the vacuum in the science chamber [94, 95]. Transferring this concept to hybrid quantum systems allows us to perform research that is driven by physical questions rather than by an existing setup. Simultaneously, the vacuum chamber has to fulfill all requirements for a quantum gas experiment.

2.1.1 Coupling atoms and cavities

The interaction of a BEC with the mode of an optical cavity has shown to give rise to diverse phenomena [81], for instance Tavis-Cummings interaction [96, 97], optomechanical effects [98, 99] and a phase transition to a self-organized state [75]. This experiment aims at extending these concepts along different directions.

Apparatus for both bosons and fermions

The choice of bosonic or fermionic atoms has profound consequences on the accessible physics. Whereas bosonic quantum gases undergo a phase transition to a BEC and show a momentum distribution that is sharply peaked around zero, fermionic atoms either keep a broad momentum distribution up to the Fermi vector [100] or show condensed properties [101, 102], depending on their two-body interaction strength. These interaction-dependent properties give rise to new physics when coupling the momentum states of a fermionic quantum gas with light fields [81]. Our apparatus should therefore be able to produce both bosonic and fermionic quantum gases. We aim at a fast preparation time using state-of-the-art cooling and

	^{87}Rb	^{40}K	
Natural abundance	27.8	0.01	%
Abundance in the enriched source [104]		14	%
Radioactive lifetime	4.9×10^{10}	1.2×10^{9}	y
Atomic mass m	86.91	39.96	amu
Vapour pressure at 20°C	3.1×10^{-7}	1.3×10^{-7}	mbar
s-wave scattering length	100	174	a_0
K-Rb s-wave scattering length [105, 106]	-185(7)		a_0
Nuclear spin I	3/2	4	
Wavelength of D_2 line (vacuum)	780.24	766.70	nm
Wavelength of D_1 line (vacuum)	794.98	770.11	nm
Natural linewidth of D_2 transition Γ	$2\pi \times 6.07$	$2\pi \times 6.04$	MHz
Ground state hyperfine splitting	$2\pi \times 6.83$	$2\pi \times 1.29$	GHz

Table 2.1: *Bosonic Rubidium ^{87}Rb and fermionic Potassium ^{40}K.* The table lists some relevant properties for each isotope. S-wave scattering lengths are given for zero magnetic field in terms of the Bohr radius a_0. ^{87}Rb and ^{40}K data from [107] and [108], respectively, if not specified differently.

trapping techniques, which constraints the geometry and the target pressure for the different regions of the vacuum chamber.

The second key criterion is the flexibility in terms of the studied setup. Most experiments choose a cavity setup in the first place, which is inserted into the vacuum chamber before the pumpdown procedure. We choose a complementary approach and include a mechanism that allows to exchange the setup at any time while maintaining vacuum conditions in the chamber. This is achieved with a transfer system that moves a science platform to a load-lock chamber that is separated from the main chamber by a gate valve. The science platform houses the studied setup, which includes cavities or different devices.

2.1.2 Implementation of the bipartite chamber approach

Vacuum pressure requirements

The collision rate of most gas molecules at room temperature and pressure is around 10^{10} Hz. In order to produce a quantum gas at temperatures close to absolute zero it must therefore be well isolated from the environment. In quantum gas experiments this is achieved by carrying out the generation of the ultracold sample inside a UHV chamber at pressures around 1×10^{-11} mBar, deep in the molecular flow regime [103]. This results in collision rates of around 1 per minute, which do not cause significant heating during one experimental duty cycle of around 10 s for the generation of a quantum gas.

UHV describes the lowest achievable pressure range and is only required for few other applications, such as high-quality MBE, material analysis and particle accelerators [103]. The key requirements for UHV compatible materials are mechanical rigidity, resistance to corrosion, low vapour pressure, clean surfaces and a low concentration of external gases. Additionally, the

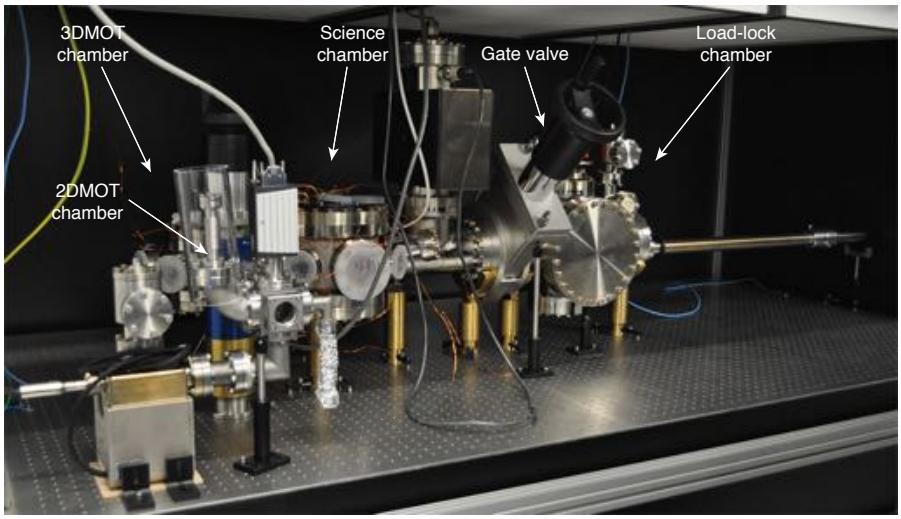

Figure 2.2: *The vacuum system.* Three different stainless steel chambers, separated by all-metal gate valves, form the vacuum system. The first one is called 2DMOT chamber and contains the atom sources. In the second chamber, a quantum gas is produced and the actual experiment takes place. It is divided into the 3DMOT chamber and the science chamber. The third chamber is the load-lock, where the science platform can be exchanged.

preparation process and the quantum gas are highly sensitive to external magnetic fields. As a consequence most vacuum chambers for quantum gas experiments, including ours, are built out of non-magnetic stainless steel.

Two-species apparatus for Rb and K

We choose ^{87}Rb and ^{40}K as bosonic and fermionic species, respectively. Some of their properties are listed in Table 2.1. The two isotopes were successfully used in combination previously [109]. Both belong to the group of alkali metals, whose elements show a simple level structure for the valence electron with closed dipole transitions at convenient optical wavelengths. The wavelengths of the D_2 transitions at 767 nm for ^{40}K and 780 nm for ^{87}Rb are close enough for common optical elements, yet far enough separated to combine and split the optical beam paths with dichroic optical elements. Additionally, their two-body collisional properties are well-suited for a fast thermalization of the atomic ensemble and a stable degenerate quantum gas. The collision rate for ^{40}K as well as the interspecies collision rate can be tuned with Feshbach resonances at easily attainable magnetic fields [53, 110]. Furthermore, this choice of isotopes allows extensions for mixtures [111] or Rydberg atoms [112].

Overview of the vacuum system

A picture of the entire vacuum system is shown in Fig. 2.2. The transfer rod for the science platform exchange is visible at the right end and connects to the load-lock chamber. The remainder of the vacuum system is dedicated to the production and probing of the quantum gas. An atomic beam is created at the opposite end of the vacuum system in the 2DMOT chamber and then sent into the 3DMOT chamber. The actual experiments are performed in the science chamber after optical transport (cf. Chap. 3). Optical viewports, coils for magnetic fields and antennae to generate RF fields are positioned nearby.

The design of the science platform and the exchange mechanism primarily aims at systems involving optical cavities, but is also well-suited for solid-state systems that do not require a cryogenic environment. Optical cavities with a high finesse are highly sensitive to changes in the optical path length

inside the cavity. Changes of the index of refraction are prohibited thanks to the UHV environment, but the physical length can in general change due to material expansion from temperature drifts and mechanical vibrations from ambient noise. For present-day cavities with finesses up to $\mathcal{F} \sim 10^6$, length stabilities at optical wavelengths λ below $\lambda/\mathcal{F} \sim 1\,\mathrm{pm}$ are required. We ensure a high passive stability with mechanically stable mounting and a multi-layer vibration isolation stage [113]. In addition, the cavity length can be actively stabilized by mirror mounts including piezo-electric elements.

Requirements for optical cavities

The driving voltage for the piezo components can be applied through a contact mechanism to the platform, which is disabled during the exchange procedure. In addition, the platform offers a number of other contacts to steer devices for other hybrid systems, such as high voltages for ion detection with a CEM or a MCP, and SMA contacts for RF signals. A thermal feedthrough allows to cool the platform or dissipate heat.

The science platform can be exchanged with a sample manipulator, which is magnetically controlled from outside the vacuum[2]. It allows to independently translate and and rotate the platform. The precise positioning of the platform is achieved by a docking station. It also serves as a junction for the contacts from vacuum feedthroughs and connects them with the platform. During the exchange the path of the science platform is led by a guiding system.

2.2 THE VACUUM CHAMBER

The entire vacuum system consists of three chambers: the 2DMOT chamber, the main vacuum chamber with the 3DMOT and the science chambers, and finally the load-lock chamber. In this section we describe in detail the design and construction of the former two, whereas the load-lock chamber is discussed in the context of the transfer system in Sec. 2.3.

2.2.1 2DMOT chamber

A main concern for the design of a quantum gas apparatus is the need to collect a large number of atoms and yet to achieve a long lifetime for cooled atoms. The production of a quantum gas requires extremely low pressures in the UHV regime, whereas the capturing of the atoms is more efficient at orders of magnitude higher pressures with the background gas ideally dominated by the desired species. This pressure ratio cannot be overcome within seconds during the experimental cycle. As a consequence, vacuum systems in quantum gas experiments typically consist of two parts at different pressures. The parts are connected by a differential pumping tube with sufficiently low conductivity to maintain the pressure ratio, but sufficiently large to transfer the atoms from one chamber to the other. Several ways exist for addressing this problem [114, 115], among which the 2DMOT stands out with high loading rates and a compact design [116]. For this reason we choose this technique to load the atomic cloud. The optimum pressure lies in the range of around 1×10^{-7} mbar. In order to obtain a lifetime of $10 - 100\,\mathrm{s}$ for the quantum gas, a pressure ratio of 10^4 has to be maintained between the 2DMOT chamber and the main vacuum region.

2DMOT as efficient atom source

The 2DMOT chamber was originally designed and built to serve as a pure ^{40}K 2DMOT. We modified and extended the components to make it com-

2 A video demonstrating the exchange of the science platform with the transfer system is available on the website: www.youtube.com/watch?v=CjjNgXaRo6g

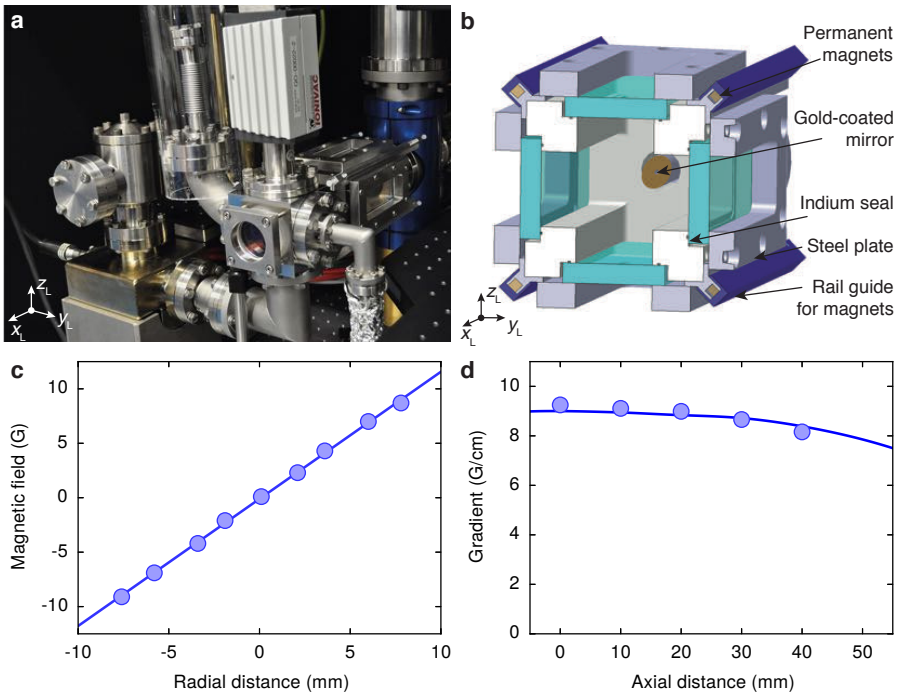

Figure 2.3: *The 2DMOT vacuum chamber.* **a,** Picture of the 2DMOT chamber with chamber body (right), the atom sources for ^{87}Rb and ^{40}K (bellows at the lower right and the top) and the ion pump (lower left). The valve connection to the main chamber is visible on the right (blue enclosure). **b,** CAD view of a cut through the 2DMOT chamber body. A gold-coated differential pumping tube reflects the counterpropagating beam to the axis of the atomic beam. The viewports are sealed to the chamber with an Indium wire and supported by means of a steel plate. Permanent magnets are positioned at each of the long chamber edges in a rail system. **c,** Displayed data shows the measurement of the magnetic field along the vertical direction in a test setup with the magnet configuration chosen similarly to the final setup. The fit (solid line) results in a gradient of 9.2(2) G/cm. **d,** Obtained gradient for several positions along the $-x_L$ axis with the origin at the center of the chamber. The solid line is a comparison with the theoretically computed gradient. Error bars from the fit are smaller than the marker size.

patible for a dual-species 2DMOT for ^{87}Rb and ^{40}K, including push and counterpropagating beams along the atomic beam axis [116]. Design, construction and tests of the original vacuum chamber with ^{39}K are described in the diploma and master theses by Roger Gehr [117], Dominik Leitz [118] and Thomas Uehlinger [119].

2DMOT chamber

A picture and a CAD view of the 2DMOT chamber are shown in Fig. 2.3a, b. The chamber body was milled from one piece of stainless steel to realize its custom design. It has a cuboid shape with four rectangular openings of 30×80 mm at the long sides for laser cooling beams with a large capture volume. Along the atomic beam axis, one additional viewport with 30 mm inner diameter gives access to the push beam.

Optical viewports

The optical viewports are unmounted fused silica substrates with a size of 40×90 mm from the supplier *Lens-Optics*. They are connected with the vacuum chamber by Indium seals. Rectangular stainless-steel frames hold them in place, separated by teflon sheets to protect the substrate surfaces from scratches. All viewports are AR coated with a broadband coating for $767 - 780$ nm on the substrate side facing towards air only. A coating on the

inner surface would risk a chemical reaction of the coating with the Indium wire that could lead to vacuum leakage.

At one end of the chamber, four CF flanges with DN 40 connections lead to the section controlling the background pressure. One of the connections comprises a pressure gauge (*Ionivac ITR90* from *Leybold*), which is a combined Pirani and ion gauge detecting the vacuum pressure both at ambient pressure and UHV. A second connection goes to a sputter ion pump (*25S-DI-2D-SC-220-N* from *Gamma Vacuum*) with a titanium-tantalum cathode and a nominal pump speed of 15 l/s. At the back of the ion pump anall-metal edge valve (*"Easy close"* from *VAT*) is included for further extension of the vacuum region or to connect a turbo-molecular pump. The chamber body is prevented from overconstraints at multiple support points by a metal bellow between the pump and the chamber body. At its inside it is lined with graphite tubes from the supplier *POCO Graphite*, which adsorb alkali metals to protect the ion pump from saturation from the atom sources [120]. The graphite tubes are held in place horizontally next to the bellow connecting the ion pump with the main chamber by a stainless steel post with 25 mm diameter from *Thorlabs*. All tubes and bellows are commercially available parts from the supplier *VACOM*.

Atom sources

The atom sources are contained in two more bellows at the remaining DN40 connections. The ^{87}Rb atom source is an ampoule from *Sigma-Aldrich* with metallic Rb of $> 98\,\%$ purity at natural abundances and a fill-in-weight of 5 g. It is placed in a DN16 metal bellow with sufficient flexibility to crack the ampoule following the chamber bakeout. A heating wire wound around the bellow gives control over the Rb vapour pressure inside the vacuum chamber, which in our case is optimum at around 40°C. The ^{40}K has been enriched to 14 % and was obtained as 30 mg of KCl salt from *Trace Sciences international*[3]. This compound has then been distilled into the ampoule as a pure metal by *Precision Glassblowing*, leaving a quantity of around 10 mg in the ampoule. For easier cracking, the ampoule has been scored with a glass cutter at the center and placed in a mount that allows to conveniently grab it with the bellow. As the experiment to date has not yet been operated with fermions, the ^{40}K ampoule remains closed.

Differential pumping tube

A differential pumping tube is connected at the opposite end of the chamber body. It is milled from a single piece of non-magnetic stainless steel, which was subsequently welded to two CF flanges on each end. It has a length of $L = 87$ mm and a conically shaped inner surface with diameters of $r_1 = 0.7$ mm and $r_2 = 2.1$ mm at the end towards and away from the 2DMOT chamber, respectively. The opening angle is adapted to the expected divergence of the atomic beam of $\theta \sim v_D/v_{\text{thermal}}$, with v_D the Doppler velocity and v_{thermal} the mean velocity of a thermal atom. The conductivity for a conical tube in the molecular flow limit is given by [103]

$$C = \frac{\pi r_1^2 v}{4}\left(1 + \frac{r_1 + r_2}{4 r_2^2} L\right) \text{l/s}. \tag{2.1}$$

For a mean velocity $v_{H_2} \sim 1900$ m/s of H_2, this results in a conductivity of $C = 5 \times 10^{-5}$ for the differential pumping tube, sufficient for the required pressure ratio.

In order to inject the counterpropagating laser beam along the axis of the atomic beam, the front end of the differential pumping tube is built as a

3 This company seems to have stopped the distribution of highly enriched ^{40}K recently. Another company, *American Elements*, still offers ^{40}K with concentrations of $> 10\,\%$.

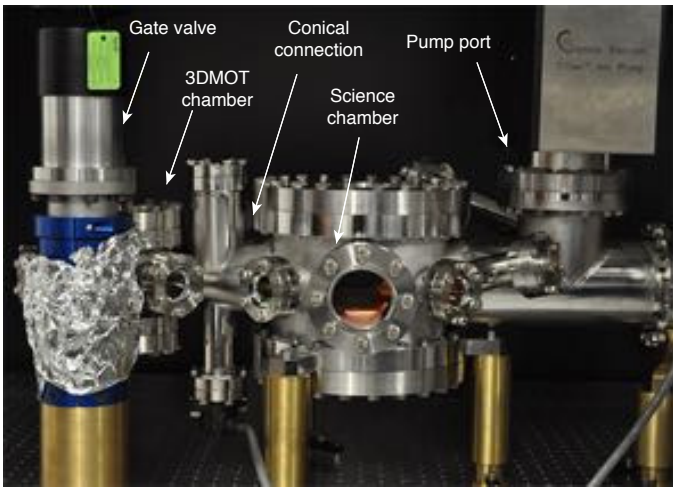

Figure 2.4: *The main vacuum chamber.* The main part of the vacuum is composed of the 3DMOT chamber (left, partially behind the valve to the 2DMOT chamber) and the science chamber (center), which are connected by a conical tube. The ion pump is visible on the right. The entire system is mounted on brass columns.

mirror that is angled by 45°. Similarly to the setup presented in [121], the surface is first given a mirror finish of 2P quality with a buffing machine. It is then coated with a gold layer of 150 nm for high reflectivity in the optical domain, followed by a second coating of 100 nm with SiO_2 to protect the gold surface. The outer diameter of the tube is 12 mm, an optimum between the size of the counterpropagating beam and the tube intrusion into the vacuum chamber. Other approaches to inject counterpropagating beams include polished copper [122] or aluminium surfaces [116], mounted flat [123] or angled mirrors [120], or mounted prisms [124].

Permanent magnets for the 2DMOT

In most setups the magnetic field gradient for the 2DMOT is created by electromagnetic coils. Here we use a different method with permanent magnets that are directly mounted onto the vacuum chamber, as shown in Fig. 2.3. At each long edge of the vacuum chamber, a rail houses up to 6 NdFeB magnets (grade 45M) from *www.supermagnete.ch*. The rails protrude the chamber length and ensure a homogeneous magnetic field gradient over the entire cooling volume. The gradient can be coarse-adjusted in the range of $5 - 13\,\mathrm{G/cm}$ by changing the number of magnets in the rails, and can be fine-tuned by $\pm 0.8\,\mathrm{G/cm}$ by changing the distance between the magnets with polyamide screws. The screws also allow to adjust the position of the zero crossing with respect to the center of the chamber. The constant magnetic field offset from the permanent magnets in the science chamber is below 1 mG and negligible compared to other sources such as the earth magnetic field. Measurements of the magnetic field gradient along the radial and longitudinal direction are shown in Fig. 2.3c, d. Further details on the permanent magnets are described in the semester thesis by Andreas Herrmann [125].

The 2DMOT chamber is connected to the main chamber with a DN40 all-metal gate valve from *VAT* that supports a pressure of 10^{-11} mbar against room pressure. The valve allows for changes at the 2DMOT chamber, e.g. replacing the atom sources or the ion pump, without compromising the vacuum in the main chamber. The valve is positioned on a brass mount with a total weight of 7.8 kg for high stability of the chamber. The height of the valve, and thereby of the entire 2DMOT chamber, can be adjusted

VIEWPORT TYPE	⌀ SUBS.	THICKN.	⌀ COAT.	NA
Science chamber top/bottom	46	5	38	0.42
Science chamber aux. top	32	4	24	0.07
Science chamber DN63	73	6	57	0.18
Science DN40	43	6	29	0.10
3DMOT chamber top/bottom	46	5	38	0.76
3DMOT chamber DN40	43	6	29	0.14

Table 2.2: *Viewports of the vacuum system.* For each viewport type the substrate diameter, the thickness (D), the diameter of the coated area and the NA for the optical access are listed. The coating area can be off-centred with respect to the centre of the substrate by up to 1 mm due to asymmetric vapour deposition. All length measures given in mm.

with a fine thread of 0.5 mm pitch built into the brass mount. The 2DMOT chamber with the gate valve is separated from the main chamber by a DN40 metal bellow, enabling the alignment of the atomic beam on the center of the 3DMOT in the main chamber.

2.2.2 *The main chamber*

The main chamber of the vacuum system is separated into two chambers that are dedicated to the cooling and the experiment with the sample, respectively. A picture of the chamber is shown in Fig. 2.4. In the *3DMOT chamber*, the atoms are captured and cooled in a 3DMOT, and then trapped in a hybrid trap with combined magnetic and optical confinement. Only close to quantum degeneracy the cloud is transported into the *science chamber*, where the actual experiment and the probing takes place. The separation of the preparation and the experimental zone allows for maximum optical and mechanical access in the science chamber, and for a design optimized to the needs of the experiment only [126].

Main chamber body

The chamber body is custom-welded from commercial non-magnetic stainless steel parts of type 316LN by the companies *VACOM* and *Kohler*. The two chamber parts have a vertically oriented cylindric shape with 104 mm and 200 mm inner diameter, respectively. They are connected by a tube that is shaped conically to give the maximum conductivity for the available space at each end. At the opposite side of the science chamber, a T-shaped DN100 tube section gives access to the load-lock chamber and the pumping section.

Optical viewports

The diameter and the height of the 3DMOT and the science chambers are chosen large enough to accomodate viewports at every 45° in the horizontal plane. With the exception of two DN63 viewports in the science chamber, which are positioned perpendicularly with respect to the long chamber axis, all horizontal viewports are of DN40 size. In order to achieve high optical access, the top and bottom flanges are built in a reentrant manner with a centered viewport at non-standard size, as illustrated in a CAD view in Fig. 2.5a. Some key dimensions of the viewports are listed in Table 2.2. The substrates consist of a synthetic fused silica compound named *Spectrosil2000* and were first mounted into their fitting by the special techniques group at *Culham Centre for Fusion Energy*, a unit of the *United Kingdom atomic energy authority (UKAEA)*. Subsequently, the substrates were AR coated on both sides by the company *Laseroptik* and then sent back for the final flange assembly. This

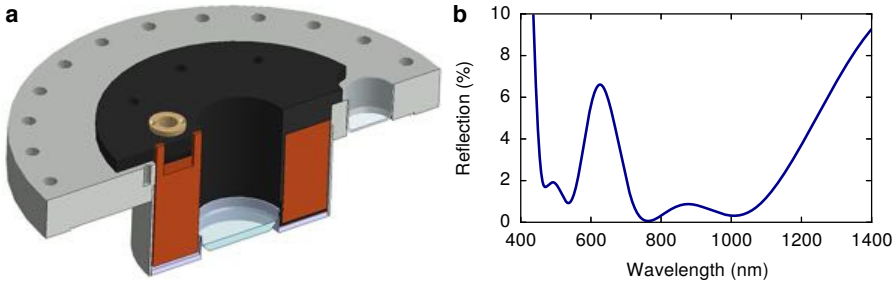

Figure 2.5: *Vacuum viewports.* **a,** Top flange of the science chamber including the science coil (brown) with aluminium mount (black) and temperature sensor (ochre). The viewports for the vertical axes of the 3DMOT and the science chambers are mounted in a reentrant flange, which enhances the optical access. The flange also provides sufficient space to bring magnetic coils close to the center of the chamber. **b,** Designed reflection spectrum for the coating of the viewports. The AR coating accounts for the Rb and K D_1 and D_2 transmission lines, electronic transitions between the $5P_{3/2}$ and a Rydberg state $NS_{1/2}$ with large $N \in \mathbb{N}$ for ^{87}Rb, far off-resonant light for cavity stabilization, as well as bare and frequency-doubled light from an Nd:YAG laser for attractive and repulsive dipole potentials.

procedure is necessary for optimal coating, because the flange fitting would reduce the coated area of the substrate and a coating of the bare substrates causes leakage at the metal-glass transition.

The design transmission spectrum for all vacuum viewports of the main vacuum chamber is shown in Fig. 2.5b. It takes into account the following wavelengths (in order of priority):

- Cooling and probing light for the atoms: Rb and K D_1 lines at 770 nm and 795 nm, and the D_2 lines 767 nm and at 780 nm
- Attractive potentials: Nd:YAG laser light at 1064 nm
- Cavity length stabilization: interferometrically with laser light at 830 nm
- Repulsive potentials: doubled Nd:YAG laser light at 532 nm
- Rydberg atoms: two-photon excitation of ^{87}Rb with $5S_{1/2} \rightarrow 5P_{3/2}$ (780 nm) and $5P_{3/2} \rightarrow NP_{3/2}$ with large $N \in \mathbb{N}$ (480 nm)

The connection between the 3DMOT and the science chamber includes a coaxial feedthrough with a floating shield SMA socket. The inner feedthrough side holds a capton-insulated cable leading to an RF coil that is placed at the entrance to the 3DMOT chamber[4]. Further electrical feedthroughs for the transfer system are placed at the bottom flange and the wall of the science chamber, including two SMA, one HV and a 19-pin feedthrough from the company *Accuglassproducts*. In addition, a high power connector from *MDC Vacuum Products* serves as thermal feedthrough. These feedthroughs are explained in more detail in Sec. 2.3.

Vaccum pumps

The UHV in the vacuum chamber is maintained by a combination of several vacuum pumps. The main pump is an ion pump with a nominal pump speed of 80 l/s (*100L-30-6D-SC-N-N* from *Gamma Vacuum*). Its working principle is based on a chain reaction of ionizing and accelerating gas molecules

4 A test after the bakeout showed a very small inductance of the connector, likely due to an internal connection of the wires. This resulted in very weak RF fields. In order to obtain sufficiently strongRF fields, we integrated an wire loop into the coil holder in the top flange of the 3DMOT chamber.

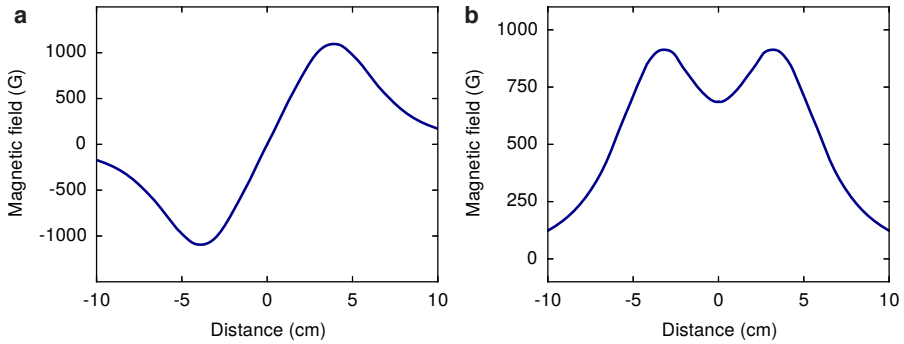

Figure 2.6: *Magnetic fields in the 3DMOT and the science chamber.* **a,** The magnetic coils for the 3DMOT chamber are connected in (quasi) anti-Helmholtz configuration and can produce gradients of up to 412 G/cm along z_L at a current of 400 A. **b,** The coils in the science chamber are connected in (quasi) Helmholtz-configuration with maximum magnetic field of 686 G in the center of the vacuum chamber at a current of 200 A. The curves are obtained from a numerical simulation of conductor loops.

towards the electrodes, where the molecules are adsorbed. This process is efficient for heavy air particles, e.g. N_2, O_2 or H_2O. Small air particles, in particular H_2, are predominantly pumped by two NEG pumps (*CapaciTorr D100* and *CapaciTorr D200* from *SAES Getters*) by particle adsorption into a porose TiZrV alloy [127–129][5]. They are placed inside the ion pump and at the connection between the two parts with nominal pump speeds of 200 l/s and 100 l/s, respectively. In addition, a *Mini Ti-ball* titanium sublimation pump from *Agilent technologies* can be activated to coat the inner surface of the vacuum chamber with a titanium layer that is reactive and adsorbs residual gas molecules. Its solid angle excludes the gate valve to ensure that the closing mechanism is unharmed. However, a titanium layer could form on the rail system on which the science platform is displaced (cf. Sec. 2.3). It is unclear if this produces dust when exchanging the platform after a high number of titanium activation cycles. The vacuum pressure is measured by a *UHV 24-p Extended Range* ionization gauge with thorium-iridium filaments from *Agilent technologies*, which is placed at the connection tube between 3DMOT and science chamber.

Vacuum pressure estimation

In the molecular flow regime ($p \ll 10^{-3}$ mbar), the expected pressure in the vacuum chamber can be determined from a calculation analogous to electrical conductances and voltages [103]. When a pump with speed S and limit pressure p_{lim} is connected to a vacuum chamber, the equilibrium pressure is given by

$$p = \frac{q}{S} + p_{lim}. \tag{2.2}$$

The total outgassing rate $q = \sum_i q_i$ is given by the outgassing rates q_i of each element of the chamber, e. g. chamber body, flange connections, feedthroughs or parts inside the chamber. The outgassing rates are usually specified by the producer, and for many materials have been measured with a high precision [134, 135]. If the pump is connected to the vacuum chamber

5 The NEG technology was developed for the accelerator rings at CERN both as a porose pump material [130, 131] and as a coating of the inner ring surface [132]. Nowadays, the coating is also commercially available at several particle accelerator centres upon request, e.g. CERN and GSI [133].

with a tube of conductance C, its speed is reduced to the effective pumping speed

$$S_{\text{eff}} = \frac{S}{1 + S/C}. \tag{2.3}$$

The pressure p' in a second chamber that is attached to the first one with a tube of conductance C is

$$p' = \frac{S}{C} p. \tag{2.4}$$

Together with Eq. 2.1 and its limit for constant radius $r_1 = r_2$, this is sufficient to estimate the pressures in our vacuum system. We obtain, under conservative assumptions, $p_{\text{Science}} \sim 7 \times 10^{-12}$ mbar for the science chamber, $p_{\text{3DMOT}} \sim 5 \times 10^{-11}$ mbar for the 3DMOT chamber, and $p_{\text{2DMOT}} \sim 2 \times 10^{-7}$ mbar for the 2DMOT chamber. The calculation excludes the ion pump in the 2DMOT chamber to simulate a dominant ^{87}Rb vapour pressure. The reliability of these simple formulas has been confirmed within several per cent by extensive Monte-Carlo studies [136, 137] and experiments [103], such that the uncertainty of the estimate for an empty vacuum chamber is mainly given by imprecise specifications of the vacuum components and incautious vacuum procedures during assembly.

The chamber is fixed on the optical table with massive brass mounts of 50 mm diameter and 2.4 kg weight each. They support the vacuum chamber at three points of the science chamber to avoid overconstraints. Additionally, a fourth identical mount supports the lower flange of the 3DMOT chamber to minimize vibrations along the long chamber axis.

Magnetic coils

The reentrant flanges not only house the optical viewports but also include coils for magnetic field generation. The flange shape allows to position the coils close to the atomic cloud and therefore to generate strong fields. Eddy currents during the switching are also reduced compared to a mounting at larger distance as the enclosed amount of metal is minimized. The coils in the science chamber are designed to reach the relevant intra- and interspecies Feshbach resonances of ^{40}K and ^{87}Rb at 202 G, 221 G and 543 G [138–140] with a current of below 200 A. The coil holders in the 3DMOT chamber house two coil pairs. The first one is designed to create the magnetic field gradient for a strongly confining quadrupole trap. The second one serves as an offset field to provide a well-defined quantization axis along the vertical axis during optical pumping and experiments at this position. It allows to create magnetic fields of up to 37 G at a current of 10 A. The electric properties of the coils are listed in Tab. 2.3, and the calculated magnetic fields at the center of the vacuum chamber are shown in Fig. 2.6. All coils were wound by the company *Oswald* in custom-designed holders that are directly screwed into the vacuum chamber. A slit in each coil holder prevents the buildup of eddy currents during the switching of the current. In addition, each holder provides a cut-out for a temperature sensor that allows to monitor the coil temperature. The coils for the quadrupole trap and the Feshbach field are wound from a $4 \times 4\,\text{mm}^2$ large wire with a hollow core of 2.5 mm diameter for water cooling. The wire is surrounded by a 0.4 mm thick capton insulation. The offset coils consist of a smaller wire with a quadratic $1 \times 1\,\text{mm}^2$ cross-sectional area without coolant hole.

Further offset coils are directly wound around the vacuum chamber on all axes in the science chamber and on the two remaining axes of the 3DMOT

COIL	N	R (MΩ)	L (μH)
Science chamber top	73	29.8	231.24
Science chamber bottom	72	29.3	227.35
3DMOT chamber top (gradient)	19	7.1	19.40
3DMOT chamber bottom (gradient)	19	7.0	19.38
3DMOT chamber top (offset)	50	269	176.5
3DMOT chamber bottom (offset)	50	269	177.1

Table 2.3: *Electric properties for the coils of the main vacuum chamber.* Shown are the winding number (N), resistance (R) and the inductance (L) at 1kHz. The measurements were done by the company at a temperature of 22 °C and confirmed in our test measurement.

chamber. The winding number of each coil is chosen such that the magnetic field from each coil pair is around 1.2 G/A at the center of the vacuum chamber. The capton-insulated wire has a round shape with a diameter of 1 mm, limiting the maximum driving current without overheating to around 8 A [141].

2.3 THE TRANSFER SYSTEM

We now turn to a description of the transfer system, starting with the load-lock chamber that is connected to the main chamber. It primarily consists of the load-lock chamber, the science platform and the docking station. In order to guarantee a successful and reliable transfer of the science platform, additional components are placed into both vacuum chambers and ensure the correct guidance, the positioning and the contact of the science platform during and after the transfer.

2.3.1 The load-lock chamber

The chamber body for the load-lock chamber is welded from non-magnetic stainless steel components of type *316LN*, which are provided by the supplier *VACOM*. Its principal component is a DN100 vacuum tube, which extends the main chamber at an equal diameter. The vacuum tube serves as the channel through which the science platform can be translated. At one side of the load-lock chamber, a DN200 flange gives large-space access to the principal tube in order to exchange the science platform. A *NEXTorr500* pump from *SAES*, which represents a combination of an NEG and an ion pump [142], is connected at its top and maintains an UHV with a pressure below 10^{-11} mbar. An additional DN40 T-shaped tube is welded at the top of the chamber body and contains connections to a *UHV 24-p Extended Range* ionisation gauge from *Agilent technologies* and an edge valve for pump down with a TMP. The load-lock and the science chamber are separated by a DN100 all-metal gate valve from *VAT*, which provides a sufficiently large diameter to pass through the science platform during the exchange process. The valve can be operated manually by a hand wheel, which is mounted at an angle of around 30° with respect to the vertical axis to reduce the total height of the vacuum system. Blind flanges opposite to the vacuum pump

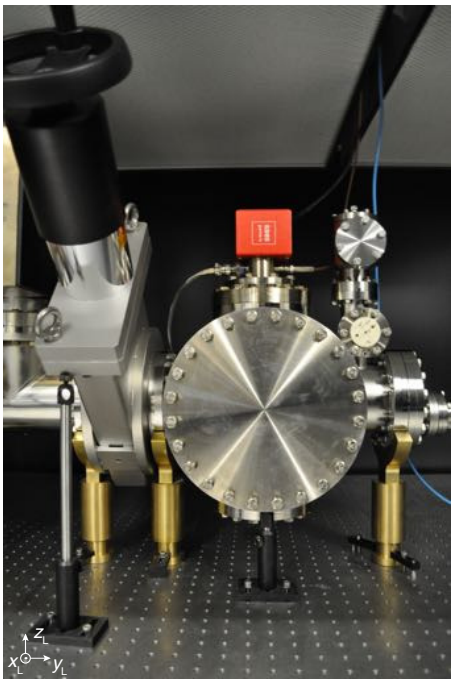

Figure 2.7: *Picture of the load-lock chamber.* The science platform can be inserted into the chamber through the DN200 flange shown at the front of the chamber. It is connected to the transfer rod (on the right, not shown) by a bajonet fastening. The vacuum in the load-lock chamber is maintainted by a *NEXTorr* pump. During a platform exchange, the load-lock chamber is vented through the edge-valve and the new platform is inserted through the DN200 flange. Then the chamber is pumped with a TMP connected to the edge valve and once UHV is reached, the gate valve is opened and the science platform is transferred by displacing the transfer rod with magnetic rings.

and the opening flange ensure a higher symmetry of the chamber during the welding process.

The sample manipulator

The sample manipulator is connected at the opposite side of the gate valve. It is an all-metal sealed linear-rotary feedthrough, which was customized by the company *Ferrovac* based on the model *RMDG40*. Similar components are typically employed as sample transporters, e. g. in MBE vacuum systems. The feedthrough consists of an elongated vacuum tube with a rod inside that can be translated or rotated thanks to two rings that are attached around the tube. The rings couple to the rod with the help of two sets of rare earth magnets on the air and the vacuum sides. The rod consists of an inner and an outer shaft with equal lengths of 890 mm. It is mounted on dry-lube coated ball bearings for high-precision guidance. The two rings allow to translate the rod over a distance of 700 mm and to independently rotate the inner and the outer shaft. The magnetic coupling supports a linear force of up to 70 N and a maximum torque of 5 Nm. A male bajonet connector is mounted at the tip of the outer shaft, and a slotted screwdriver extends from the tip of the inner shaft.

Vacuum chamber mounts

The chamber is lying on top of two sickle-shaped brass mounts that sustain the chamber without overconstraining it, as it is already fixed to the main chamber. However, a third mount is directly fixed to the end of the rod, correcting a residual angle originating from a deformation during bakeout.

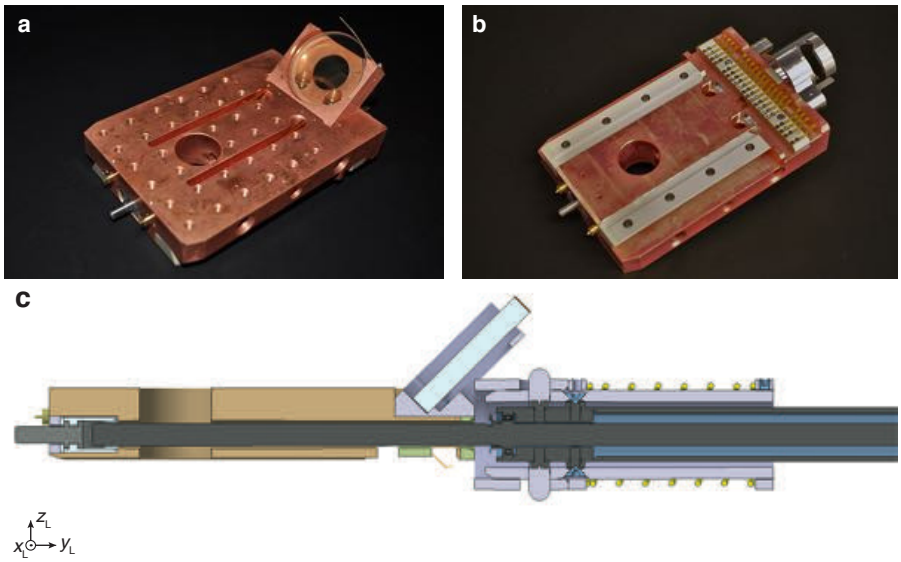

Figure 2.8: *The exchangeable science platform* **a,** Top view of the platform with OFHC body, angled mirror for optical access along the axis of the platform transfer and high-resolution optical access along the vertical direction. **b,** Bottom view of the platform with PEEK guidance parts and the contact bar providing steering voltages for electrical devices on the platform. **c,** CAD view of the platform attached to the sample manipulator. It has an outer shaft with bajonet fastening and an inner shaft with a screwdriver that passes through the platform and controls a screw at the platform front end to attach it to the docking station.

2.3.2 The science platform

Each employed science platform is different and designed according to the needs of the specific setup. In the following, we show the properties of an empty platform that contains only the elements required for the transfer and for positioning and contacting to the docking station. An exemplary model is shown in Fig. 2.8.

Design of the science platform

The platform body consists of OFHC copper with a size of $118 \times 80 \times 20\,\mathrm{mm}^3$. The center of the vacuum chamber—the position of the quantum gas—is situated 10 mm above the upper surface. A cut-out below the quantum gas position facilitates optical access from below. Its diameter and angle of aperture match the NA of the viewport in the lower reentered flange. A dove-tail construction made of PEEK ensures a precise guiding into the docking station with a reproducibility of around 10 µm. The required width was determined with gauge cylinders that allow its reproduction in future platforms with a high precision, see Fig. 2.9.

Mirror to retrieve optical access on the transport axis

The optical access inside the chamber along the axis of the transfer rod is blocked by the gate valve between the load-lock and the main vacuum chamber. We retrieve this optical axis by including a mirror into the platform that is mounted at its back with an angle of 45° from the horizontal. It deflects beams along the axis of the transfer rod to the vertical direction through a viewport in the top flange, see Sec. 2.2.2. The mirror substrate has a diameter of 40 mm and a thickness of 6 mm and is HR coated for $760 - 1064\,\mathrm{nm}$ at 45°. The mirror is fixed with a copper streak and can be replaced according to the needs.

Electrical contacts

At its lower back the platform includes a bar with 20 gold-coated OFHC copper contacts that allow to steer electronic devices on the platform. The

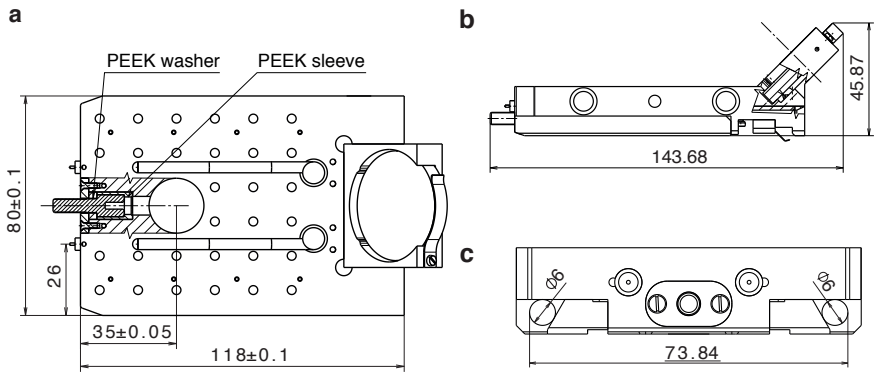

Figure 2.9: *Technical drawings of the science platform* **a,** Top view with a cut through the front screw bearing that connects the platform to the docking station. **b,** Side view showing the mirror angled at 45° for optical access along the transfer axis. **c,** Front view with SMA contacts. The width of the science platform including the angled dove-tail wings was determined with gauge cylinders. All measures in mm.

contacts connect to the docking station, where cables are guided to two electrical feedthroughs, see Fig. 2.8. One of the contacts is compatible with HV up to 10 kV. It is further separated from the other contacts to avoid a vacuum breakthrough [141]. All other contacts are designed to withstand voltages up to 500 V. The front end of the platform features two SMA connectors that stem from UHV-compatible coaxial cables from the producer *Accuglassproducts*, where the cap nut was prised open. They are placed in a tailored opening and fixed with screws.

Mechanical construction of the transfer rod

Two mechanisms are required for a platform exchange, see Fig. 2.8: the transfer rod needs to connect with the platform that can be removed after the exchange, and the platform needs to connect with the docking station to stay at its well-defined position. The former is achieved with a female bajonet receptor at the back of the platform. It is custom made from non-magnetic stainless steel and tailored to fit the male part on the transfer rod. The latter is realised with a slotted screw with M6 thread at the front end of the platform that connects to a thread in the docking station. It is driven by a screwdriver at the front end of the transfer rod and placed inside a bearing made of non-magnetic stainless steel and PEEK. The measures of the screw mechanism are chosen to minimize the contact of the screwdriver to only the screw, and the material choice was optimized to prevent dust production during screwing and insertion of the screwdriver.

As the platform contains a number of parts for electrical insulation, thermal conductance and the guiding system, it is prompt to virtual leaks. The design minimizes surface contact and incorporates venting channels and holes wherever necessary [103]. The screw holes are vented equally by an opening to the thread or a hollow core.

2.3.3 Docking station

The purpose of the docking station is to provide the suitable environment for positioning, thermal contact, vibration isolation, and electrical connections of the science platform. Its design is illustrated in Fig. 2.10. The base consists of two layers of non-magnetic stainless steel, which are designed to yield a high mass for an efficient vibration isolation. The layers are separated

Vibration isolation

by cylinders made of *Viton*, a vacuum-compatible fluoroelastomer material. The cylinders are placed close to the nodes of the lowest eigenmodes of the structure to suppress the coupling to external noise [113]. Vertical OFHC cylinders secure the structure from tipping over, e.g. during the platform exchange. The lowest layer is directly screwed into the bottom flange. The rings result in masses of 1.2 kg and 3.9 kg for the lower and the upper layer, respectively. We can model the transfer function of the system by approximating its behaviour with coupled damped harmonic oscillators [113]. As shown in Fig. 2.10, we obtain a resonance at ~ 40 Hz and a suppression of more than -60 dB at a frequency of 1 kHz.

The top layer of the docking station is made of OFHC, providing a good thermal contact with the front surface of the science platform. A cut-out clears the view to the viewport in the bottom flange. The thermal environment can be controlled through an OFHC stranded wire with large thermal conductivity that connects the platform with a thermal feedthrough. The electrical connections are combined at a PEEK bar with 20 contacts to capton-insulated ribbon cables that consist of stranded wire of silver-plated copper with a thickness of 0.3 mm (28 AWG). In addition, two female SMA connectors guide the signal through coaxial cables to the vacuum feedthroughs at the bottom flange.

Guiding mechanisms

The platform is guided by several components to ensure that it reaches the docking station. Starting from the gate valve, it is supported by a rail system that catches the runners of the platform and brings the platform to the appropriate height. At the docking station, the platform is again guided laterally by two wedged PEEK blocks before it reaches the dove-tail rail. To fix the platform to the docking station, the screw at the platform top can be turned into a screw hole.

2.4 ASSEMBLY AND BAKEOUT

The procedures to achieve UHV conditions vary among different research facilities. In the following, we describe the approach that was followed in our experiment.

Electropolishing

The welded body of the main vacuum chamber and of the load-lock were electropolished by the company *Stalderfinish*. This process is an electrochemical abrasion technique, in which the metal is removed by placing the component as anode in an electrolyte liquid. As a result, the surface roughness and thereby the total surface area is reduced.

Cleaning procedure

Subsequently, all parts were cleaned for around 60 min in an ultrasonic bath with a 1:9 mixture of an ultrasound cleaner (*Tickopur R60* from *Bandelin*) and tap water. Then the parts were rinsed in deionized water to wash away the soap. The bakeable parts were then baked at 300 °C under air in an oven. Finally, the components were placed in an ultrasound bath of first acetone and then methanole (spectroscopic quality with $> 99.5\%$ purity) for ~ 60 min. Large components that do not fit into the bath container were wiped instead. This two-step cleaning procedure is necessary, because acetone is a strong solvent but leaves residues during evaporation, which then have to be removed with methanole. The *Viton* cylinders were prebaked at 200° and 10^{-5} mbar over two days to reduce the outgassing, and then wiped with methanole. During cleaning and assembly, all parts were handled with nitril gloves, since some latex gloves can bear traces of powder. To temporarily protect cleaned parts, we used oil-free alumnium foil from the company *All-foil*.

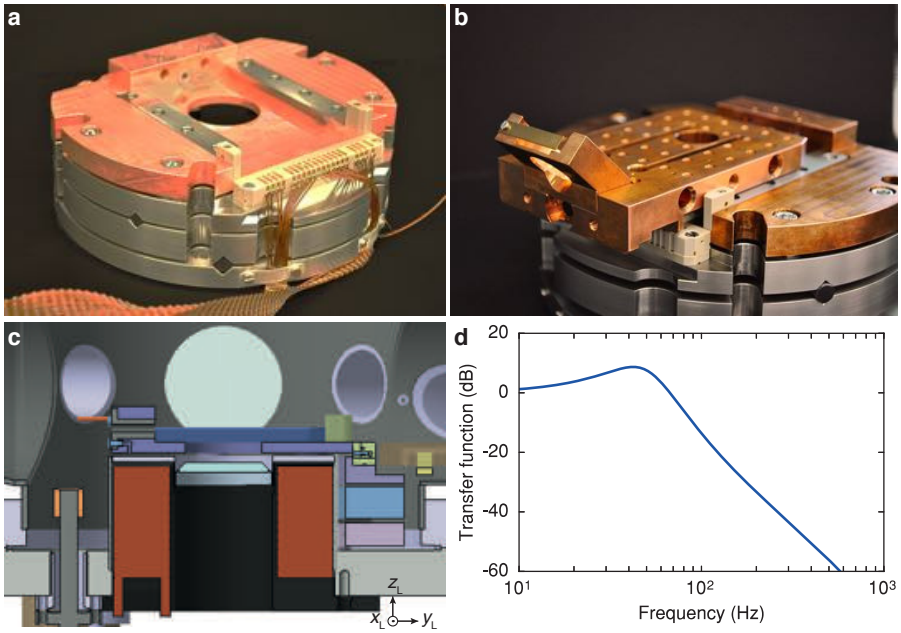

Figure 2.10: *The docking station* **a,** Top view of the docking station. It consists of stainless-steel rings (gray) separated by *Viton* (dark gray) and a copper housing for the platform at the top (red). The contact bar with the capton-insulated wires provides the steering voltages to the platform. **b,** The science platform slides into the decking station with a dove-tail shaped guidance system. **c,** Cut of the science chamber with docking station. The rail system for guidance towards the docking station is visible on the right. **d,** Simulation of the vibration isolation with coupled damped harmonic oscillators for a two-layer system with 1.2 kg und 3.9 kg.

The electrical feedthroughs, the viewports and other fragile components were closed with annealed copper gaskets, as they require a lower tightening torque. All other flange connections are closed with standard OFHC gaskets. The screws for flange tightening are of nonmagnetic stainless steel (grade A4). To inhibit the formation of permanent metal-metal bonds between screws and nuts, all threads were brushed with vacuum grease from the company *Molykote*[6]. The screws were tightened with plate nuts in a crisscross pattern with around 90° a time until the flange metal faces would barely touch. Annealed copper gaskets should be turned less per iteration.

Bakeout procedure for the main and the load-lock chamber

The closed vacuum chamber was then wrapped in alumnium foil, heat tape and thermal insulation. The temperature was monitored by six sensors that were directly attached to the chamber body at different positions and served as feedback for the heat tape current controller. The pressure during the bakeout procedure was monitored in the science chamber and the load-lock chamber. After connecting a TMP, we linearly increased the temperature to 200 °C (limited by the *Viton*) over 8 h, held the temperature until the desired pressure was reached, and decreased the temperature to 70 °C. Then, the NEG and ion pumps were activated. After a second ramp to room temperature the pressure fell below the range of the ion gauge. No measurable leak was detected when applying He to the flange connections.

2DMOT bakeout procedure

The 2DMOT chamber was assembled in a second step, after the main chamber had been baked out[7]. The cleaning procedure was followed similarly to the main chamber, but without the prebaking at 300 °C under air. The viewports were then connected with an Indium wire with 1 mm diameter that was laid into a groove of $0.7 \times 1\,\mathrm{mm}^2$. This measure was chosen to obtain a $5 - 15\,\%$ higher cross section for the wire than for the groove. Indium is toxic and therefore should be handled with gloves. The bakeout of the 2DMOT chamber was performed similar to the main vacuum chamber, but at a temperature of 80 °C, sufficiently below the melting point of Indium at 156 °C. Following the bakeout and ion pump activation we obtained a pressure of 1×10^{-9} mbar. A measurement with an RGA identified H_2 as the dominant molecule after bakeout. After breaking the ampoule through the bellow and heating it to ~ 40 °C, the pressure gradually increased up to 1×10^{-7} mbar over several days.

6 A cleaner alternative are silver-plated screws.

7 Due to a machining mistake in the welding of the differential pumping tube, the 2DMOT chamber is rotated by $5 - 10°$ around its long axis.

3

PREPARING AND PROBING A BOSE-EINSTEIN CONDENSATE

Before the actual experiment is performed, the BEC is prepared in an experimental cycle that includes the trapping, cooling and the transport of the atomic cloud into the cavity setup. The preparation sequence is designed to yield a fast cycle time while maintaining a stability that allows the experiment to run without supervision. In future, this will enable us to acquire large datasets. Here, we first give an overview of the entire experimental cycle and then separately explain every step of the preparation and probing process, including a detailed description of the required optical, electrical and mechanical components. We put particular emphasis on the presentation of the transport of the atomic cloud, which is based on a new technique involving focus-tunable lenses.

CHAPTER CONTENTS

Overview of the experimental cycle

The entire experimental cycle for the preparation of the BEC, the experiment and the probing lasts around 8 s. Fig. 3.1 illustrates the key steps and shows the cycle on a time bar. The cycle contains the following steps:

MOT We create an almost collimated beam of ^{87}Rb atoms in the 2DMOT chamber and therefrom load atoms into the 3DMOT in the adjacent chamber with a rate of 2.5×10^{10} atoms/s. After a loading time of 0.5 s, we capture around $5(1) \times 10^9$ atoms at 390(10) µK.

MOLASSES COOLING We switch off the gradient field of the 3DMOT and perform molasses cooling for 5 ms. This results in a temperature of 7.4(8) µK without detectable atom loss.

MAGNETIC TRAP After switching off the repumping laser beams and depumping the atoms into the $|F = 1\rangle$ hyperfine states for 5 ms, we switch off all beams and capture the atoms in a magnetic quadrupole trap with a field gradient of 90 G/cm. Without additional optical pumping, we capture around 40 % of the atoms. We ramp up the magnetic field

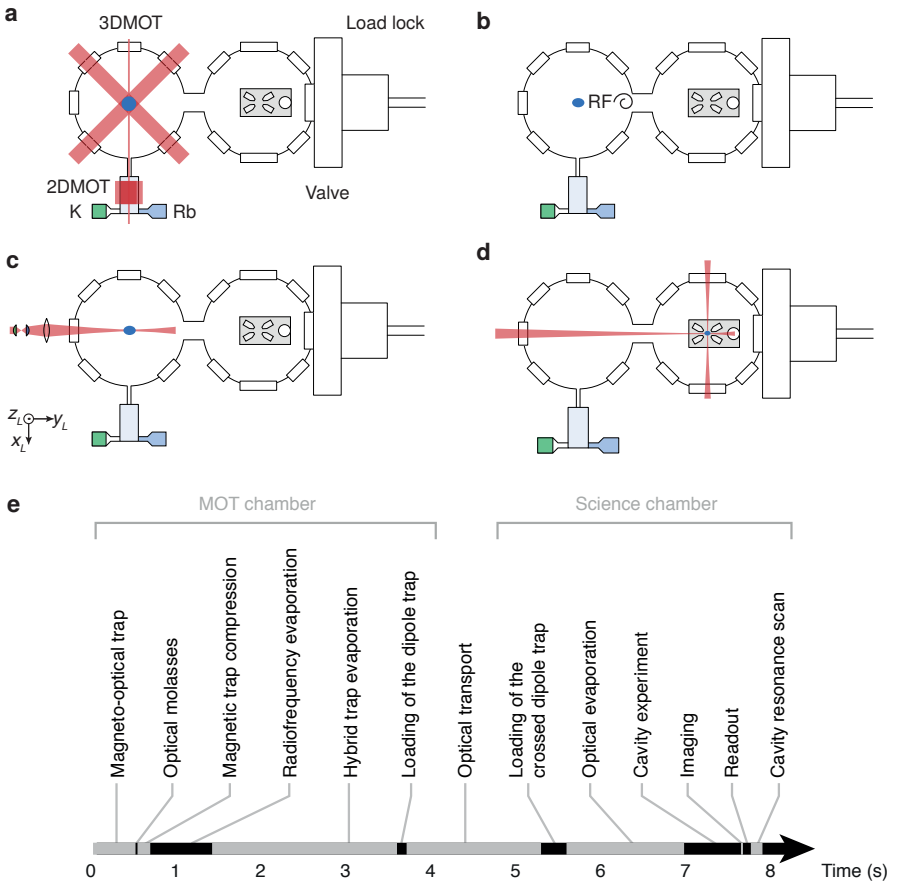

Figure 3.1: *Overview of the experimental cycle.* The pictures **a–d** show top views of the chamber at different points of the preparation sequence. **a,** ^{87}Rb atoms are loaded in a 3DMOT from an atomic beam created in a 2DMOT, followed by molasses cooling. **b,** The laser-cooled atoms are loaded in a magnetic trap and evaporative cooling with a ramped RF field is performed. **c,** The atoms are loaded in a dipole trap and transported into the Science chamber by displacing the trap focus. **d,** After the transport, the atoms are loaded in a crossed dipole trap and optically evaporated until reaching an almost pure BEC. Gravity points along $-z_L$. Adapted from [143]. **e,** Illustration of the experimental cycle on a time bar. The entire cycle lasts around 8 s.

to 403 G/cm within 0.2 s to increase the atomic collision rate, ending up at a temperature of 80(5) μK.

RF EVAPORATION We apply an RF field to the tightly trapped atoms that couples the magnetically trapped $|F = 1, m_F = -1\rangle$ state with the untrapped $|F = 1, m_F = 0\rangle$ state. Within 0.7 s the RF frequency is ramped from 52 MHz to 25 MHz to cool the atoms with forced evaporation. We end up with around $2.5(3) \times 10^8$ atoms at a temperature of 35(3) μK.

HYBRID TRAP We now load the atoms into a hybrid trap with axial magnetic and radial optic confinement. To this end, we linearly decrease the magnetic gradient to 25 G/cm over 2.2 s. Simultaneously, an optical dipole beam is ramped up to 3.3 W over 1.5 s creating a dipole trap of $U_0 = -k_B \times 195\,\mu K$ potential depth. At the same time we linearly decrease the RF frequency to 4 MHz to compensate for the weaker magnetic confinement. We end up with a dense cloud of $1.8(1) \times 10^7$ atoms at 9.4(1) μK.

OPTICAL TRANSPORT By gradually switching off the magnetic field gradient over 0.1 s, the atoms are trapped in a pure dipole potential. We transfer the cloud from the 3DMOT chamber to the science chamber by displacing the focus of the dipole beam with a tunable lens in an s-shaped ramp over 1.6 s. The atom number and temperature does not change significantly during the transport.

CROSSED DIPOLE TRAP We switch on an additional dipole beam along the x_L axis, perpendicular to the transport beam, within 10 ms with a power of 1 W, and then lower the power of the transport beam to 1.2 W over 0.3 s in order to achieve similar trap depths of $U_0 = -k_B \times 50\,\mu K$ for both beams. After 0.1 s free evaporation, we obtain a cloud with $4.1(1) \times 10^6$ atoms at 11.3(2) μK. The temperature is further reduced with two linear evaporation ramps. During the first one, the power of the transport beam and the crossed dipole beam are linearly lowered over 0.5 s to 0.12 W and 0.14 W, respectively, creating a trap depth of to $U_0 = -k_B \times 14\mu K$ with similar contributions from both beams. We obtain atomic clouds right above the critical point for the BEC with $1.23(6) \times 10^6$ atoms at 1.1(1) μK. The second evaporation ramp of 0.8 s is linear again with a final trap depth of $U_0 = -k_B \times 2.1\mu K$. We achieve almost pure BECs of $2.13(5) \times 10^5$ atoms, which can be increased in size with longer 3DMOT loading and evaporation ramps.

3.1 INFRASTRUCTURE

Laboratory environment

The experiment is arranged in a room with an area of 24 m^2. An optical table from the company *Newport* houses the vacuum chamber for capturing, cooling and probing the atomic cloud as well as the required optical setup. The table has a size of 240 cm × 120 cm and is floated with pressurized air to suppress mechanical vibrations. The laser beams are generated and prepared on a second, equally-sized optical table in the same room and then guided to the main optical table through PM single-mode optical fibres. A second room connecting to the main labratory serves as a preparation lab for new developments, and also houses the dipole trap laser due to space constrains.

The room temperature is stabilized by an air-conditioning system to around ±0.5° C. A secondary air-conditioning system generates filtered air

with a set temperature below room temperature. The filtered air exits flow boxes from the company *Camfil*, producing a laminar vertical air flow on the optical tables. The optical tables are enclosed by composite aluminium panels *Alubond*, which are mounted in an *ITEM* structure without mechanical contact to the optical table in order to avoid mechanical vibrations. This results in an almost dust-free environment with an increased temperature stability of $\pm 0.05°$ C. Residual fluctuations of the environmental parameters are due to the unregulated humidity taking values of between $20 - 80\%$.

Environment control system

All environmental parameters are monitored and logged in an ENVICO system developed within the group [144]. It consists of a base unit cumulating diverse sensor types. Here, their measurements are read out and stored in a MySQL database. The base unit also allows to set limits to each sensor and provides a 5 V pull-down line that is used as an interlock, e. g. for cooling water, magnetic coils and high-power lasers.

Experiment control hardware

We use a control system involving five computers in a client-server architecture to control the experiment and acquire data. Each step in the experimental cycle involves the control of 36 analog-output channels, 64 digital-output channels and further devices steered via a LAN network. All analog and digital channels are galvanically separated from the steered devices by opto-couplers or transimpedance amplifiers. The set values in terms of magnetic fields, laser beam intensities and frequencies are monitored on oscilloscopes, frequency counters and a wave-meter (*WS7* from *HighFinesse*).

Experiment control software

On a software level, the control framework is based on the language C++ and has been developed within our group [145]. The timing of the experimental cycle can be edited by a control program with a GUI in a matrix-type representation with timing edges on one axis and hardware channels on the second axis. Each entry describes a constant or time-dependent value for the specific hardware channel at the corresponding time edge. The description is saved in XML format and sent to the main *runner* computer, which interprets the description and uploads the results into all hardware devices. The timing of all devices is controlled by TTL pulses with a precision of 100 ns, synchronized by a 10 MHz clock that is stabilized with a GPS receiver. If no changes are made, the last XML file is automatically repeated as an idle sequence to ensure thermalization of the experimental setup. The XML file is shared with three more computers for readout of CCD cameras and SPCMs. The acquired images and photon data include the XML file as metadata to allow reconstruction of the employed sequence at a later point.

3.2 LASER COOLING

The first step of the experimental cycle is based on Doppler cooling [146, 147]. In brief, the cooling effect originates from the Doppler shift that brings the transition frequency of an atom on resonance with a red-detuned beam propagating opposite to the velocity of the atoms. As a consequence, photon scattering is enhanced for moving atoms compared to resting atoms. As a consequence, the recoil momentum from photon absorption establishes an effective friction force. An additional restoring force of the photon scattering is achieved by spatially modifying the detuning with a Zeeman shift, which increases the photon scattering rate with the distance from the trap center. Counterpropagating beams along all three spatial directions allow for isotropic cooling and trapping of the atomic cloud in a 3DMOT.

Loading a 3DMOT from a 2DMOT

An efficient way to capture the atoms in the 3DMOT is provided by a 2DMOT, which creates an atomic beam of high brilliance by laser cooling

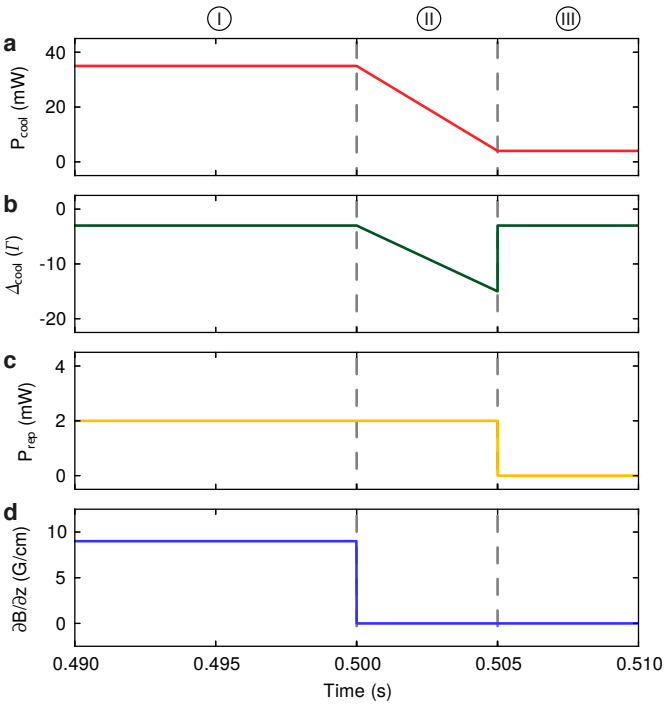

Figure 3.2: *Timeline of the laser cooling stage.* All laser cooling beams as well as the magnetic field gradient are switched on at $t = 0$. The 3DMOT (I), the molasses (II) and the depumping stage (III) are separated by dashed lines from left to right. The traces show **a,** the power of the cooling light per beam, **b,** its detuning from the atomic resonance, **c,** the power of the repumper light in each beam and **d,** the magnetic field gradient.

and trapping the atoms along two directions only [116, 148]. We use an extended variant, the so-called 2D+MOT, which contains an additional pair of beams along the axis of the atomic beam to also control the velocity distribution along the propagation axis. This setup has shown very high flux rates in previous experiments [116, 120–124, 148–152].

We then switch off the magnetic field gradient and perform laser cooling with an optical molasses, see e. g. [153, 154]. This technique is based on the fact that both the scattering rate and the light shift in a polarization lattice are not only spatially varying but also depend on the Zeeman sublevel. If a high photon scattering rate and a positive light potential coincide for the Zeeman sublevels, a phenomenon called *Sisyphos* effect takes place, where the potential energy that the atoms gain from climbing potential hills is removed with scattered photons. This process is fundamentally limited by the atomic recoil energy and temperatures on the order of 1 µK can be achieved, well below the Doppler limit [154, 155]. At the end of the laser cooling sequence we switch off the repumping laser in order to depump all atoms into the lowest hyperfine states. The entire laser cooling stage is illustrated on a timeline in Fig. 3.2.

Molasses cooling

3.2.1 Laser system

Parts of the laser system have been described in [156]. It is based on three diode lasers [157, 158] at 780 nm. Two of them (*DL pro* by *Toptica*) achieve

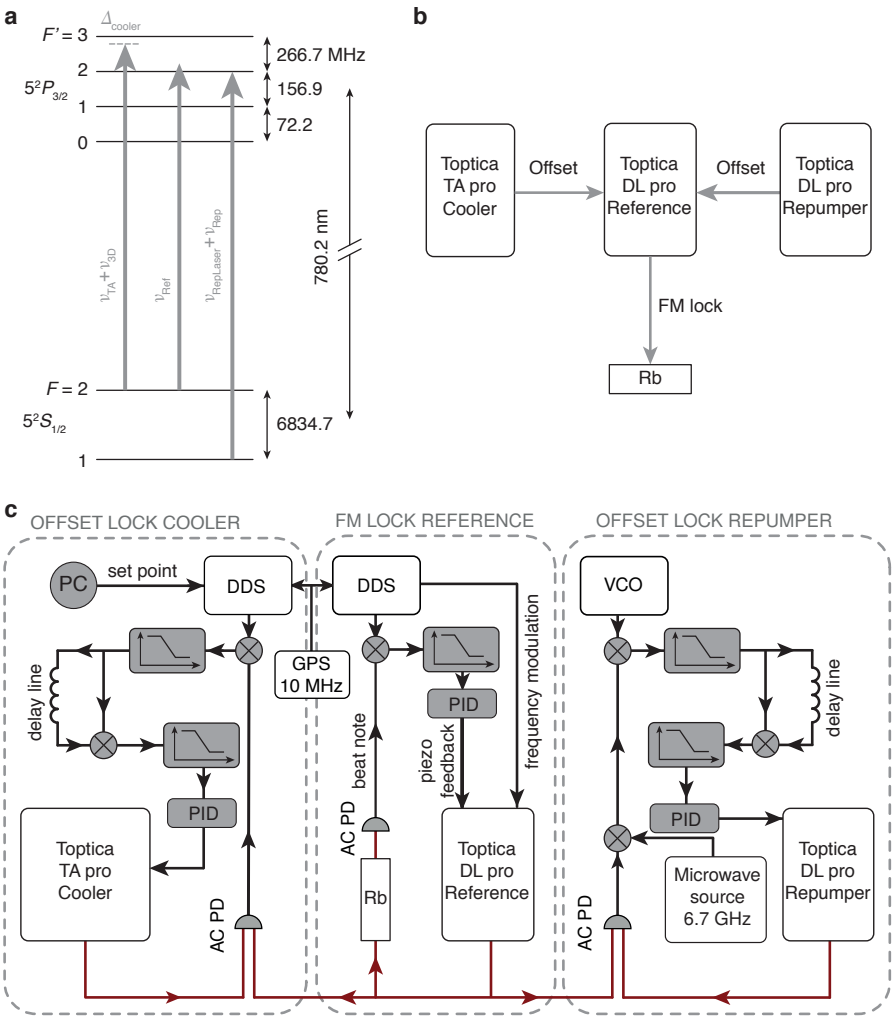

Figure 3.3: *Frequency stabilization for laser cooling and probing.* **a,** Level scheme for the D_2 line of ^{87}Rb with the transitions indicated that are adressed by the lasers. The frequency of the reference laser is 18.8 MHz higher than the $|F = 2\rangle \rightarrow |F' = 2\rangle$ transition. The frequency of the cooling laser is near resonant with the $|F = 2\rangle \rightarrow |F' = 3\rangle$ transition after passing an AOM, and can be adjusted during the experimental cycle. The repumping laser adresses the $|F = 1\rangle \rightarrow |F' = 2\rangle$ transition after passing an AOM. **b,** Locking scheme for the laser frequencies. The reference laser is FM locked to the crossover between the $|F = 2\rangle \rightarrow |F' = 1\rangle$ and the $|F = 2\rangle \rightarrow |F' = 3\rangle$ transitions with a Rb vapour cell. The cooling and repumping lasers are both offset locked to the Reference laser. **c,** Electronic setup for frequency locking. For each lock, the error signal is created by mixing the beat signal from an AC PD with a LO and subsequent low-pass filtering. The offset lock additionally requires a delay cable to generate the error signal. The frequencies are then stabilized within a PID loop. In order to increase the laser frequeny stability, the LOs for reference and cooling lasers are provided by a GPS stabilized DDS.

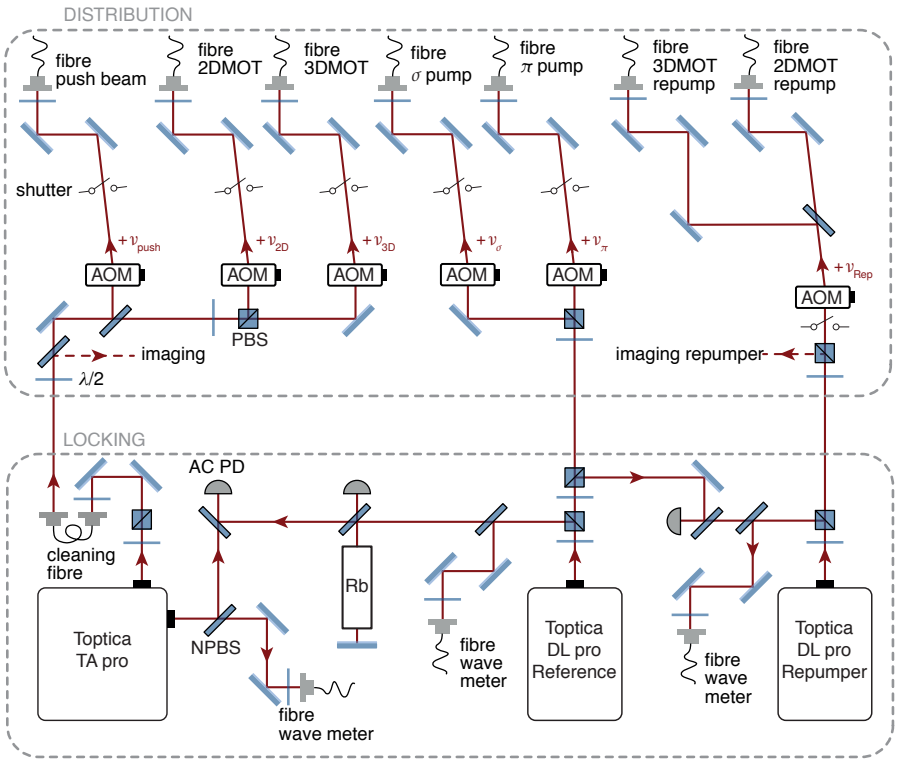

Figure 3.4: *Optical setup of the laser system.* The setup is divided in two parts for frequency stabilization and beam distribution. In the stabilization part beat notes between the three lasers are generated and a small part of the light is sent to a wavemeter to monitor the frequencies. Additionally, the mode profile of the cooling laser is cleaned with an optical fibre. In the distribution part, the laser beams are split into several paths. Each beam is mechanically shuttered and its frequency is adjusted with an AOM before being sent to the experiment table through an optical fibre.

a total output power of 80 mW and serve as frequency reference and the repumping laser. The third laser includes a TA stage (*TA pro* by *Toptica*), which raises the maximum output power to 2.1 W. This laser provides the light for laser cooling and imaging.

Level scheme for rubidium

The level scheme for the D_2 line of ^{87}Rb and the stabilization scheme for the laser frequencies are shown in Fig. 3.3a. We first lock the reference laser to a Rb vapour cell using FM spectroscopy [159] with a modulation frequency of 10.9 MHz. We choose the crossover of the $|F = 2\rangle \rightarrow |F' = 1\rangle$ and $|F = 2\rangle \rightarrow |F' = 3\rangle$ transitions as a resonance line, which exhibits higher signal-to-noise ratio than the bare resonances [160]. We use a DDS as modulation frequency, yielding an enhanced frequency stability compared to a VCO.

Laser lock scheme

The frequencies of the other two lasers are stabilized with offset locks to the reference laser [161], see Fig. 3.3b,c. For the repumping laser, we first record the beat signal with the reference laser on an AC PD and mix it with a home-built MW source at 6.7 GHz. The resulting low-pass filtered signal has a frequency of 133 MHz and is used to generate the lock signal for the offset lock with the help of a delay cable with fixed time delay and therefore frequency-dependent phase delay. A PID loop stabilizes the laser then to a set frequency offset between the two lasers, which is determined by a VCO signal. The frequency of the cooling laser is stabilized in a similar way, but with a DDS serving as LO. The beat signal between cooling and reference

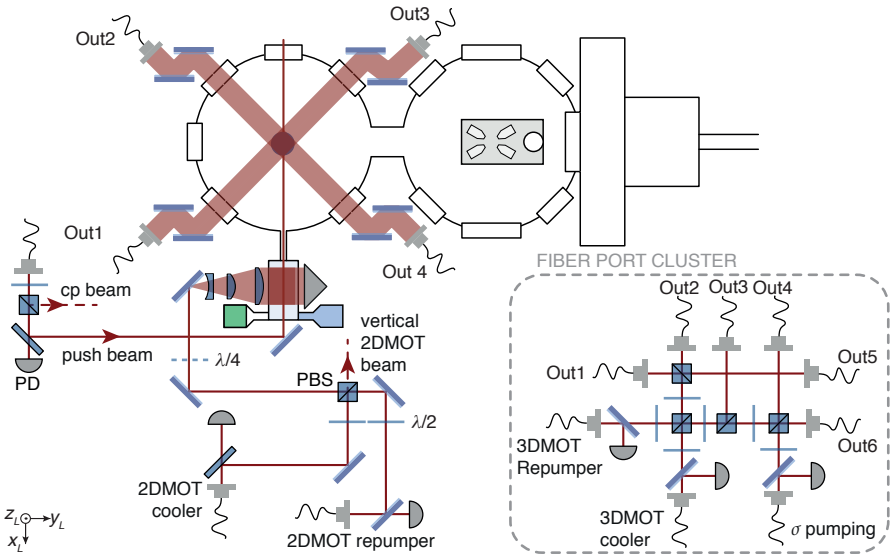

Figure 3.5: *Optical setup for laser cooling.* The cooling and repumping light for the transverse 2DMOT beams is mixed and split at a PBS and subsequently expanded with cylindrical lenses and retroreflected by a prism. The push beam and the counterpropagating (cp) beam confine the velocity distribution along x_L to optimize the number of captured atoms. The cooling and repumping light of the 3DMOT is mixed in a fibre optical beamport cluster with six output beams in optical fibres. To improve visibility, the vertical 2DMOT and 3DMOT beams are not shown but have a similar optical setup.

laser lies in the range of $50 - 170$ MHz and does not require down-mixing. It can be steered via ethernet connection from the computer by adjusting the setpoint for the DDS frequency with the runner PC.

Optical setup of the laser system

The optical setup for the laser system consists of two parts, as shown in Fig. 3.4. The first part serves to stabilizing and monitoring the laser frequencies. The FM signal from the Rb spectroscopy and the beat signals are recorded on AC PD (*BPX65* from *Siemens*) with home-built amplification and filtering electronics. Each laser frequency is monitored on the wavemeter. We use the non-amplified auxiliary output of the TA laser for frequency locking and monitoring. The mode profile of the amplified output is cleaned with an optical fibre (1 m long PM single-mode fibre from *Schäffter+Kirchhoff*) to achieve high coupling efficiencies at each point in the further course of the beam path.

In the second part of the laser system the beams are distributed for the 2DMOT, the 3DMOT and for optical pumping. We use AOMs (*ATM-801A2* from *IntraAction*) for fast switching and frequency separation. To fully suppress residual light [162], each beam is additionally switched with a mechanical shutter (*SR475* from *SRS*). Most optical elements, in particular mirrors, waveplates and PBSs, are from the company *Lensoptics*. Finally, the beams are directed into PM single-mode fibres from *Schäffter+Kirchhoff* and *Thorlabs* to transfer the laser beams to the vacuum system on the second optical table.

3.2.2 2DMOT

Optical setup on the experiment table

The optical setup for the 2DMOT is shown in Fig. 3.5. After exiting the fibre collimators (*60FC-L-4-M30-02* from *Schäffter+Kirchhoff*) at a $1/e^2$ beam diam-

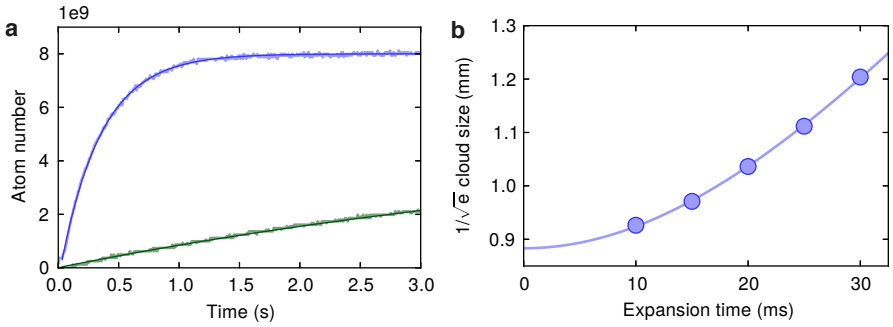

Figure 3.6: *Laser cooling properties.* **a,** Atom number during the loading process obtained from the recorded fluorescence signal with push beam (blue) and without (green). We extract $1/e$ loading constants of $0.34(1)$ s with push beam and of $5.74(1)$ s without push beam from an exponential fit (solid lines) to the data, corresponding to loading rates of 2.5×10^{10}/s and 9×10^{9}/s. **b,** Width of the molasses-cooled cloud after different expansion times. We extract the molasses temperature of $T = 7.4(8)\mu K$ from a fit with the function $\sigma(t) = \sqrt{\sigma_0^2 + k_B T t^2/m}$, where k_B is the Boltzmann constant and σ_0 the initial cloud size.

eter of 4.8 mm, the cooling and the repumping beams for the 2DMOT are first mixed and split with a PBS into two paths. Each path contains around 170 mW cooling and 20 mW repumping light. Subsequently, the polarization of the beams is rendered circular with a $\lambda/4$ waveplate. Before entering the chamber, each beam is expanded to an elliptic shape with an aspheric lens (*C560-TME-B* from *Thorlabs*) with focal length 13.9 mm and two cylindrical lenses of 51 mm (*LJ1728L1-B* from *Thorlabs*) and 150 mm (*LJ1895L1-B* from *Thorlabs*) focal length. The resulting $1/e^2$ beam diameter of each beam is $(2w_x, 2w_y) = (52, 18)$ mm. After passing the 2DMOT vacuum chamber, the beams are retroreflected with prisms from *Lensoptics* with a chamfer width < 0.05 mm. The double reflection ensures the correct σ^+ polarization for the reflected beam without need for an additional $\lambda/4$ retardation plate.

Push and counterpropagating beams

The push beam and the counterpropagating beam exit from the same fibre collimator (*60FC-T4-M25-37* from *Schäffter+Kirchhoff*) with a $1/e^2$ beam diameter of 4.0 mm and 50 mW optical power. The power is split between the two paths with variable ratio at a PBS. In the experiment, we did not see an appreciable improvement of the loading rate when including the counterpropagating beam and omitted it in the cirrent configuration. The power of each beam is permanently monitored on a PD. All elements of the optical setup for the 2DMOT are AR coated at $767 - 780$ nm to support the D_2 lines for both Rb and K.

We optimize the 2DMOT in terms of beam alignment, power ratio, polarization and the magnetic field gradient. The fluorescence signal of the 3DMOT gives approximate information on the loaded atom number. We record the fluorescence light on a PD and calibrate the atom number with absorption images of the 3DMOT. The resulting loading curve with and without the push beam is shown in Fig. 3.6a. Presumably, even higher loading rates could be achieved with the setup, as neither the detuning of the 2DMOT nor the background pressure has been optimized yet.

Loading rate

3.2.3 3DMOT and optical molasses

The optical setup for the 3DMOT is shown in Fig. 3.5. The six laser beams for the 3DMOT are generated by mixing the light for cooling and repumping in a fibre optical beamport cluster from *Schäffter+Kirchhoff*. A third, auxiliary input beam provides light for σ pumping for one of the output beams. All three input beams feature a PD port for power monitoring. The PD signal for the cooling light is also used to actively stabilize its power with feedback on the AOM generated from home-built PID electronics. In order to obtain a sufficient long-term stability, the fibre cluster has been thermally cycled several times prior to delivery. The optical elements of the cluster are AR coated for $767 - 780\,\mathrm{nm}$ and the employed waveplates are zero-order at 773 nm to be compatible with light at the D_2 transitions of both Rb and K. Each output beam is sent to a fibre collimator (*60FC-Q773-4-M150-37* from *Schäffter+Kirchhoff*), which produces a collimated beam with a $1/e^2$ diameter of 28 mm with adjustable polarization thanks to a built-in $\lambda/4$ plate.

Fibre optical beamport cluster

We optimize the 3DMOT separately from the 2DMOT parameters by first aligning all six beams until the optical molasses is stable, and then optimizing magnetic field gradient and detuning. The highest loading rate is obtained for a 3DMOT detuning of $-3.2\,\Gamma$ and a magnetic field gradient of $(\partial_x B, \partial_y B, \partial_z B) = (4.5, 4.5, -9.0)\,\mathrm{G/cm}$. In order to achieve molasses cooling, we suddenly switch off the magnetic field and ramp the detuning to $\Delta = -15\,\Gamma$ over 5 ms, while the power in each cooling beam is lowered to 4 mW. We determine the temperature from the fitted width of the atomic cloud on absorption images with different expansion times, as shown in Fig. 3.6b. In a final step, we switch off the repumper to depump all atoms to the $|F = 1\rangle$ manifold. This transfers around 40 % of the atoms into the low-field seeking $|F, m_F\rangle = |1, -1\rangle$ state. Optical pumping [126] did not result in a higher fraction, likely due to residual magnetic fields creating an ill-defined quantization axis for small offset fields.

Temperature after molasses cooling

3.3 MAGNETIC TRAPPING

The molasses-cooled cloud has a phase space density that is around six orders of magnitude away from Bose-Einstein condensation. Higher phase-space densities can be achieved in tight conservative traps, for instance optical dipole traps. However, loading atoms from the molasses directly into an optical trap requires large laser power, because the beam diameter has to be chosen according to the cloud size. As a consequence, we first trap the atoms in a magnetic trap, which makes use of the forces on the permanent magnetic dipole moment of the neutral atoms in an inhomogeneous magnetic field, and provides large trap depths and capture ranges [163].

Large confinement with magnetic quadrupole traps

3.3.1 Coil circuit and water cooling

The circuit for the gradient coil pair in the 3DMOT chamber and the Feshbach coil pair for offset fields in the science chamber is shown in Fig. 3.7. The gradient coils are driven by a low-noise power supply (*SM 15-400* from *Delta Elektronika*), which can produce currents up to 400 A resulting in magnetic field gradients of 413 G/cm. The Feshbach coils are driven by a second power supply (*SM 30-200* from *Delta Elektronika*) with 200 A maximum output, yielding magnetic fields up to 681 G. The current in each coil pair is monitored with a flux sensor (*DS600UBSA-10* from *Danisense*), and the tem-

Electric circuit

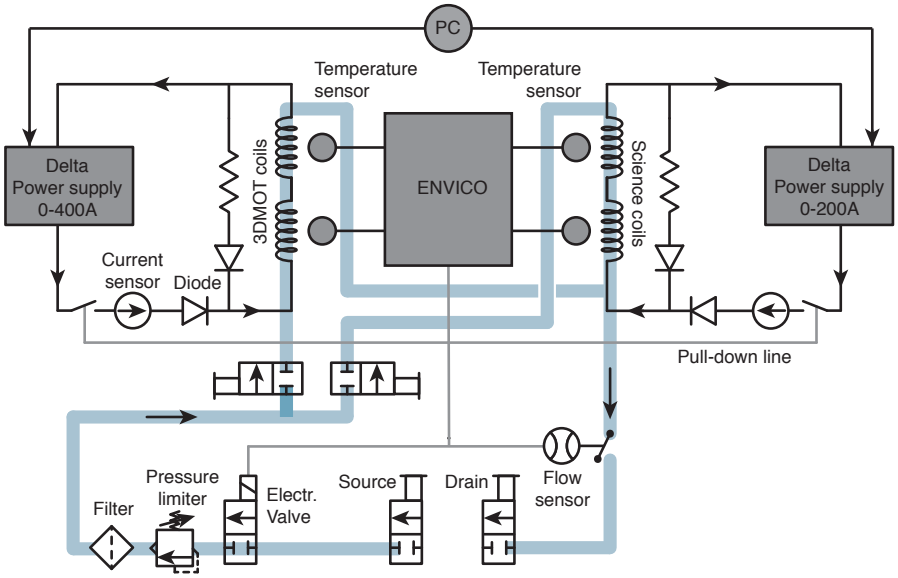

Figure 3.7: *Electronic and water cooling circuits of the magnetic coils.* The circuit for the coils in the 3DMOT and the science chamber are identical. Each coil pair is driven by a low-noise power supply, whose output is steered with the set voltage from the PC. After switching off the fields, the current is dissipated in a high-power resistor. The cooling water is supplied from one source of 6 bar and is used for both coil pairs in parallel. The temperature is monitored in each coil separately with temperature sensors that are connected to the ENVICO system. As soon as a coil temperature or water flow exceeds the set limits the interlock is activated.

perature is continuously monitored and stored in a database with the *Envico* system (see Sec. 3.1). During the experimental cycle, the output current of each power supply is controlled with an analog input voltage and digitally switched by acting on the internal interlock of the power supply.

Water cooling circuit

We inject deionized water from the building cooling water circuit into the hollow-core wire out of which the coils are wound. The water has a temperature of $\sim 19°$ C and a long-term stability of around $\pm 1°$ C. Our cooling water circuit is implemented with copper tubes and PVC hoses that are connected with *Swagelok* and *Serto* connections. At the source, the standard pressure of 6 bar is reduced to 2 bar with a pressure regulator. The circuit is then split into two parts that lead to the two coil pairs and recombine at the drain. Here, the water flow is measured with a flow-switch sensor from the company *ETA*. The temperature sensors and the flow sensor are connected to the pull-down interlock line, which switches off the coils when the temperature or the water flow are beyond the limits.

The offset coils along each axis in both chambers are driven by low-noise power supplies from the company *Statron* without additional circuitry. Their output currents are steered with a $0 - 10$ V analog input voltage.

3.3.2 Quadrupole trapping

Trapping potential

We use the same anti-Helmholtz coil pair as for the 3DMOT to produce a quadrupole field for magnetic trapping of the form $B(\mathbf{r}) = (x/2, y/2, -z)B'$ with the magnetic field gradient B'. Around the trap minimum, the atoms experience a trapping potential of the form:

$$V(x, y, z) = -\boldsymbol{\mu} \cdot \mathbf{B}(x, y, z) = -g_F m_F \mu_B \, |B(x, y, z)| \,, \tag{3.1}$$

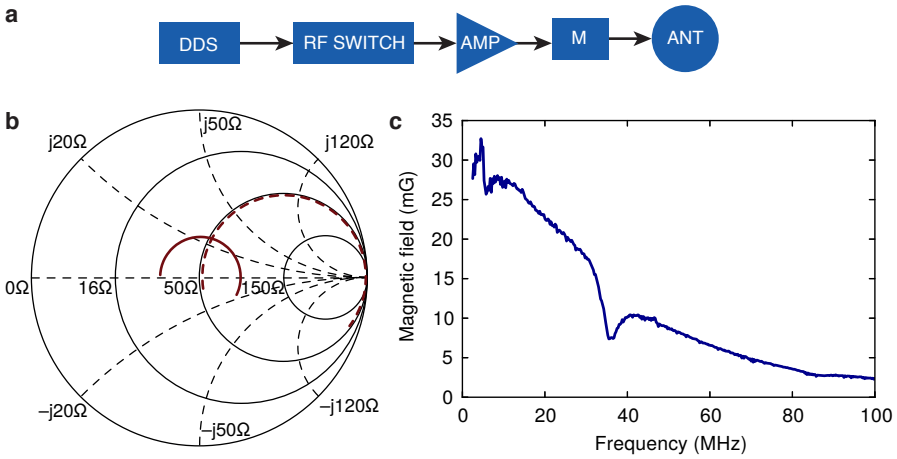

Figure 3.8: *Setup for RF evaporation.* **a,** RF components for the signal generation with amplifier (AMP), impedance matching (M) and antenna (ANT). **b,** Smith chart showing the impedance over the required frequency range of $1-100\,\mathrm{MHz}$ for the bare coil (dotted red line) and including a $6\,\mathrm{dB}$ attenuator (solid red line). **c,** Magnetic field measurement with a pickup coil showing the emission from the RF coil. Adapted from [164].

where g_F is the Landé factor, m_F is the magnetic quantum number and μ_B the Bohr magneton. As a consequence, only atomic states with a positive product $g_F m_F$ (called *low-field seekers*) can be trapped in a quadrupole field. After optical depumping the atoms are in the $F = 1$ state and since $g_F = -1/2$ we solely capture the fraction in the $|F, m_F\rangle = |1, -1\rangle$ state.

Mode matching the atoms

The catch gradient after laser cooling is optimized for matching the atomic cloud with the trapped state [126]. We subsequently compress the cloud by ramping up the magnetic field gradient to $403\,\mathrm{G/cm}$ in order to maximize the collision rate for fast thermalization during evaporative cooling.

3.3.3 RF evaporation

Evaporative cooling is achieved by continuously removing atoms from the trap that have a kinetic energy higher than the ensemble average. The temperature of the remaining atoms after rethermalization is then lower compared to the initial one. This technique has first been realised with spin-polarised hydrogen [165], and subsequently proved to be key for the first realization of a BEC [166]. In a magnetic trap, this technique can be applied by lowering the effective trap depth with RF induced transitions between the magnetically trapped and untrapped Zeeman sublevels. The quadrupole trapping potential that we employ is ideally suited for evaporative cooling,

Runaway regime of evaporative cooling

because it allows for *runaway evaporation* with increasing collision rate due to its linear potential [166]. Indeed, a characterization of the evaporation process revealed our setup to work in this limit thanks to a low background pressure providing a life-time of $65(1)\,\mathrm{s}$ for the trapped atoms [143]. Bose-Einstein condensation, however, can not be achieved in a quadrupole trap, because of loss from Majorana spin flips to untrapped Zeeman sublevels [126]. They occur at the trap center, when the Larmor frequency $\omega_L = |\mu|B/\hbar$ is on the order of the instantaneous angular trapping frequency and the atomic magnetic moment cannot adiabatically follow the direction of the

magnetic field any more. Different magnetic trap geometries have been developped to overcome this limit [126].

The setup for forced RF evaporation is shown in Fig. 3.8 and has been described in [164]. The RF frequency is sent via ethernet to a home-built DDS, which generates the signal. The DDS output can be digitally switched with a TTL signal acting on an RF switch. The signal is then amplified to a power of 30 W with an amplifier (*LZY-22+* from *Mini-Circuits*).

RF antenna

We use a single wire loop with a diameter of 44 mm as RF coil, which is mounted in the top flange of the 3DMOT chamber 2 mm above the optical viewport and 26 mm above the trap center. Because of its high inductance, the wire is not well impedance-matched over the required RF range of $1-100$ MHz. We therefore place a passive high-power attenuator in π-bridge form (*JFW* from the supplier *Emitec*) in front of the antenna, which results in broadband impedance matching at the expense of an overall smaller signal strength.

3.4 DIPOLE TRAPPING

Optical dipole traps are based on the AC-Stark effect, which describes the shift of an atomic resonance frequency in an oscillating electric field E due to the atomic polarizability α, i.e. $U \propto (\alpha \mathbf{E}) \cdot \mathbf{E}$. The intensity distribution of a focussed laser beam can then generate a 3D trapping potential. A review on optical dipole traps can be found in [167]. For an atom with frequency ω_0 and linewidth Γ of an atomic resonance, the offset for a far off-resonance laser beam at frequency ω_L is given by

Light shift in an oscillating electric field

$$U(r,z) = \frac{3\pi c^2}{2\omega_0^2} I(r,z) \frac{\Gamma}{\Delta}, \tag{3.2}$$

where $\Delta = \omega_L - \omega_0$ is the detuning of the laser frequency and $I(x,y,z)$ the space-dependent intensity. For $\Delta < 0$ (called *red-detuned*), the light shift is negative and a laser beam with finite diameter produces an attractive potential with a minimum at the point of highest intensity. The opposite effect is obtained for *blue-detuned* light with $\Delta > 0$.

Atoms can be trapped at the focus of a red-detuned laser beam with Gaussian intensity profile, where the intensity is highest. The corresponding trapping potential is

Trapping potential for a gaussian beam

$$U(r,z) \approx -U_0 + \frac{1}{2} m\omega_r^2 r^2 + \frac{1}{2} m\omega_z^2 z^2, \tag{3.3}$$

with the potential $U_0 > 0$ at the trap minimum and radial and longitudinal trapping frequencies $\omega_r = \sqrt{4U_0/mw_0^2}$ and $\omega_z = \sqrt{2U_0/mz_R^2}$, respectively. The laser beam is characterized by its waist w_0 and Rayleigh length z_R (see Appx. A).

Parts of the setup have been described in [143, 168, 169].

3.4.1 *Laser system and optical setup*

For optical trapping, we use light at a wavelength of 1064 nm, which is produced by a Nd:YAG laser (*Mephisto MOPA 36NE* from *Coherent*). The laser system for the dipole traps is shown in Fig. 3.9. First, the laser beam passes an optical isolator (*FI1060-5SC-BP* from *Linos*) and is collimated with an achromatic lens (*LA1162* from *Thorlabs* with focal length $f = 400$ mm). The

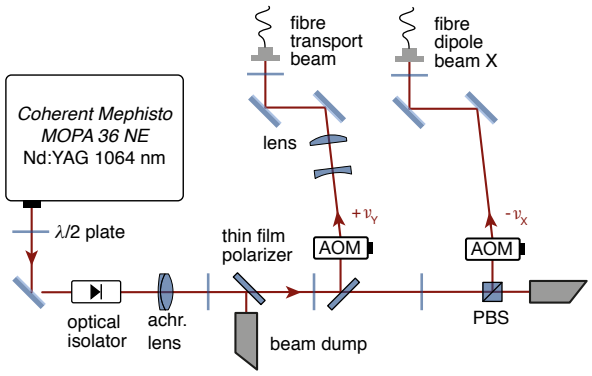

Figure 3.9: *Laser system for the optical dipole traps.* The paths for the transport beam and the dipole beam X are generated from the same laser and then shifted in frequency by $+\nu_Y = 80\,\text{MHz}$ and $-\nu_X = -80\,\text{MHz}$, respectively. They are guided to the experiment table with optical fibres.

splitting into the beam paths has to be achieved with thin film polarizers (*Laseroptic Garbsen*) instead of PBSs due to the high power of up to 40 W. We reflect the majority of the power into the path for the transport beam, where it passes an AOM (*ATM801A2* from *IntraAction*). To optimize the fibre coupling, a 10 : 3 telescope with spherical lenses of focal lengths $f_1 = -75\,\text{mm}$ and $f_2 = 250\,\text{mm}$ (*LC4513-B* and *LA1461-C* from *Thorlabs*) adjusts the beam diameter to the appropriate size. We then couple the beam with a fibre collimator (*60FC-SMA-T-4-M25-37* from *Schäffter+Kirchhoff*) into a PCF (*LMA-PM-15*from *NKT Photonics*, which supports the high employed optical power of up to 6 W. A smaller fraction of the original laser beam serves as second dipole beam along the x_L axis and is coupled into an optical fibre. We use opposite diffraction orders of the two AOMs to avoid interference of the two dipole beams inside the vacuum chamber.

Intensity stabilization with a logarithmic PD

On the experiment table, the transport beam exiting the PCF is collimated with a fibre collimator (*60FC-SMA-T-4-M40-54* from *Schäffter+Kirchhoff*) to a $1/e^2$ beam radius of 3.9 mm. After polarization cleaning with a PBS, a fraction of the power is directed to a PD with a logarithmic current-voltage converter from *Texas Instruments*. We use a servo controller (*LB1005* from *Newport*) to stabilize the power over a range of $0.01 - 7\,\text{W}$ without changing background noise. A second PD has a linear power-voltage characteristic and is used for monitoring. Before the vacuum chamber, the transport beam is combined with the imaging beam on a dichroic mirror. The residual light passing from the transport beam is imaged on a CCD camera to monitor size and position of the beam before and after the optical transport. Similarly, the light exiting the vacuum chamber is directed on a beam dump and residual reflection from the dichroic mirror is monitored on a CCD camera.

A laser beam along x_L forms a crossed dipole trap together with the transport beam. It has an elliptical shape with the short axis along z_L to compensate for gravity. The beam obtains its shape with a fibre collimator (*60FC-4-E15x5-1064* from *Schäffter+Kirchhoff*), which includes cylindrical lenses for $1/e^2$ output beam radii of $(w_x, w_z) = (2.5, 7.5)\,\text{mm}$ along the horizontal and the vertical axes, respectively. A small fraction of the light is sent to a PD for intensity stabilization, whereas the remainder of the beam is focussed into the vacuum chamber with an achromatic lens (*AC508-400-B* from *Thorlabs*) to a $1/e^2$ radius of $(w_y, w_z) = (54, 18)\,\mu\text{m}$.

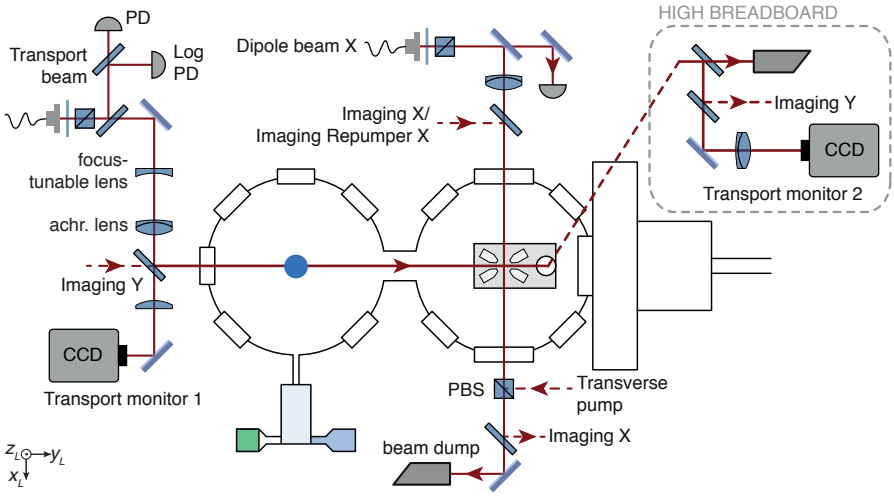

Figure 3.10: *Optical setup for the dipole traps.* The transport beam from the PCF is intensity-stabilized with a logarithmic PD and then passes the setup with the tunable lenses, which produce a displaceable focus inside the vacuum chamber. The beam position and size is monitored with two CCD cameras. The beam for the crossed dipole trap obtains an elliptical shape from cylindrical lenses in the fibre collimator and is then focussed into the vacuum chamber.

3.4.2 *Hybrid trap with optical and magnetic confinement*

The next step in the preparation process employs a hybrid trap, where the radial confinement is provided by an optical dipole beam and the axial confinement is enhanced by a quadrupole potential whose center is offset by Δz along the direction of gravity to avoid Majorana spin-flips [170]. The combined optical and magnetic potential allows to achieve higher densities and faster evaporation times. The axial trapping frequency is given by

Trapping potential for the hybrid trap

$$\omega_y = \sqrt{\frac{\mu_B B' |m_F g_F|}{4 m \Delta z} + \frac{2U_0}{m z_R^2}}. \tag{3.4}$$

During the loading of the hybrid trap the quadrupole potential also acts as a reservoir to directly feed the tightly confining hybrid trap, resulting in an efficient evaporation process thanks to the advantageous phase-space density [171, 172]. We obtain a cloud of $1.8((1) \times 10^7$ atoms at $9.4(1)\,\mu$K.

3.4.3 *Transport with focus-tunable lenses*

Transport of cold atoms between two vacuum chambers has been achieved first magnetically by displacing the field minimum [173, 174]. Optical transport is typically achieved by translating a focussing lens on an air-bearing stage [175]. Approaches with optical lattices either only work along the direction of gravity [176] or require the generation of Bessel beams [177].

With our experiment, we introduce a new approach based on focus-tunable lenses. They are known from a number of techniques in industry [178–181] and provide a simple and compact alternative to the established transport methods. Parts of this section have been published in:

Optical transport with focus-tunable lenses

J. Léonard, M. Lee, A. Morales, T. M. Karg, T. Esslinger and T. Donner

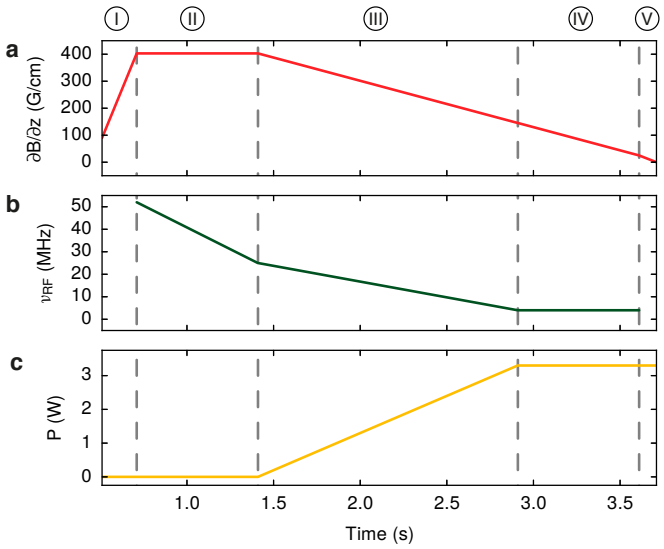

Figure 3.11: *Timeline of the magnetic trap and the hybrid trap stage.* The dashed lines separate the loading of the quadrupole trap (I), RF evaporation therein (II), transfer to the hybrid trap (III), RF evaporation in the hybrid trap (IV) and loading of the optical dipole trap (V). The traces show **a,** the magnetic field gradient, **b,** the RF evaporation frequency and **c,** the dipole beam power.

Optical transport and manipulation of ultracold atoms using focus-tunable lenses
New J. Phys. **16,** 093028 (2014)

Two focus-tunable lenses

The first generation setup, which is presented in the publication, employs two focus-tunable lenses of the type *EL-10-30* from the company *Optotune*. It allows to independently control the position and the size of the focus by separately adjusting the two focal lengths. Transfer efficiencies of $80-90\,\%$ at $1-2\,\mu K$ heating can be achieved for atomic clouds consisting of up to 2×10^7 atoms at temperatures around $10\,\mu K$. No lateral drift rate could be detected, but longitudinally we observed a slow drift, which was compensated with a current adjustment. The tunable focus size allows to explore a large range of densities, with possible applications in optimized trap transfer and novel schemes of evaporative cooling.

Single focus-tunable lens with larger aperture and temperature sensor

Since the implementation of the second generation setup, we instead use a focus-tunable lens of the type *EL-16-40-TC*, which offers a number of advantages over the previous model. The increased lens aperture of 16 mm permits the use of larger beam diameters resulting in smaller trap sizes. Its tunable focal length lies in the range of $(-300, 300)\,mm$ through ∞, producing smaller spherical aberations thanks to the reduced lens curvature. Furthermore, an integrated temperature sensor can be used to increase the long-term stability by employing a feed-forward on the focal length.

The working principle is shown in Fig. 3.12a, b. The lens body is filled with a low-optical absorption liquid and the surface is sealed off with an elastic polymer membrane. A coil at the lens rim can act on the membrane by applying a current. As a consequence, the liquid is mechanically pressed from the outer area to the lens center and the membrane curvature increases. We mount the lenses with a vertical optical axis in order to reduce the wavefront errors to $0.1-0.2\,\lambda$, with $\lambda = 1064\,nm$ the wavelength of the trapping laser.

Optical setup for transport at constant waist size

The optical setup is illustrated in Fig. 3.12c. In principle, a focus displace-

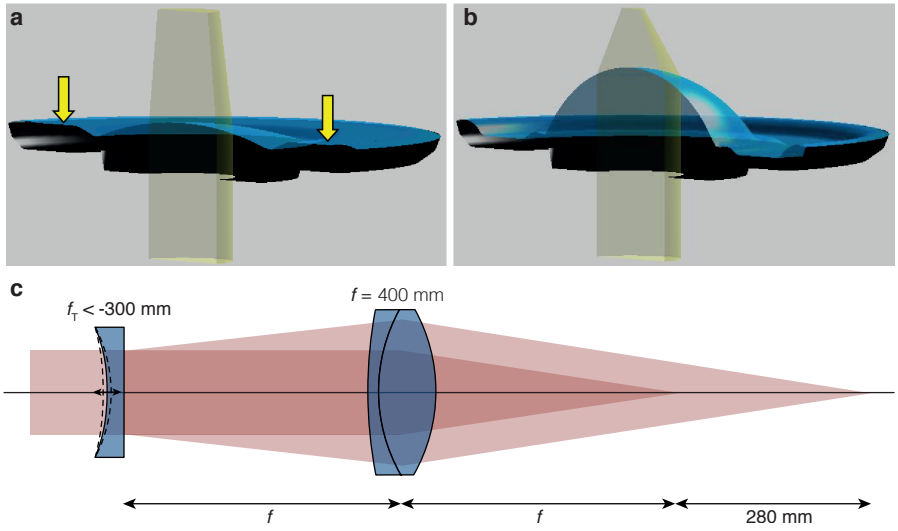

Figure 3.12: *Optical setup with focus-tunable lenses.* **a–b,** Working principle of the focus-tunable lenses. When a current is applied to the coil at the lens rim, it acts on the membrane and presses liquid from the outer area to the lens center, thereby increasing the membrane curvature. Adapted from [182]. **c,** Lens setup for the optical transport. We choose the separation between the tunable lens f_T and the static lens equal to the focal length $f = 400\,\mathrm{mm}$ of the latter. For this configuration, the divergence and thus the waist size remains constant.

ment can be achieved using a single tunable lens with positive focal length f_T to focus a collimated beam. However, this comes at the cost of a change in waist size. We therefore use an additional static lens with $f = 400\,\mathrm{mm}$. The diameters in the beam focus before and after transport (Fig. 3.12c) are equal if their divergences are, which requires the beam sizes at the static lens to have the same ratio as the focus distances from the lens. This situation can be achieved by choosing the distance between the two lenses equal to the focal length f of the static one. Changing the beam diameter at the static lens by adjusting f_T from infinity to negative values therefore displaces the focus at constant beam diameter.

Constant beam focus during transport

This behaviour can be derived more rigorously with ray optics. Consider a ray parallel to the optical axis at distance r_0, which enters the focus-tunable lens. The effective focal length of the tunable lens is f_T, and d_1 and d_2 denote the distances between the two lenses and from the trapping position, respectively. In the thin lens approximation, the ray propagation T and the ray diffraction R at a lens can be described with the ray transfer matrices:

$$T[d] = \begin{pmatrix} 1 & d \\ 0 & 1 \end{pmatrix}, \quad R[f] = \begin{pmatrix} 1 & 0 \\ -1/f & 1 \end{pmatrix}. \tag{3.5}$$

Starting from the focus-tunable lens, the full propagation through the system is described by:

$$\begin{pmatrix} r_1 \\ \alpha \end{pmatrix} = T[d_2] \cdot R[f] \cdot T[d_1] \cdot R[f_T] \cdot \begin{pmatrix} r_0 \\ 0 \end{pmatrix} \tag{3.6}$$

giving the following condition for the final beam divergence α:

$$\alpha = -r_0 \left(\frac{1 - d_1/f}{f_T} + \frac{1}{f} \right). \tag{3.7}$$

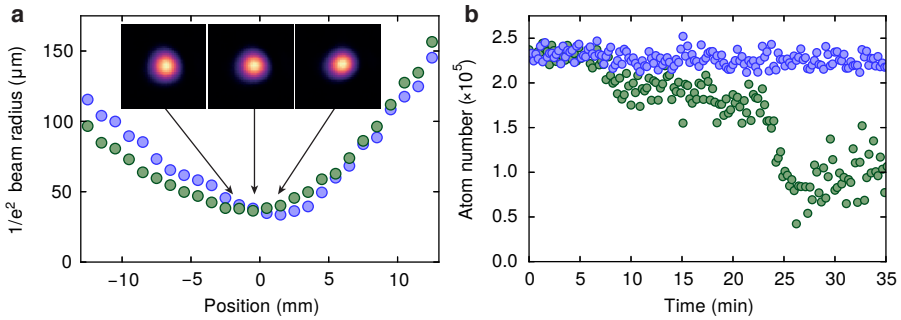

Figure 3.13: *Transport beam properties.* **a,** Measurement of the $1/e^2$ beam radius through the focus at the position after transport along the horizontal (blue) and the vertical (green) axis. The insets display pictures of the beam at -1, 0 and $+1$ mm from the focus position (from left to right). **b,** Atom number stability in the BEC after the optical transport. The data show a long-term measurement of the atom number with (blue) and without (green) temperature feed forward. An average over the full measurement with feed forward of 90 min results in a mean atom number of $2.21(9) \times 10^5$.

Requiring that the divergence α is independent from the focus position (and thus f_T) results in the condition $d_1 = f$.

Temperature sensor for current feed-forward

We observe a slightly astigmatic beam profile away from the focus together with the typical asymmetric beam divergence, as shown in Fig. 3.13a. This does, however, not affect the trapping potential in the focus. In addition, the focal length of the tunable lens is sensitive to the ambient temperature, which causes long-term drifts of the atom number. We use the integrated temperature sensor of the lens to read out its temperature and feed forward on the current driver. The result is an improved atom number stability that shows relative fluctuations of $3-4\%$ over several hours. Without the feed-forward, similar stabilities are only maintained for a thermalized apparatus over $10-30$ min.

3.4.4 *Optical evaporation in a crossed dipole trap*

Optical evaporation

Forced evaporation in an optical dipole trap can be achieved by lowering the trap depth with the optical beam power. According to Eqns. 3.2 and 3.3, the intensity is directly proportional to the trap depth, $U_0 \propto I$, but at the same time the trapping frequencies are reduced as $\omega_r, \omega_z \propto \sqrt{I}$. This leads to a reduction of the collision rate despite the increasing phase space density and the *runaway* regime is essentially inaccessible, except with the introduction of additional techniques like dimple traps [183], compressing dipole traps [184] or magnetic field gradients [185].

Optical evaporation presents the last step of the preparation sequence. We load the atomic cloud into the crossed dipole trap by first instantaneously switching on the crossed dipole beam and lowering the transport beam power to a similar trap depth. After 0.1 s free evaporation, we obtain $4.1(1) \times 10^6$ atoms at a temperature of 11.3(2) µK. We approximate the theoretically expected exponential evaporation ramp with two linear ramps over 0.5 s and 0.8 s and obtain almost pure condensates with $2.13(5) \times 10^5$ atoms.

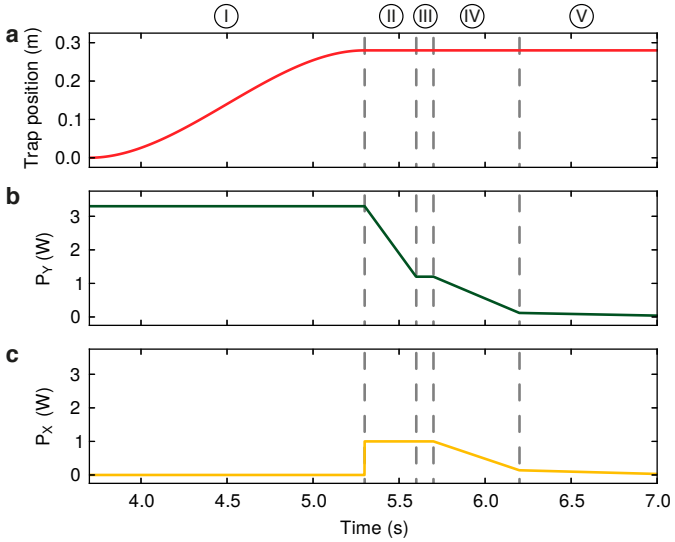

Figure 3.14: *Timeline of the dipole trap stage.* The dashed lines separate the optical transport (I), the crossed dipole trap loading (II), free evaporation in the crossed dipole trap (III) and finally two linear ramps for forced evaporation (IV-V). The traces show **a,** the focus position of the transport beam, **b,** the power in the transport beam along y_L and **c,** the power in the crossed dipole beam along x_L.

3.5 IMAGING

The main imaging method that is applied in the experiment is absorption imaging. In brief, a resonant laser beam is sent to the atomic cloud and the shadow cast from light absorption is imaged onto a CCD camera. In the limit of probe beam intensities small compared to the saturation intensity [107], the absorption is proportional to the atomic density and the intensity profile after passing the atomic cloud follows the Lambert-Beer law [126]:

Absorption imaging

$$I(x,y) = I_0(x,y)\exp\left(-\sigma_0 \int n(x,y,z)dz\right) \tag{3.8}$$

Here, $I_0(x,y)$ describes the initial transverse intensity profile and $\sigma_0 = 3\lambda^2/2\pi$ is the resonant atom-photon scattering cross-section for the wavelength λ. This expression allows to deduce the integrated line density from the intensity ratio:

$$\bar{n} = \int n(x,y,z)dz = -\frac{1}{\sigma_0}\log\left[\frac{I(x,y)}{I_0(x,y)}\right] \tag{3.9}$$

We take two successive pictures with and without the atomic cloud at the end of each sequence to obtain $I(x,y)$ and $I_0(x,y)$. A third image, called *dark*, is subtracted from the other two to account for stray light.

In addition to the *in situ* density distribution, we can also image the atomic cloud after releasing it from the trap and letting it expand ballistically. When choosing an expansion time t that is long compared to the inverse trapping frequency, this converts the initial density distribution to a momentum-distribution [126].

The laser system for the imaging beams is shown in Fig. 3.15. We use light on the $|F=2\rangle \rightarrow |F'=3\rangle$ transition, which requires additional repumping light on the $|F=1\rangle \rightarrow |F'=2\rangle$ transition to transfer the atoms to the higher hyperfine state. The optical power from the path with the cycling transition

Laser system for absorption imaging beams

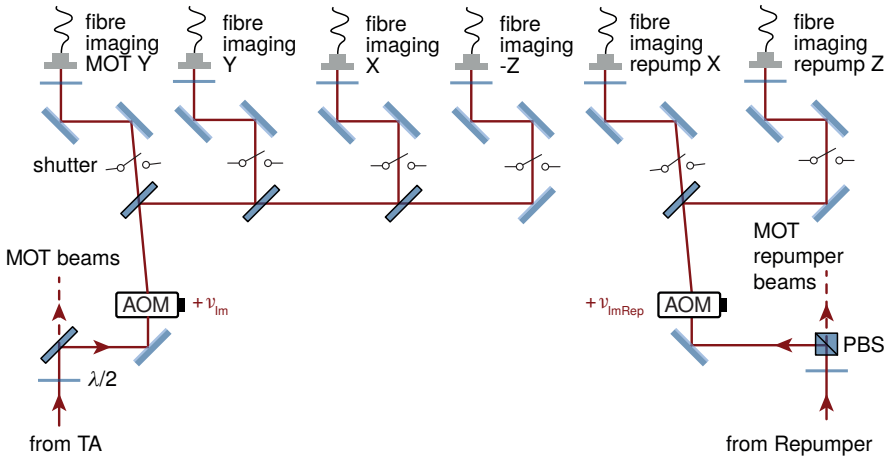

Figure 3.15: *Laser system for imaging.* The imaging light on the $|F = 2\rangle \rightarrow |F' = 3\rangle$ transition is provided by the cooling laser. It is shifted in frequency with an AOM and then split into four paths for imaging along all axes in the science chamber, as well as along the y_L axis in the 3DMOT chamber. In order to transfer the atoms to the $|F = 2\rangle$ state prior to the imaging sequence, they are exposed to repumping light on the $|F = 1\rangle \rightarrow |F' = 2\rangle$ transition. This light is split off the repumping laser and can be applied on the x_L and the z_L axis in the science chamber, perpendicularly to the chosen imaging axis.

	Camera	Res.	Magn.	Eff. pixel size
Imaging X	GX-FW-28S5M-C	4.8 µm	2.2	2.07 µm
Imaging Y	FL2G-13S2M-C	11.1 µm	0.9	4.21 µm
Imaging Z	GX-FW-28S5M-C	4.4 µm	2.2	2.05 µm
MOT X	FL2-03S2M-C	7.5 µm	2.0	3.62 µm
MOT Y	FL2-03S2M	10.2 µm	0.7	10.72 µm

Table 3.1: *Properties of the imaging systems.* The table includes the amera type, the resolution, of the imaging system, the magnification factor and the effective pixel size in the object plane (pixel size divided by magnification). All cameras are from the company *PointGrey*.

passes an AOM and is then split into four beams. The repumping beam must not copropagate with the imaging beam, because its light would be captured by the camera and affect the recorded density distribution. We therefore prepare two separate ports for rempumping beams along the x_L and z_L direction in the science chamber.

Imaging system on the experiment table

The optical setup on the experiment table is shown in Fig. 3.16. Imaging systems on all three axes in the science chamber (as well as along the transport axis in the 3DMOT chamber) provide access to the cloud along all directions. Additionally, the cloud can be imaged along x_L in the 3DMOT chamber with fluorescence imaging. The vertically travelling *Imaging Z* beam is focussed into the aspheric lens of the cavity setup to retrieve a collimated imaging beam (see Sec. 4.1).

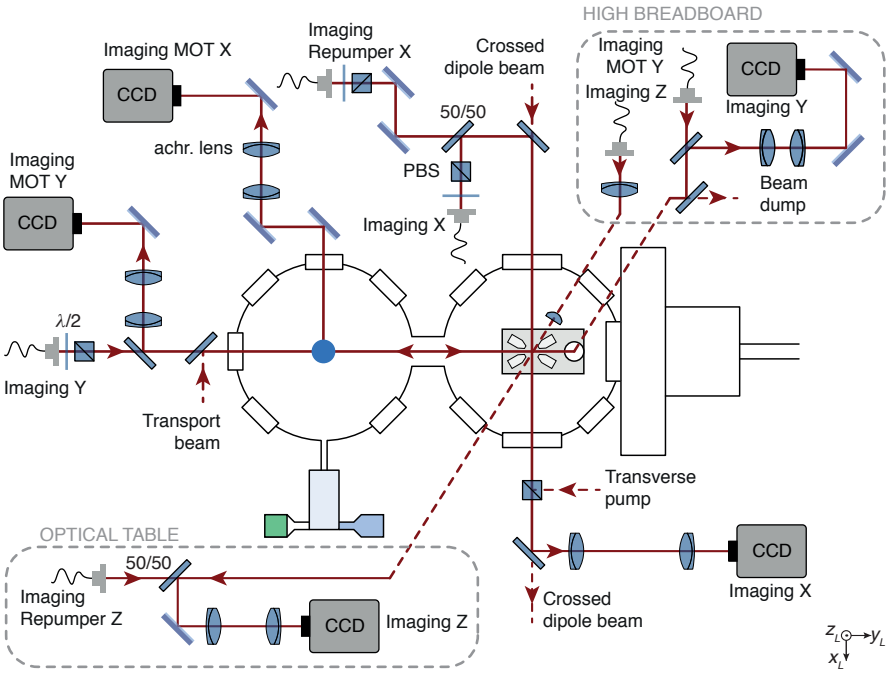

Figure 3.16: *Optical setup for imaging.* Five imaging systems provide access to the cloud along three axes in the science chamber and along x_L and y_L in the 3DMOT chamber. Optical elements are mounted at the chamber level if not specified in the figure. The vertically travelling *Imaging Z* beam is focussed into the aspheric lens of the cavity setup.

4 TWO CROSSED OPTICAL CAVITIES

The central setting of quantum optics consists of a two-level system interacting with a quantized light field, for instance an atom in an optical cavity. Extensions of this system to multiple optical cavities have so far been hampered by the challenging technical demands to maintain a sufficiently high atom-light coupling. In this chapter we describe the construction, implementation and characterization of a setup with two optical cavities whose modes cross at an angle of 60°. After presenting all setup components individually, we turn towards the frequency stabilization and the probing of the cavities. We conclude with a characterization of the cavity setup and the interaction with a BEC. The relevant properties of optical cavities are described in Appx. A, and an introduction to atom-light interactions can be found in Appx. B.

CHAPTER CONTENTS

Coupling single or multiple atoms to an optical cavity has shown to give rise to numerous phenomena, both for the internal [186] and the external degrees of freedom [81]. A long-standing goal is the extension of this setting to two or more cavity modes. One approach consists of coupling to several modes in a single cavity, for instance with orthogonally polarized or higher order transverse modes [81]. However, such a system comes at the drawback of lacking control over the mode properties, including the resonance frequencies, mode shapes directions and decay rates. This could be overcome by simultaneously coupling to the modes of different optical cavities. Here we present the development of a setup with two crossed cavities. The main technical challenges are:

Extending quantum optics to two independent modes

Technical challenges

- *Compact design:* In principle, two mirrors can be approached arbitrarily close until a mode volume is achieved that is small enough for strong light-matter interaction. This regime is routinely reached in cavity QED. When crossing two cavities, the minimal cavity length is given by the mirror diameter. This required the mirrors to have a smaller size than commercially available substrates.

- *Mode overlap:* The cavity mirrors have to be aligned with a high precision to ensure that the modes are not skew. In particular in the dispersive interaction regime, where the cavity photons give rise to a dipole

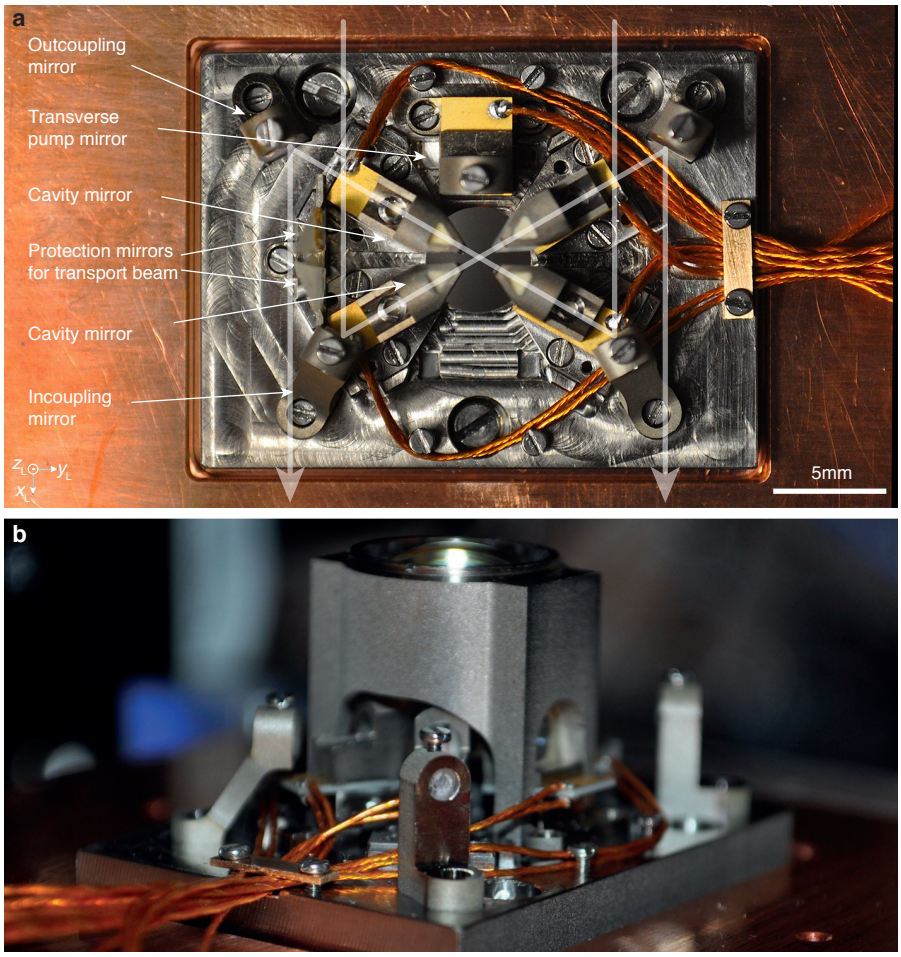

Figure 4.1: *The crossed cavities setup.* **a,** The optical cavities consist of two mirror pairs crossing at 60°. The cavity axes are accessed with four auxiliary mirrors that reflect the cavity in- and outputs towards optical viewports. A 1D lattice potential can be formed by retroreflecting a laser beam at the transverse pump mirror. The atomic cloud is transported into the setup in the focus of a dipole beam along the horizontal direction. Two mirrors protect the setup from thermal expansion due to absorbed light from this beam. Shaded arrows illustrate the beam paths for the cavity in- and output. **b,** Side view of the complete setup including the aspheric lens for high-resolution imaging.

potential, skew cavity axes not only reduce the interaction strength but also induce shear forces on the atomic cloud.

- *Crossing angle*: For dispersively coupled atoms, the emerging dipole potential is set by the geometry of the setup. Choosing a crossing angle of 60° rather than orthogonal cavity modes offers a much wider range of accessible phenomena, because the interference patterns of both cavity fields with a third standing wave, the transverse pump, that mediates the coupling are mutually compatible. The vacuum chamber, as for most quantum gas setups, only exhibits viewports at angles of every 45°.

The cavity setup presented here meets all three challenges. It constitutes the first science setup that was successfully inserted into the vacuum chamber using the transfer system presented in Chap. 2.

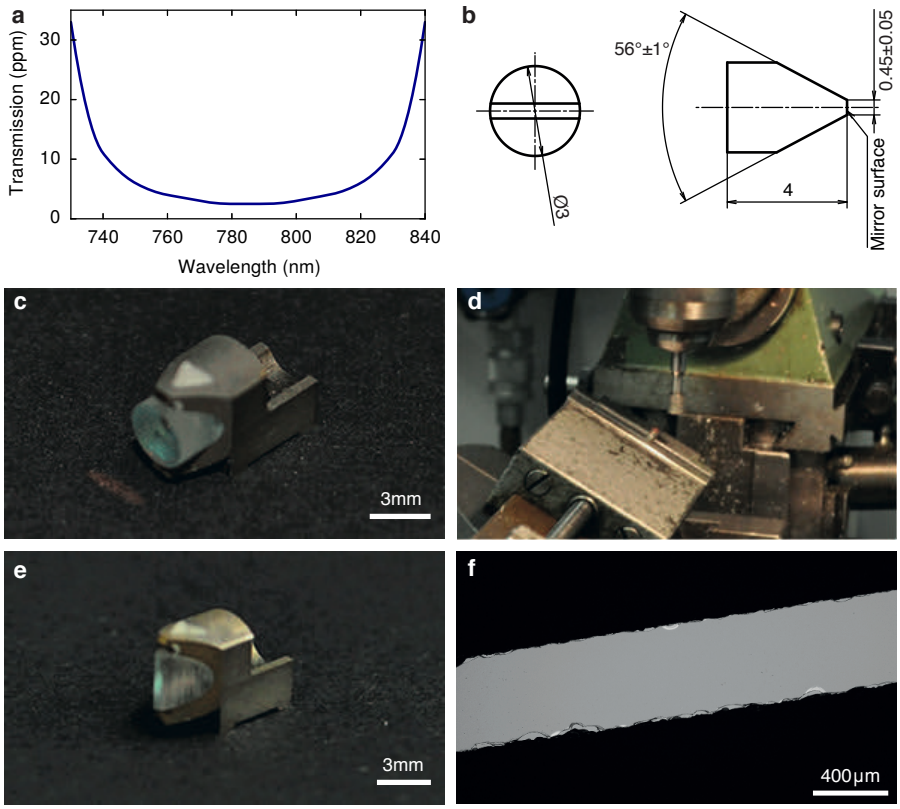

Figure 4.2: *Machining of the cavity mirrors.* **a,** The design curve for the dielectric coating for 0° AOI has a transmission minimum around a wavelength of 780 nm with 2 ppm transmission. At 830 nm the transmission is around 15 ppm. **b,** Technical drawing of the target substrate dimensions. **c,** Substrate in the titanium mount before machining. It is enclosed by the mount with a pocket tailored to fit the mirror, and additionally fixed with glue at the top and the bottom (white triangle). **d,** The cavity mirrors were machined with a fine-grained diamond wheel mounted on a mill. **e,** Wedged substrate after machining. The wedging reduces the mirror surface to a thin vertical stripe. **f,** Image of the mirror surface in dark-field microscopy after substrate machining. The edges show a width of around 50 µm.

4.1 THE CAVITY SETUP

A sketch of the cavity setup is shown in Fig. 4.1. The cavities consist of two pairs of mirrors with a cylindrically formed substrate. To approach them closely and increase the atom-photon interaction we optimized their shape by milling down the coated surface to the minimum diameter required to support the cavity mode.

The mirror mounts are built in a way to favour a matching mode height for the two cavities. The overlap of the cavity modes was maximized prior to inserting the setup into the vacuum, and it was reconfirmed after the bakeout from the alignment procedures (see Sec. 4.3.2. Since the vacuum chamber does not feature viewports on the cavity axes, the cavities have to be coupled *in vacuo* with four coupling mirrors. A fifth mirror with its optical axis at 60° from each cavity axis serves as a retroreflector for a 1D lattice potential, which will be used as a transverse pump (see Chap. 5). Finally, two high-power mirrors protect the cavity setup from thermal expansion due to absorbed light from the transport laser beam. The setup is completed by an aspheric lens for high-resolution imaging.

In the following, the design and assembly of the setup is described for each component individually.

4.1.1 Mirror machining

Mirror substrates

The cavity mirrors consist of a superpolished BK7 substrate from the company *Research Electro-Optics* with 3 mm diameter and 4 mm length. The substrate curvature has a radius of 75 mm and is centered with respect to the substrate axis with a tolerance of 20 µm. The substrates are coated with a stack of SiO_2/TiO_2 layers with a 40 nm wide reflection band centered at 780 nm, see Fig. 4.2a. The cavity mirrors stem from the same coating badge as the ones used in the setup described in [187, 188].

Most experiments choose short cavity geometries to increase the vacuum Rabi coupling (see Appx. A). In order to approach the cavity mirrors as close as possible, we machine the substrate with a mill, similarly to the technique applied in previous work with a single cavity [189]. We choose an edge-type target shape for the substrate, providing a mirror surface diameter of 0.45(5) mm and an opening angle of 56(1)°, slightly smaller than the angle of 60° between the cavity axes (see Fig. 4.2b). A further reduction of the mirror surface would compromise the finesse for the fundamental Gaussian mode. Shorter crossed cavities would be feasible only with reduced mode diameter by choosing higher mirror curvature, for example with fiber cavities [190, 191].

The milling procedure is shown in Fig. 4.2c-f. In order to securely place the workpiece in the mill vice, the substrate was already framed into the final mirror mount of the cavity setup and screwed to an aluminium block. The mirror substrate is additionally glued to the mount at two points at the top and the bottom. Here and for all purposes in the following, we used the vacuum-compatible glue *Masterbond EP21TCHT-1*. We start with the bare substrates and protect the mirror surface by applying *FirstContact* polymer solution on the coating. The mirrors are machined on a commercial mill (*A50F65 V* from *Golay-Buchel*) with a diamond wheel of grit size D30 (i. e. a micro grain size below 30 µm) and 6 mm diameter from the company *Haefeli*. We cut off the substrate material in slices of 10 µm at the highest possible spinning frequency of 4000 rpm. No water was used during the milling in order to avoid dissolving the polymer. Instead, the diamond wheel was cleaned with a humid tissue after every $3-5$ ground slices.

Milling procedure

Auxiliary mirrors

The cavity mirrors are in- and outcoupled with four auxiliary mirrors that reflect beams on the cavity axes towards two DN63 viewports along the x_L axis. We use substrates from *Lens-Optics* with 4 mm diameter and an HR coating at $780-830$ nm with equal phase shift for s- and p-polarised light for the AOI of 30°. Due to geometric constraints, we reduce the substrate diameter symmetrically with a similar procedure as for the cavity mirror substrates. The substrate is mounted on a circularly rotatable platform that allows to remove the material until a cylindrical shape with 2.8 mm diameter is reached.

Protective mirrors

We also machine the shape of two protective mirrors shielding the cavities from the transport beam. They consist of a fused silica substrate from *Laseroptik Garbsen* with an HR coating for $1030-1090$ nm at $0-45°$ AOI. The coating resists high powers up to 500 kW/cm^2. The machined mirrors are prism-shaped with an angle of 22.5° between the mirror and the optical axis to reflect the beam out of the chamber through the viewports at 45° from the y_L axis. The base of the prism is triangular with an acute angle close

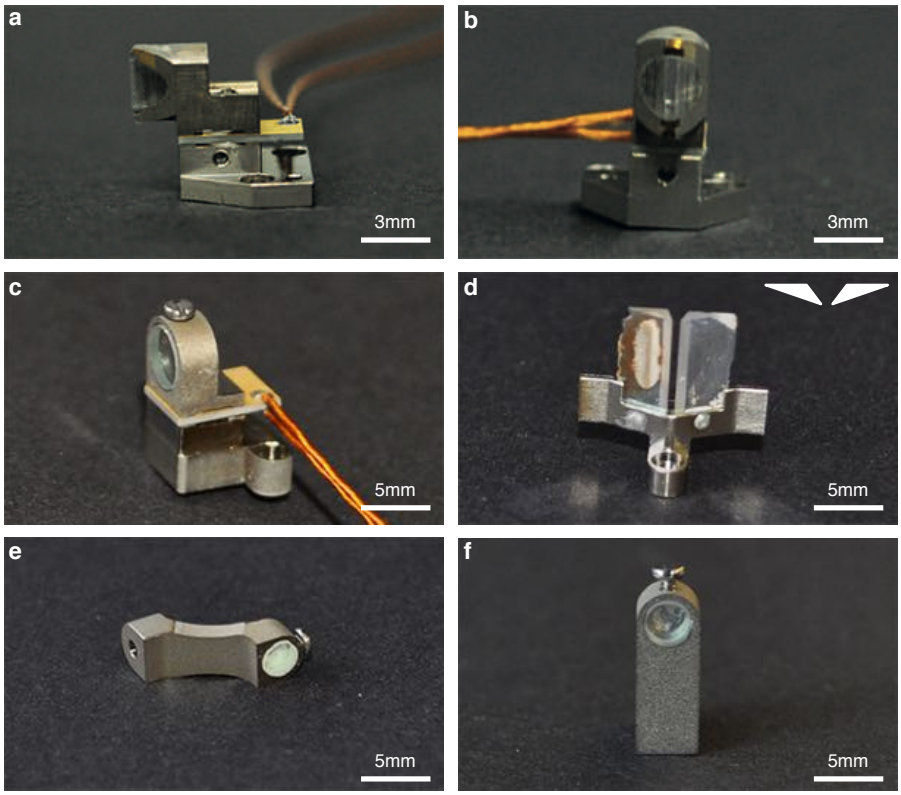

Figure 4.3: *Mirror mounts for the cavity setup.* **a,** Side view of the cavity mirror mount. The top part contains the cavity mirror in a circular pocket of tailored diameter. It is glued on top of a piezo component, which in turn is glued on the base part of the mount. **b,** Front view of the cavity mirror mount. The reflective mirror surface is visible at the centre with an elongated rectangular shape. **c,** Isometric view of the pump mirror mount. In contrast to the cavity mirrors, this mirror is fixed to the mount with an M1-threaded screw. **d,** Mount for the mirrors for protection from the transport beam. The shape of the machined substrate is illustrated in white at the upper right of the picture. The reflective surface is at the long side of the triangle. White and brown parts on the back side of the left mirror are residues of the vacuum-compatible glue. **e,** Mount for the input mirror. The mirror is fixed with an M1-threaded screw. The overhanging design separates the axes of the input and output beams. **f,** Mount for the output mirror. The mirror is fixed with an M1-threaded screw.

to the optical axis of the transport beam to inhibit light scattering from the uncoated surface. Pictures of the machined mirrors and an illustration of the prism base shape is shown in Fig. 4.3. During the milling process the mirror surface was protected with the same polymer and the substrate was fixed on a stainless steel mount with vacuum compatible glue. The mount was removed after the machining by slowly heating it to the melting point of the glue at around 100° C.

4.1.2 Mirror mounting on the base plate

During the bakeout it is crucial that the cavity setup recovers its initial dimensions on a micrometer scale. Prior to builing this setup, a first version was developped with the mirrors fixed by a layer of vacuum compatible glue of 1 mm height. As glue can deform and shrink during the curing pro-

cess, this led to displaced cavity mirrors with a mode distance of ~ 200 µm, larger than the $1/e^2$ mode diameter of ~ 100 µm. A central design criterion for the new setup was to minimize possible drifts of the cavity modes and ensure the mode overlap to persist after the vacuum bakeout.

Cavity mirror mount

The mount for the cavity mirrors consists of two titanium parts with a piezo component in between, see Fig. 4.3. The top part houses the cavity mirror and also serves as holding support during the milling. The diameter of each substrate was determined with a calliper with a precision of 2 µm, according to which a hole was then drilled to fit the substrate with a tolerance of 5 µm. Two triangular pockets give space for vacuum-compatible glue to fix the mirrors. The pocket position at the top and the bottom predefines the axis of potential birefringence that arises from stress during substrate machining. The mounts are built from a single titanium block, which is first prepared as a whole and only divided into several pieces in a last step. This method reduces the uncertainty of the relative heights for the cavity mirrors.

Piezo elements

The top part with the mirror is glued to the piezo component after machining. All employed piezo elements are *NCE51* shear plate actuators from *Noliac* with 0.5 mm height and 2 µm stroke over a range of ±320 V. We obtained an increased precision in the height of the piezo elements by cutting them all from the same sheet. Their shape is custom-made and matches the size of the top mirror mount except for additional space at the back for the soldering connection to the driving voltage cables. The cables are UHV compatible capton-insulated stranded wires, which are soldered to the piezo element with a silver connection. The mount presents a pocket at its bottom side as well as a vertical hole through the entire part, which allow the glue to expand without influencing the height of the cavity mirror. Each cable is guided to a contact plate of the science platform to steer the piezo components with electrical feedthroughs.

In the final step the top part together with the piezo actuator is glued to the base part, which includes a similar pocket for glue. The relative positioning of the titanium parts is set by a mechanical limit stop, which is attached to the structure during the curing of the glue. Pictures of the assembled mount are shown in Fig. 4.3a, b.

Transverse pump mirror

The substrate for the transverse pump mirror is made of BK7 with a diameter of 4 mm. The surface pointing towards the cavity mirrors is AR coated at 1064 nm and for a reflection of 95(1) % at 767 − 830 nm and 0° AOI. The opposite side is AR coated for both wavelength ranges. This coating choice allows to insert a number of beams along a single axis, although the *in vacuo* mirror in principle blocks the optical access: an attractive dipole potential at 1064 nm, imaging light at 780 nm, repumping light for the imaging at 780 nm and a retro-reflected transverse pump lattice at 785 nm. The mirror mount is similar to the cavity mirror mounts and likewise features a piezo component to control its longitudinal position.

The coupling mirrors are inserted into titanium mirror mounts and fixed with M1-threaded screws, which hold the mirror at the cavity mode height. The mirror axes are set to an angle of 30° with respect to the cavity axes, such that the reflected beams meet the vacuum viewports perpendicularly. The protective mirrors for the transport beam are fit into a custom mount with limit stops that define their distance. They were ensured to be parallel by inserting a plate of 0.40 mm width between the substrates during the glue curing. Afterwards, the slit width was measured with a microscope to be 0.42(5) mm. This value is chosen slightly smaller than the design space of 0.47 mm between two cavity mirrors to prevent stray light on the side areas,

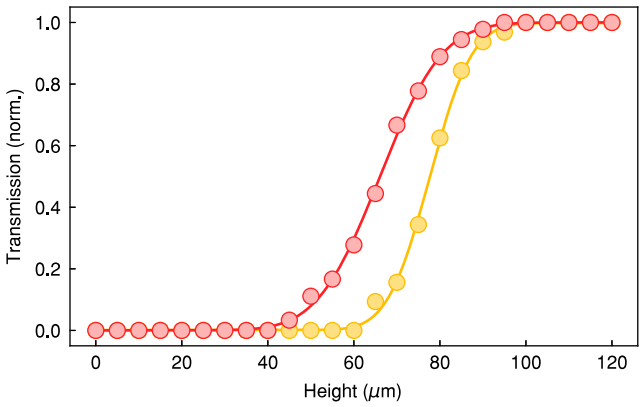

Figure 4.4: *Matching the vertical mode positions.* Transmission of the fundamental mode for cavity 1 (red) and 2 (yellow) for different heights of a needle. We extract a mode height difference of 11.6(3) µm from an error function fit to the data (solid lines).

but as large as possible to avoid cutting the dipole beam during transport into the setup.

All mirrors as well as all other elements are positioned on a titanium base plate with a size of $40 \times 30\,\mathrm{mm}^2$ and a height of 5 mm. Each cavity mirror mount is fixed on the base plate with several M1 screws. Its position is defined by mechanical limit stops integrated into the base plate with position tolerances of 5 µm. The positions of all other mirror mounts are set by pockets in the base plate and cannot be adjusted further. Finally, the entire base plate is integrated into the platform body with three M2 screws at positions chosen for eigenmode suppression [113].

Mode alignment

The high-precision mounts ensure that the cavities are in principle vertically positioned with a combined tolerance of only 12 µm and no further alignment would be necessary. However, in case of additional misalignment the modular design of the setup allows to readily readjust the cavity mirrors by unscrewing the mounts and inserting thin pieces of foil between the mount and the base plate. We determine the mode heights of the cavities by recording the cavity transmission while lowering a tip into the modes, as shown in Fig. 4.4. The tip consists of a steel wire with 100 µm diameter, which is vertically mounted on a 3D translational stage. The recorded light signal drops at a height difference that is equal to the mode height mismatch. We first observe a mismatch of around 100 µm, possibly due to misalignment when glueing the piezo or an off-centered mirror curvature beyond the specifications. By inserting a 100 µm thick molybdenum foil below the lower pair of cavity mirrors, we could compensate for this mismatch. We ensured that the mount did not misalign during the final bakeout by thermally cycling the setup to 120°C at UHV. After the thermal cycling, we measure a residual mismatch of 11.6(3) µm, far below the mode diameters of $\approx 100\,\mu\mathrm{m}$ (cf. Tab. 4.3).

The science platform that houses the setup is built identically compared to the one presented in Chap. 2, except for the setup presented here. The top surface features a pocket and three holes with M2 threads for the base plate.

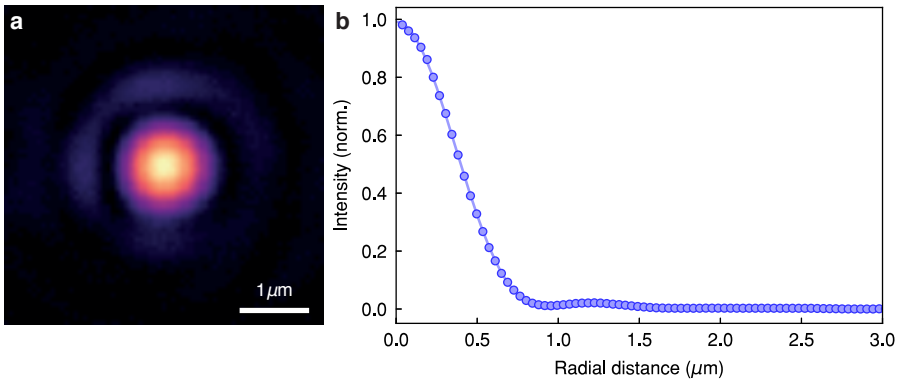

Figure 4.5: *Point-spread function of the imaging system.* **a,** Image of the point-like source from the FIB test target on a test setup with 38 nm effective pixel size. Two rings from the Airy pattern can be distinguished. **b,** The data points show an azimuthal average of the picture in (**a**). Fitting an Airy pattern to the data confirms a diffraction limited Rayleigh resolution of 860 nm after deconvolution with the test target size.

4.1.3 *The aspheric lens*

The setup is completed by an aspheric lens that allows for high-resolution imaging of the *in situ* density sdistribution. The lens (*A12-10HPX-U-B-Ultra* from *Asphericon*) has a focal length of 10 mm and a working distance of 7.6 mm at the design wavelength of 780 nm. Its NA of 0.55 is chosen according to the available optical access to the cavity setup along the vertical direction. Prior to including the lens into the setup, its properties were studied in a test setup by imaging a point-like source from a test target that was produced in an FIB setup. The knowledge of the PSF is sufficient to completely characterize an imaging system since the underlying Fourier optics is linear. The intensity distribution of the Airy pattern is given by [192]

Optical characterization

$$I(\rho) \propto \left(\frac{2j_1(\rho)}{\rho}\right)^2, \tag{4.1}$$

with $j_1(\rho)$ the first order Bessel function of first kind and $\rho = 3.8/r_0$ the radial distance scaled by the resolution r_0. The Rayleigh resolution is defined as the first zero of $I(\rho)$. A measurement of the PSF at 780 nm is shown in Fig. 4.5. The corresponding resolution is consistent with the diffraction limit. The alignment of the aspheric lens to the point source tolerates a lateral displacement up to 20 µm and an axial displacement up to 100 µm without considerable loss in resolution.

Lens mount

The lens is framed in a titanium mount that is positioned on top of the cavity setup. We verify its position with respect to the cavity mode crossing similarly as before by the drop in the cavity transmission. We then displace the tip until an electric contact to the ground plate signals the travelled distance. An offset of 50 µm in the vertical distance was then corrected with molybdenum sheets below the lens mount.

4.2 LOCKING AND PROBING THE CAVITIES

In the experiment, the BEC is exposed to probe fields on each cavity axis and in the transverse direction along x_L. Performing experiments with the optical cavities requires independent control of all three probe field frequencies as well as the resonance frequency of each cavity. This demands for a

laser system that provides five different laser frequencies whose frequencies can all be tuned independently with respect to each other. The tuning range is set by the free spectral range, which describes the frequency difference to the adjacent fundamental mode, see Appx. A. From the dimensions of our science cavities we expect $\nu_{FSR} \approx 50\,\text{GHz}$.

Active stabilization of an optical cavity is typically obtained interferometrically with the PDH locking technique [193, 194]. The technique makes use of the frequency-dependent phase shift of the light reflected from a cavity across its resonance. When modulating the incoming laser frequency ν with a frequency ν_{mod}, the resulting error signal shows three zero crossings, at ν and at $\nu \pm \nu_{mod}$.

Pound-Drever-Hall technique

Different research groups employ a number of methods to stabilize the cavity resonance frequency without affecting the atomic dynamics. One possibility is a spatial separation of the stabilization light from the atoms by using a higher order TEM mode with vanishing electric field amplitude on the cavity axis [83, 195]. Another option is to weakly drive a fundamental gaussian mode that is sufficiently far off-resonance with the atomic transitions to create a potential that is small compared to the chemical potential of the cloud. This requires the cavity mirrors to be reflective at a frequency other than the probe frequency, often resulting in a compromise between the two frequencies. A convenient choice is a probe laser that is frequency-doubled with respect to the stabilization laser [196].

We choose a stabilization laser with a wavelength of 830 nm. The transmission of the cavity mirrors at this wavelength is ten times larger than at 780 nm (see Fig. 4.2), sufficiently low to achieve a cavity resonance stabilization that is small compared to the linewidth at the probe frequency. As the stabilization frequency is rather close to the atomic D1 and D2 lines, it is crucial to work at very low intracavity powers in order to avoid an influence on the atomic density distribution. A similar stabilization scheme is used in [188, 197]

Length stabilization

The probing and the stabilization of the science cavities consists of two steps. First, the frequency-tunable light beams for stabilizing and probing each cavity are generated with a laser system on a separate table. This light is then guided to the science cavities, where it is coupled and its intensity is read out for stabilization and probing of the cavities.

4.2.1 *The cavity laser system*

The schematics of the locking scheme are illustrated in Fig. 4.6a. The passively stable frequency reference for probe and stabilization laser is provided by a *transfer cavity* [198–200]. Its long-term stability of 100 MHz/day can be further increased by stabilizing its resonance frequency with respect to a rubidium vapour cell or a wavemeter. Both lasers are locked to a fundamental gaussian mode of the transfer cavity. Their frequencies can be displaced in parallel by changing the length of the transfer cavity. For control of their relative detuning, the probe light is phase-modulated and the 1st sideband is locked to the transfer cavity. We recover a monochromatic laser beam by passing it through a second cavity, the *cleaning cavity*, which is placed before the transfer cavity. The cleaning cavity is necessary in order to be able to freely adjust the laser frequency without influencing the transfer cavity error signal. Its resonance frequency is locked to the first sideband, thereby reflecting the carrier and the -1st sideband. Tuning the modulation frequency leaves the sideband frequency constant but changes

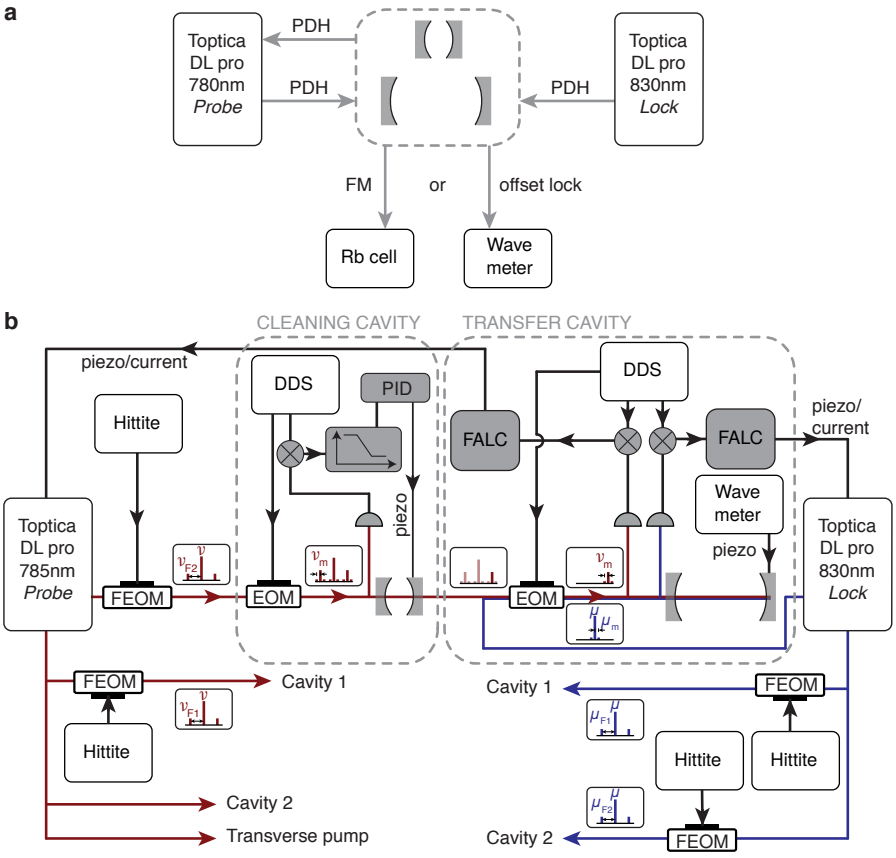

Figure 4.6: *Lock setup for the cavity laser system.* **a,** Schematic view of the lock setup. The stabilization laser at a wavelength of 830 nm and the probe laser at 785 nm are locked on a passively stable transfer cavity with the PDH technique. The passive frequency stability of the transfer cavity can be increased by a FM lock to a rubidium vapour cell or an offset lock to a wave meter. **b,** Electronic setup of the laser system. In order to shift the probe laser frequency ν with respect to the stabilization laser frequency μ, the former is first phase-modulated with frequency ν_{F1} and one sideband is filtered by a cleaning cavity. The feedback for the cleaning cavity lock is generated in a PID circuit, the locks to the transfer cavity are processed by FALC units for distributed feedback to piezo and current of the lasers. Two beams from the stabilization laser are then send to the science cavities after passing FEOMs that create frequency-tunable sidebands μ_{F1} and μ_{F2} to which their resonance frequencies are stabilized. The cavity probe frequencies are adjusted relative to each other by another FEOM with frequency ν_{F2} for cavity 2.

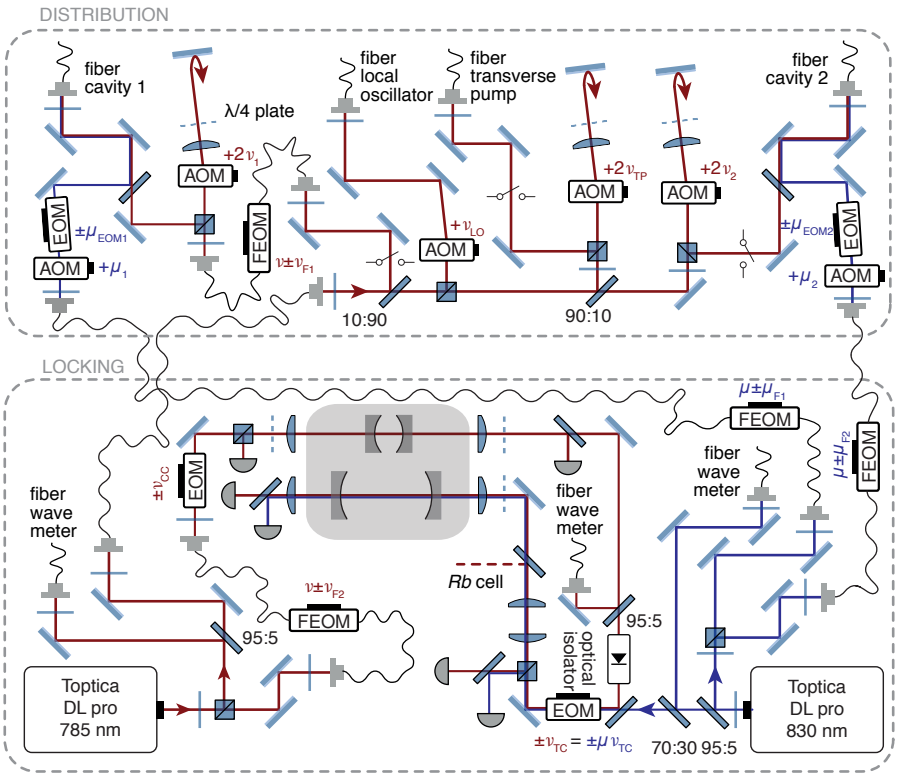

Figure 4.7: *Optial setup of the cavity laser system.* The setup consists of two parts for locking and distribution of the laser beams, respectively. In the first part, the error signals for the cleaning and the transfer cavity locks are generated. Part of the laser power is sent to a wavemeter for frequency monitoring. In the second part, the light from the probe and the lock laser are split and mixed in all required paths and each beam can be switched with a mechanical shutter. Power ratios at the NPBSs are always given as reflection:transmission. Laser frequency separation is achieved with dichroic mirrors.

the laser frequency. Finally, the light for probing and stabilizing each cavity is generated by splitting the main laser beams and producing frequency-shifted sidebands by separately phase-modulating the light in each path.

The RF signals are generated with self-built DDSs that are synchronized with a 10 MHz clock with GPS stability. We adjust the relative frequencies of the probe and stabilization beams with FEOMs (*NIR-MPX-800* from *Photline*), which allow for phase modulation with a band-width of $0 - 12$ GHz. They are mounted on a copper plate that is temperature stabilized to 55° C for an increased stability in the sideband power. The modulation frequencies are generated by frequency-tunable MW sources (*HMC-T2220* from *Hittite*), which can be programmed via LAN. The feedback signals for the transfer cavity locks are generated with FALC units from the company *Thorlabs*.

Optical setup

The optical setup is illustrated in Fig. 4.7. The probe and stabilization light is generated by two tunable diode lasers (*DL pro* from *Toptica*) at wavelengths of 785 nm and 830 nm, respectively. A part of the probe laser is split off the main beam and sent to an FEOM, which adds frequency sidebands at $\pm\nu_{F_2}$ by phase-modulation. Before reaching the cleaning cavity, the beam is modulated with an EOM [201] at a fixed frequency of $\nu_{CC} = 90$ MHz for PDH locking of the cleaning cavity to the positive sideband at $+\nu_{F_2}$. Transmission and reflection are again recorded on PDs. The beam passes an optical isolator, which suppresses the buildup of an interference with the backreflection

	Transfer cavity	Cleaning cavity	
Free spectral range	1.144(1)	34.49(1)	GHz
Cavity length	131.1(1)	4.349(1)	mm
Mirror radius of curvature	500	30	mm
Mirror reflectivity	99.84	99.84	%
Transverse mode spacing	23.4(1)	5910(10)	MHz
Finesse $\mathcal{F}$	2530(30)	1885(10)	
Linewidth	0.453(5)	18.3(1)	MHz

Table 4.1: *Properties of the transfer and the cleaning cavity.* All quantities are derived from measurements at a wavelength of 785 nm. The transfer cavity linewidth at 830 nm is 0.720(8) MHz, resulting in a reduced Finesse of $\mathcal{F} = 1590(20)$.

from the transfer cavity. An empty port offers the option to actively stabilize the transfer cavity with a spectroscopy cell or a wavemeter. The beam is then combined with a part of the stabilization laser and both beams are phase-modulated at $\nu_{TC} = 77$ MHz with an EOM for PDH locking to the transfer cavity. For each wavelength, the transmission and reflection are recorded on PDs for monitoring and error signal generation, respectively.

Transfer and cleaning cavities

The transfer and the cleaning cavity are mounted on a 24 kg stainless steel suspension block. For passive mechanical stability, the block is supported and damped with sorbothane hemispheres at three points and shielded from acoustic noise by a wooden enclosure. The transfer cavity is built with a carbon fiber tube as a spacer between the two mirror substrates in order to minimize thermal expansion [202]. Its length is chosen to obtain a FSR of $\nu_{FSR} \sim 1$ GHz, small compared to the tuning range of the FEOMs. The transfer cavity linewidths of 453(5) kHz and 720(8) kHz for probe and stabilization light are on the order of the expected science cavity linewidths. The cleaning cavity is built from two separately mounted mirrors and has a linewidth of 18.3(1) MHz, in between the laser linewidth and the FEOM modulation frequencies. The optical properties of the transfer and the cleaning cavities are listed in Tab. 4.1.

Susceptibility to environmental parameters

The long-term stability of the transfer cavity is limited by environmental parameters α_i, like temperature, pressure and humidity. In case one of these parameters changes, the PDH lock counteracts changes of the optical path length at 780 nm by changing the cavity length. At 830 nm, the index of refraction might have changed by a different amount and therefore the frequency of the 830 nm laser is displaced. The change is given by [203]

$$\frac{\partial f}{\partial \alpha_i} = \left(\frac{\partial n_1}{\partial \alpha_i} n_2 - \frac{\partial n_2}{\partial \alpha_i} n_1 \right) \frac{f}{n_1 n_2} \tag{4.2}$$

where n_1 and n_2 are the refractive index at 780 nm and 830 nm, respectively. For standard atmospheric conditions, this results in drifts of around -0.4 MHz/°C and 0.1 MHz/mbar. The stability of the environmental parameters in the lab reduces the drift to around 0.1 MHz, acceptable for the experiment. In order to fully suppress the drift, the transfer cavity could be placed in vacuum. An according setup has already been prepared for our experiment [204].

In the second stage, the light from the probe and the stabilization laser is divided and distributed. The stabilization light is split into two paths each

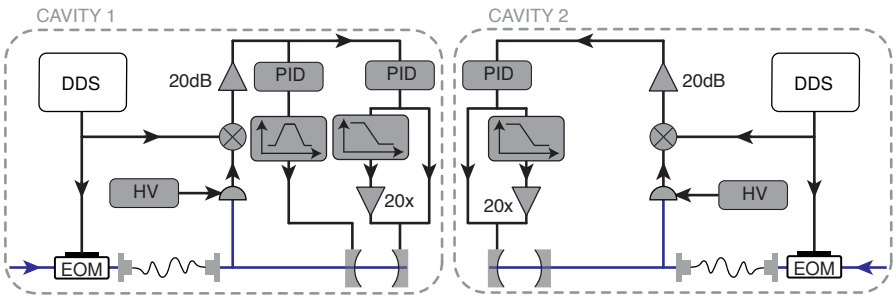

Figure 4.8: *Electronic setup for frequency stabilization of the science cavities.* Each science cavity is locked to the stabilization beam with the PDH locking technique. The low-pass filters with 50 Hz cut-off frequency separate the high-frequency feedback signal from the DC voltage, which is then amplified to achieve a voltage span that is sufficient to reach several FSR. The recombined signal is then fed back to the piezo of a cavity mirror. The feedback for the lock of cavity 1 has an additional band-pass filter for enhanced feedback around a mechanical resonance of the cavity setup at 1.8 kHz.

containing an FEOM to separately shift the two cavity frequencies. Each beam then passes an AOM for intensity stabilization and an EOM for PDH locking to the science cavities. The probe beam is divided into light for each cavity axis and for the transverse pump. Their relative frequencies can be adjusted with AOMs in double-pass configuration [205]. For relative frequency differences higher than the AOM double-pass bandwidth of 2×40 MHz, the probe beam of cavity 1 is phase-modulated with a FEOM and the cavity can be probed with the sideband. Each beam can be switched with a mechanical shutter.

4.2.2 *Science cavity lock*

Each science cavity is locked to the stabilization beam sideband from phase-modulation with the FEOM using the PDH locking technique. This allows to control the resonance frequency by adjusting the FEOM frequency. A schematic view of the electronic setup is shown in Fig. 4.8. For each lock, the beat signal is recorded with a *C30902EH* PD with a bias voltage of ~ 200 V for increased sensitivity. The error signal is then created by mixing down the signal with the modulation frequency for the EOM on the preparation table and subsequently amplified. The modulation frequency is provided by a GPS-stabilized DDS. The feedback signal is created in a PID box (with dominating proportional and integral terms) with ± 10 V output. This voltage has to be amplified, since the piezo stroke for one FSR is around 200 V. In order to avoid compromised lock characteristics from amplified noise, we only amplify the DC output voltage up to 50 Hz and leave the high-frequency feedback signal unaffected.

Mechanical resonance

For cavity 1, we observe a mechanical resonance at 1.8 kHz, which couples to acoustic noise and creates a modulation of the cavity resonance frequency. We suppress the resonance by adding a second PID loop (with dominating derivative term) whose feedback signal is filtered with an active band pass filter of *Sallen-Key* type [206], which is centred at the resonance frequency. We apply the feedback to the second piezo mirror and observe much lower spectral noise when recording the transmission of the cavity. The feedback

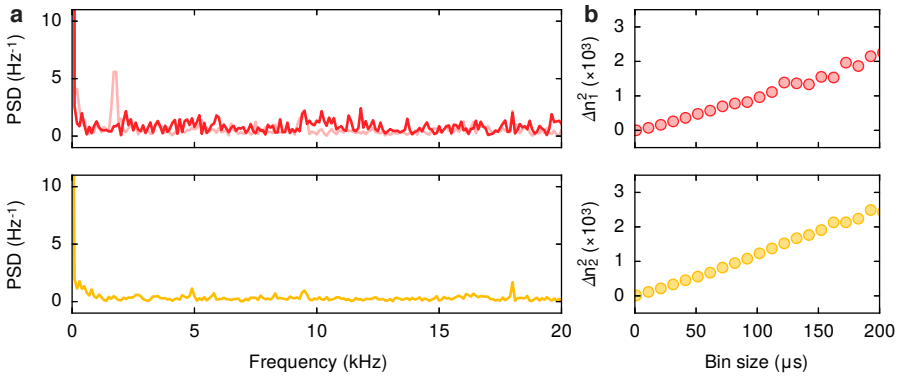

Figure 4.9: *Science lock performance.* **a,** Power spectral density (PSD) of the transmission for cavity 1 (red) and 2 (yellow) at 780 nm. The cavity resonance is detuned by one half-linewidth with respect to the probing frequency, such that fluctuations in the resonance frequency convert into power fluctuations. The shaded red line shows the behaviour without the second feedback loop. **b,** Variance of the photon number from an average of different bin sizes. The linear scaling indicates a shot noise-limited performance.

to cavity 2 consists of a single PID loop only since mechanical resonances are negligible.

The lock characteristics for both cavities are shown in Fig. 4.9. The noise spectrum is obtained with a Fourier transform of the photon traces recorded on the SPCMs. We observe a flat distribution over the full range of the piezo bandwidth of $0 - 20$ kHz. We can further analyze the lock behaviour by calculating the variance of the photon number averaged over different bin sizes of the recorded photon trace. We observe a linear scaling for both cavities, as is characteristic for shot noise-limited performance.

Optical setup

The optical setup for the science cavity lock is shown in Fig. 4.10. For each cavity, the lock light exits from an optical fiber from *Schäffter+Kirchhoff* and is first polarization-cleaned at a PBS. Subsequently, 90% of the light is reflected at a NPBS and sent to two PDs for intensity stabilization with a servo controller (*LB1005* from *Newport*). The beam then passes a second NPBS with 10% transmission, which reflects 90% of the light travelling back from the science cavity after reflection. The reflection from the NPBS is then directed to a fast PD to generate the lock signal. At the cavity output, the transmission of the lock light is recorded on a high-gain PD. The beam is focussed into the cavities and recollimated at the output with achromatic lenses of 300 mm focal length (*AC254-300-B* from *Thorlabs*).

4.2.3 *Probe light and photon detection*

Setup for cavity probe light

The probe light exits from the same optical fiber as the stabilization light and shares the beam path until reaching the science cavities. Before the science cavities, the beam passes two wave-plates with $\lambda/2$ and $\lambda/4$ retardation for light at 785 nm and λ retardation for light at 830 nm. This allows to change the input polarization for the probe light without altering the electronic lock signal. Custom-made band-pass filters from *Semrock* with HT at 830 nm and 10% or 1% transmission at 785 nm allow us to attenuate the probe light to intracavity photon numbers $n \sim 10^{-3}$ without substantial noise on the intensity regulation.

Transverse pump setup

The optical setup for the transverse pump lattice is shown in Fig. 4.10.

Beam	Frequency
Probe laser ν (785 nm)	384.66085 THz
Probe transfer cavity	$\nu + \nu_{F_2}$
Probe cavity 1	$\nu + \nu_{F_1} + 2\nu_1$
Probe cavity 2	$\nu + 2\nu_2$
Probe transverse pump	$\nu + 2\nu_{TP}$
Probe local oscillator	$\nu + \nu_{LO}$
Lock laser μ (830 nm)	361.64287 THz
Lock transfer cavity	μ
Lock cavity 1	$\mu + \mu_{F_1} - \mu_{EOM_1} + \mu_1$
Lock cavity 2	$\mu - \mu_{F_2} + \mu_{EOM_2} + \mu_2$

Table 4.2: *Frequencies for the cavity laser system.* The frequencies ν of the probe laser and μ of the stabilization laser are modified by a number of elements. The probe light for the cavities and the transverse pump passes AOMs in double-pass configuration, causing frequency offsets ν_{F_1}, ν_{F_2} and ν_{TP}, respectively. All probe frequencies are adjusted with respect to the stabilization frequencies with a FEOM at ν_{F_2} and the probe frequency for cavity 1 is additionally controlled with ν_{F_1} with respect to the others. The cavity resonance frequencies are determined by the tunable FEOM frequencies μ_{F_1} and μ_{F_2}, as well as by the fixed frequencies ν_{EOM_1}, ν_{EOM_2} of the EOMs and ν_1, ν_2 of the AOMs.

The beam exiting the fiber is collimated to a $1/e^2$ diameter of 2.7 mm. After a PBS for polarization cleaning 10% of the power is directed to a PD for intensity stabilization. The beam then passes an achromatic lens with $f = 250$ mm focal length (*AC254-250-B* from *Thorlabs*), which focusses the beam into the vacuum on the plane of the transverse pump mirror. The beam polarization is set to V, such that it can be combined with the imaging beam in a PBS. The retroreflected beam is aligned by maximizing the power that is coupled back through the optical fiber.

Photon detection

At each cavity output, the leaking light is directly guided to a fiber-coupled SPCM (*COUNT-100C-FC* from *LaserComponents*). Photon detection is signalled by a TTL pulse generated from an internal avalanche PD and high-speed electronics. At 785 nm, they provide a high quantum-efficiency of 60% with a maximum photon count rate of 20×10^6 photons/s and a dark count rate of 100 photons/s. The TTL pulses are sent to a digitizer unit (*MCS6* from *FAST ComTec*). We then read out the stored arrival times with a home-built software environment based on the programming languages Python, C and Matlab. The software is an extension of the version described in [207].

4.3 CHARACTERIZATION OF THE SCIENCE CAVITIES

4.3.1 Cavity properties

After inserting the cavity setup into the vacuum chamber we determine the key cavity properties from transmission scans with probe light. For these measurements the cavity resonance remains constant, while a weak probe

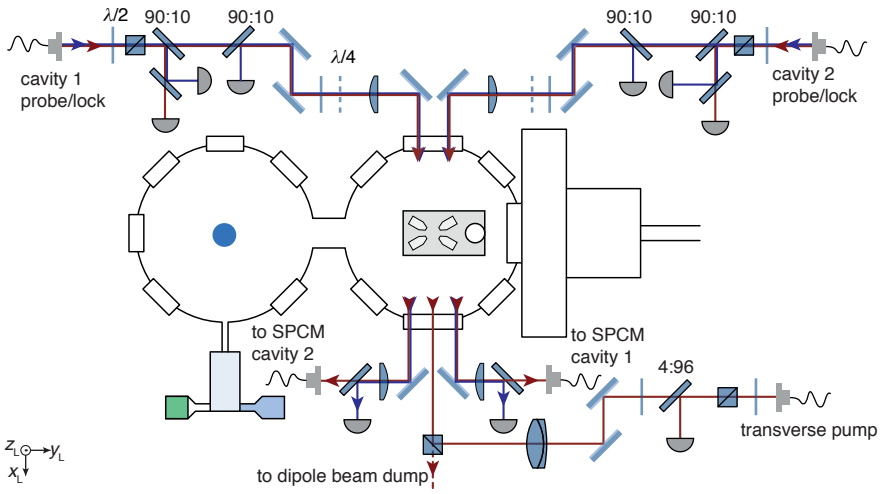

Figure 4.10: *Optical setup for the science cavities.* For each cavity, the light for probing and stabilization exits a common optical fibre. One part is reflected on PDs for intensity stabilization, whereas the remainders are directed to the science cavity. The input polarization of the probe light is controlled with wave plates. After being reflected at the science cavity, the stabilization light is sent to a PD to create the error signal. Alternatively, the transmitted stabilization light can be detected on a DC PD. The cavity output light is recorded on a fiber-coupled SPCM. The transverse pump beam is also intensity-staibilized with the signal recorded on a PD after the fibre output. The remainder of the beam is subsequently focussed to the position of the retroreflecting mirror inside the vacuum. Power ratios at the NPBSs are always given as reflection:transmission. Laser frequency separation is achieved with dichroic mirrors.

beam is ramped across the cavity resonance by applying a time-dependent AOM frequency.

- **FSR:** The FSR is determined by measuring the cavity transmission for two consecutive longitudinal modes while stabilizing its length. This allows us to infer the cavity length L with a high precision from the connection $\nu_{FSR} = c/2L$. We measure the FSR at the probe wavelength 785 nm. The cavity length can differ by $\sim 1\,\mu m$ for the lock laser light, because of the wavelength-dependent intrusion of the cavity field into the substrate [208].
- **Linewidth:** We obtain the cavity linewidth $\Delta\nu$ from a Lorentzian fit to the photons recorded at a resonance scan with the probe laser. It allows to deduce the photon decay rate $\kappa = 2\pi\Delta\nu/2$ and, from the cavity length, the Finesse $\mathcal{F}$. The measured value constitutes an upper bound, since the resonance is convolved with the laser linewidth and the stability of the resonance frequency. This influence could be eliminated by measuring the cavity decay rate in a ringdown measurement [209].
- **Birefringence:** The birefringence of the s- and the p-polarized eigenmodes of the cavity is obtained from a similar resonance scan. By recording the transmission for different input polarizations we can determine the eigenaxes of the cavity modes.

A summary of the key properties can be found in Tab. 4.3. The input coupling fraction and mirror loss rates are of main interest for the photon detection efficiency, which is treated in Sec. 4.3.3.

	Cavity 1	Cavity 2	
FSR	61.26(1)	53.49(1)	GHz
Length	2448.8(5)	2804.2(5)	µm
Decay rate κ	$2\pi \times 147(4)$	$2\pi \times 800(11)$	kHz
Finesse $\mathcal{F}$	$208(6) \times 10^3$	$33.4(5) \times 10^3$	
Mirror radius of curvature	75	75	mm
Transverse mode spacing	4.99	4.67	GHz
TEM_{00} mode waist w_0	48.7	50.4	µm
Vacuum Rabi coupling g_0	$2\pi \times 1.95$	$2\pi \times 1.77$	MHz
Q-factor	$1.30(4) \times 10^9$	$0.24(1) \times 10^9$	
Purcell factor	10.45(31)	1.57(2)	
Single atom cooperativity	4.5	0.7	
Birefringence of TEM_{00}	3.88(6)	4.17(3)	MHz

Table 4.3: *Properties of the science cavities.* All values are deduced from the specified mirror curvature and the measurements of the FSR, cavity linewidth and birefringence. The eigenmodes of the both cavities are close to H and V. The V polarized mode has the higher frequency.

4.3.2 *Positioning a quantum gas at the mode crossing*

Alignment procedure

When preparing the BEC inside the science cavity setup, an alignment procedure is required that gives a position uncertainty small compared to all beam diameters. We employ a method that is based on the dispersive effect of the probe light on the atoms. On-axis probe light with a frequency that is red-detuned from the atomic resonance frequency gives rise to an attractive potential with the shape of the cavity mode. As a consequence, the minimum position of the atomic trap is displaced for any intracavity light field if the trap is not centered on the cavity mode. We convert this displacement into a momentum by applying a probe pulse on the cavity axis that has a length of 1 ms, which is on the order of T/4, where T is the trap oscillation time. Following the pulse, we switch off all potentials and perform absorption imaging after ballistic expansion.

The result is shown in Fig. 4.11. We observe an opposite displacement for positive and negative misalignment from the cavity mode center. The center-of-mass momentum is most strongly affected when positioning the cloud around one $1/e^2$ mode radius away from the center. We can perform these mesurements along all axes and align the cloud until no momentum is transferred along any direction when probing either of the cavities.

This method is ideal as long as the collective dispersive shift is smaller than the cavity linewidth. If the cavity resonance frequency is significantly shifted by the atoms, the potential from the probe light and the position of the atoms depend on each other and the method is more challenging to apply. Alternative alignment approaches are base on the critical point for self-organization (see Chap. 5) Kapitza-Dirac diffraction or the dispersive shift. However, none of these methods shows a zero-crossing at the ideal alignment position, in contrast to the technique presented above.

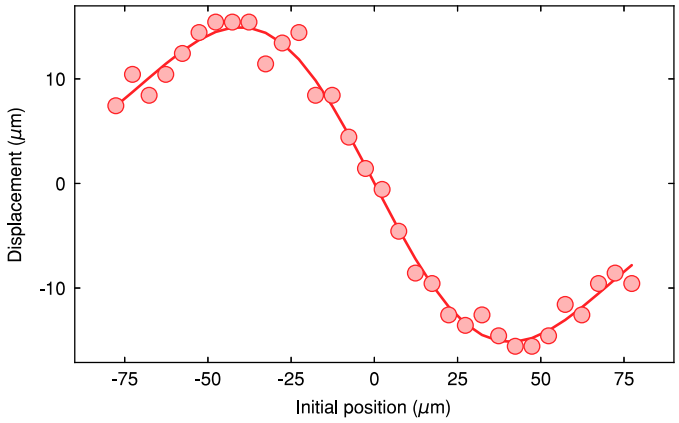

Figure 4.11: *Aligning the BEC to the cavity mode center.* We apply a probe pulse of 1 ms length along the cavity axis and measure the position of the atomic cloud after 25 ms ballistic expansion. The data points show the displacement as a function of the trap position. The solid line shows a fit to the data, where the fit function is the derivative of a Gaussian.

4.3.3 *Measuring intracavity photon numbers*

Kapitza-Dirac diffraction

We use the dispersive interaction with the atoms to calibrate the intracavity photon number. Our method is based on determining the lattice depth per intracavity photon. A number of techniques exist to calibrate the lattice depth of optical lattice potentials [210]. We use Kapitza-Dirac diffraction, where the atomic cloud is exposed to a lattice pulse of length τ, which creates the potential $V = V_0 \cos(kx^2)$ wich $V_0 < 0$. In the Raman-Nath regime with $\tau \ll 1/\omega_{rec}$ [211], we can neglect the kinetic energy and the time evolution for a BEC in the motional ground state $|0\rangle$ is only given by the potential:

$$|\psi(t)\rangle = \exp\left(-\frac{i}{\hbar}\int_0^t V dt'\right)|0\rangle = \exp\left(-\frac{iV_0 t}{2\hbar}\cos(2k\hat{x})\right)|0\rangle\,. \tag{4.3}$$

We have ignored a constant phase factor $\exp(V_0\tau/2\hbar)$. With the identity $\exp(ia\cos(b)) = \sum_{\nu\in\mathbb{Z}} = i^\nu j_\nu(a)e^{i\nu b}$ for the Bessel functions of the first kind j_ν, the atomic wave function takes the form

$$|\psi(t)\rangle = \sum_{\nu\in\mathbb{Z}} i^\nu j_\nu\left(\frac{V_0 t}{2\hbar}\right)|2\hbar k\nu\rangle\,. \tag{4.4}$$

The fraction of atoms in the momentum state $|2\hbar k\nu\rangle$ is therefore given by $p_\nu = j_\nu(V_0 t/2\hbar)^2$. We can record the atomic momentum distribution from absorption images after ballistic expansion and determine the probabilities p_ν for different lattice depths.

The result is shown in Fig. 4.12. We determine the lattice depth per beam power in the probe pulse from a fit of Eq. 4.4 to the data. A second measurement of the photon count rate per probe pulse with the SPCM suffices to extract the lattice depth per intracavity photon.

The lattice depth per intracavity photon is given by $U_0 = \frac{g_0^2}{\Delta_a}$ with the detuning $\Delta_a = \omega_p - \omega_a$ between the laser frequency and the atomic resonance (see Appx. A). Comparing the photon counting rate on the SPCM with the above measurement of the intracavity lattice depth, we can infer the detection efficiency for an intracavity photon as $(\eta_1, \eta_2) = (9.7(4)\%, 2.0(1)\%$.

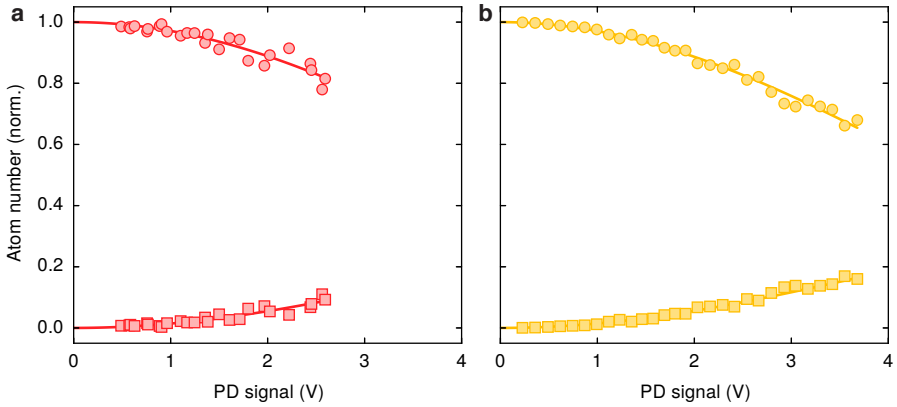

Figure 4.12: *Intracavity lattice depth calibration.* We expose the atomic cloud to a short pulse of 10 µs length after a short expansion time of 1 ms to reduce the density and ensure a ballistic expansion. The momentum distribution is then measured after additional 24 ms of ballistic expansion. The occupation probability in the momentum ground state (circles) and the momentum state at $|\pm 2\hbar k\rangle$ (squares) are shown for cavity 1 (red) and 2 (yellow). The images are obtained in absorption imaging after 25 ms ballistic expansion (including 1 ms before the lattice pulse).

Part II

REALIZATION OF A SUPERSOLID

5

SELF-ORGANIZATION IN A RECTANGULAR LATTICE

Atoms dispersively coupled with the light field of an optical cavity can undergo a phase transition to a self-organized state. In previous realizations the coupling was mediated by a transverse pump beam orthogonal to the cavity axis. In our system, the pump has a non-orthogonal angle, which changes the situation qualitatively. The first part of this chapter contains a theoretical description of the system, followed by measurements of the phase transition to the self-ordered state. Finally, we present studies on its sensitivity to dissipation, temperature and magnetic field.

CHAPTER CONTENTS

The interaction of an atomic ensemble with a cavity mode gives rise to a number of collective effects [81]. In the following we focus on a particular phenomenon called self-organization, which occurs when the atoms are coherently driven transversely to the cavity field. For sufficiently strong driving strength, the system undergoes a phase transition to a crystalline state, accompanied by the onset of a light field in the cavity [75, 212].

Photon scattering in free space

In order to develop an intuitive picture of this effect, we start by considering photon scattering processes at a single atom at position $\mathbf{r}$ in free space. The atom is illuminated by an off-resonant light field that coherently scatters photons into any direction with a phase $\propto e^{i\mathbf{k}\cdot\mathbf{r}}$ inherited from the incoming light field with wave-vector $\mathbf{k}$ [213]. The phase becomes restricted to 0 or π when considering a standing-wave with an electric field $\propto \cos(\mathbf{k}\cdot\mathbf{r})$ instead, because the function is real-valued. For two atoms, the spatial phase dependence of the scattered light leads to a position-dependent interference of the scattering amplitudes. The situation is illustrated in Fig. 5.1. Analogous to Young's interference experiment [192], the scattering amplitudes from an incoming plane wave of wavelength λ interfere constructively for angles θ, where the distance between the atoms is $\lambda/\cos(\theta)$ and multiples thereof. Correspondingly, destructive interference occurs for distances in between. Extending the situation to higher atom numbers and two dimensions with an incoming standing wave field, the transverse pump, creates a situation similar to the Bragg condition for light scattering from a crystal lattice.

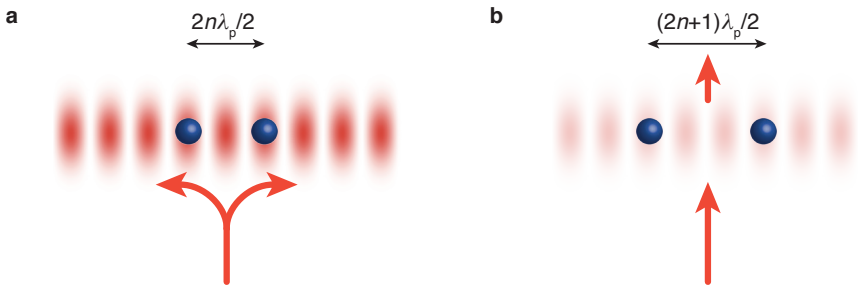

Figure 5.1: *Coherent light scattering of two atoms.* **a,** Two atoms separated by $2n\lambda_p/2$ ($n \in \mathbb{N}$) scatter photons from an incoming plane wave with wavelength λ_p. The scattering amplitudes interfere *constructively* for the perpendicular direction. **b,** In contrast, for a distance $(2n+1)\lambda_p/2$, no light is scattered in the perpendicular direction, since the scattering amplitudes interfere *destructively*.

Photon scattering in optical cavities

Coherent light scattering of cold atoms has been studied in free space [214] and with optical lattices [215–220]. In these systems, the scattering amplitude is proportional to the amplitude of the incoming light. The situation changes when a threshold mechanism is present that favors a homogenous atomic distribution with no light scattering, for instance by placing an atomic ensemble in an optical cavity, as illustrated in Fig. 5.2. This results in two effects: first, the preferred angle for the light scattering is set by the cavity mode thanks to the Purcell effect [221], thereby suppressing every atomic order that is incommensurate with the lattice constant allowed by the Bragg condition for the cavity angle. Second, the cavity is frequency-selective by its eigenmode and scattering light at a frequency below the cavity resonance costs energy proportional to the detuning (see Appx. A).

Phase transition to a self-organized state

In terms of the involved energy scales, the process can be interpreted as a competition between the kinetic energy associated with the scattering processes and the potential energy that the atoms gain from the attractive potential of the light fields. While the former favors a homogeneous density distribution without wavefunction curvature, the latter pulls the atoms towards the potential minima and creates a periodic modulation. We obtain a threshold behaviour with two different qualitative situations: for small coupling strengths the atomic distribution remains flat and no cavity field is present. As soon as the coupling strength exceeds a critical value, the kinetic energy associated with the density modulation of the atomic wave function is overcome and the system enters a self-organized phase with periodic ordering and macroscopic population of the cavity mode. This corresponds to a second order phase transition. In the case of orthogonal transverse pump beam, the phase transition has been studied for thermal atoms [212, 222], as well as with a BEC for coupling with a single [75, 223, 224] and with several cavity modes [79, 225]. A similar mechanism is also present for atoms in free space with feedback based on the Talbot effect [77].

5.1 THEORETICAL FRAMEWORK

The previous qualitative description can be captured by a quantum optical description of a BEC that is dispersively coupled to an optical cavity. This situation has only been studied in the case of an orthogonal transverse pump. Since the transverse pump is not orthogonal to the cavity modes in our setup, in the following we develop a general framework for arbitrary angles between the cavity mode and the transverse pump lattice and discuss

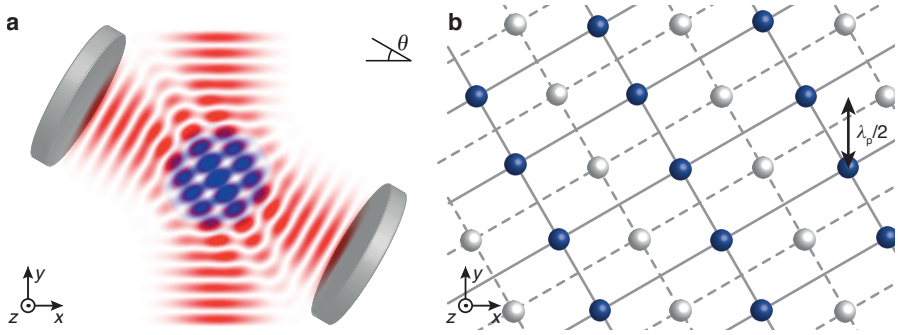

Figure 5.2: *Self-organization in an optical cavity.* **a,** A BEC is placed inside an optical cavity and illuminated by a transverse pump lattice. The angle between the cavity and the transverse pump lattice is θ. **b,** Site positions of the interference lattice of the transverse pump and the cavity fields for a relative phase of 0 (blue) or π (white). The density modulations are displaced by half a lattice constant, which is set by the transverse pump wavelength λ_p. No other relative phases between the two light fields are possible due to the boundary conditions of the cavity mirrors.

its implications on the self-organization phase transition. Furthermore, we give an alternative description of the system in terms of photon-mediated interactions between the atoms. Finally, the limit of an orthogonal pump is recovered, thereby connecting the results to previous work.

5.1.1 *Phase transition with discrete symmetry breaking*

In this section, we will use a mean-field expansion (or ϕ^4 theory) to describe the self-organization phase transition in a general language. This approach was originally developed by Landau for thermal phase transitions [226] and presents a powerful tool for describing phase transitions in various field theoretical contexts [1]. However, fluctuations are neglected by Landau theory, which can play an important role in the vicinity of the phase transition. Landau's theory was therefore soon extended: first by Ginzburg in the context of superconductors [227] to also incorporate local fluctuations, and then by Wilson, who used renormalization group theory to incorporate the universal character of spatial and temporal fluctuations around the critical point [228, 229]. For our system, the global atom-cavity coupling suppresses the universal spatial fluctuations, and a non-local description is sufficient. However, since we are considering a system at zero temperature, the mean-field expansion has no temperature dependence. Although the expansion instead dependson the coupling parameter λ we use the term Landau theory in analogy to the original expansion.

Landau theory forms the basis of a group-theoretical description of phase transitions. In this theory, we introduce an order parameter that distinguishes two phases by measuring the degree of order: while the order parameter is zero in the normal phase, it acquires a nonzero value in the ordered phase past the critical point. From a group-theoretical perspective, the order parameter is associated with one of the irreducible representations of a subgroup of the system symmetry in the high-symmetry phase [230]. Let H be the symmetry group describing the normal (high-symmetry) and L the symmetry group describing the ordered (low-symmetry) phase. Then L is a subgroup of H and the order parameter presents an irreducible representation of the group G with $G \oplus L = H$. The symmetry of G is called *broken* and

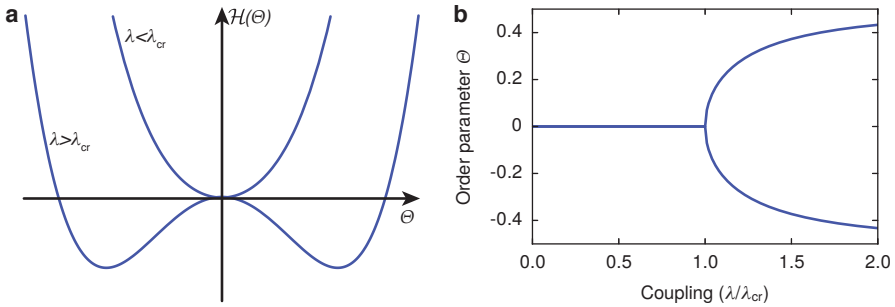

Figure 5.3: *Effective potential for a scalar order parameter.* **a,** The effective potential qualitatively changes across the phase transition. In the normal phase with $\lambda < \lambda_{cr}$, the effective potential has one minimum at the origin. When entering the ordered phase with $\lambda > \lambda_{cr}$, two minima at finite expectation value appear symmetrically around the origin. **b,** The order parameter acquires a finite expectation value when the system enters the ordered phase. It has two different solutions with $\mathbb{Z}_2$ symmetry.

the number of elements of G corresponds to the number of ground states among which the system picks one upon entering the ordered phase.

In Landau theory, the free energy is expanded in powers of the order parameter. The order parameter values at the minima of the effective potential determine the allowed groups of the ordered phase. Since we are dealing with a quantum phase transition at zero temperature, the concept of free energy reduces to the mean-field energy. Instead of the temperature, the expansion coefficients then depend on the coupling λ that controls the phase transition [231]. The order parameter Θ is scalar for our system, since the atoms can form a density modulation on either the even or the odd sites of the chequerboard lattice (see Fig. 5.2). At the absence of a symmetry breaking field, the mean-field expansion of the mean-field Hamiltonian $\mathcal{H}_\lambda$ only contains even powers of Θ and we obtain the following expansion up to fourth order:

$$\mathcal{H}_\lambda(\Theta) = \frac{r}{2}\Theta^2 + \frac{g}{4}\Theta^4 + \mathcal{O}(\Theta^6), \tag{5.1}$$

with r, g functions of λ. The expectation value of Θ in equilibrium is determined by the global minimum of $\mathcal{H}_\lambda(\Theta)$ and Θ hence follows the condition

$$\left.\frac{\partial \mathcal{H}_\lambda(\Theta)}{\partial \Theta}\right|_{\lambda=\text{const}} = 0. \tag{5.2}$$

This equation has two solutions, $\Theta = \pm\sqrt{-r/g}$ if $-r/g > 0$, and only one solution, $\Theta = 0$, elsewhere. The critical point λ_{cr} is therefore marked by $-r/g = 0$. We interpret this result by considering the shape of the effective potential across the phase transition, as illustrated in Fig. 5.3. The coefficient r remains positive throughout the *normal phase* with $\lambda < \lambda_{cr}$ and the shape is determined by the parabolic contribution. A single minimum exists at $\Theta = 0$. The situation changes if $r < 0$, where the inverted parabola causes the effective potential to exhibit two minima symmetrically around zero. The order parameter acquires a finite expectation value throughout the *ordered phase* with $\lambda > \lambda_{cr}$.

Effective potential across the phase transition

The Landau expansion shows a parity symmetry with the $\mathbb{Z}_2$ symmetry group, since it stays invariant under $\Theta \to -\Theta$. When crossing the phase transition and entering the ordered phase, the system has to choose among the two solutions for the order parameter. It is therefore not $\mathbb{Z}_2$-invariant

Order parameter with parity symmetry

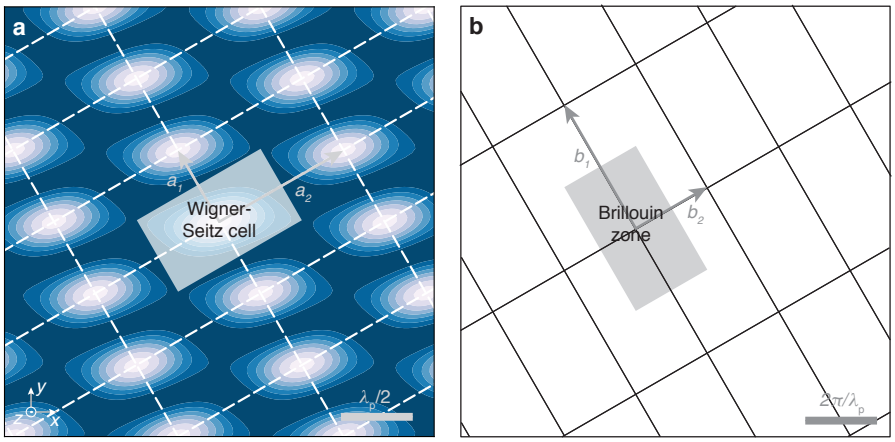

Figure 5.4: *Unit cell in real and momentum space.* **a,** The density modulation from the self-organization is periodic with the lattice vectors $\mathbf{a}_1$ and $\mathbf{a}_2$. The corresponding Wigner-Seitz cell has a rectangular shape. **b,** The reciprocal lattice is spanned by the vectors $\mathbf{b}_1$ and $\mathbf{b}_2$. The shape of the Brillouin zone is inverted with respect to the Wigner-Seitz cell.

any longer and shows a lower symmetry than the underlying Hamiltonian. This process is called *spontaneous symmetry breaking*. Experimentally, the system is always subject to symmetry breaking fields that can be included by odd powers of Θ in the Hamiltonian expansion. Even if their amplitudes are small, they can be dominant close to the critical point and determine the outcome of the order parameter [232].

5.1.2 Momentum mode expansion

We now switch from a phenomenological description of the phase transition to a microscopic picture that is specific to our system. The following description is restricted to the x-y plane, which is spanned by the cavity and the transverse pump lattice, as illustrated in Fig. 5.2. We can construct the Wigner-Seitz cell from the geometry of the interference pattern between transverse pump and cavity mode, see Fig. 5.4. It is spanned by the lattice vectors:

Wigner-Seitz cell

$$\mathbf{a}_1 = -\frac{\lambda_p}{2}\frac{\sin(\theta)}{1+\cos(\theta)}\mathbf{e}_x + \frac{\lambda_p}{2}\mathbf{e}_y, \tag{5.3}$$

$$\mathbf{a}_2 = \frac{\lambda_p}{2}\frac{\sin(\theta)}{1-\cos(\theta)}\mathbf{e}_x + \frac{\lambda_p}{2}\mathbf{e}_y, \tag{5.4}$$

where $\theta \in [0, \pi]$ is the angle between the transverse pump and the cavity, λ_p is the wavelength of the transverse pump, and $\boldsymbol{e_x}$ and $\boldsymbol{e_y}$ are the unit vectors pointing along x and y, respectively. The Wigner-Seitz cell is rectangular, since the two vectors are orthogonal and have different lengths. Its area is

$$\mathcal{A} = |\mathbf{a}_1 \times \mathbf{a}_2| = \frac{\lambda_p^2}{2}\frac{\sin(\theta)}{1-\cos^2(\theta)}. \tag{5.5}$$

For the reciprocal lattice, the Brillouin zone can be constructed from the atomic momentum modes that are accessible by photon scattering processes.

The transverse pump and the cavity mode can be described by the wave vectors

$$\mathbf{k}_p = k\mathbf{e}_y \tag{5.6}$$
$$\mathbf{k}_c = -k\sin(\theta)\mathbf{e}_x + k\cos(\theta)\mathbf{e}_y, \tag{5.7}$$

where $k = 2\pi/\lambda_p$ is the wavenumber for all photons. In lowest order, the momentum states that are accessible from the ground state at zero momentum are the combinations $|\pm\mathbf{k}_p \pm \mathbf{k}_c\rangle$. We can construct the reciprocal lattice from the basis vectors:

Brillouin zone

$$\mathbf{b}_1 = \mathbf{k}_p + \mathbf{k}_c = -k\sin(\theta)\mathbf{e}_x + k\,(1+\cos(\theta))\,\mathbf{e}_y, \tag{5.8}$$
$$\mathbf{b}_2 = \mathbf{k}_p - \mathbf{k}_c = \quad k\sin(\theta)\mathbf{e}_x + k\,(1-\cos(\theta))\,\mathbf{e}_y. \tag{5.9}$$

The area of the Brillouin zone is accordingly

$$\mathcal{A}_{BZ} = |\mathbf{b}_1 \times \mathbf{b}_2| = 2k^2\sin(\theta). \tag{5.10}$$

The real and reciprocal lattice vectors fulfill the relation $\mathbf{a}_i \cdot \mathbf{b}_j = 2\pi\delta_{ij}$ for $i,j \in \{1,2\}$, confirming the phase-space condition $\mathcal{A}\mathcal{A}_{BZ} = (2\pi)^2$.

The self-organization phase transition for a BEC in an optical cavity can be described in terms of photon scattering processes. The following derivation presents a generalization of the existing theoretical framework [81] to arbitrary angles between transverse pump and cavity. The dispersive interaction of an atom with the quantized field of an optical cavity is described in Appx. A. Here we start with the many-body Hamiltonian for an atomic ensemble that is coupled to an optical cavity and transversely pumped by a standing-wave lattice:

Dispersive atom-light interaction
Many-body localization

$$\begin{aligned}\hat{\mathcal{H}}_{mb} =& -\hbar\Delta_c\hat{a}^\dagger\hat{a} \\ &+ \int_{\mathcal{A}} d\mathbf{r}\hat{\psi}^\dagger(\mathbf{r})\left[\frac{\hat{\mathbf{p}}^2}{2m} + V(\mathbf{r}) + \hbar\frac{h(\mathbf{r})g(\mathbf{r})}{\Delta_a}(\hat{a}^\dagger + \hat{a})\right. \\ &\qquad \left. + \hbar\frac{g^2(\mathbf{r})}{\Delta_a}\hat{a}^\dagger\hat{a} + \hbar\frac{h^2(\mathbf{r})}{\Delta_a}\right]\hat{\psi}(\mathbf{r}) \\ &+ \frac{U}{2}\int_{\mathcal{A}} d\mathbf{r}d\mathbf{r}'\hat{\psi}^\dagger(\mathbf{r})\hat{\psi}^\dagger(\mathbf{r}')\hat{\psi}(\mathbf{r}')\hat{\psi}(\mathbf{r})\end{aligned} \tag{5.11}$$

Here, $\Delta_c = \omega_p - \omega_c$ is the detuning of the transverse pump at frequency ω_p from the cavity mode at frequency ω_c, and $\Delta_a = \omega_p - \omega_a$ is the detuning from the atomic resonance at ω_a. Cavity photons are created (annihilated) by the operator $\hat{a}^\dagger$ ($\hat{a}$) and $\hat{\psi}^\dagger(\mathbf{r})$ ($\hat{\psi}(\mathbf{r})$) is the atomic field operator that creates (annihilates) an atom at position $\mathbf{r} = (x,y)$.

The cavity mode and the transverse pump are described by the mode profiles $g(\mathbf{r}) = g_0\cos(\mathbf{k}_c\cdot\mathbf{r})$ and $h(\mathbf{r}) = \Omega_p\cos(\mathbf{k}_p\cdot\mathbf{r})$, respectively. The Gaussian envelope of both modes can be ignored since the cloud diameter is small compared to the mode diameter. $\mathbf{p}$ is the momentum of an atom and m its mass. Atomic collisions are captured with the rescaled 2D contact interaction $U_{2D} = \mathcal{A}\bar{n}U$, rescaled from the 3D interaction $U = 4\pi\hbar^2 a/m$ with the s-wave scattering length a and the 3D atomic density $\bar{n}$ [2]. The reduction to s-wave scattering is valid in our experimental regime at ultra-low temperatures, since all higher order scattering processes are negligible.

Hamiltonian terms

We now give a brief physical interpretation of each term in the Hamilto-

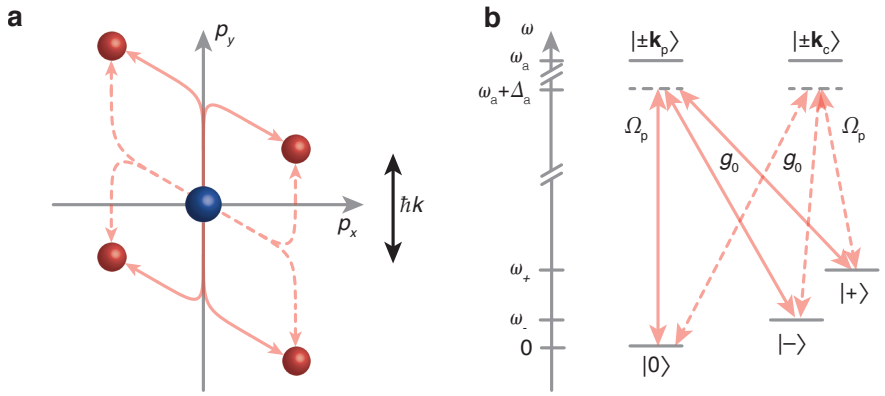

Figure 5.5: *Three-mode expansion in momentum space.* **a,** Atoms from the ground-state BEC at $|\mathbf{p}\rangle = |0\rangle$ (blue) are coupled to excited momentum states (red) by two-photon scattering processes. Solid (dashed) lines correspond to the absorption (emission) of a transverse pump photon and the creation (annihilation) of a cavity photon. The inverse processes occur equally but are not shown for clarity. We combine the excited momentum states to two standing-wave modes $|+\rangle$ and $|-\rangle$ at high and low kinetic energy, respectively. **b,** The scattering paths can be visualized as Raman channels whose coupling $\eta = -\Omega_p g_0/\Delta_a$ is set by the transverse pump Rabi frequency Ω_p, the cavity vacuum Rabi frequency g_0 and the atom-pump detuning Δ_a.

nian. The part $\frac{\hat{\mathbf{p}}^2}{2m} + V(\mathbf{r})$ describes the free evolution of the atoms in the trapping potential $V(\mathbf{r})$, and $-\hbar\Delta_c$ characterizes the evolution of the cavity mode in a frame rotating with the transverse pump frequency (see Appx. A). Atomic collisions are captured by the last term. The remaining three terms reflect the atom-light interactions in terms of two-photon processes with amplitudes $U_c = \hbar\frac{g^2(\mathbf{r})}{\Delta_a}$, $U_p = \hbar\frac{h^2(\mathbf{r})}{\Delta_a}$ and $U_i = \hbar\frac{h(\mathbf{r})g(\mathbf{r})}{\Delta_a}$ for cavity-cavity, pump-pump and pump-cavity photon scattering, respectively. They can be interpreted as the lattice potentials created by the cavity field, the transverse pump field and interference between the two.

Photon scattering between pump and cavity

The key part of the Hamiltonian is the latter term, describing the pump-cavity interaction. The process can be interpreted as follows: first, a pump photon is virtually absorbed by an atom, which thereby gains one photon momentum along the pump axis in the direction of the photon. In a second step, the photon is scattered into the cavity mode, yielding an atomic momentum kick along the cavity axis in the direction opposite to the emitted photon. Since both the transverse pump and the cavity mode are standing waves, both directions are possible for the transferred momentum in each of the two steps. All atoms in the BEC start in the momentum state $|\mathbf{p}\rangle = |0\rangle$ and can be transferred to the excited momentum states $|\pm\mathbf{k}_p \pm \mathbf{k}_c\rangle$ depending on the scattering direction. The reverse processes are equally possible, where a cavity photon is virtually absorbed and subsequently emitted into the transverse pump beam. The momenta of the excited states are illustrated in Fig. 5.5a. They form two pairs of equal absolute momentum with opposite direction. Pump-cavity photon scattering at an acute angle results in a smaller absolute momentum at lower kinetic energy $\hbar\omega_-$ than photon scattering at an obtuse angle at kinetic energy $\hbar\omega_+$.

Expansion in momentum modes

The standing-wave character of both involved light fields eliminates information about the photon direction and the scattering processes couple to a coherent superposition of all excited momentum states instead. For symmetry reasons momentum states at the same kinetic energy are expected to

equally contribute to the superposition state. This allows to combine each pair of momentum states to a single one:

$$|+\rangle = \frac{1}{\sqrt{2}}\left(|\hbar\mathbf{k}_p + \hbar\mathbf{k}_c\rangle + |-\hbar\mathbf{k}_p - \hbar\mathbf{k}_c\rangle\right) \tag{5.12}$$

$$|-\rangle = \frac{1}{\sqrt{2}}\left(|\hbar\mathbf{k}_p - \hbar\mathbf{k}_c\rangle + |-\hbar\mathbf{k}_p + \hbar\mathbf{k}_c\rangle\right). \tag{5.13}$$

Standing-wave character of excited states

The constituents of these states each have one photon momentum along the cavity and pump axis. Whereas the individual momentum states have running wave character, $|+\rangle$ and $|-\rangle$ describe standing waves with the reciprocal lattice vectors $\mathbf{b}_1$ and $\mathbf{b}_2$ and kinetic energies $\hbar\omega_+$ and $\hbar\omega_-$, respectively. Including the initial state at zero momentum, the momentum states can be described by the real-space wave-functions

$$\psi_0 = \sqrt{\frac{1}{\mathcal{A}}} \tag{5.14}$$

$$\psi_+ = \sqrt{\frac{2}{\mathcal{A}}}\cos\left[(\mathbf{k}_p + \mathbf{k}_c)\cdot\mathbf{r}\right] = \sqrt{\frac{2}{\mathcal{A}}}\cos(\mathbf{b}_1\cdot\mathbf{r}) \tag{5.15}$$

$$\psi_- = \sqrt{\frac{2}{\mathcal{A}}}\cos\left[(\mathbf{k}_p - \mathbf{k}_c)\cdot\mathbf{r}\right] = \sqrt{\frac{2}{\mathcal{A}}}\cos(\mathbf{b}_2\cdot\mathbf{r}) \tag{5.16}$$

All states are normalized to $\int_{\mathcal{A}} d\mathbf{r}|\psi_i|^2 = 1$ with $i \in \{0,+,-\}$. The small number of accessible momentum states allows to restrict the Hilbert space by expanding the atomic field operator in this basis

$$\hat{\psi}(\mathbf{r}) = \psi_0\hat{c}_0 + \psi_+\hat{c}_+ + \psi_-\hat{c}_-. \tag{5.17}$$

The operators $\hat{c}_0^\dagger$ ($\hat{c}_0$) and $\hat{c}_\pm^\dagger$ ($\hat{c}_\pm$) create (annihilate) an atom in the motional ground and excited states, respectively. We insert the expression in Eq. 5.17 into the many-body Hamiltonian in Eq. 5.11, similar to [233]. In the following analytical discussion, the external trapping potential and the atomic collisions are neglected as they only lead to minor quantitative modifications of the results.

Kinetic energy

We now evaluate the integral for each term separately. The kinetic energy results in

$$\int_{\mathcal{A}} d\mathbf{r}\hat{\psi}^\dagger\frac{\hat{\mathbf{p}}^2}{2m}\hat{\psi} = 2\left(1+\cos\theta\right)\hbar\omega_{rec}\hat{c}_+^\dagger\hat{c}_+ + 2\left(1-\cos\theta\right)\hbar\omega_{rec}\hat{c}_-^\dagger\hat{c}_-, \tag{5.18}$$

with the recoil frequency $\omega_{rec} = \hbar k^2/2m$ for an atom of mass m. The two terms show the kinetic energies $\hbar\omega_+ = 2(1+\cos\theta)\hbar\omega_{rec}$ and $\hbar\omega_- = 2(1-\cos\theta)\hbar\omega_{rec}$ for the high- and low-energetic momentum states. Equivalently, the results for the kinetic energies can be obtained from $\hbar\omega_+ = \hbar^2\mathbf{b}_1^2/2m$ and $\hbar\omega_- = \hbar^2\mathbf{b}_2^2/2m$.

Cavity potential

The next term is the cavity potential:

$$\begin{aligned}\int_{\mathcal{A}} d\mathbf{r}\hat{\psi}^\dagger\hbar U_c\cos^2(\mathbf{k}_c\cdot\mathbf{r})\hat{\psi} =& \hbar\frac{U_c}{2}(\hat{c}_0^\dagger\hat{c}_0 + \hat{c}_+^\dagger\hat{c}_+ + \hat{c}_-^\dagger\hat{c}_-) \\ &+ \hbar\frac{U_c}{4}\left(\hat{c}_+^\dagger\hat{c}_- + \hat{c}_-^\dagger\hat{c}_+\right)\end{aligned} \tag{5.19}$$

Since the total atom number $N = \hat{c}_0^\dagger\hat{c}_0 + \hat{c}_+^\dagger\hat{c}_+ + \hat{c}_-^\dagger\hat{c}_-$ is constant, this term corresponds to a shift of the cavity resonance thanks to the atomic cloud

acting as a dispersive medium. It effectively renormalizes the detuning from the cavity resonance to $\tilde{\Delta}_c = \Delta_c - NU_c/2$. The term in the second line creates a remixture of the high and low-energetic states, but its influence is weak for our parameter choice.

Transverse pump potential

The term describing the transverse pump potential yields a constant energy offset, which can be discarded:

$$\int_{\mathcal{A}} d\mathbf{r}\hat{\psi}^\dagger \left[\hbar U_p \cos^2(\mathbf{k}_p \cdot \mathbf{r})\right] \hat{\psi} = \hbar U_p. \tag{5.20}$$

Pump-cavity interaction

The remaining expression describes the scattering of pump photons into the cavity mode and vice versa. After performing the integration we obtain

$$\int_{\mathcal{A}} d\mathbf{r}\hat{\psi}^\dagger \left[\hbar\eta(\hat{a}^\dagger + \hat{a})\cos(\mathbf{k}_p \cdot \mathbf{r})\cos(\mathbf{k}_c \cdot \mathbf{r})\right] \hat{\psi} = \hbar\frac{\eta}{2\sqrt{2}}(\hat{c}_+^\dagger \hat{c}_0 + \hat{c}_-^\dagger \hat{c}_0 + \text{h.c.}) \tag{5.21}$$

We use the scattering rate $\eta = -\frac{\Omega_p g_0}{\Delta_a}$. In summary, the resulting Hamiltonian with all considered terms is given by

$$\begin{aligned}\hat{\mathcal{H}} =& -\hbar\tilde{\Delta}_c \hat{a}^\dagger \hat{a} + \hbar\omega_+ \hat{c}_+^\dagger \hat{c}_+ + \hbar\omega_- \hat{c}_-^\dagger \hat{c}_- \\ &+ \hbar\frac{\lambda}{\sqrt{N}}(\hat{c}_+^\dagger \hat{c}_0 + \hat{c}_-^\dagger \hat{c}_0 + \text{h.c.}),\end{aligned} \tag{5.22}$$

where we made use of the short notation $\lambda = \eta\sqrt{N}/2\sqrt{2}$ for the Raman coupling. This Hamiltonian is exact in the limit of weak atomic contact interactions and weak driving, where higher order momentum modes are not populated yet.

We now study the ground state of this Hamiltonian. The time evolution of each operator $\hat{A}$ is governed by its Heisenberg equation $i\hbar\partial\hat{A}/\partial t = \left[\hat{A}, \hat{\mathcal{H}}\right]$, yielding the equations:

Heisenberg equations

$$\begin{aligned} i\frac{\partial \hat{a}}{\partial t} &= -\tilde{\Delta}_c \hat{a} + \frac{\lambda}{\sqrt{N}}\left(\hat{c}_-^\dagger \hat{c}_0 + \hat{c}_+^\dagger \hat{c}_0 + \text{h.c.}\right) \\ i\frac{\partial \hat{c}_\pm}{\partial t} &= \omega_\pm \hat{c}_\pm + \frac{\lambda}{\sqrt{N}}\hat{c}_0\left(\hat{a}^\dagger + \hat{a}\right) \\ i\frac{\partial \hat{c}_0}{\partial t} &= \frac{\lambda}{\sqrt{N}}\left(\hat{c}_- + \hat{c}_+\right)\left(\hat{a}^\dagger + \hat{a}\right)\end{aligned} \tag{5.23}$$

In steady-state the time evolution of each operator vanishes and we obtain a set of coupled equations that determine the ground state expectation value for each operator. The equations do not have an analytic solution, but can be solved numerically.

We can, however extract the critical point analytically by analyzing the Hessian of the Hamiltonian with respect to the expectation values of the operators [234, 235]. The Hessian is positive definite (i.e., all eigenvalues are positive) in the normal phase and becomes indefinite at the critical point. Using the minor criterion for definite matrices, we obtain the condition:

Critical point

$$\omega_+\omega_- + (\omega_+ + \omega_-)\frac{4\lambda^2}{\tilde{\Delta}_c} > 0, \tag{5.24}$$

which shows the range of λ for the normal phase. The critical point is therefore

$$\lambda_{cr} = \sqrt{\frac{-\tilde{\Delta}_c \bar{\omega}}{4}}. \tag{5.25}$$

The reduced frequency $\bar{\omega}$ is defined as $\bar{\omega}^{-1} = \omega_+^{-1} + \omega_-^{-1}$. For a cavity-pump angle of 60°, it takes the value $\bar{\omega} = \sqrt{3}\omega_{rec}/2$.

Symmetry breaking at the phase transition

Let us consider the symmetry breaking at the phase transition. The Hamiltonian in Eq. 5.22. manifests a parity symmetry for the simultaneous transformation $(\hat{a}_i, \hat{c}_{i\pm}) \to -(\hat{a}_i, \hat{c}_{i\pm})$ on the photonic and atomic field operators [234, 236]. It is generated by the operator $\hat{C} = \hat{a}^\dagger \hat{a} + \sum_{s=\pm} \hat{c}_s^\dagger \hat{c}_s$, which describes the total number of excitations in the system. The operators for the photonic and atomic fields transform under the corresponding unitary transformation $U = e^{i\theta C}$ as follows:

$$\hat{a} \to \hat{U}\hat{a}\hat{U}^\dagger = e^{i\theta}\hat{a} \tag{5.26}$$

$$\hat{c}_\pm \to \hat{U}\hat{c}_\pm\hat{U}^\dagger = e^{i\theta}\hat{c}_\pm \tag{5.27}$$

As a consequence, the Hamiltonian transforms as:

$$\begin{aligned}
&\hat{\mathcal{H}} \to \hat{U}\hat{\mathcal{H}}\hat{U}^\dagger \\
&= -\hbar\tilde{\Delta}_c \hat{a}^\dagger\hat{a} + \hbar\omega_+ \hat{c}_+^\dagger\hat{c}_+ + \hbar\omega_- \hat{c}_-^\dagger\hat{c}_- \\
&+ \hbar\frac{\lambda}{\sqrt{N}}\left(e^{i\theta}\hat{a}^\dagger + e^{-i\theta}\hat{a}\right)\left(e^{i\theta}\hat{c}_+^\dagger\hat{c}_0 + e^{i\theta}\hat{c}_-^\dagger\hat{c}_0 + \text{h.c.}\right) \\
&= \hat{\mathcal{H}} \text{ if } \theta \in \{0, \pi\}
\end{aligned} \tag{5.28}$$

We see that the Hamiltonian stays invariant under the unitary transformation $\hat{U}$ only if $\theta \in \{0, \pi\}$. The underlying symmetry group is $\mathbb{Z}_2$. This symmetry is broken at the phase transition, where the sign of the field operators amounts to 0 or π for the phase of the light field or, equivalently, to atoms crystallizing on odd or even sites of a chequerboard lattice with rectangular geometry.

Experimental parameter regime

In our setup, the angle between transverse pump and cavity axis is $\theta = 60°$, resulting in $\omega_+ = 3\omega_{rec}$ and $\omega_- = \omega_{rec}$. We work with a BEC of typically $N = 2 \times 10^5$ ^{87}Rb atoms and transverse pump lattice depths up to $70\hbar\omega_{rec}$. The detuning Δ_a from the atomic resonance is around 2.57 THz and the vacuum Rabi frequency of the cavity is $2\pi \times 1.95$ MHz, corresponding to a dispersive shift of $U_c \sim 2\pi \times 1.48$ Hz per atom. $\Delta_c/2\pi$ is typically adjusted in the range from resonance to -10 MHz, either by tuning the pump frequency ω_p or by changing the cavity length and thereby ω_c. A list of relevant cavity parameters is given in Chap. 4.

5.1.3 Photon-mediated interactions

Separation of atomic and photonic time scales

The atom-cavity coupling can be reinterpreted in terms of photon-mediated interactions [237]. The dynamics of the photonic and the atomic fields takes place at well separated time scales, since $\omega_+, \omega_- \ll |\Delta_c|$. For the parameters of our system, the ratio is around two orders of magnitude and the light field hence adiabatically follows the atomic motion. The evolution of the light field for the general field operator is

$$i\frac{\partial\hat{a}}{\partial t} = -\tilde{\Delta}_c\hat{a} + \eta\int_{\mathcal{A}} d\mathbf{r}\hat{\psi}^\dagger(\mathbf{r})\cos(\mathbf{k}_p\cdot\mathbf{r})\cos(\mathbf{k}_c\cdot\mathbf{r})\hat{\psi}(\mathbf{r}). \tag{5.29}$$

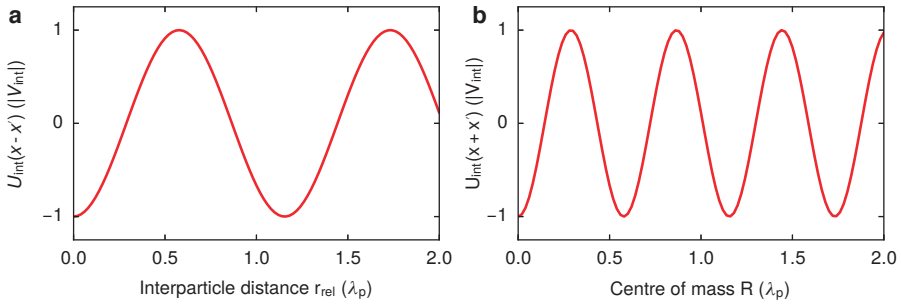

Figure 5.6: *Photon-mediated interactions in an optical cavity.* **a,** Interaction potential for the relative position of two particles along x for $y = 0$ for $V_{int} < 0$. The interactions favour a distance of $\lambda_p/\cos(\theta)$, thereby selectively enhancing periodic density correlations. **b,** The interactions also depend on the center of mass of the two particles. The potential pins the periodic sample on a grating with half the periodicity. This is a direct consequence of the discrete nature of the symmetry breaking at the phase transition.

Adiabatic elimination of the photon field

The separation of timescales for the photonic and the atomic evolution allows to set $\partial\hat{a}/\partial t \approx 0$ and to eliminate the light field from the many-body Hamiltonian in Eq. 5.11. We obtain a reduced Hamiltonian with an effective photon-mediated interaction among the atoms:

$$\begin{aligned}\hat{\mathcal{H}}_{int} &= \int_{\mathcal{A}} \hat{\psi}^\dagger(\mathbf{r}) \frac{p^2}{2m} \hat{\psi}(\mathbf{r}) d\mathbf{r} \\ &= \int_{\mathcal{A}} \int_{\mathcal{A}} \hat{\psi}^\dagger(\mathbf{r}) \hat{\psi}^\dagger(\mathbf{r}') U_{int}(\mathbf{r}, \mathbf{r}') \hat{\psi}(\mathbf{r}') \hat{\psi}(\mathbf{r}) d\mathbf{r} d\mathbf{r}'\end{aligned} \tag{5.30}$$

with the interaction potential

$$U_{int}(\mathbf{r}, \mathbf{r}') = V_{int} \cos(\mathbf{k}_p \cdot \mathbf{r}) \cos(\mathbf{k}_c \cdot \mathbf{r}) \cos(\mathbf{k}_p \cdot \mathbf{r}') \cos(\mathbf{k}_c \cdot \mathbf{r}'), \tag{5.31}$$

where $V_{int} = 2\hbar\lambda^2/N\tilde{\Delta}_c$ is the strength of the interaction. In our experiments we typically set $\tilde{\Delta}_c < 0$, yielding $V_{int} < 0$. Let us consider the spatial character of this interaction potential for the case of two particles. Eq. 5.31 can be rewritten in terms of their distance $\mathbf{r}_{rel} = \mathbf{r} - \mathbf{r}'$ and their center of mass $\mathbf{R} = (\mathbf{r} + \mathbf{r}')/2$:

$$U_{int}(\mathbf{r}, \mathbf{r}') = \frac{V_{int}}{4} \left[\cos(2\mathbf{k}_p \cdot \mathbf{R}) + \cos(\mathbf{k}_p \cdot \mathbf{r}_{rel})\right] \left[\cos(2\mathbf{k}_c \cdot \mathbf{R}) + \cos(\mathbf{k}_c \cdot \mathbf{r}_{rel})\right]. \tag{5.32}$$

Spatial character of the interaction potential

The spatial character along x for negative interaction strength is shown in Fig. 5.6. We can see that it shows a minimum for a relative distance $\lambda_p/\cos\theta$ between the particles. Such a minimum is required for a structural phase transition, as it induces the particles to arrange on a regular pattern with the corresponding lattice constant. However, two properties of the potential let it stand out among other interaction potentials between particles: first, the potential is periodic in $\lambda_p/\cos\theta$, hence creating a potential that extends over the entire cavity mode. Second, the potential also influences the center of mass of the particles. Only two positions per lattice constant exist, which is equivalent to the $\mathbb{Z}_2$ symmetry breaking of the phase transition.

If instead $V_{int} > 0$, the graphs in Fig. 5.6 are inverted for $V_{int} > 0$. In this case, the potential shows minima for relative positions $(n + 1/2)\lambda_p/\cos\theta$. This condition can be fulfilled for two particles only, since a third particle

would be separated from either of the particles by an even number of lattice constants. The situation is therefore frustrated and also for a system with larger particle numbers no phase transition takes place, since periodic density correlations are suppressed.

5.1.4 Limit of orthogonal transverse pump

Two-mode description

In the case of an orthogonal transverse pump with $\theta = 0°$, all four excited momentum states have the same kinetic energy $2\hbar\omega_{rec}$. This allows to combine them to a single state with equal contributions $|\pm\hbar k, \pm\hbar k\rangle = \sum_{\mu,\nu\in\{+,-\}} = |\mu\hbar k, \nu\hbar k\rangle /2$. The real-space wave-functions take the form:

$$\psi_0 = \sqrt{\frac{1}{A}} \tag{5.33}$$

$$\psi_1 = \sqrt{\frac{1}{A}}\cos(kx)\cos(ky) \tag{5.34}$$

We can therefore expand the field operator by $\hat{\psi} = \psi_0\hat{c}_0 + \psi_1\hat{c}_1$. This reduces the Hamiltonian to

$$\begin{aligned}\hat{\mathcal{H}}_\perp =& -\hbar\tilde{\Delta}_c\hat{a}^\dagger\hat{a} + 2\hbar\omega_{rec}\hat{c}_1^\dagger\hat{c}_1 + \hbar\frac{U_c}{4}\hat{a}^\dagger\hat{a}\hat{c}_1^\dagger\hat{c}_1 \\ &+ \hbar\frac{\eta}{2}\left(\hat{a}^\dagger + \hat{a}\right)\left(\hat{c}_1^\dagger\hat{c}_0 + \hat{c}_0^\dagger\hat{c}_1\right)\end{aligned} \tag{5.35}$$

Analogous to the non-orthogonal situation, the Hamiltonian breaks a $\mathbb{Z}_2$ symmetry at the critical point $\lambda_{cr} = \sqrt{\omega\omega_0/4}$. The Heisenberg equations even allow for an analytical solution for the expectation values [234]. Alternatively the system can be described as a macroscopic spin-1/2 system, by employing the Schwinger representation for the spin algebra [75, 233]:

$$\hat{S}_- = \hat{c}_0^\dagger\hat{c}_1 \tag{5.36}$$

$$\hat{S}_+ = \hat{c}_1^\dagger\hat{c}_0 \tag{5.37}$$

$$\hat{S}_z = \frac{1}{2}\left(\hat{c}_1^\dagger\hat{c}_1 - \hat{c}_0^\dagger\hat{c}_0\right) \tag{5.38}$$

This results in the Hamiltonian

$$\begin{aligned}\hat{\mathcal{H}}_\perp =& \hbar\omega\hat{a}^\dagger\hat{a} + \hbar\omega_0\hat{S}_z + \hbar\frac{\lambda_\perp}{\sqrt{N}}\left(\hat{a}^\dagger + \hat{a}\right)\left(\hat{S}_+ + \hat{S}_-\right) \\ &+ \frac{N\hbar\omega_0}{2} + \hbar\frac{U_c}{4}\left(\hat{S}_z + \frac{N}{2}\hat{a}^\dagger\hat{a}\right)\end{aligned} \tag{5.39}$$

Dicke Hamiltonian

Dicke quantum phase transition

We have used the notation $\omega = -\tilde{\Delta}_c$, $\omega_0 = 2\omega_{rec}$ and $\lambda_\perp = \eta\sqrt{N}/2$. The first line corresponds to the Dicke Hamiltonian, which was originally introduced to describe the collective interaction of an ensemble of two-level systems with a single mode of an electromagnetic field [238]. Here the two level-system is provided by the ground and the excited momentum states, which are coupled by Raman processes instead of a direct electromagnetic transition. This allows to reach the coupling strengths required to enter the superradiant phase [81]. The terms in the second line are negligible when the population in the excited state is small compared to the total particle number. This is always the case in the regime where the two-mode expansion is valid and hence these terms can be neglected. More details on the realization of the Dicke phase transition with a BEC coupled to an optical cavity can be found in [207].

We see from the term $\hbar U_c \hat{S}_z/4$ that the dispersive shift depends on the excited state population, in contrast to the situation with a non-orthogonal transverse pump. If ω is chosen small enough, the interplay with this so-called *optomechanical term* is expected to show chaotic effects, limit cycles and superfluid phase slips [234, 236, 239].

5.2 THE PHASE DIAGRAM

In this section we consider the phase diagram of the self-organization phase transition in terms of the the coupling strength λ and the pump-caity detuning Δ_c. We start with a numerical analysis of the expectation values for the excited momentum states and the light fields and then turn to a comparison with the experimentally measured phase diagram.

5.2.1 *Numerical mean-field solution*

In order to describe the self-organization phase transition, we define the order parameter

Order parameter

$$\Theta = \frac{1}{N} \langle \hat{\psi} | \cos(\mathbf{k}_p \cdot \mathbf{r}) \cos(\mathbf{k}_c \cdot \mathbf{r}) | \hat{\psi} \rangle , \tag{5.40}$$

which measures the overlap of the atomic density with the interference pattern of the cavity mode and the transverse pump. The order parameter remains in the range $-1 \leqslant \Theta \leqslant 1$. It is zero throughout the normal phase and takes a positive (negative) value when the wave function has larger contribution on the even (odd) sites of the interference pattern. In a classical picture of localized atoms, the order parameter counts the imbalance of atoms on the even and odd sites. In the three-mode description, the order parameter reads:

$$\Theta = \frac{1}{N} \langle \hat{\psi} | \hat{c}_+^\dagger \hat{c}_0 + \hat{c}_-^\dagger \hat{c}_0 + \text{h.c.} | \hat{\psi} \rangle , \tag{5.41}$$

The order parameter can be determined by solving the Heisenberg equations in Eq. 5.23. To that end, we are interested in the expectation value of the operators, which we define as $\langle \hat{a} \rangle = \sqrt{N}\alpha$ and $\langle \hat{c}_i \rangle = \sqrt{N}\psi_i$ for $i \in \{+, -, 0\}$. This is equivalent to directly starting from the Hamiltonian in mean-field approximation. The expectation values of the atomic fields are normalized as $\psi_+^2 + \psi_-^2 + \psi_0^2 = 1$ to account for atom number conservation. As a consequence of the $\mathbb{Z}_2$ symmetry breaking, the expectation values can only take real values up to a global phase that can be ignored.

We perform a numerical simulation in the (λ, Δ_c) plane. Apart from the atom-light interactions, it also takes into account cavity decay by adding a dissipation term $-\kappa\hat{a}$ to Eq. 5.23. Furthermore we account for atomic contact interactions with a collision term $\psi_i^2 N g$ for $i \in \{0, +, -\}$. The result for the numerically obtained phase diagram is shown in Fig. 5.7. For constant Δ_c, we observe that the excited momentum states are macroscopically populated for coupling strengths λ beyond the critical point (Fig. 5.7a). The population of the ω_- momentum state is consistently higher than for the ω_+ state. For increasing Δ_c the critical point is displaced to higher coupling strengths (Fig. 5.7c). An exception is the region close to the cavity resonance, where the critical point diverges again, because the influence of cavity dissipation increases (see Sec. 5.3.1).

Phase diagram

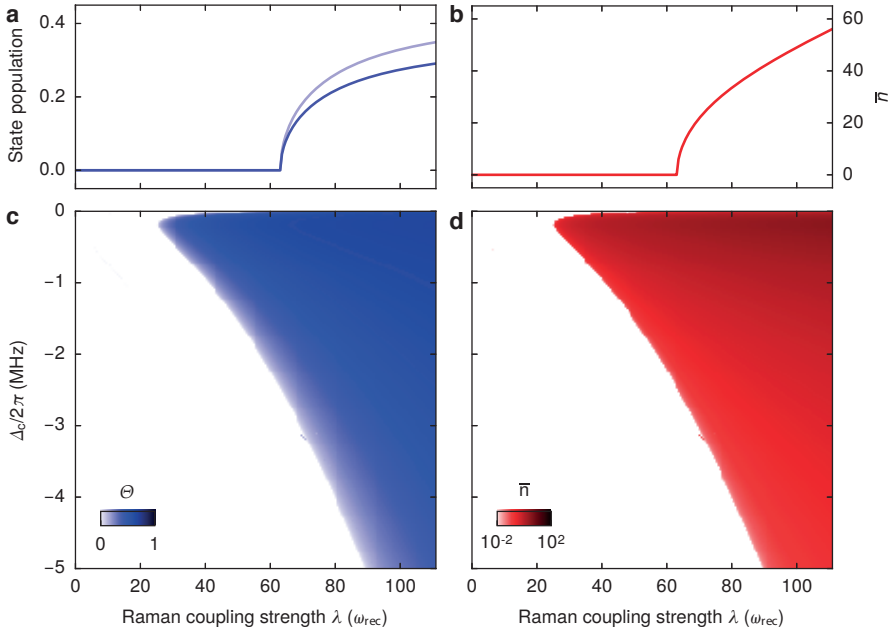

Figure 5.7: *Mean-field simulation of the phase diagram.* Numerical solution of the mean-field equations for the experimental parameters described at the end of Sec. , and including dissipation and atomic collisions. **a,** Atomic order parameter across the phase transition for $\Delta_c/2\pi = 2.5\,\mathrm{MHz}$. The contributions from the ψ_+ (orange) and the ψ_- (green) mode are shown individually. **b,** Mean photon number across the phase transition. **c,** Full phase diagram for the order parameter. **d,** Phase diagram for the intracavity photon number $\bar{n}$ (in logarithmic scale).

The order parameter is directly linked to the intracavity light field α with

$$\alpha = \frac{\eta\Theta}{\tilde{\Delta}_c} \tag{5.42}$$

This becomes clear by setting $\partial\hat{a}/\partial t = 0$ in Eq. 5.29 and taking the expectation value on both sides. Indeed, we find in the numerical simulation that the phase boundary for the atomic order parameter and the intracavity light field coincide (Fig. 5.7b,d). The connection allows us to extract information about the strength of the density modulation from the cavity light field in real time.

5.2.2 *Observing the phase transition*

Superradiance at the critical point

We start the experiment with a BEC prepared as described in Chap. 3. The transverse pump frequency is set to a negative detuning of $\Delta_c/2\pi = -2.0\,\mathrm{MHz}$ from the cavity resonance. We can adjust the Raman coupling strength with the transverse pump power, because of the relation $\lambda \propto \Omega_p$. To observe the onset of self-organization, we gradually increase the pump power over time. Simultaneously, we record the photons leaking from the cavity on an SPCM and infer the intracavity photon number. The corresponding photon trace is shown in Fig. 5.8a. For small lattice depths we record no light at the cavity output. Once the pump power reaches the critical value, the intracavity photon number abruptly increases, signalling the onset of self-organization.

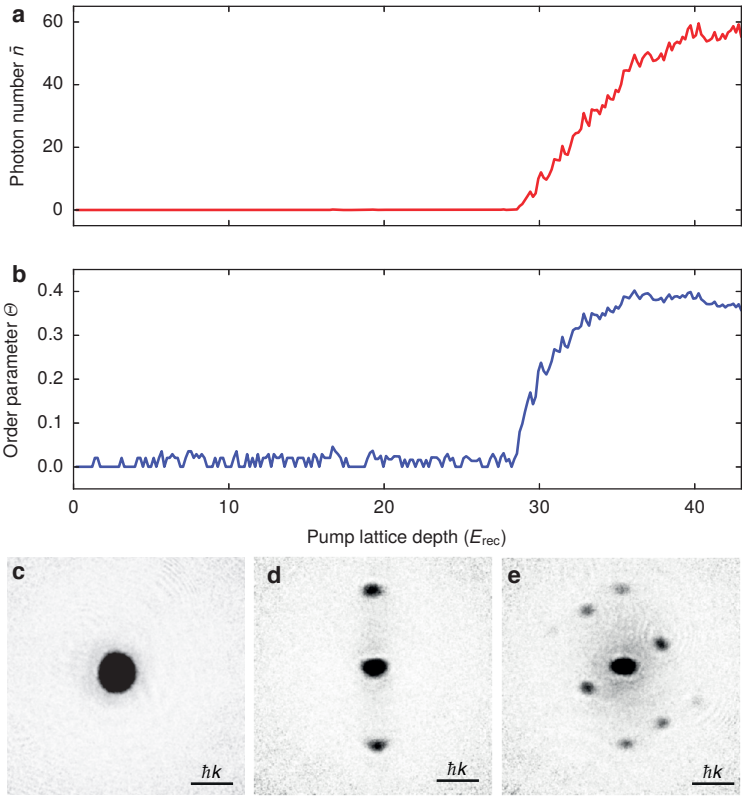

Figure 5.8: *Observation of the self-organization phase transition.* **a,** Recorded photon number $\overline{n}$ for a linear ramp over 100 ms of the pump lattice depth up to $43(1)\,\hbar\omega_{rec}$ at $\Delta_c = -1.8$ MHz. The photon number shows the sudden onset of the phase transition by a macroscopic population of the cavity mode. The data are binned in intervals of 1 ms. **b,** Order parameter across the phase transition, deduced from the photon trace with Eq. 5.42. **c-e,** Pictures of the atomic momentum distribution recorded with absorption imaging after 25 ms ballistic expansion. The distribution depends on the pump lattice depth and shows only zero momentum without any transverse pump (**c**), two additional momentum peaks at $\pm\hbar\mathbf{k}_p$ in the normal phase (**d**) and four additional momentum maxima within the self-organized phase (**e**), signalling the presence of a density modulation.

The connection between the intracavity light field and the density modulation allows us to extract the order parameter. We infer the intracavity light field as $|\alpha| = \sqrt{\overline{n}}$ and use Eq. 5.42 to obtain Θ. The result is shown in Fig. 5.8b. In contrast to the cavity field, the order parameter saturates already shortly after the critical point, indicating a strongly self-organized cloud or increased heating deep in the organized phase.

Atomic density order

We can also access the atomic momentum distribution directly from absorption imaging after a free expansion of the cloud. We stop the transverse pump ramp at different lattice depths, then suddenly turn off all trapping potentials and allow the atomic wavefunction to freely expand. This translates the initial momentum distribution to a real-space distribution (see Sec. 3.5), which can be imaged on a CCD camera. Throughout the normal phase, we observe the expected momentum distribution of a condensate loaded into a lattice potential (Fig. 5.8c,d). Upon entering the self-organized phase, the momentum distribution qualitatively changes and four additional interference maxima at $\mathbf{p} = \pm\mathbf{k}_p \pm \mathbf{k}_c$ appear (Fig. 5.8e).

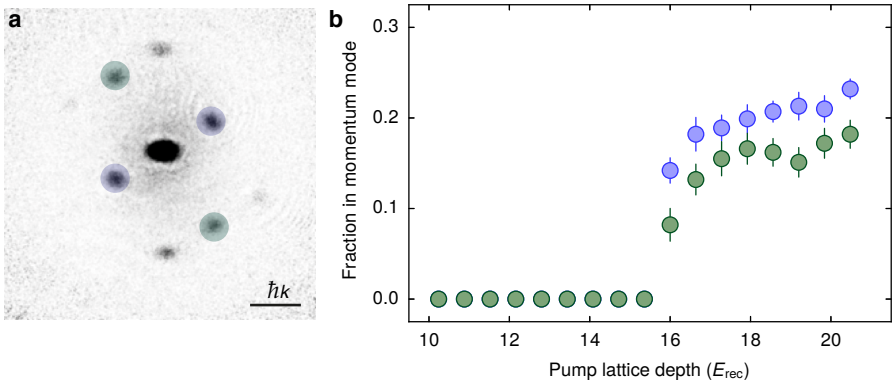

Figure 5.9: *Composition to the excited momentum state.* **a,** Picture from absorption imaging after 25 ms ballistic expansion. We observe a larger fraction of the atoms in the ω_- mode (shaded blue) than in the ω_+ mode (shaded green). **b,** Occupation numbers for the ω_- mode (blue) and the ω_+ mode (green) as a function of the pump lattice depth. We observe a consistently higher population in the low-energetic mode.

This provides evidence for the acquired density modulation according to the interference pattern of the transverse pump and the cavity fields.

Unequal population of the momentum modes

We study the population of the ω_+ and the ω_- momentum modes separately as a function of pump lattice depths by interrupting the ramp at different lattice depths and recording absorption images of the atomic cloud. We deduce the fraction of atoms in each mode by counting the atoms in each interference maxima. The result is shown in Fig. 5.9. The number of atoms in the ω_- mode is consistently higher than in the ω_+ mode, in agreement with our theoretical model.

5.2.3 *Mapping out the phase diagram*

Eq. 5.25 predicts that the critical point shifts towards higher pump lattice depths when the pump frequency is further detuned from the cavity resonance. We can experimentally map out the phase boundary by gradually increasing the power for different values of Δ_c and recording the photons at the cavity output. The deduced intracavity photon numbers are shown in Fig. 5.10.

A sharp phase boundary is visible over a wide range of the pump-cavity detuning Δ_c. The critical pump lattice depth $V_{cr} \propto \lambda_{cr}^2$ scales approximately linearly with the detuning Δ_c, in agreement with the expected self-organization threshold. We do not observe light scattering for detunings in the range $|\Delta_c| < N|U_c|/2 \sim 2\pi \times 0.1\,\mathrm{kHz}$, where the dispersive shift displaces the cavity resonance by $N|U_c|/2$ such that $\tilde{\Delta}_c > 0$ and scattering becomes energetically unfavourable. The intracavity photon numbers increase as the pump-cavity detuning Δ_c aproaches the shifted resonance frequency from below.

We compare our measurements with the phase boundary that is obtained numerically from the mean-field description, including the cavity decay and the atomic contact interaction. We obtain good agreement between the measurements and the theoretical model.

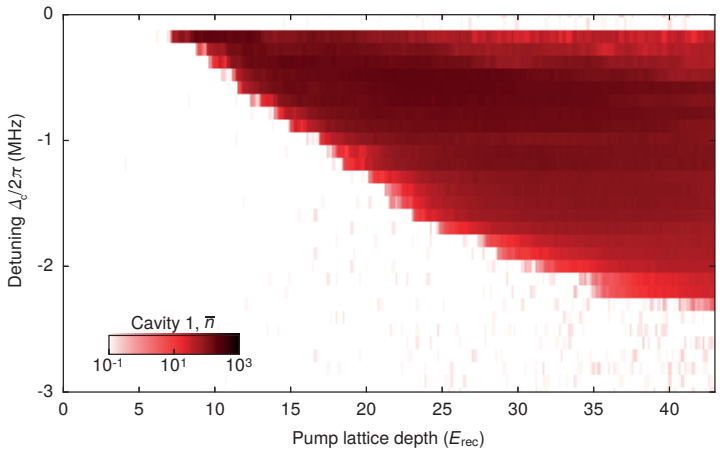

Figure 5.10: *Phase diagram for self-organization with a single cavity.* We map out the phase diagram by recording the intracavity photon number in lines of constant detuning Δ_c with transverse pump ramp up to a lattice depth of $43(1)\,\hbar\omega_{rec}$. All data are binned in intervals of 0.5 ms.

5.3 ASPECTS BEYOND SELF-ORGANIZATION

In this section we go beyond the standard description of self-organization in terms of a few-mode expansion at zero temperature. We study the influence of three effects on the phase diagram: photon dissipation, finite temperature, and the birefringence of the cavity mode.

5.3.1 *Dissipation of the cavity photons*

Atomic self-organization in an optical cavity realizes a driven-dissipative system, where energy flows in terms of photons from the transverse pump via the atoms into the cavity and eventually leaves the system by cavity dissipation. We have so far neglected this property, except for the numerical simulation shown in Fig. 5.7. In the Heisenberg equation, this can be taken into account by introducing a finite cavity decay rate κ:

Driven-dissipatice system

$$i\frac{\partial \hat{a}}{\partial t} = (-\tilde{\Delta}_c - i\kappa)\hat{a} + \frac{\lambda}{\sqrt{N}}\left(\hat{c}_-^\dagger \hat{c}_0 + \hat{c}_+^\dagger \hat{c}_0 + \text{h.c.}\right). \tag{5.43}$$

The connection between the order parameter and the cavity field is accordingly modified to

$$\alpha = \frac{\eta\Theta}{\tilde{\Delta}_c + i\kappa}. \tag{5.44}$$

We deduce from this expression that the cavity field is not strictly in phase with the transverse pump lattice, but acquires a phase delay when its frequency approaches the cavity resonance. Furthermore, its magnitude is decreased compared to the dissipationless situation.

For our system, the atomic and the photonic time scales remain well separated since $\omega_+, \omega_- \ll \kappa$. Similarly as in Eq. 5.25 we can analyze the Hessian matrix and obtain the critical coupling in the presence of dissipation

$$\lambda_{cr} = \sqrt{\frac{(\tilde{\Delta}_c^2 + \kappa^2)\overline{\omega}}{-4\tilde{\Delta}_c}}. \tag{5.45}$$

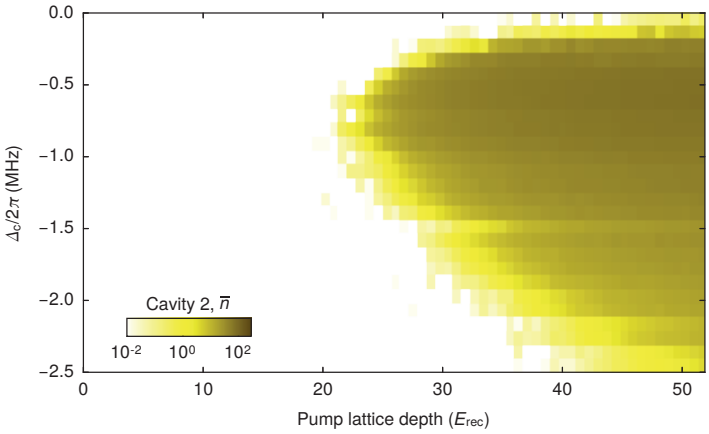

Figure 5.11: *Influence of cavity dissipation on the phase diagram.* We map out the phase diagram for cavity 2, which has a decay rate of $\kappa_2 = 2\pi \times 800(11)$ kHz, around five times more than cavity 1. The measurements are taken in lines of constant detuning Δ_c with a linear ramp of the transverse pump over 100 ms. In comparison to Fig. 5.10, the critical point is displaced towards higher coupling strengths over the entire range of detunings from the transverse pump. All data are binned in intervals of 1 ms.

Influence of dissipation on the phase boundary

We can infer that the phase boundary is displaced towards higher critical couplings for $\kappa > 0$. The critical point with the smallest coupling strength can be found at $\tilde{\Delta}_c^{\min} = -\kappa$ with the coupling $\lambda_{cr}(\tilde{\Delta}_c^{\min}) = \sqrt{\kappa\overline{\omega}/2}$. This is in contrast to the dissipationless situation without minimum. We can recover Eq. 5.25 from this formula in the limit of $\kappa \ll |\tilde{\Delta}_c|$.

All measurements shown so far were performed with cavity 1, which has a decay rate of $\kappa_1 = 2\pi \times 147(4)$ kHz (see Chap. 4). We perform the same measurements with the second cavity of the science setup, whose decay rate $\kappa_2 = 2\pi \times 800(11)$ kHz is approximately a factor of five larger. The resulting phase diagram is shown in Fig. 5.11. We observe an overall displacement of the critical point towards higher coupling strengths in comparison to the phase diagram for cavity 1 in Fig. 5.10. As expected from the above discussion, the critical point with the smallest coupling strength can be found at $\tilde{\Delta}_c \approx -\kappa$.

5.3.2 *Finite temperature*

Similar to fluctuations from photon dissipation, thermal fluctuations also shift the the critical point to higher coupling strengths. This was first derived for the Dicke phase transition [240] and can be extended to the present situation with self-organization in a rectangular lattice:

$$\lambda_{cr} = \sqrt{\frac{-\tilde{\Delta}_c\overline{\omega}}{4\tanh(\beta\hbar\overline{\omega}/2)}}. \tag{5.46}$$

Higher critical couplings at finite temperature

Here $\beta = 1/k_B T$ with the temperature T and the Boltzmann constant k_B. For constant $\tilde{\Delta}_c$ the critical point is displaced to higher values at $T > 0$. This result is slightly modified when taking into account beyond mean-field effects [241].

We study the temperature dependence of the critical point by measuring the self-organization phase transition with atomic ensembles at different temperatures, across the critical temperature of the BEC. Experimentally this is achieved by varying the duration and the laser power of the evapo-

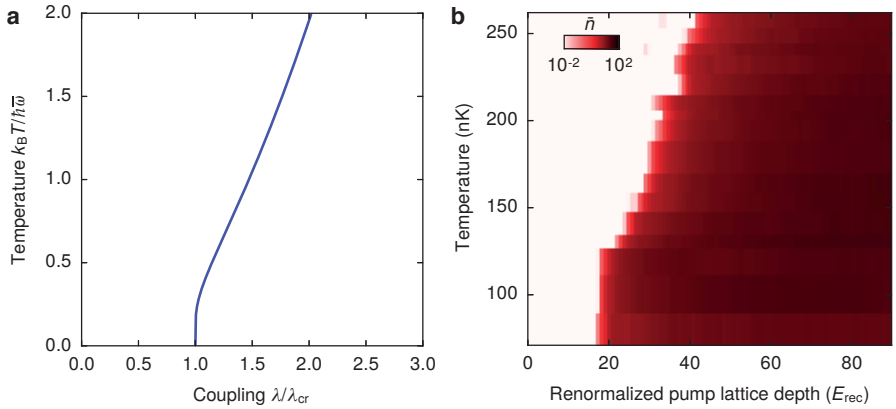

Figure 5.12: *Self-organization at finite temperature.* **a,** Phase boundary for $T > 0$, according to Eq. 5.46. The horizontal axis is normalized to the critical point at $T = 0$. **b,** Measurement of the phase diagram at finite temperature. The horizontal axis is renormalized by the atom number N/N_{min}, with the smallest atom number N_{min} among the measurements. The intervals for the data binning are in the range of $1.0 - 1.6$ ms.

rative cooling sequence. The atom numbers vary between $N = 1.6 - 2.6 \times 10^5$, which we take into account by renormalizing the lattice depth V with N/N_{min}, because of the scaling relation $\eta \propto \sqrt{NV}$. The result is presented in Fig. 5.12 and shows qualitative agreement with the theoretical prediction.

5.3.3 Spin-dependent order and instability

Our description so far considers a single ground state at zero momentum that is coupled to a single photon field. However, the modes of an optical cavity always come in pairs of orthogonal polarization and in general the atomic coupling to both modes has to be accounted for. The mode frequencies are degenerate for rotationally symmetric mirrors, but show a frequency difference in the presence of a birefringence. The machined substrate and the mount of the cavity mirrors predefine the polarization axes within few degrees to the x-y plane (H) and the z axis (V) with a birefringence frequency splitting of 3.88(6) MHz for cavity 1 (see Chap. 4).

Vertical quantization axis

Let us consider the coupling to both polarization modes for different directions of the quantization axes. We always choose the transverse pump polarization along V. For a vertical quantization axis along z, the differential cross section vanishes for the H polarized cavity mode and is maximum for the V polarized mode. As a consequence, self-organization to the H mode is expected to be strongly suppressed and only self-organization to the V mode should appear.

Rotated quantization axis

The situation changes for a quantization axis in the x-y plane. If the quantization axis is parallel to the transverse pump beam, along the y axis, the transverse pump can drive σ transitions between different Zeeman sublevels. The amplitude for scattering to both cavity modes is finite but strongly suppressed, circularly polarized photons have a much smaller differential cross-section at 60° than along the quantization axis. No scattering occurs if the quantization axis points along y, since the V-polarized transverse pump light cannot excite the atoms.

We study this effect by measuring the phase diagram for different magnetic field strengths, as shown in Fig. 5.13. At the absence of a magnetic

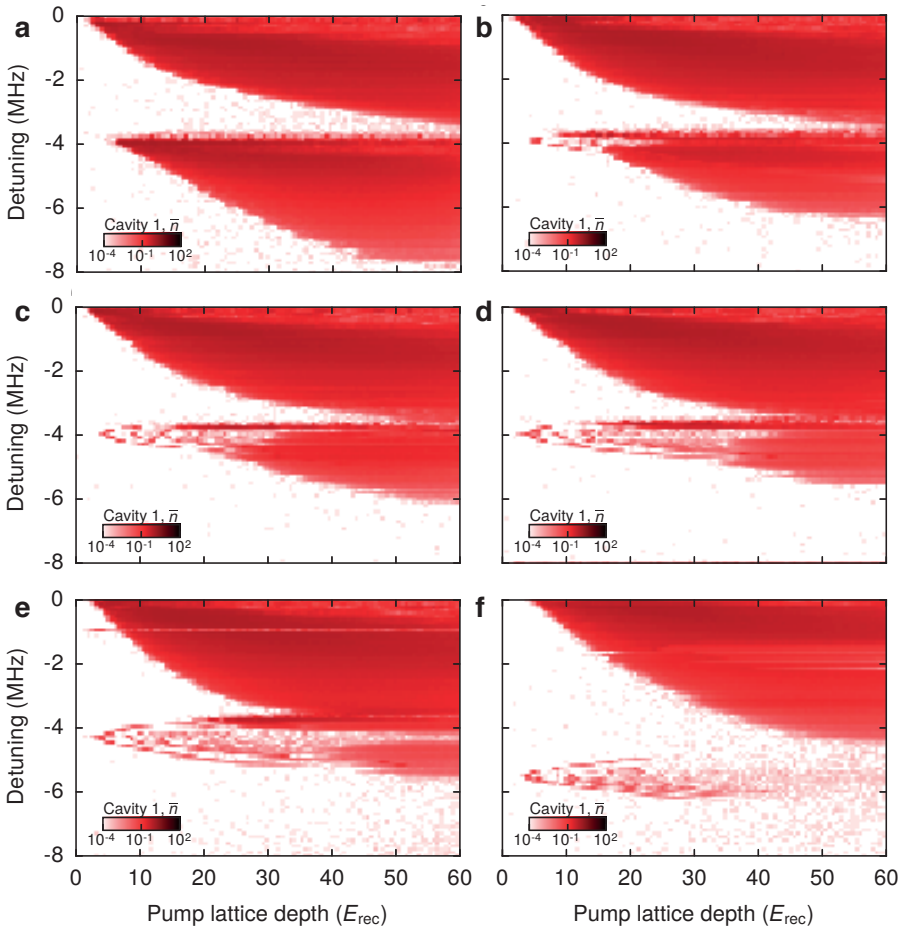

Figure 5.13: *Spin-dependent self-organization.* We record the phase diagram by ramping the transverse pump lattice depth up to 60 E_{rec} over 100 ms for different pump-cavity detunings Δ_c. The panels show measurements at different magnetic fields along the z axis with **a,** at $B_z = 0$ G, **b,** at $B_z \approx 0.01$ G, **c,** at $B_z \approx 0.05$ G, **d,** at $B_z \approx 0.1$ G, **e,** at $B_z = 0.2$ G and **f,** at $B_z = 1$ G. Values for the low magnetic field strengths are only approximate, because of a residual offset of in the current regulation. All data are binned in intervals of 1 ms.

Transitions among the Zeeman sublevels

field, the exact direction of the quantization axis is unknown since it points along the earth magnetic field, or along residual magnetic fields that are present at the position of the atoms. When applying no magnetic field, we observe self-organization separately to the H and the V polarised cavity mode when the detuning Δ_c is set to small negative values for the respective resonance. A slope change of the phase boundary shows the suppression of self-organization at $\Delta_c/2\pi \approx -3$ MHz, where the detuning is small and positive with respect to the V-polarised cavity mode. The critical point for self-organization into the V polarised cavity mode increases when applying a magnetic field, signalling a rotation of the quantization axis towards z. For a magnetic field of $B_z = 1$ G, no spin-dependent self-organization is visible over the entire range covered by the measurements.

The two-photon scattering process from the V polarised transverse pump into the H polarised cavity mode involves a σ_+ transition between the Zeeman sublevels $|F = 1, m_F = -1\rangle \rightarrow |F = 1, m_F = 0\rangle$, followed by σ transitions among all three Zeeman sublevels. We can detect the atomic spin state by

Stern-Gerlach separation with a magnetic field gradient [126] and observe similar occupation numbers in all three Zeeman states.

Instability boundary

The disappearance of the V polarised self-organization is accompanied by the onset of an instability boundary at detunings resonant with the H polarised cavity mode. This behaviour is reminiscent to the observation of a superradiant instability for atom-cavity scattering from a running wave [242]. We interpret this observation in an analogous way for the spin degree of freedom, similar to optical pumping. This interpretation is supported by the observed atom occupation in all spin components after the ramp, and by the fact that the feature shifts to higher frequencies when applying a magnetic field gradient because of the Zeeman shift. Self-organization involving the spin degree of freedom has been explored theoretically [243] and experimentally [244, 245] before, but without considering competition of two birefringent cavity modes.

In order to ensure that spin transitions are fully suppressed, we performed all measurements presented in this thesis at a magnetic field strength of $B = 34\,G$ and the description with a single cavity mode remains valid.

6

COMPETING ORDERS WITH TWO OPTICAL CAVITIES

Competing order parameters and their corresponding symmetries are an intriguing concept that appears in systems of different physical context. We study competing orders by coupling a BEC to two crossed cavities, where the density orders associated with self-organization to each cavity compete. We start with a general discussion of competing order within the Landau framework, before showing on a microscopic level that competing order can be realized in our setup. Independent adjustment of the coupling to each cavity allows us to map out the full phase diagram, which we put into the context of the previously presented theory. We close the chapter by showing the relation of the system to other quantum-optical models.

CHAPTER CONTENTS

At a phase transition, the thermodynamic properties of a system change abruptly, mostly accompanied by a change in the ground-state symmetry. This behaviour can be captured by an order parameter, which signals the transition from a normal to an ordered phase when acquiring a non-zero expectation value. The order parameter can be interpreted as the representation of a symmetry group corresponding to the symmetry that is broken at the phase transition.

Two competing order parameters

An interesting situation arises in systems exhibiting two different types of order that can be controlled individually. When both control parameters are set to similar values, the interaction between the two orders becomes relevant and determines the number of phases in the phase diagram. As illustrated in Fig. 6.1, two qualitatively different situations can arise [246]:

- Repulsive scenario (three phases): Apart from the normal phase without any order two more phases exist, each showing non-zero expection value for one order parameter. The two ordered phases are separated by a first-order phase transition.
- Attractive scenario (four phases): In addition to the previous three phases a fourth phase exists, where both order parameters have non-zero expectation value. All phase boundaries are continuous phase transitions.

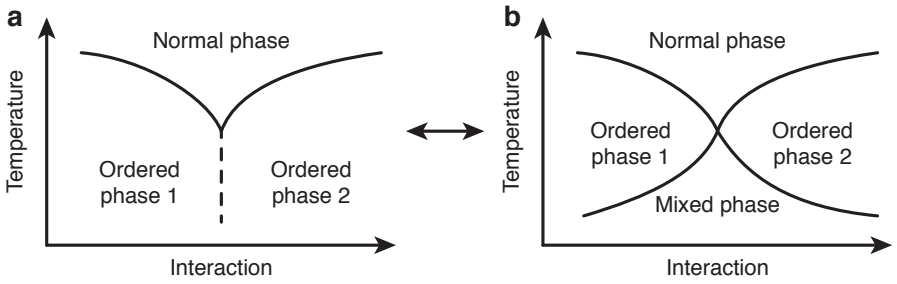

Figure 6.1: *Schematic phase diagram for competing order.* When two order parameters compete, two different situations can arise. **a,** Repulsive scenario: Apart from the normal, disordered phase two more phases exist, each showing non-zero expectation value for one order parameter. The two order parameters are hence mutually exclusive. **b,** Attractive scenario: In addition, a fourth phase with intertwined order exists, where both order parameters have nonzero expectation value.

The physics in the vicinity of the multicritical point, where both control parameters are set to their critical couplings, is referred to as *competing orders* [246]. Models with competing order parameters were first studied in the context of supersolid helium [247], where the existence of multicritical points was pointed out, at which different phases meet. The repulsive scenario features a tricritical point, which separates the two ordered phases and the normal phase. In contrast, four transition lines intersect in the attractive scenario and form a tetracritical point. In general, the multicritical point is of particular interest from a group theoretical perspective, as it combines the symmetries that are broken separately at the phase transition to each ordered phase [248–251] and can exhibit anomalous behaviour [252].

Competing order with two cavities

We investigate this situation by studying the competing order associated to self-organization with two optical cavities. Since the underlying processes can be described by a quantum-optical model, this allows to connect the microscopic theory of atom-photon interactions with an effective Landau theory, which is solely based on symmetry arguments. This is different from most applications of competing order, such as supersolidity [247] and SO(5) theory [253].

Parts of this chapter have been published as:

> J. Léonard, A. Morales, P. Zupancic, T. Esslinger and T. Donner
> *Supersolid formation in a quantum gas breaking a continuous translational symmetry*
> *Nature* **543**, 87-90 (2017)

6.1 THEORETICAL FRAMEWORK

In this section we develop a theoretical description of competing order with two cavities, first in the generic language of Landau expansion, and then in a quantum optical picture describing photon scattering. The experimental setup involving a BEC and two crossed cavities is illustrated in Fig. 6.2.

6.1.1 Competition of two order parameters

Symmetry groups for two order parameters

Landau theory in its original form, as presented in Chap. 5, considers only a single order parameter. However, the formalism can be adapted to account

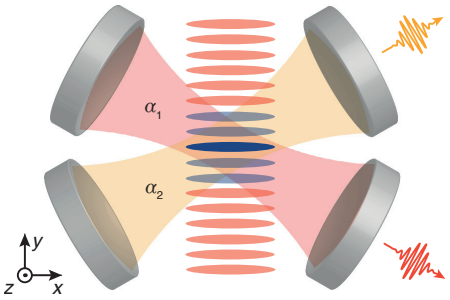

Figure 6.2: *Setup for competing self-organization with two cavities.* A BEC (blue stripes) is cut into slices by a transverse pump lattice potential (red stripes) and coupled to the modes of cavity 1 (red) and 2 (yellow). We infer the absolute values of the intracavity field amplitudes α_1 and α_2 from the intracavity photon numbers $n_1 = |\alpha_1|^2$ and $n_2 = |\alpha_1|^2$, which we measure by recording the photons leaking from the cavities.

for two different order parameters Θ_1 and Θ_2 [254, 255]. In this extension, the two order parameters are irreducible representations of the subgroups G_1 and G_2 of the group H that describes the normal (high-symmetry) phase [230]. The symmetry group L describing the ordered (low-symmetry) phase is a subgroup of H with $L \oplus (G_1 \oplus G_2) = H$. Generally, the symmetries associated to G_1 and G_2 can be broken individually or simultaneously, leaving the system in a phase with the correspondingly reduced symmetry.

Mean-field expansion

Similarly to Eq. 5.1, we expand the mean-field energy as a function of the two order parameters Θ_1 and Θ_2. Both are scalar order parameters, since they describe self-organization with the two cavity fields. The expansion of the Hamiltonian in even powers up to fourth order contains the following terms:

$$\begin{aligned}\mathcal{H}(\Theta_1,\Theta_2) =& \frac{r_1}{2}\Theta_1^2 + \frac{r_2}{2}\Theta_2^2 \\ &+ \frac{g_1}{4}\Theta_1^4 + \frac{g_2}{4}\Theta_2^4 + \frac{g_{12}}{4}\Theta_1^2\Theta_2^2 + \mathcal{O}(\Theta_1^m\Theta_2^n)|_{m+n=6}\,.\end{aligned} \tag{6.1}$$

In general, the coefficients r_1, r_2, g_1, g_2 and g_{12} are all functions of λ_1 and λ_2. The mean-field energy is invariant under the two inversion transformations $\Theta_i \to -\Theta_i$ and therefore exhibits a $\mathbb{Z}_2 \oplus \mathbb{Z}_2$ symmetry. This symmetry group is isomorph to the *Klein four group* K_4, since both can be represented by the pairs $\{e, a, b, c\} = \{(1,1),(1,-1),(-1,1),(-1,-1)\}$ under component-wise multiplication. Another example for the *Klein four group* is the symmetry group of a non-quadratic rectangle. The *Klein four group* is not cyclic, since it cannot be created as the powers of a single element. For symmetric coupling $-r_1/g_1 = -r_2/g_2$, however, the mean-field energy is additionally invariant under the transformation $\Theta_1 \to \Theta_2$. This extends the Klein group to the cyclic group C_4, which is the symmetry group of a square (represented by the rotation group $\{0°, 90°, 180°, 270°\}$).

The expectation values of Θ_1 and Θ_2 in equilibrium are determined by the global minimum of $\mathcal{H}(\Theta_1,\Theta_2)$ and Θ_1 and Θ_2. It is set by the condition $\partial\mathcal{H}(\Theta_1,\Theta_2)/\partial\Theta_i = 0$, yielding the system of equations:

$$\begin{aligned}\Theta_1\left(r_1 + g_1\Theta_1^2 + \frac{g_{12}}{2}\Theta_2^2\right) &= 0 \\ \Theta_2\left(r_2 + g_2\Theta_2^2 + \frac{g_{12}}{2}\Theta_1^2\right) &= 0\end{aligned} \tag{6.2}$$

This set of equations has several solutions. One solution is that both $\Theta_1 = 0$ and $\Theta_2 = 0$, as is the case in the normal phase, where no symmetry

Ground-state solutions for the order parameters

is broken. $-r_i/g_i > 0$ for either $i = 1$ or $i+2$, the corresponding order parameter Θ_i acquires the nonzero value $\Theta_i = \pm\sqrt{-r_i/g_i}$, whereas the other one remains at zero value. This breaks the $\mathbb{Z}_2$ symmetry associated to Θ_i and leaves the system in a state with reduced symmetry $L \oplus G_j$ ($j \neq i$).

The outcome of the last solution with $\Theta_1, \Theta_2 \neq 0$ depends on the values of the coefficients. Let us divide the two equations by the prefactors and require the terms in brackets to disappear. They form a system of two equations that are linear in Θ_1^2 and Θ_2^2. Its determinant $\chi = g_1 g_2 - g_{12}^2/4$ defines the number of minima for the mean-field energy. We obtain three different scenarios depending on the value of χ, as illustrated in Fig. 6.3 [251]:

- $\chi < 0$: No solution exists with both order parameters being nonzero simultaneously. The phase diagram spanned by λ_1 and λ_2 shows three regions: the normal phase with $\Theta_1 = \Theta_2 = 0$, a phase with $\Theta_1 \neq \Theta_2 = 0$ (Ordered 1) and a phase with $\Theta_2 \neq \Theta_1 = 0$ (Ordered 2). In the ordered 1 phase, the mean-field energy has two global minima along the Θ_1 axis. Upon approaching the symmetrically coupled situation of $-r_1/g_1 = -r_2/g_2$, two additional local minima along the Θ_2 axis appear, which become global minima as soon as the point with symmetric coupling is crossed. The coefficient χ determined the range over which the system supports four minima, and therefore also sets the width of the hysteresis loop for a closed path in the phase diagram, as well as the latent heat involved in crossing the phase boundary. As a consequence, the two ordered phases are separated by a first order phase transition. Such a system corresponds to the repulsive scenario in Fig. 6.1):

- $\chi > 0$: Four solutions exist with both order parameters being nonzero simultaneously with the values $\Theta_1 = \pm\sqrt{(g_2 r_1 - g_{12} r_2)/\chi}$ and $\Theta_2 = \pm\sqrt{(g_1 r_2 - g_{12} r_1)/\chi}$. In this scenario, the order parameters are said to *intertwine*. For symmetric coupling $-r_1/g_1 = -r_2/g_2$, the minima are positioned along the diagonal and the anti-diagonals on a square in the Θ_1-Θ_2 plane, symmetrically to the origin. When coupling asymmetrically, the square side along the more weakly coupled order parameter shortens until the minima merge pairwise and the ordered phase with only two different ground states is entered. The coefficient χ determines the extent of the intertwined phase in the phase diagram. Such a system corresponds to the attractive scenario in Fig. 6.1.

- $\chi = 0$: If the determinant of the system of equations vanishes, neither phase separation nor intertwining occurs. Instead, the two $\mathbb{Z}_2$ symmetries give rise to an *enhanced* $U(1)$ symmetry if the couplings are symmetric, i.e. $-r_1/g_1 = -r_2/g_2$. In terms of the effective potential, this can be pictured by a rotation in the Θ_1-Θ_2 plane. As soon as the coupling acquires a finite asymmetry, the rotational symmetry is lost and the effective potential only presents two minima along the axis of the more strongly coupled order parameter. This is the limiting case between the other two scenarios and will be the subject of Chap. 7.

This straightforward expansion for $G \oplus H$ models forms the basis to a number of effects in physics. Apart from the well-studied examples mentioned at the beginning of the chapter, there are connections to matrix models that play a role in condensed matter, nuclear physics, QCD physics and 2D quantum gravity [256]. For $\chi < 0$ and two $\mathbb{Z}_2$ symmetric order parameters, the first order phase transition is identical with the Coleman-Weinberg

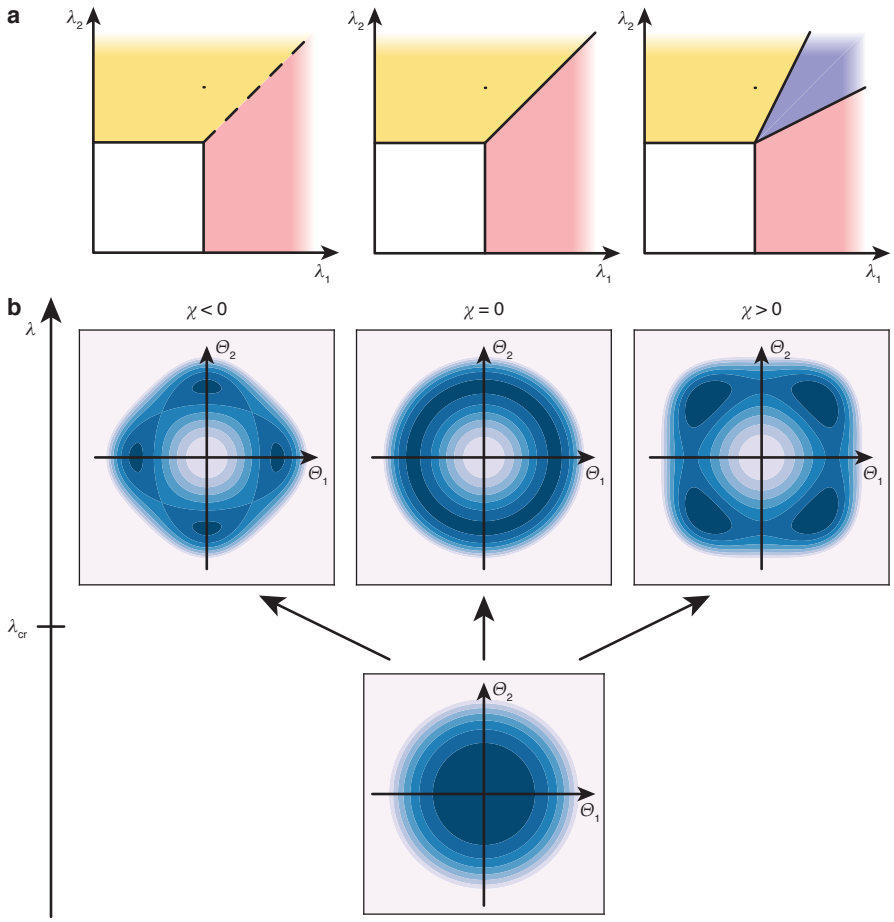

Figure 6.3: *Scenarios for competing orders.* The topology of the phase diagram and the Landau potential are determined by the value of χ. **a,** Phase diagrams as a function of the two couplings λ_1 and λ_2, which are monotonous in r_1 and r_2, respectively. If $\chi < 0$, the order parameters are mutually exclusive and the two ordered phases are separated by a first order phase transition. If $\chi > 0$, an additional phase exists with both order parameters at nonzero values. All phase transitions are continuous. In the special case of $\chi = 0$, an enhanced symmetry is present along the phase boundary at $\lambda_1 = \lambda_2$. **b,** Effective potential for two $\mathbb{Z}_2$ symmetries and identical couplings $\lambda = \lambda_1 = \lambda_2$. In the normal phase with $\lambda < \lambda_{cr}$, the effective potential has a parabolic shape with a single minimum at $\Theta_1 = \Theta_2 = 0$. For $\lambda > \lambda_{cr}$, the potential depends on the determinant χ. If $\chi < 0$, the minima are positioned on the Θ_1 and Θ_2 axes, prohibiting common order for both order parameters. If $\chi > 0$, the minima are rotated to the diagonal and the anti-diagonal, allowing for simultaneous order in both Θ_1 and Θ_2. The limiting case occurs if $\chi = 0$ and the number of solutions is infinite thanks to an enhanced $U(1)$ symmetry.

mechanism for mass generation through spontaneous symmetry breaking beyond the standard model [257, 258].

6.1.2 Momentum mode expansion

Common unit cell for both density orders

Before unifying the self-organization to both cavities in a single description, let us investigate the shape of the unit cell. The rectangular Wigner-Seitz cells for the two density modulation (see Fig. 5.4) do not match as they are mirrored with respect to the y axis. We can construct an extended unit cell including two sites, but which is compatible with both density orders. One possibility is the cell spanned by the lattice vectors:

$$\mathbf{a}_1 = -\frac{\lambda_p}{2}\frac{2\sin(\theta)}{1+\cos(\theta)}\boldsymbol{e}_x + \frac{\lambda_p}{2}\boldsymbol{e}_y, \tag{6.3}$$

$$\mathbf{a}_2 = \frac{\lambda_p}{2}\frac{2\sin(\theta)}{1+\cos(\theta)}\boldsymbol{e}_x + \frac{\lambda_p}{2}\boldsymbol{e}_y, \tag{6.4}$$

where $\theta \in [0, 180°]$ is the angle between the transverse pump and the cavity, λ_p is the wavelength of the transverse pump and $\boldsymbol{e}_x$ and $\boldsymbol{e}_y$ are the unit vectors pointing along x and y, respectively. The cell is symmetric with respect to the y axis, because $\mathbf{a}_1 \cdot \boldsymbol{e}_x = -\mathbf{a}_2 \cdot \boldsymbol{e}_x$. Since the two vectors have the same length but are not orthogonal it has a rhombic shape, as displayed in Fig. 6.4. The area of the cell is:

$$\mathcal{A} = |\mathbf{a}_1 \times \mathbf{a}_2| = \frac{\lambda_p^2}{2}\frac{\sin(\theta)}{1+\cos(\theta)}. \tag{6.5}$$

Reciprocal unit cell

The unit cell of the reciprocal lattice can be constructed from the atomic momentum modes that are accessible by photon scattering processes. We describe the transverse pump and the cavity mode by the wavevectors

$$\mathbf{k}_p = k\boldsymbol{e}_y \tag{6.6}$$

$$\mathbf{k}_1 = -k\sin(\theta)\boldsymbol{e}_x + k\cos(\theta)\boldsymbol{e}_y \tag{6.7}$$

$$\mathbf{k}_2 = k\sin(\theta)\boldsymbol{e}_x + k\cos(\theta)\boldsymbol{e}_y, \tag{6.8}$$

where $k = 2\pi/\lambda_p$ is the wavenumber for all photons. In lowest order, the momentum states that are accessible from the ground state at zero momentum are the combinations $|\pm\mathbf{k}_p \pm \mathbf{k}_i\rangle$ for each cavity $i \in \{1, 2\}$. We can construct the reciprocal lattice from the basis vectors:

$$\mathbf{b}_1 = \mathbf{k}_p - \mathbf{k}_1 = -k\sin(\theta)\boldsymbol{e}_x + k\,(1-\cos(\theta))\,\boldsymbol{e}_y, \tag{6.9}$$

$$\mathbf{b}_2 = \mathbf{k}_p + \mathbf{k}_2 = k\sin(\theta)\boldsymbol{e}_x + k\,(1-\cos(\theta))\,\boldsymbol{e}_y. \tag{6.10}$$

The area of the Brillouin zone is accordingly

$$\mathcal{A}_{BZ} = |\mathbf{b}_1 \times \mathbf{b}_2| = 2k^2\sin(\theta)\,(1-\cos(\theta))\,. \tag{6.11}$$

The real and reciprocal lattice vectors fulfill the condition $\mathbf{a}_i \cdot \mathbf{b}_j = 2\pi\delta_{ij}$ for $i, j \in \{1, 2\}$, resulting in $\mathcal{A}\mathcal{A}_{BZ} = (2\pi)^2$.

Many-body Hamiltonian

We start the derivation of a theoretical description for competing order with two cavities by extending the two-cavity many-body Hamiltonian in

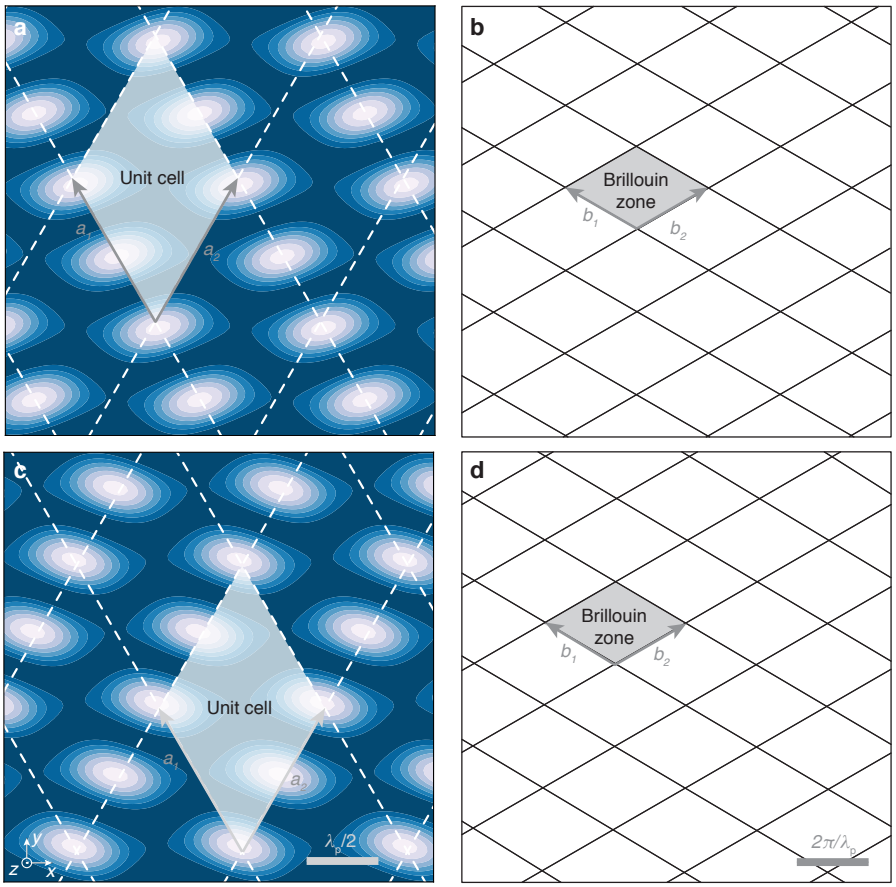

Figure 6.4: *Extended unit cell in real and momentum space.* The unit cell compatible with the self-organization to each cavity includes two lattice sites. **a,** The density modulation from the self-organization to cavity 1 is periodic with the lattice vectors $\mathbf{a}_1$ and $\mathbf{a}_2$. The elementary unit cell in real-space has a rhomboid shape with the same acute angle as between the pump and each cavity axis. **b,** The reciprocal lattice is spanned by the vectors $\mathbf{b}_1$ and $\mathbf{b}_2$. The shape of the Brillouin zone is inverted with respect to the unit cell. **c-d,** The density modulation for self-organization to cavity 2 is horizontally (along x) mirrored with respect to cavity 1. Since the unit cell (**c**) is symmetric along x, its geometry remains unchanged. The same argument holds for the reciprocal space (**d**).

Eq. 5.11 (cf. Appx. B):

$$\begin{aligned}\hat{\mathcal{H}}_{\mathrm{mb}} = &-\sum_{i=1,2}\hbar\Delta_i\hat{a}_i^\dagger\hat{a}_i \\ &+\int_{\mathcal{A}}\hat{\psi}^\dagger(\mathbf{r})\Bigg[\frac{\hat{\mathbf{p}}^2}{2m}+V(\mathbf{r}) \\ &+\sum_{i=1,2}\Big(\hbar\frac{h(\mathbf{r})g_i(\mathbf{r})}{\Delta_a}(\hat{a}_i^\dagger+\hat{a}_i)+\hbar\frac{g_i^2(\mathbf{r})}{\Delta_a}\hat{a}_i^\dagger\hat{a}_i\Big) \\ &+\hbar\frac{g_1(\mathbf{r})g_2(\mathbf{r})}{\Delta_a}(\hat{a}_1^\dagger\hat{a}_2+\hat{a}_2^\dagger\hat{a}_1)+\hbar\frac{h^2(\mathbf{r})}{\Delta_a}\Bigg]\hat{\psi}(\mathbf{r})\,d\mathbf{r} \\ &+\frac{U_{2D}}{2}\int_{\mathcal{A}}d\mathbf{r}d\mathbf{r}'\hat{\psi}^\dagger(\mathbf{r})\hat{\psi}^\dagger(\mathbf{r}')\hat{\psi}(\mathbf{r}')\hat{\psi}(\mathbf{r}).\end{aligned} \tag{6.12}$$

The index $i \in \{1,2\}$ labels the two cavities. $\hbar$ is the reduced Planck constant and $\mathbf{r} = (x,y)$ and $\mathbf{r}' = (x',y')$ are the spatial coordinates that are integrated over the unit cell with area A. The field operator $\hat{\psi}^\dagger$ ($\hat{\psi}$) creates (annihilates) an atom at position $\mathbf{r}$ with mass m. The bare atomic dynamics is captured with the momentum operator $\hat{\mathbf{p}}$, the harmonic trapping potential $V(\mathbf{r})$ and collisions with the 2D contact interaction $U_{2D} = A\overline{n}U$, rescaled from the 3D interaction $U = 4\pi\hbar^2 a/m$ with the s-wave scattering length a and the 3D atomic density $\overline{n}$ [2].

The cavity modes are described by the creation (annihilation) operators $\hat{a}_i^\dagger$ ($\hat{a}_i$). Their frequencies ω_i are detuned from the atomic resonance frequency ω_a by the negative detuning $\Delta_a = \omega_p - \omega_a$, which is large compared to the atomic decay rate for the electronically excited state and to the hyperfine splittings of the D2 transition. The cavity detunings from the transverse pump frequency are given by Δ_i with $\Delta_i \ll \Delta_a$. Since the size of the atomic cloud is small compared to the Gaussian envelopes of the cavity modes, we approximate the modes by plane waves $g_i(\mathbf{r}) = g_i\cos(\mathbf{k}_i\cdot\mathbf{r})$.

The transverse pump lattice beam has a similar diameter as the cavity modes and can be equally considered as a plane wave $h(\mathbf{r}) = \Omega\cos(\mathbf{k}_p\cdot\mathbf{r}+\phi)$ with Rabi frequency Ω. At this point, we included the spatial phase ϕ of the transverse pump lattice. When considering only one cavity, the relative position of the standing waves from the cavity mode and the transverse pump displaced the interference pattern without any effect on the physical behaviour. This situation changes when considering two cavities and the transverse pump lattice, leading to three spatial phases that would overdefine the interference pattern in 2D. As a result, we obtain three standing waves that interfere in two dimensions, out of which only two lead to an in-plane displacement, but the third can affect the interaction.

Let us discuss the meaning of each term of this Hamiltonian separately. $\frac{\mathbf{p}^2}{2m}+V(\mathbf{r})$ describes the free evolution of the atoms in the harmonic trapping potential $V(\mathbf{r})$, and $-\hbar\Delta_i$ describes the free evolution of each cavity mode in a frame rotating with the transverse pump frequency (see Appx. A). The last term describes the atomic contact interaction. The remainder of the Hamiltonian captures the atom-light interaction in a variety of terms corresponding to all possible combinations of two-photon transitions. The rate of the cavity-cavity and the pump-pump two-photon processes are set by $\hbar\frac{g_i^2(\mathbf{r})}{\Delta_a}$ and $\hbar\frac{h^2(\mathbf{r})}{\Delta_a}$, respectively. The term $\hbar\frac{h(\mathbf{r})g_i(\mathbf{r})}{\Delta_a}$ describes two-photon processes between the pump and cavity i. Additionnally, two-photon processes between the two cavities occur with a rate $\hbar\frac{g_1(\mathbf{r})g_2(\mathbf{r})}{\Delta_a}$. Since the in-

teraction is dispersive, each atom-light interaction term can be reinterpreted as an attractive lattice potential from the interference of the participating fields.

Expansion in momentum space

Similarly to the discussion in Chap. 5 the Hilbert space can be greatly reduced by only considering the momentum states that can be reached to first order by two-photon processes starting from the momentum ground state $|\mathbf{k}\rangle = |0\rangle$. The four accessible momentum states from the pump-photon interaction are

$$\begin{aligned} |+\rangle_i &= \frac{1}{\sqrt{2}}\left(|\hbar\mathbf{k}_p + \hbar\mathbf{k}_i\rangle + |-\hbar\mathbf{k}_p - \hbar\mathbf{k}_i\rangle\right) \\ |-\rangle_i &= \frac{1}{\sqrt{2}}\left(|\hbar\mathbf{k}_p - \hbar\mathbf{k}_i\rangle + |-\hbar\mathbf{k}_p + \hbar\mathbf{k}_i\rangle\right), \end{aligned} \tag{6.13}$$

with $i \in \{1, 2\}$ denoting the involved cavity. The interaction with each cavity therefore provides access to one state at kinetic energy $\hbar\omega_+ = 3\hbar\omega_{rec}$ and one at $\hbar\omega_- = \hbar\omega_{rec}$. The normalized real-space wave-functions of these states are

Real-space wave functions

$$\begin{aligned} \psi_0 &= \sqrt{\frac{1}{\mathcal{A}}} \\ \psi_{i+} &= \sqrt{\frac{2}{\mathcal{A}}}\cos\left[(\mathbf{k}_p + \mathbf{k}_i)\cdot\mathbf{r}\right] \\ \psi_{i-} &= \sqrt{\frac{2}{\mathcal{A}}}\cos\left[(\mathbf{k}_p - \mathbf{k}_i)\cdot\mathbf{r}\right]. \end{aligned} \tag{6.14}$$

In addition, we have to take into account the cavity-cavity coupling. This gives rise to two more states

$$\begin{aligned} |+\rangle_{12} &= \frac{1}{\sqrt{2}}\left(|\hbar\mathbf{k}_1 - \hbar\mathbf{k}_2\rangle + |-\hbar\mathbf{k}_1 + \hbar\mathbf{k}_2\rangle\right) \\ |-\rangle_{12} &= \frac{1}{\sqrt{2}}\left(|\hbar\mathbf{k}_1 + \hbar\mathbf{k}_2\rangle + |-\hbar\mathbf{k}_1 - \hbar\mathbf{k}_2\rangle\right) \end{aligned} \tag{6.15}$$

with the corresponding wave functions

$$\begin{aligned} \psi_{12+} &= \sqrt{\frac{2}{\mathcal{A}}}\cos\left[(\mathbf{k}_1 - \mathbf{k}_2)\cdot\mathbf{r}\right] \\ \psi_{12-} &= \sqrt{\frac{2}{\mathcal{A}}}\cos\left[(\mathbf{k}_1 + \mathbf{k}_2)\cdot\mathbf{r}\right]. \end{aligned} \tag{6.16}$$

If we neglect higher order scattering processes, the atoms can only occupy these seven momentum states and we can expand the atomic field operator in the basis

$$\hat{\psi} = \psi_0\hat{c}_0 + \sum_{i\in\{1,2,12\}}\left(\psi_{i-}\hat{c}_{i-} + \psi_{i+}\hat{c}_{i+}\right). \tag{6.17}$$

We carry out the integrals in the Hamiltonian of Eq. 6.12 using a similar nomenclature as in the case of a single cavity. We introduce the lattice depths $\hbar U_i = \hbar g_i^2/\Delta_A$ for the cavities and $\hbar U_p = \hbar\Omega_p^2/\Delta_A$ for the transverse pump potential. The dispersive shift for each cavity renormalizes the cavity detunings as $\tilde{\Delta}_i = \Delta_i - NU_i/2$. The pump-cavity scattering processes have the rates $\lambda_i = \sqrt{N}\eta_i/2\sqrt{2}$ with $\eta_i = -\Omega_p g_i/\Delta_A$. Analogously, the cavity-cavity scattering term has a rate $\lambda_{12} = \sqrt{N}\eta_{12}/2\sqrt{2}$ with $\eta_{12} = -g_1 g_2/\Delta_A$. We choose the negative signs for η_i and η_{12} to obtain positive scattering rates

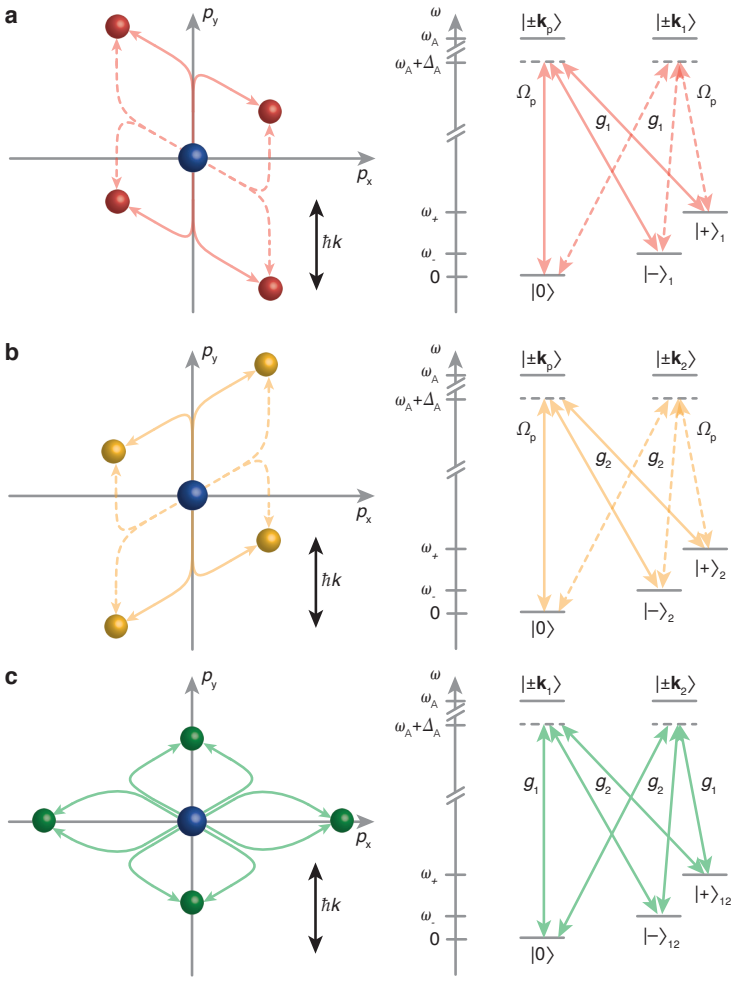

Figure 6.5: *Seven-mode expansion in momentum space.* **a,** Momentum modes from two-photon processes involving the transverse pump and cavity 1. The excitation paths shown as solid (dashed) lines correspond to the creation (annihilation) of a cavity photon. Light scattering between the pump field and the cavity mode induces Raman couplings between the zero momentum state $|p\rangle = |0\rangle$ and the excited states $|+\rangle$ and $|-\rangle$ at energies $\hbar\omega_+$ and $\hbar\omega_-$, respectively. The scattering amplitude is determined by the transverse pump Rabi frequency Ω_p and the vacuum Rabi frequency g_1 of the cavity. **b,** Analogous momentum modes for cavity 2. All processes are mirrored with respect to the p_y axis. **c,** Momentum modes from two-photon processes involving both cavities. The excitation paths shown as solid (dashed) lines correspond to the annihilation of a photon in cavity 1 (2) and the creation of a photon in cavity 2 (1). If $\Theta = 60°$, the condition $\mathbf{k}_1 + \mathbf{k}_2 = \mathbf{k}_p$ is satisfied and all $|-\rangle$ and all $|+\rangle$ states are degenerate.

and coupling strengths, different from the standard notation in the theory of self-organization with a single cavity [81]. The resulting Hamiltonian is

$$\begin{aligned}\hat{\mathcal{H}} = \sum_{i=1,2}\Big[&-\hbar\tilde{\Delta}_i \hat{a}_i^\dagger \hat{a}_i + \hbar\omega_+ \hat{c}_{i+}^\dagger \hat{c}_{i+} + \hbar\omega_- \hat{c}_{i-}^\dagger \hat{c}_{i-} \\ &+ \frac{\hbar\lambda_i}{\sqrt{N}}\left(\hat{a}_i^\dagger + \hat{a}_i\right)\left(\hat{c}_{i+}^\dagger \hat{c}_0 + \hat{c}_{i-}^\dagger \hat{c}_0 + \text{h.c.}\right)\Big] \\ &+ \hbar\omega_+ \hat{c}_{12+}^\dagger \hat{c}_{12-}^\dagger + \hbar\omega_- \hat{c}_{12-}^\dagger \hat{c}_{12-}^\dagger \\ &+ \frac{\hbar\lambda_{12}}{\sqrt{N}}\left(\hat{a}_1^\dagger \hat{a}_2 + \hat{a}_2^\dagger \hat{a}_1\right)\left(\hat{c}_{12+}^\dagger \hat{c}_0 + \hat{c}_{12-}^\dagger \hat{c}_0 + \text{h.c.}\right).\end{aligned} \tag{6.18}$$

6.1.3 *Phase transitions of the system*

The system dynamics is governed by the set of Heisenberg equations

$$\begin{aligned} i\frac{\partial \hat{a}_i}{\partial t} =& -\tilde{\Delta}_i \hat{a}_i + \frac{\lambda_i}{\sqrt{N}}\left(\hat{c}_{i-}^\dagger \hat{c}_0 + \hat{c}_{i+}^\dagger \hat{c}_0 + \text{h.c.}\right) \\ &+ \frac{\lambda_{12}}{\sqrt{N}}\hat{a}_j\left(\hat{c}_{12+}^\dagger \hat{c}_0 + \hat{c}_{12-}^\dagger \hat{c}_0 + \text{h.c.}\right) \\ i\frac{\partial \hat{c}_0}{\partial t} =& \sum_{i=1,2}\frac{\lambda_i}{\sqrt{N}}\left(\hat{c}_{i-} + \hat{c}_{i+}\right)\left(\hat{a}_i^\dagger + \hat{a}_i\right) \\ &+ \frac{\lambda_{12}}{\sqrt{N}}\left(\hat{a}_1^\dagger \hat{a}_2 + \hat{a}_2^\dagger \hat{a_1}\right)\left(\hat{c}_{12+} + \hat{c}_{12-}\right) \\ i\frac{\partial \hat{c}_{i\pm}}{\partial t} =& \omega_\pm \hat{c}_{i\pm} + \frac{\lambda_i}{\sqrt{N}}\hat{c}_0\left(\hat{a}_i^\dagger + \hat{a}_i\right) \\ i\frac{\partial \hat{c}_{12\pm}}{\partial t} =& \omega_\pm \hat{c}_{12\pm} + \frac{\lambda_i}{\sqrt{N}}\hat{c}_0\left(\hat{a}_i^\dagger + \hat{a}_i\right) + \frac{\lambda_{12}}{\sqrt{N}}\hat{c}_0\left(\hat{a}_1^\dagger \hat{a}_2 + \hat{a}_2^\dagger \hat{a_1}\right) \end{aligned} \tag{6.19}$$

Critical couplings

In the limit of weak cavity-cavity coupling, that is $\lambda_{12} \ll \lambda_1, \lambda_2$, we can derive the critical couplings similarly to the calculation shown in Sec. 5.7 and obtain

$$\begin{aligned}\lambda_{cr,1} &= \sqrt{-\tilde{\Delta}_1 \overline{\omega}/4} \\ \lambda_{cr,2} &= \sqrt{-\tilde{\Delta}_2 \overline{\omega}/4}\end{aligned} \tag{6.20}$$

with $\overline{\omega}^{-1} = \omega_+^{-1} + \omega_-^{-1}$.

The Hamiltonian in Eq. 6.18 shows a parity symmetry with respect to each cavity, that is, it remains unchanged upon the simultaneous transformation $(\hat{a}_i, \hat{c}_{i\pm}) \to -(\hat{a}_i, \hat{c}_{i\pm})$ on the photonic and atomic field operators. The symmetries can be captured by the operators

$$\hat{C}_i = \hat{a}_i^\dagger \hat{a}_i + \sum_{s=\pm}\left[\hat{c}_{is}^\dagger \hat{c}_{is} + \hat{c}_{12s}^\dagger \hat{c}_{12s}\right]. \tag{6.21}$$

The corresponding unitary transformations $U = e^{i\theta\hat{C}_i}$ act on the atomic and photonic operators as follows:

$$\hat{a}_i \to \hat{U}\hat{a}_i\hat{U}^\dagger = e^{i\theta}\hat{a}_i \tag{6.22}$$

$$\hat{c}_\mu \to \hat{U}\hat{c}_\mu\hat{U}^\dagger = e^{i\theta}\hat{c}_\mu \tag{6.23}$$

for $i \in \{1,2\}$ and $\mu \in \{1+, 1-, 2+, 2-, 12+, 12-\}$ counting all excited momentum modes. We therefore obtain for the full Hamiltonian

$$\hat{\mathcal{H}} \to \hat{U}\hat{\mathcal{H}}\hat{U}^\dagger = \hat{\mathcal{H}} \text{ if } \theta \in \{0, \pi\} \tag{6.24}$$

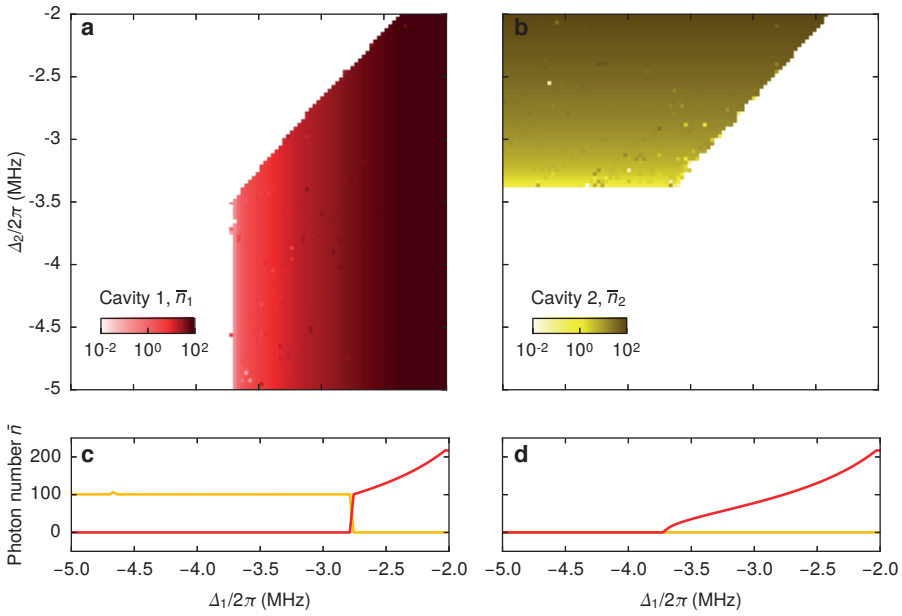

Figure 6.6: *Mean-field solution of the phase diagram.* **a,b,** Mean intracavity photon numbers $\bar{n}_i = |\alpha_i|$ for cavity 1 (**a**) and 2 (**b**) as a function of the pump–cavity detunings Δ_1 and Δ_2. **c,d** Photon traces for cavity 1 (red) and 2 (yellow) as a function of Δ_1, for $\Delta_2/2\pi = -4.0\,\mathrm{MHz}$ (**c**) and $-2.5\,\mathrm{MHz}$ (**d**). The Raman coupling λ is fixed to the experimental value of the transverse pump lattice depth of $38\hbar\omega_{\mathrm{rec}}$ and the intercavity coupling λ_{12} is neglected. The mean-field model includes cavity decay, contact interactions, different vacuum Rabi frequencies g_i and the transverse pump potential.

Symmetries of the Hamiltonian

The Hamiltonian remains invariant under the unitary transformation $\hat{U}_i$ only if $\theta \in \{0, \pi\}$. The underlying symmetry groups are $\mathbb{Z}_2$. The two symmetries can be broken individually at the phase transition to a self-organized state for each cavity. The choice of sign of the field operators corresponds to a choice of 0 or π for the phase of the light field in cavity i, which is equivalent to atoms crystallizing on odd or even sites of a chequerboard lattice with rhomboid geometry.

6.2 PHASE DIAGRAM

We now turn to the phase diagram determined by the competing orders of the two cavities. We start with a numerical analysis of the Hamiltonian, thereby connecting to the generic scenarios presented at the beginning of the chapter. The simulation is then compared to the experimental measurements.

6.2.1 Numerical results

We define the two order parameters

$$\begin{aligned} \Theta_1 &= \langle\hat{\psi}|\cos(\mathbf{k}_p\cdot\mathbf{r})\cos(\mathbf{k}_1\cdot\mathbf{r})\,|\hat{\psi}\rangle \\ \Theta_2 &= \langle\hat{\psi}|\cos(\mathbf{k}_p\cdot\mathbf{r})\cos(\mathbf{k}_2\cdot\mathbf{r})\,|\hat{\psi}\rangle\,, \end{aligned} \tag{6.25}$$

Order parameters

each measuring the overlap of the atomic density distribution with the interference pattern of the respective cavity mode and the transverse pump. A nonzero Θ_i signals the presence of self-organization with cavity $i \in \{1, 2\}$,

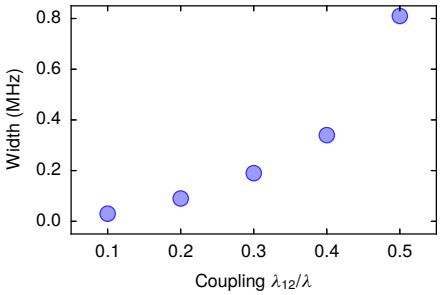

Figure 6.7: *Intertwined order in the two-cavity system.* We extract the width of the phase with intertwined order for different coupling strengths λ_{12} at the detuning $\Delta_1 = \Delta_2 = -3\,\mathrm{MHz}$. The width increases with λ_{12} and shows a negligible size for our experimental parameters.

remaining in the range $-1 \leqslant \Theta_i \leqslant 1$. We are interested in the expectation value of the atomic and photonic operators, which we define as $\langle \hat{a}_i \rangle = \sqrt{N}\alpha_i$ for the cavity modes $i \in \{1, 2\}$ and $\langle \hat{c}_\mu \rangle = \sqrt{N}\psi_\mu$ for the atomic modes $\mu \in \{1\pm, 2\pm, 12\pm\}$. The atomic modes fulfill the normalization condition $\sum_\mu \psi_\mu^2 = 1$. All expectation values can also take real values due to the $\mathbb{Z}_2$ symmetry breaking. In analogy to Eq. 5.42 the atomic order parameters and the photon fields are connected by the relation

$$\begin{aligned} \alpha_1 &= \frac{\eta\Theta_1}{\tilde{\Delta}_1} \\ \alpha_2 &= \frac{\eta\Theta_2}{\tilde{\Delta}_2}. \end{aligned} \tag{6.26}$$

We numerically calculate α_1 and α_2 for our experimental parameters in the plane spanned by Δ_1 and Δ_2 and include photon dissipation and contact interactions in the same way as described in Sec. 5.2.1. The result is shown in Fig. 6.6. Three distinct phases are visible with neither cavity occupied, or either of the two showing a nonzero photon number. The cavity fields exclude each other and a region with finite light fields in both cavities simultaneously is not visible. This points either towards the repulsive scenario with $\chi < 0$, or towards $\chi \gtrsim 0$ with an overlap region below the resolution.

Width of the phase with intertwined order

We calculate the phase diagram for different values of λ_{12} and extract the diagonal width of the overlap region each time at $\Delta_1/2\pi = \Delta_2/2\pi = -3\,\mathrm{MHz}$. The result is shown in Fig. 6.7. The region with both cavities simultaneously occupied grows with increasing λ_{12}, signalling a phase with intertwined order. For our experimental parameters, $\lambda_{12} < 1\%$, which places us in a regime with unresolvable intertwined order at $\chi \gtrsim 0$.

6.2.2 *Measurement of the phase diagram*

We characterize the competing orders in the system by exploring the phase diagram spanned by the cavity detunings Δ_1 and Δ_2. This is equivalent to adjusting the couplings λ_1 and λ_2, because the critical point depends on the detuning, see Eq. 6.20. Starting point of the experiment is an optically trapped BEC exposed to an attractive transverse pump lattice potential with wavelength $\lambda_p = 785.3\,\mathrm{nm}$ and recoil frequency $\omega_{rec} = 2\pi \times 3.7\,\mathrm{kHz}$, restricting the motion of the atoms to the x–z plane (for experimental details, see Methods). While leaving λ constant and independently changing the detunings Δ_1 and Δ_2, we simultaneously record the photons leaking from both

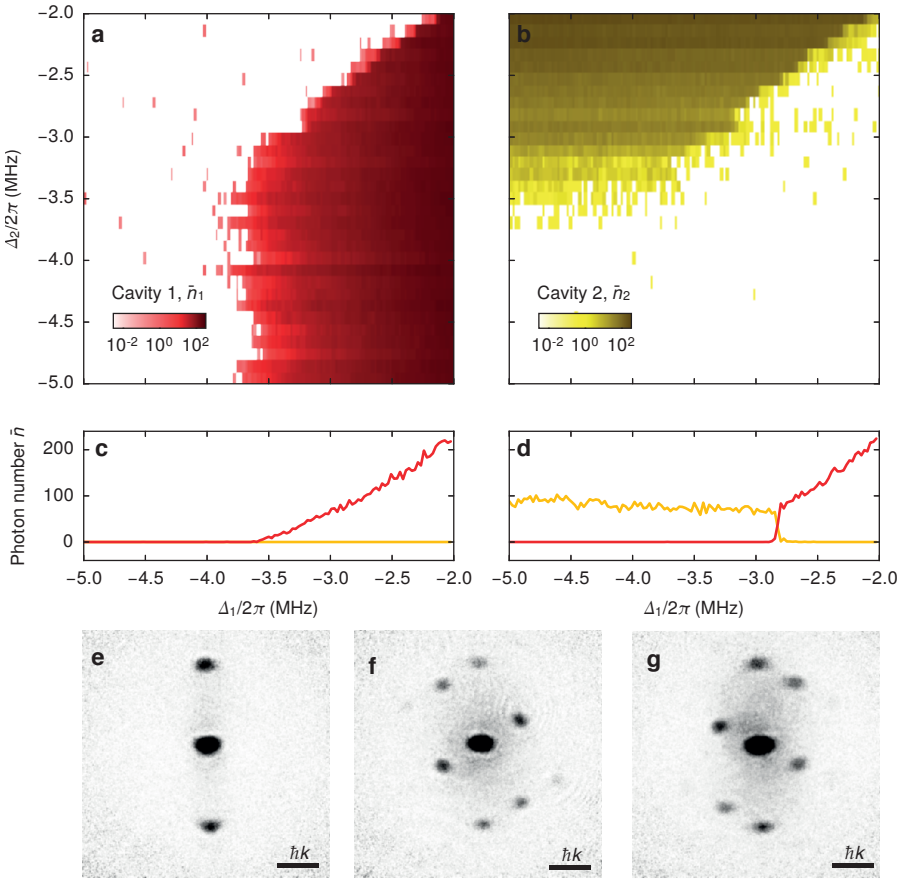

Figure 6.8: *Competing orders in the two cavity–system.* **a–b,** Mean intracavity photon numbers $\bar{n}_i = |\alpha|_i^2$ as a function of the cavity-pump detunings Δ_1 and Δ_2 for a constant transverse pump lattice depth of $38(1)\,\hbar\omega_{rec}$. Each horizontal line was taken for both cavities simultaneously in a single run of 25 ms. **c–d,** Photon traces for cavity 1 (red) and 2 (yellow) as a function of Δ_1, for $\Delta_2/2\pi = -4.0$ MHz (**c**) and -2.5 MHz (**d**). All data are binned in intervalls of 0.5 ms. **e–g,** Absorption images of the atomic momentum distribution, recorded along the z–axis after 25 ms of ballistic expansion with the gas prepared inside the normal phase (**e**) and the self-organized phases to cavity 1 (**f**) and 2 (**g**). Black areas show high atomic densities. The scale bar denotes the length corresponding to a single photon recoil momentum ħk.

cavities, giving us real-time access to the intracavity light fields. Due to the concurrence of photonic and atomic excitations, the intracavity light fields allow us to access the degree of atomic ordering.

The result is shown in Fig. 6.8a, b. For each cavity, we observe a buildup of the cavity field at a critical point (Fig. 6.8c) indicating the transition to a self-organized state. Three regions are immediately visible: one normal phase without an intracavity field, and two self-organized phases to cavity 1 (SO1) and 2 (SO2).

6.2.3 *Realization of two lattice supersolids*

Measure phase coherence

In order to probe the superfluidity of the atomic cloud, we measure its phase coherence. We suddenly turn off all trapping potentials and allow the atomic wavefunction to expand freely. Subsequently, we perform absorption imaging perpendicular to the cavity plane, see Fig. 6.8 (e-g). The presence

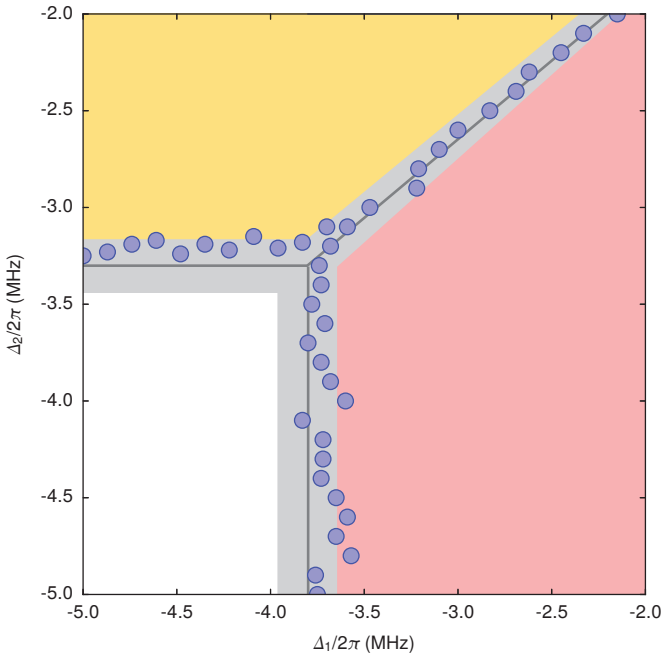

Figure 6.9: *Phase diagram for competing self-organization.* The phase boundaries (blue data points) extracted from the recorded photons separate the normal phase (white), the SO1 phase (red) and the SO2 phase (yellow). The gray area shows the result of the numerical simulation including experimental uncertainties.

of narrow interference maxima reflecting the initial momentum distribution shows the superfluidity of the cloud [109]. In the normal phase, we solely observe the BEC and the momentum peaks at $\pm 2\hbar k$ along the direction of the transverse pump. For finite intracavity field, additional interference maxima appear at momenta of the involved scattering processes depicted in Fig. 6.5c. From the interference maxima we conclude that the observed self-organized phases are lattice supersolids with periodicity $d = \lambda_p/\sin(60°)$. Their broken parity symmetry corresponds to the Hamiltonian in Eq. 6.18 being invariant under the unitary transformation $\alpha_i \to -\alpha_i$ and accordingly for $\hat{c}_{i+}$ and $\hat{c}_{i-}$ for each cavity $i \in \{1, 2\}$. The presence of a lattice supersolid is accompanied by an atomic density modulation along the x–axis forming at discrete positions 0 or $d/2$.

6.2.4 *Extracting the phase boundaries*

We distinguish the three phases in the data of Fig. 6.8 by the presence of photons in either cavity or in neither one. In order to extract the phase boundaries we calculate the differential mean intracavity photon number $\overline{n} = \overline{n}_1 - \overline{n}_2$. The transition point Δ_{cr} between the normal phase and each ordered phase is then determined by approximating the region around the phase boundary with the fit function $\overline{n}_i = \max(A(\Delta_i - \Delta_{cr}), 0)$ for positive (negative) slope A for cavity 1 (2). The transition between the SO1 and the SO2 phase is determined by $\min(|\overline{n}|)$, i.e. the point where the differential photon number vanishes.

We establish a phase diagram by combining the determined transition points. The result is shown in Fig. 6.9. We identify three phases with $\alpha_1 = \alpha_2 = 0$, $\alpha_1 \neq 0 = \alpha_2$ and $\alpha_1 = 0 \neq \alpha_2$. The critical point between the

normal and the self-organized phases remains independent of the detuning from the more weakly coupled cavity. The phase boundary between the self-organized phases has constant slope and follows the condition $\Delta_1 \approx \Delta_2$.

We compare the data with the expected phase boundaries from the numerical simulations shown in Fig. 6.6 and find good agreement. The gray region includes 20 % uncertainty of the atom number as well as fluctuations of the cavity resonance and the transverse pump frequency of 50 kHz each. The phase boundaries between the normal and the self-organized phases are not expected to happen at the same detuning due to a difference in the decay rates of the two cavity fields (see Sec. 5.3.1). This effect also shifts the phase boundary between the self-organized phases slightly off-diagonal. We therefore achieve symmetric coupling to both cavities for cavity 2 slightly closer detuned to the transverse pump frequency than cavity 1.

6.3 RELATION TO OTHER MODELS

We have shown that our system realizes the canonical example of two competing order parameters, which finds application in different contexts of physics [246]. Here we present a few examples that illustrate the relevance of the underlying principle for the presented phase diagram and discuss the close connection to our system.

6.3.1 SO(5) theory

Antiferromagnetismand superconductivity are two states of matter that can occur next to each other in phase diagrams for strongly correlated systems and influence their mutual properties [248, 253, 259]. Examples include high-temperature cuprates, heavy-fermion compounds and organic superconductors. An antiferromagnet breaks an SO(3) symmetry, whereas a superconductor breaks the U(1) (or SO(2)) symmetry associated to the phase invariance.

Unifying antiferromagnetic and superconducting order

SO(5) theory unifies these two basic states from symmetry principles, based on the postulate that a single microscopic interaction gives rise to both the antiferromagnetic and superconducting order. The phenomenology is captured with an expansion of the free energy identical to Eq. 6.1 [253, 260]:

$$\mathcal{F}(\phi_1, \phi_2) = \frac{r_1}{2}\phi_1^2 + \frac{r_2}{2}\phi_2^2 + \frac{g_1}{4}\phi_1^4 + \frac{g_2}{4}\phi_2^4 + \frac{g_{12}}{4}\phi_1^2\phi_2^2 \tag{6.27}$$

Here, ϕ_1 and ϕ_2 are vector order parameters with 2 and 3 components, respectively. The order parameters can be combined to one *superspin* order parameter $\phi = (\phi_1, \phi_2)$. Despite the fact that the symmetry groups of the order parameters are different from the $\mathbb{Z}_2$ symmetries for self-organization, many aspects of the interplay between the two orders are maintained. In our system, however, both self-organized phases are indeed caused by the same microscopic principle, namely photon scattering between the transverse pump and the respective cavity.

Phase transition types in cuprates

Within this framework, the mixing term $\chi = g_1 g_2 - g_{12}^2/4$ (or λ_{12} in Eq. 6.18 determines the type of transition between the antiferromagnetic and the superconducting phase [253]. The type-1 transition corresponds to the repulsive scenario with a first order phase transition from the antiferromagnetic to the superconducing state. In the attractive scenario (type 2), the two phases are separated by two second-order phase transitions with

an additional phase of intertwined order in between. In the limiting case of $\chi = 0$ (type-1.5), the phase with intertwined order has disappeared, but the transition remains second order as no latent heat is involved yet. The phase transition shows an enhanced symmetry (see Chap. 7), except if fractionalized excitations are present [248].

Simulating doped and undoped superconductors

Setting our system in that context amounts to reinterpreting the situation of symmetric coupling with $\lambda = \lambda_1 = \lambda_2$ as an undoped superconductor. In the language of SO(5) theory, the doping corresponds to a rotation of the two order parameters with respect to each other, i.e. an SO(5) rotation restricted to a lower symmetry by the individually broken SO(3) and U(1) symmetries. We can simulate this effect by introducing an asymmetry $\lambda_1 \neq \lambda_2$ in the couplings. In the attractive scenario, the order parameters Θ_1 and Θ_2 are rotated by 90° when passing between the SO1 and the SO2 phase through the mixed intertwined ordered phase. For our experimental parameters with $\chi \approx 0$ this rotation happens for any finite asymmetry, but the system in principal allows to determine the extend of the intertwined phase, see Chap. 11. An analogous behaviour occurs in an 2D optical lattice around half filling [261, 262].

6.3.2 The LMG model

The LMG model originally has been introduced in nuclear physics to describe phase transitions and giant resonances in nuclei [263]. Later, the model has been proposed to describe different systems, for instance magnetic molecules [264], interacting spin systems [265] or interacting bosons on a double well [266, 267]. Its simplicity and exact solvability has also triggered studies investigating the role of entanglement at quantum phase transitions [268–272].

Simulating the XY model infinite coordination number

Conceptually, the model describes an ensemble of N spin-1/2 systems with independent coupling along the x and the y components or, equivalently, the XY model in the limit of infinite coordination number [273]. It can be described by the Hamiltonian:

$$\mathcal{H}_{\mathrm{LMG}} = -\hbar h \hat{S}_z + \hbar \frac{\gamma_1}{N} \hat{S}_x^2 + \hbar \frac{\gamma_2}{N} \hat{S}_y^2 \tag{6.28}$$

with the spin transition frequency h and individual couplings γ_1 and γ_2. For $\gamma_2 = 0$, the system is identical to the Dicke model (see Sec. 5.1.4).

For small coupling γ_1, γ_2, the macroscopic spin points down and $\langle \hat{S}_z \rangle = -N/2$. At the same time, the expectation values for the transverse spin components vanish, i.e. $\langle \hat{S}_x \rangle = 0$ and $\langle \hat{S}_y \rangle = 0$. When increasing either of the coupling strengths past the critical point $\gamma_{\mathrm{cr}} = h/4$, the system undergoes a phase transition to a state with either $\langle \hat{S}_x \rangle \neq 0$ or $\langle \hat{S}_y \rangle \neq 0$. Consequently, the system can be interpreted as two competing order parameters each representing one spin component.

Equivalence to mean-field LMG model

Self-organization with two cavities is adequately described by the LMG model in mean-field approximation. This can be shown by adiabatically eliminating the photon fields in Eq. 6.18. We neglect the influence of the momentum modes at energy $\hbar\omega_+$ here, since they do not change the qualitative discussion, and obtain the Hamiltonian:

$$\hat{\mathcal{H}} = \sum_{i\in\{1,2\}} \left[\hbar\omega_- \hat{c}_{i-}^\dagger \hat{c}_{i-} + \frac{\hbar\lambda^2}{\Delta_i} \left(\hat{c}_{i-}^\dagger \hat{c}_0 + \hat{c}_{i-} \hat{c}_0^\dagger \right)^2 \right] \tag{6.29}$$

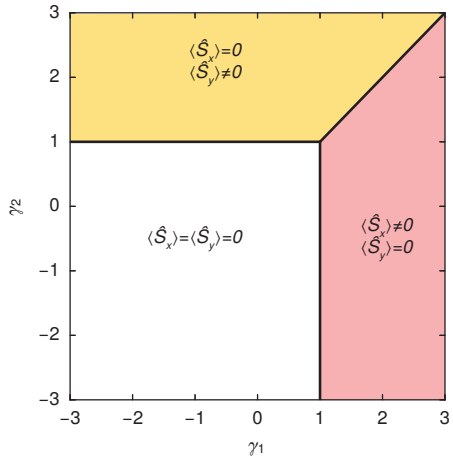

Figure 6.10: *Phase diagram of the LMG model.* The LMG model exibits three different phases with either all spins pointing down ($\langle \hat{S}_x \rangle = \langle \hat{S}_y \rangle = 0$), a finite population along x ($\langle \hat{S}_x \rangle \neq 0 = \langle \hat{S}_y \rangle$) or along y ($\langle \hat{S}_x \rangle = 0 \neq \langle \hat{S}_y \rangle$). All phase transitions are continuous.

We interpret the atomic ensemble as a spin of length $N/2$ and identify the momentum mode operators with a Schwinger-like representation

$$\begin{aligned} \langle \hat{S}_x \rangle &= \langle \hat{c}_{1-}^\dagger \hat{c}_0 + \hat{c}_{1-} \hat{c}_0^\dagger \rangle \\ \langle \hat{S}_y \rangle &= \langle \hat{c}_{2-}^\dagger \hat{c}_0 + \hat{c}_{2-} \hat{c}_0^\dagger \rangle \\ \langle \hat{S}_z \rangle &= \langle \hat{c}_{1-}^\dagger \hat{c}_{1-} + \hat{c}_{2-}^\dagger \hat{c}_{2-} \rangle . \end{aligned} \tag{6.30}$$

This corresponds to the LMG model with the spin transition frequency $-h = \omega_-$ and the couplings $\gamma_i = \lambda^2/\Delta_i$. However, the operators themselves do not form a spin algebra, since $\left[\hat{S}_x, \hat{S}_y\right] = 0$. As a consequence, the analogy is only valid on the mean field level. This is why we have directly used the expectation values in Eq. 6.30.

The symmetry properties for the LMG model and for the two-cavity self-organization remain the same, since the relations $\hat{S}_x \to -\hat{S}_x$, $\hat{S}_y \to -\hat{S}_y$, as well as $\hat{S}_x \to \hat{S}_y$ for symmetric coupling $\gamma_1 = \gamma_2$ are valid. This results in a phase diagram with the same topology, as can be seen in Fig. 6.10. However, the interplay of the order parameters beyond the mean-field level is different for the two systems. This could be observed, for instance, by considering spin squeezing and correlations between the two quadratures [274–276].

6.3.3 *Two-mode Dicke models*

The fact that the Dicke model only exhibits a discrete symmetry breaking has stimulated research to develop quantum optical models that would show a continuous symmetry breaking instead. Let us reconsider the Dicke model, as introduced in Sec 5.1.4:

$$\hat{\mathcal{H}} = \hbar\omega \hat{a}^\dagger \hat{a} + \hbar\omega_0 \hat{S}_z + \frac{\hbar\lambda}{\sqrt{N}} \left(\hat{a}^\dagger + \hat{a}\right) \left(\hat{S}_+ + \hat{S}_-\right). \tag{6.31}$$

It describes the interaction λ of an ensemble of N spin-1/2 systems of energy $\hbar\omega_0$ with a photon field of energy $\hbar\omega$, represented by the creation (annihilation) operator $\hat{a}^\dagger$ ($\hat{a}$). This model exhibits a $\mathbb{Z}_2$ symmetry, but the U(1)

Lack of continuous symmetries in quantum optics

symmetry is hindered by the counterrotating terms $\hat{a}^\dagger \hat{S}_+$ and $\hat{a}\hat{S}_-$. Even though these terms are neglected with the rotating wave approximation in the Jaynes-/Tavis-Cummings model [277], the retrieved U(1) symmetry cannot be broken without going to coupling strengths that are beyond the valid range of the approximation. As a result, continuous symmetry breaking is inhibited.

Several quantum-optical models have been proposed exhibiting a continuous symmetry that can be broken, mostly based on a two-mode extension of the Dicke model [278–282]. The idea on which these proposals found is to construct a Dicke-type model with a second discrete symmetry lying in quadrature to the first one. If the couplings to both quadratures can be independently adjusted, the situation is analogous to two competing order parameters. Due to the absence of coupling between the field quadratures, these models are typically forced to a situation of $\chi = 0$ without a phase of intertwined order, but in exchange allow for squeezing and correlations.

We discuss here exemplary the model studied in [281]. We consider a spin of length $N/2$ with transition frequency ω_0 that is coupled to two photon modes of equal frequency ω with creation (annihilation) operators $\hat{a}^\dagger$ ($\hat{a}$) and $\hat{b}^\dagger$ ($\hat{b}$). The Hamiltonian reads:

$$\begin{aligned}\hat{\mathcal{H}} =& \hbar\omega \hat{a}^\dagger \hat{a} + \hbar\omega \hat{b}^\dagger \hat{b} + \hbar\omega_0 \hat{J}_z \\ &+ \hbar \frac{\lambda_1}{\sqrt{N}} \left(\hat{J}_+ + \hat{J}_-\right)\left(\hat{a}^\dagger + \hat{a}\right) + \hbar \frac{\lambda_2}{\sqrt{N}} \left(\hat{J}_+ - \hat{J}_-\right)\left(\hat{b}^\dagger - \hat{b}\right).\end{aligned} \tag{6.32}$$

Here, $\hat{J}_z$, $\hat{J}_+$ and $\hat{J}_-$ form a spin algebra, and λ_1 and λ_2 are coupling constants. Similarly to two-mode self-organization, the Hamiltonian can be divided into two parts, each considering the coupling to one photonic mode. As a consequence the phase diagram has the same topology and includes competing orders with an enhanced U(1) symmetry for $\lambda_1 = \lambda_2$. However, the two modes act on the same spin, leading to similar beyond-mean-field effects as for the LMG model.

7

SUPERSOLID FORMATION IN A QUANTUM GAS

In this chapter, we show how the continuous translational symmetry of a homogeneous quantum gas can be broken by coupling it with the light fields of two optical cavities. This realizes a supersolid state, which is characterized by the coexistence of spatial order and superfluidity. First, we explain how the continuous symmetry arises from two discrete ones by coupling the quantum gas equally to both cavities. We then describe the main results of the supersolid phase, including the density distribution and its connection to the light fields. Finally, the degeneracy of the continuous symmetry is discussed.

CHAPTER CONTENTS

The introduction of optical lattices to quantum gas experiments has led to the exploration of a wealth of phenomena associated with lattice models [109]. In the context of condensed matter physics, atoms tunneling in a sinusoidal potential simulate mobile electrons that are subject to the periodic potential of the fixed ions in a solid. Yet, the potential formed by an optical lattice is not self-consistent, but externally imposed onto the quantum gas. This intrinsically prevents the simulation of condensed matter effects that include more than the electronic motion, for instance lattice phonons, dislocations or structural phase transitions. Realizing a genuinely self-ordered solid with a quantum gas has remained a challenge.

Structure formation requires potential minimum

In general, structure formation requires an interaction potential showing a minimum at finite distance r_0, as illustrated in Fig. 7.1a. The interaction between two atoms is governed by a competition of the repulsive Pauli blocking at short distance and the attractive van-der-Waals interaction at large distances. The resulting potential causes the atoms to arrange in a periodic manner when interaction energy dominates over kinetic energy. The minimum distance r_0 is typically below 1 nm. The interparticle distance in a BEC is typically on the order of 100 nm, and the minimum in the interaction potential is too short-ranged to be of relevance for structure formation. Engineering interactions that are as long-ranged as the interparticle distance has become an important objective for experiments with quantum gases. The research is driven by the quest for a particular solid: the *supersolid*. This long-sought quantum state is thought to combine the properties of a super-

Long-range interactions in quantum gases

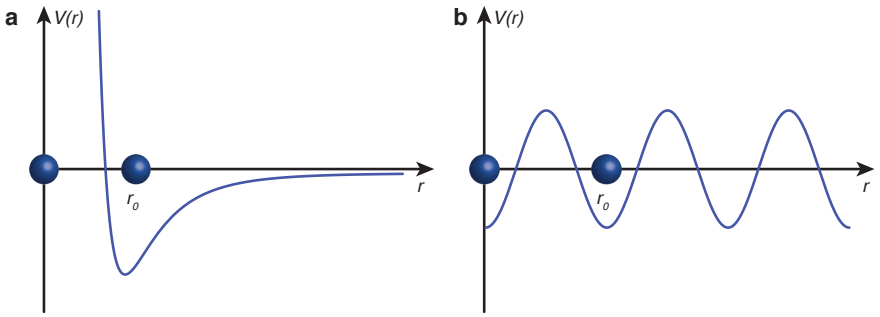

Figure 7.1: *Long-range interaction potentials* **a,** An interaction potential created by an atom at position $r = 0$ is seen by a second atom at finite distance. It exhibits a minimum at r_0, as a consequenc of competition between repulsive Pauli blocking of the electrons in valence shells and the attractive van-der-Waals interaction. With cold atoms, the equilibrium distance r_0 can be engineered to be on the order of the interatomic distance. **b,** The effective interaction from atom-cavity coupling shows a minimum at finite distance and is tunable in strength. The potential is periodic in space and extends over the entire cavity mode.

fluid and a solid, in that it shows phase coherence and a periodic density modulation.

The supersolid has been attempted in a number of cold atoms platforms, most prominently atoms with strong magnetic dipole moment [54–58], polar molecules [62–68], Rydberg atoms [69, 70, 72, 73] and atom-light interaction [77, 283]. None of them has shown a solid phase so far, although first signatures of spatial order in highly excited and short-lived systems have been observed [71, 77, 284].

Atom-light interaction has proven strong enough for collective effects [81]. The formation of a density modulation has first been observed as self-organization in a thermal cloud that is coupled to an optical cavity and subject to a transverse pump beam [212], and then with a BEC [75]. However, the cavity mode restricts the position of the density modulation to only two, see Chap. 5. Since in the latter realization the BEC maintains its superfluidity, the self-organized state corresponds to a *lattice supersolid* with only two possible crystal positions. Thus, a supersolid that can form at any point in space has remained elusive.

Here we report on the realization of such a supersolid. The starting point is a BEC of ^{87}Rb atoms, which has a broken gauge symmetry since it is described by a coherent wave function [285] and shows superfluidity [286]. We induce crystallization of the BEC by coupling the atoms to two optical cavities that cross at an angle of 60°. This gives rise to a long-range interaction potential as shown in Fig. 7.1 [237]. The wavelength λ_p of the cavity photons determines the length scale of the interactions, and therefore the equilibrium distance between the atoms is on the order of the interatomic distance. Different from the van-der-Vaals potential, this interaction however is periodic in space and extends over the full cavity mode (cf. Sec. 7.1.3).

Parts of this chapter have been published in the following publication:

> J. Léonard, A. Morales, P. Zupancic, T. Esslinger and T. Donner
> *Supersolid formation in a quantum gas breaking a continuous translational symmetry*
> *Nature* **543**, 86-90 (2017)

7.1 THEORETICAL FRAMEWORK

The continuous symmetry that is broken at the superfluid-supersolid phase transition is an *enhanced symmetry* that emerges from the discrete symmetries associated with the two cavities. The fact that a continuous symmetry can arise from discrete ones might seem counterintuitive at first sight. In this section, we approach this effect from different perspectives. We start with the canonical example of the XY model, which can be constructed from two Ising models. More generally, symmetry enhancement can be revealed in Landau theory by fine-tuning the coefficients of the mean-field energy expansion. We then show that the same phenomenon is visible in the microscopic Hamiltonian for certain Raman coupling strengths, and finally explain how the symmetry enhancement can be interpreted as a cancelled centre-of-mass term in the photon-mediated interactions.

7.1.1 Symmetry enhancement from competing orders

Let us consider a Hamiltonian with two competing orders, each characterized by an order parameter that is associated with a certain symmetry. At an enhanced symmetry, the Hamiltonian parameters are fine-tuned such that the underlying symmetry groups of the two order parameters are extended to a single one with higher symmetry. It is instructive to illustrate this concept with an intuitive example. We consider the standard Ising spin chain with transverse field, see Fig. 7.2:

$$\hat{\mathcal{H}} = -J_x \sum_{\langle i,j\rangle} \hat{S}_i^x \hat{S}_j^x - h \sum_i \hat{S}_i^z, \tag{7.1}$$

with the transverse field h and the coupling J between each pair $\langle i, j\rangle$. This Hamiltonian has a $\mathbb{Z}_2$ symmetry, since it is invariant under $\hat{S}_i^x \to -\hat{S}_i^x$. At the critical point, the magnetization $\langle S^x\rangle$ acquires a nonzero value that can be positive or negative. The symmetry is consequently broken.

Symmetry-enhancement in the XY model

We can introduce a second $\mathbb{Z}_2$ symmetry in the Hamiltonian by adding a perpendicular coupling term of equal strength.

$$\hat{\mathcal{H}} = -J \sum_{\langle i,j\rangle} \left(\hat{S}_i^x \hat{S}_j^x + \hat{S}_i^y \hat{S}_j^y\right) - h \sum_i \hat{S}_i^z, \tag{7.2}$$

with $J = J_x = J_y$. The Hamiltonian is now invariant under $\hat{S}_i^x \to -\hat{S}_i^x$ and $\hat{S}_i^y \to -\hat{S}_i^y$. When the system crosses the critical point it develops nonzero magnetizations $\langle \hat{S}^x\rangle$ along x and $\langle \hat{S}^y\rangle$ along y. However, the symmetry that is broken is a rotational symmetry rather than two $\mathbb{Z}_2$ symmetries, since the total magnetization $\langle \hat{S}\rangle = \left(\langle \hat{S}^x\rangle, \langle \hat{S}^y\rangle\right)$ can point along any direction in the x-y plane, only keeping $\left|\langle \hat{S}\rangle\right|$ constant: a continuous symmetry has emerged from two discrete ones [258].

More generally, symmetry enhancement can be described in Landau theory with two order parameters Θ_1 and Θ_2 associated with the symmetry groups G_1 and G_2 [230]. Let us consider the mean-field energy in Eq. 6.1 for the situation of symmetric coupling to both order parameters, i. e. $\lambda = \lambda_1 = \lambda_2$. The Landau expansion up to fourth order then reads:

$$\mathcal{H}(\Theta_1, \Theta_2) = \frac{r}{2}(|\Theta_1|^2 + |\Theta_2|^2) + \frac{g}{4}(|\Theta_1|^4 + |\Theta_2|^4) + \frac{g_{12}}{4}|\Theta_1|^2 |\Theta_2|^2, \tag{7.3}$$

with all coefficients r, g, g_{12} functions of λ. The symmetry properties of this Hamiltonian are inherited from the order parameters, thus it remains invariant under transformations in $G_1 \oplus G_2$. In the case of self-organization

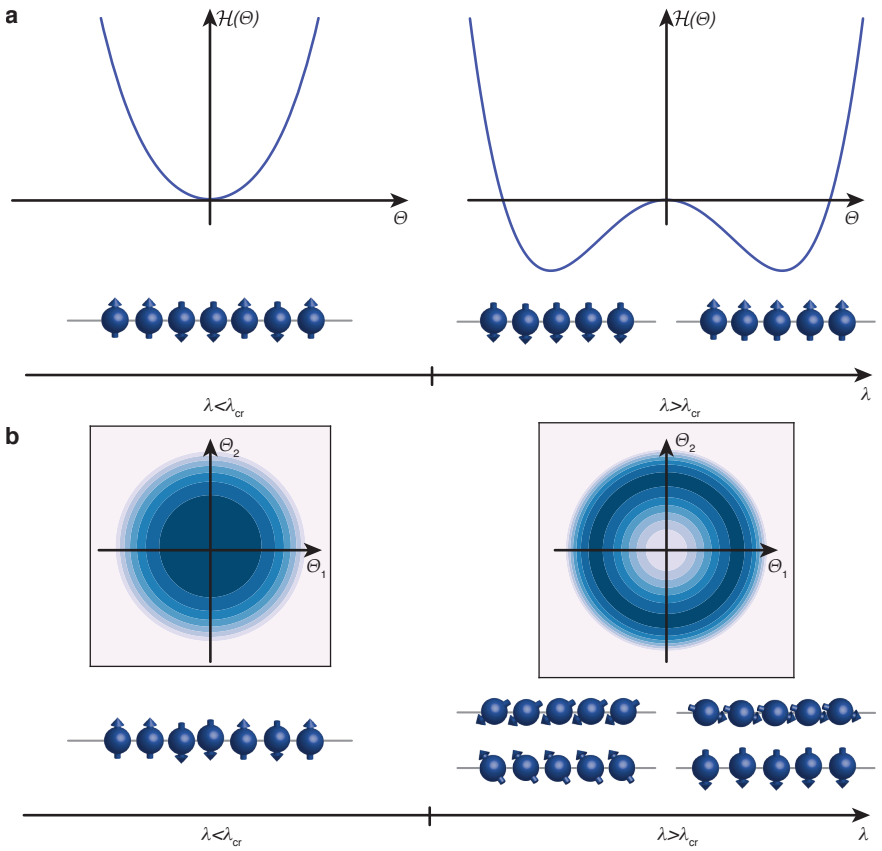

Figure 7.2: *Symmetry enhancement from competing order.* **a,** Ising-type symmetry breaking. At small interaction strength, the magnetization disappears and each spin points up or down. When increasing the interaction across the critical point, two ground states appear with all spins either pointing down or up. The magnetization acquires a non-zero value and the $\mathbb{Z}_2$ symmetry of the Hamitonian is broken. **b,** XY-type model, constructed from two Ising models with equally strong spin interactions along two quadratures. In the normal phase the spins are not oriented and the magnetization is zero. In the ordered phase, all spins align in the plane, breaking a continuous (rotational) symmetry.

with two cavities, Θ_1 and Θ_2 are scalar and individually exhibit $\mathbb{Z}_2$ with the transformations $\Theta_1 \to -\Theta_1$ and $\Theta_2 \to -\Theta_2$. Since both couplings are identical, the Hamiltonian is additionally symmetric under exchange of the two order parameters $\Theta_1 \to \Theta_2$, which already extends the symmetry group to the cyclic group C_4.

We can further extend the symmetry group of the Hamiltonian by imposing a second restriction on the coefficients in the expansion. For convenience, let us use the parametrization

$$\mathcal{H}(\Theta_1,\Theta_2) = \frac{r}{2}(|\Theta_1|^2+|\Theta_2|^2) + \frac{g}{4}(|\Theta_1|^2+|\Theta_2|^2)^2 + \zeta|\Theta_1|^2|\Theta_2|^2\,, \quad (7.4)$$

with the intertwining parameter $\xi = (g_{12}-2g)/4$. We can see that for $\xi = 0$ the two $\mathbb{Z}_2$ symmetries together form an $SO(2)$ symmetry for the order parameter $\Theta = (\Theta_1,\Theta_2)$ or, alternatively, a $U(1)$ symmetry with $\Theta = \Theta_1 + i\Theta_2$, since the vector spaces $\mathbb{R}^2$ and $\mathbb{C}$ are isomorph. We can visualize this scenario in terms of the effective potential, as illustrated in Fig. 7.2b. In the normal phase, the effective potential has a parabolic shape and exhibits a single minimum with $\Theta_1 = \Theta_2 = 0$. When increasing λ across the critical

Continuous symmetry from two discrete ones

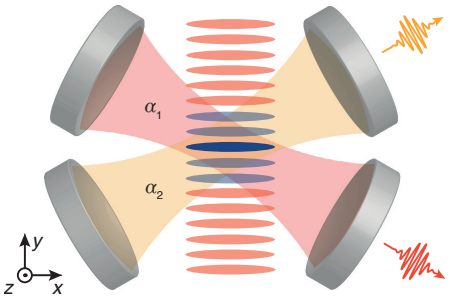

Figure 7.3: *Setup for creating a supersolid.* A BEC (blue stripes) is cut into slices by a transverse pump lattice potential (red stripes) and coupled to the modes of cavity 1 (red) and 2 (yellow). We infer the absolute values of the intracavity field amplitudes α_1 and α_2 from the intracavity photon numbers $\bar{n}_1 = |\alpha_1|^2$ and $\bar{n}_2 = |\alpha_2|^2$, which we measure by recording the photons leaking from the cavities.

point with $r(\lambda = \lambda_{cr}) = 0$, the potential changes to a 'sombrero' shape with an infinite number of ground states at constant radius $|\Theta| = \sqrt{|\Theta_1|^2 + |\Theta_2|^2}$. The order parameters are therefore not individually determined but can only take the values:

$$\begin{aligned} \Theta_1 &= \cos(\theta)\,|\Theta| \\ \Theta_2 &= \sin(\theta)\,|\Theta| \end{aligned} \tag{7.5}$$

with $\theta \in [0, 2\pi]$. The amplitude of the order parameter takes the value $|\Theta| = \sqrt{-r/g}$.

In summary, a fine-tuning of the coefficients in the mean-field expansion can lead to a higher symmetry of the Hamiltonian in a reduced parameter space. The $\mathbb{Z}_2 \oplus \mathbb{Z}_2$ symmetry in the Hamiltonian was first extended to the cyclic group K_4 and then further to the rotation group SO(2). Geometrically, this corresponds to extending the symmetry group of a non-quadratic rectangle first to a square and then to a circle. These geometries are also reflected by the minima positions in the effective potential, which are equivalent to the ground state manifold of the Hamiltonian.

Since enhanced symmetries require to confine the underlying theory to a lower dimension, they are also called *hidden* or *accidental* symmetries [287]. From the perspective of the lower dimensional theory, an enhanced symmetry can be understood as a residual of a multicritical point in a higher dimensional phase diagram. The concept of symmetry enhancement from two order parameters is central to many aspects in modern physics, for example high-temperature superconductors [253, 288], extensions of the standard model [258, 289, 290] or cosmology [251, 291].

7.1.2 *Momentum mode expansion*

We consider the setup with a BEC coupled to two optical cavities (see Fig. 7.3). A microscopic picture of the coupled system is obtained by considering Raman processes between transverse pump and cavity modes which coherently transfer atoms between the motional ground state and excited momentum states, as shown in Fig. 7.4. In Chap. 6 we have seen that for our parameters cavity-cavity scattering is neglible and $\lambda_{12} \ll \lambda_1, \lambda_2$ and there-

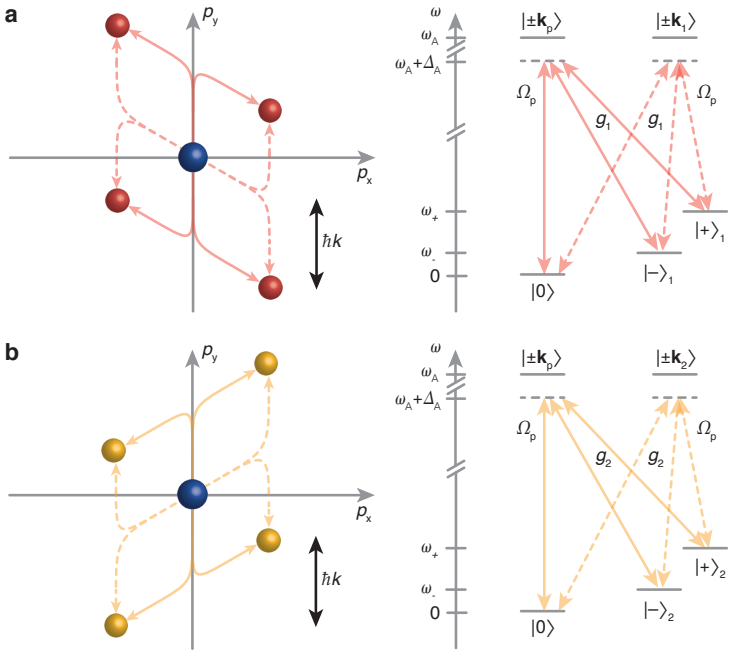

Figure 7.4: *Five-mode expansion in momentum space.* **a,** Momentum modes from two-photon processes involving the transverse pump and cavity 1. The excitation paths shown as solid (dashed) lines correspond to the creation (annihilation) of a cavity photon. Light scattering between the pump field and the cavity mode induces Raman couplings between the zero momentum state $|p\rangle = |0\rangle$ and the excited states $|+\rangle$ and $|-\rangle$ at energies $\hbar\omega_+$ and $\hbar\omega_-$, respectively. The scattering amplitude is determined by the transverse pump Rabi frequency Ω_p and the vacuum Rabi frequency g_1 of the cavity. **b,** Analogous momentum modes for cavity 2. All processes are mirrored with respect to the p_y axis. Since the cavities and the transverse pump all cross at angles of $\Theta = 60°$, the condition $\mathbf{k}_1 + \mathbf{k}_2 = \mathbf{k}_p$ is satisfied and the $|-\rangle$ and the $|+\rangle$ states are degenerate.

fore $\langle\Theta_{12}\rangle = 0$. We consider the Hamiltonian in Eq. 6.18 at the absence of cavity scattering, setting $\tilde{\Delta}_c \equiv \tilde{\Delta}_1 = \tilde{\Delta}_2$ and $\lambda \equiv \lambda_1 = \lambda_2$:

$$\hat{\mathcal{H}} = \sum_{i=1,2}\Big[-\hbar\tilde{\Delta}_c\hat{a}_i^\dagger\hat{a}_i + \hbar\omega_+\hat{c}_{i+}^\dagger\hat{c}_{i+} + \hbar\omega_-\hat{c}_{i-}^\dagger\hat{c}_{i-} + \frac{\hbar\lambda}{\sqrt{N}}\left(\hat{a}_i^\dagger + \hat{a}_i\right)\left(\hat{c}_{i+}^\dagger\hat{c}_0 + \hat{c}_{i-}^\dagger\hat{c}_0 + \text{h.c.}\right)\Big], \tag{7.6}$$

where $\hbar$ is the reduced Planck constant and N is the atom number. The atoms are described by creation (annihilation) operators $\hat{c}_0^\dagger$ ($\hat{c}_0$) for the motional ground state as well as for the high- and the low energy states with $\hat{c}_{i+}^\dagger$ ($\hat{c}_{i+}$) and $\hat{c}_{i-}^\dagger$ ($\hat{c}_{i-}$), respectively, associated with cavity $i \in \{1,2\}$. The photon fields are denoted by $\hat{a}_i^\dagger$ ($\hat{a}_i$) with detuning $\tilde{\Delta}_c = \omega_p - \omega_c - NU_c/2 < 0$ between resonance frequency ω_c and transverse pump laser frequency ω_p, including the dispersive frequency shift $U_c/2$ per atom.

Rotational symmetry of the Hamiltonian

This Hamiltonian is invariant under the reflection symmetry $(\hat{a}_i, \hat{c}_{i\pm}) \to -(\hat{a}_i, \hat{c}_{i\pm})$, which corresponds to a $\mathbb{Z}_2$ symmetry. Together with the invariance of the Hamiltonian under exchange of the two cavities $(\hat{a}_1, \hat{c}_{1+}, \hat{c}_{1-}) \to$

$\hat{a}_2, \hat{c}_{2+}, \hat{c}_{2-}$, this gives rise to a rotational symmetry:

$$\begin{aligned} \hat{a}_1 \to \hat{a}_1' &= \hat{a}_1 \cos\theta - \hat{a}_2 \sin\theta \\ \hat{a}_2 \to \hat{a}_2' &= \hat{a}_1 \sin\theta + \hat{a}_2 \cos\theta \\ \hat{c}_{1\pm} \to \hat{c}_{1\pm}' &= \hat{c}_{1\pm} \cos\theta - \hat{c}_{2\pm} \sin\theta \\ \hat{c}_{2\pm} \to \hat{c}_{1\pm}' &= \hat{c}_{1\pm} \sin\theta + \hat{c}_{2\pm} \cos\theta, \end{aligned} \tag{7.7}$$

for any $\theta \in [0, 2\pi]$. The corresponding generator $\hat{C}$ of the symmetry $\hat{U}(\theta) = e^{i\theta\hat{C}}$ is the Hermitian operator

$$\hat{C} = -i\Big[\hat{a}_1^\dagger \hat{a}_2 - \hat{a}_2^\dagger \hat{a}_1 + \sum_{s=\pm}\Big(\hat{c}_{1s}^\dagger \hat{c}_{2s} - \hat{c}_{2s}^\dagger \hat{c}_{1s}\Big)\Big]. \tag{7.8}$$

It satisfies $[\hat{C}, \hat{\mathcal{H}}] = 0$ and as a result the Hamiltonian $\hat{\mathcal{H}}$ stays invariant under $\hat{U}$:

$$\begin{aligned} \hat{\mathcal{H}} &\to \hat{U}\hat{\mathcal{H}}\hat{U}^\dagger \\ &= \sum_{i=1,2}\Big[-\hbar\tilde{\Delta}_c \hat{a}_i'^\dagger \hat{a}_i' + \hbar\omega_+ \hat{c}_{i+}'^\dagger \hat{c}_{i+}' + \hbar\omega_- \hat{c}_{i-}'^\dagger \hat{c}_{i-}' \\ &+ \frac{\hbar\lambda}{\sqrt{N}}\Big(\hat{a}_i'^\dagger + \hat{a}_i'\Big)\Big(\hat{c}_{i+}'^\dagger \hat{c}_0 + \hat{c}_{i-}'^\dagger \hat{c}_0 + \text{h.c.}\Big)\Big], \\ &= \hat{\mathcal{H}} \end{aligned} \tag{7.9}$$

This continuous symmetry is spontaneously broken at the phase transition when $\lambda = \lambda_{cr}$. The transformation in Eq. 7.7 shows that the symmetry breaking happens both in the atomic and in the photonic fields with the same angle θ. We can therefore extract the phase of the atomic order parameter $\tan\theta = \langle\hat{\Theta}_2\rangle / \langle\hat{\Theta}_1\rangle$ from the light fields via $\tan\theta = \langle\hat{a}_2\rangle / \langle\hat{a}_1\rangle$.

7.1.3 *Photon-mediated interactions*

Much like for the single cavity system, we can describe the atom-light coupling by an effective photon-mediated interaction between the atoms. The evolution for the light fields follows from Eq. 6.12:

$$i\frac{\partial \hat{a}_i}{\partial t} = -\tilde{\Delta}_c \hat{a}_i + \eta \int_{\mathcal{A}} d\mathbf{r}\psi^\dagger(\mathbf{r}) \cos(\mathbf{k}_p \cdot \mathbf{r} + \beta) \cos(\mathbf{k}_i \cdot \mathbf{r})\psi(\mathbf{r}). \tag{7.10}$$

Adiabatic elimination of the light field

Since $\omega_+, \omega_- \ll |\tilde{\Delta}_c|$, we can set $\partial\hat{a}_i/\partial t \approx 0$ and eliminate the light field from the Hamiltonian:

$$\begin{aligned} \hat{\mathcal{H}}_{lr} &= \int_{\mathcal{A}} \hat{\psi}^\dagger(\mathbf{r}) \frac{p^2}{2m} \hat{\psi}(\mathbf{r}) d\mathbf{r} \\ &= \int_{\mathcal{A}} \int_{\mathcal{A}} \hat{\psi}^\dagger(\mathbf{r}) \hat{\psi}^\dagger(\mathbf{r}') U_{lr}(\mathbf{r}, \mathbf{r}') \hat{\psi}(\mathbf{r}') \hat{\psi}(\mathbf{r}) d\mathbf{r} d\mathbf{r}' \end{aligned} \tag{7.11}$$

with the interaction potential

$$U_{int}(\mathbf{r}, \mathbf{r}') = \sum_{i\in\{1,2\}} V_i \cos(\mathbf{k}_p \cdot \mathbf{r} + \beta) \cos(\mathbf{k}_i \cdot \mathbf{r}) \cos(\mathbf{k}_p \cdot \mathbf{r}' + \beta) \cos(\mathbf{k}_i \cdot \mathbf{r}') \tag{7.12}$$

where $V_1 = V_{int}\cos(\theta)$ and $V_2 = V_{int}\sin(\theta)$ with the interaction strength $V_{int} = 2\hbar\lambda^2/N\tilde{\Delta}_c$. For two particles, the interaction potential can be rewrit-

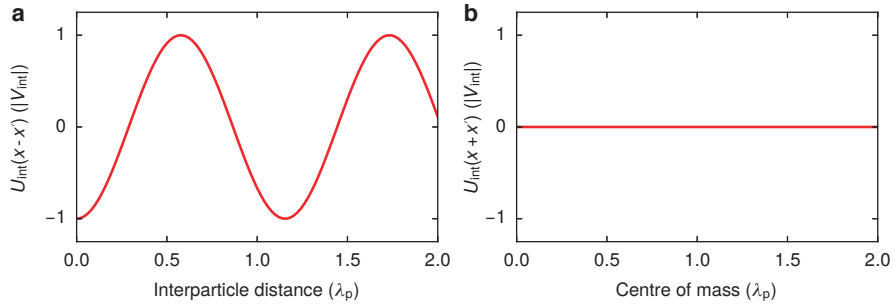

Figure 7.5: *Translationally invariant photon-mediated interactions.* **a,** Interaction potential for the relative position of two particles along x for $y = \lambda/8$ and $V_{int} < 0$ at the transverse pump phase $\beta = \pi/2$. The interactions favour a distance of $\lambda_p/\cos(\theta)$, thereby selectively enhancing periodic density correlations. **b,** The interactions do not depend on the center of mass of the two particles. As a consequence, the density modulation can form at any position, which represents a prerequisite to break continuous translational symmetry.

ten in terms of their distance $\mathbf{r}_{rel} = \mathbf{r} - \mathbf{r}'$ and their center of mass $\mathbf{R} = (\mathbf{r} + \mathbf{r}')/2$:

$$U_{int}(\mathbf{r}, \mathbf{r}') = \sum_{i\in\{1,2\}} \frac{V_i}{4} \left[\cos(2\mathbf{k}_p \cdot \mathbf{R} + 2\beta) + \cos(\mathbf{k}_p \cdot \mathbf{r}_{rel})\right] \left[\cos(2\mathbf{k}_i \cdot \mathbf{R}) + \cos(\mathbf{k}_i \cdot \mathbf{r}_{rel})\right], \tag{7.13}$$

The spatial phases of the standing wave profiles of the two cavity modes can be neglected, as they lead to a displacement in the x-y plane only. In general, the spatial character of the interaction potential depends on both the centre of mass and the relative position of the two particles. Its shape can be modified with the spatial phase β of the transverse pump.

Let us have a closer look at the interaction potential for $\beta = \pi/2$. We consider only one slice of the transverse pump lattice and restrict the discussion to the x-axis with $y \equiv \lambda/8$. Here the term $\cos(2\mathbf{k}_p \cdot \mathbf{R} + 2\beta)$ disappears, since $\mathbf{k}_p \perp \mathbf{e}_x$ and $\cos(2k\lambda/8 + \pi) = 0$. This leaves only the two terms $\cos(2\mathbf{k}_i \cdot \mathbf{R})$, which can be combined as:

$$\begin{aligned} &\frac{1}{2}\left[\cos(\theta)\cos(2\mathbf{k}_1 \cdot \mathbf{R}) + \sin(\theta)\cos(2\mathbf{k}_2 \cdot \mathbf{R})\right] \\ &= \cos(2\mathbf{k}_1 \cdot \mathbf{R} + \theta) + \cos(2\mathbf{k}_1 \cdot \mathbf{R} - \theta) + \sin(2\mathbf{k}_2 \cdot \mathbf{R} + \theta) + \sin(2\mathbf{k}_2 \cdot \mathbf{R} - \theta) \\ &= 0 \quad \forall\theta \in [0, 2\pi]\,. \end{aligned} \tag{7.14}$$

Absence of a center-of-mass term

This is the key difference compared to the interaction potential for a single cavity (cf. Fig. 5.6), where the interaction potential has a centre of mass dependence with two minima per lattice constant. For two cavities, the absence of a centre-of-mass dependence is the origin of breaking continuous translational symmetry. The graphs in Fig. 7.5 show the spatial dependence of the interaction potential for the case of $\beta = \pi/2$ and $V_{int} < 0$. The potential shows a minimum at a relative distance of $\lambda_p/\cos\theta$ between the particles, similar to the situation of a single cavity. Yet, the interaction does not influence the centre of mass position.

The above discussion does also hold for $V_{int} > 0$. In this case, the potential shows minima for relative positions $(n + 1/2)\lambda_p/\cos\theta$, which cannot be fulfilled for more than two particles, since a third particle would be separated

from either of the particles by an even number of lattice constants. As a result, the interaction suppresses fluctuations with wavelengths of the lattice constant.

The lattice structure of the density modulation is perfectly rigid, because it is determined by the interference potential of the light fields. As a result, the crystallization is defect-free and homogeneous, because all atoms couple equally to the cavity modes, and the presence of phonons at nonzero wavenumbers is inhibited.

7.2 REAL-SPACE DENSITY DISTRIBUTION

In the previous section we have already seen that the effective photon-mediated interactions do not exhibit a centre-of-mass dependence. This is a first indication that the continuous symmetry has a spatial component. In this section, we reveal this connection more directly by considering the interference pattern that arises when both cavity modes have a finite field amplitude. We will see that the minima of the interference pattern are displaced for different ratios of the cavity fields, which creates a dipole potential that influences the atomic distribution.

7.2.1 Supersolid potential

The self-consistent potential in the supersolid phase is formed from the interference between the transverse pump field and the two cavity fields. We derive here the relation between the ratio of the coherent cavity fields α_1 and α_2 and the position of the density pattern. The combined potential can be written as

$$U(\mathbf{r}) = \frac{\hbar |\Omega(\mathbf{r})|^2}{\Delta_a} \tag{7.15}$$

with the total field amplitude $\Omega(\mathbf{r})$ at position $\mathbf{r}$. The total field amplitude consists of contributions from the transverse pump and each cavity mode,

$$\Omega(\mathbf{r}) = \sum_{i\in\{p,1,2\}} \Omega_i \cos(\mathbf{k}_i \cdot \mathbf{r} + \beta_i), \tag{7.16}$$

where Ω_p is the transverse pump Rabi frequency and $\Omega_1 = g_1\alpha_1, \Omega_2 = g_2\alpha_2$ are the Rabi frequencies of the two cavities fields. They are determined by the vacuum Rabi frequencies g_1, g_2 and the intracavity photon numbers α_1, α_2.

Spatial phases of the standing-wave potentials

The temporal phases between the three standing wave lattices do not have to be considered, since all photons stem from the same transverse pump frequency and no phase delay is introduced during photon scattering thanks to the negative detuning, $\Delta_a < 0$, from the atomic resonance [213]. The spatial phases β_i, however, are generally non-zero, since they describe the relative position of the three standing wave potentials. We set $\beta_1 = \beta_2 = 0$ by choosing the origin of the coordinate system appropriately. The atomic spatial distribution is then determined by the phase $\beta_p \equiv \beta$ of the transverse pump standing wave, which we can change with a piezo–electric actuator attached to the retroreflecting transverse pump mirror (see Ch. 4). For our experimental parameters $U_p \gg U_1, U_2$ such that the atoms are separated into 2D layers in the x–z plane at $ky + \beta = \pi n, n \in \mathbb{Z}$, where $k = 2\pi/\lambda_p$.

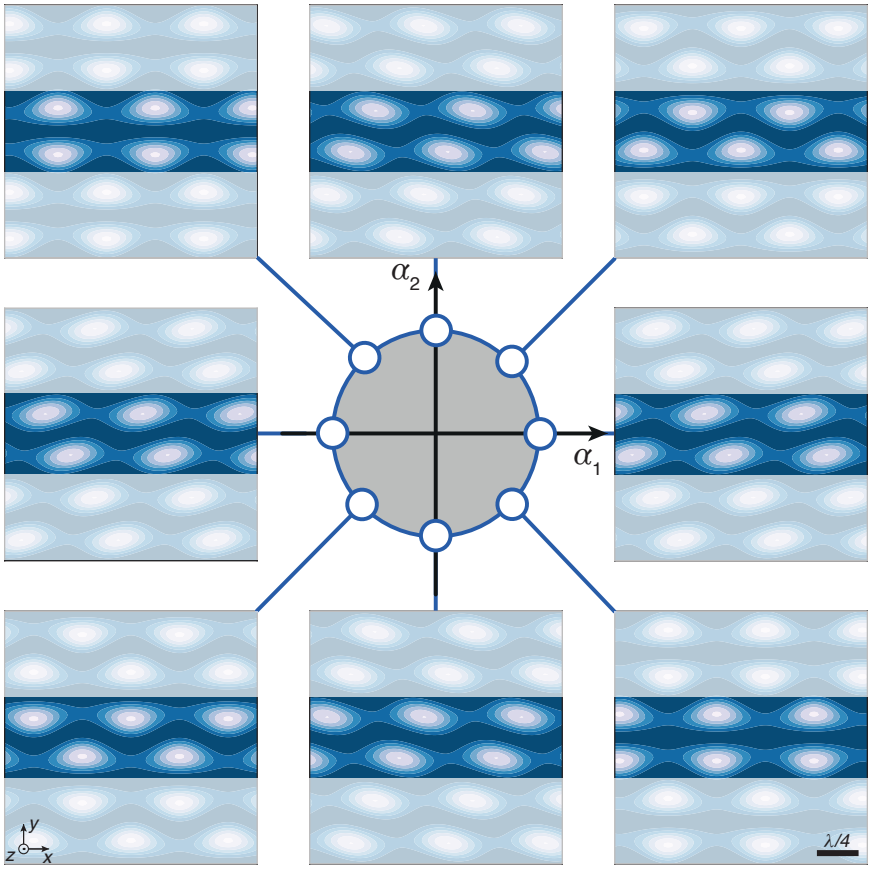

Figure 7.6: *Interference potential for different cavity field ratios.* The ground-state manifold for equal couplings and detunings in $\mathcal{H}$ is a circle in the space of the cavity fields α_1 and α_2. For each combination of fields, the interference potential in Eq. 7.17 between transverse pump and cavity fields for $\beta = \pi/2$ has its minima at different positions. Following the circle counter-clockwise, every second line moves left (top highlighted line) while the others move right (bottom highlighted line).

Within each layer we obtain

$$\begin{aligned} U(x) = \frac{\hbar}{\Delta_a} \Big| & \Omega_p \cos(2\beta) \\ & + \Omega_c \Big[(\cos\theta + \sin\theta)\cos(\beta/2)\cos(\sqrt{3}\pi x) \\ & + (\cos\theta - \sin\theta)\sin(\beta/2)\sin(\sqrt{3}\pi x) \Big] \Big|^2 , \end{aligned} \tag{7.17}$$

where $\Omega_1 = \Omega_c \cos\theta$ and $\Omega_2 = \Omega_c \sin\theta$. The angle θ is determined by $\tan(\theta) = \alpha_1/\alpha_2$ and corresponds to the outcome of the symmetry breaking in terms of the photon fields.

Let us consider two special cases of this expression. If the position of the transverse pump standing wave is $\beta = \pi/2$, the expression simplifies to

$$U(x) = \frac{\hbar}{\Delta_a} \left| -\Omega_p + \Omega_c \cos(\theta + \sqrt{3}\pi x - \pi/4) \right|^2 . \tag{7.18}$$

Connection between position and cavity fields

The position of this potential depends on θ and its minima are displaced by $2/\sqrt{3}\lambda$, which is the lattice constant. The lattice depth does not change with θ. For $\beta = 3\pi/2$ the sign in front of Ω_c changes and accordingly the

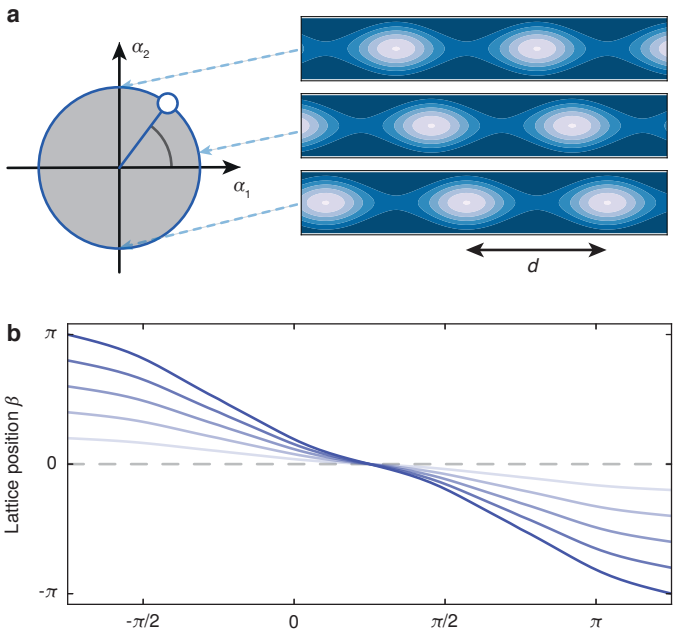

Figure 7.7: *Lattice position in the U(1) symmetry.* **a,** The continuous symmetry of the cavity light fields has a direct connection to the position of the density modulation. The contour plots show the interference potential for different field combinations (α_1, α_2). Each phase of the order parameter describes a different point in real space. **b,** The position of the lattice minima is monotonous in the order parameter phase θ with an approximately linear dependence. Different solid lines show transverse pump lattice positions of $\beta = \pi/2$, $\beta = 0.8 \times \pi/2$, $\beta = 0.6 \times \pi/2$, $\beta = 0.4 \times \pi/2$ and $\beta = 0.2 \times \pi/2$. The range of accessible lattice positions decreases, but the number of ground states remains infinite, except for $\beta = 0$ (dashed line).

minima are displaced in the opposite direction. The potential for different order parameter phases θ is illustrated in Fig. 7.6. Two neighbouring layers in the center are highlighted, which indeed move in opposite directions, so that the translation is staggered.

The situation changes for $\beta = 0$, for which Eq. 7.17 reduces to:

$$U(\mathbf{x}) = \frac{\hbar}{\Delta_a} \left| -\Omega_p + \Omega_c \left(\cos\theta + \sin\theta\right) \cos(\beta/2) \cos(\sqrt{3}\pi x) \right| . \tag{7.19}$$

The potential depth changes with θ, wheras the position remains constant since $\cos(\sqrt{3}\pi x)$ is independent of θ. We can evaluate the minima position for different values of β and finite range of lattice positions over which the continuous symmetry extends for $\beta \neq 0$, as shown in Fig. 7.7. The range increases with β, reaching the lattice constant $2/\sqrt{3}\lambda$ at $\beta = \pi/2$, and then decreases again until $\beta = \pi$. We choose $\beta \approx \pi/2$ in our experiments such that in the broken $U(1)$ symmetry each realization of cavity fields corresponds to a different translation.

7.2.2 *Transverse pump lattice*

Possible lattice geometries

The fact that the range of accessible lattice positions depends on the transverse pump phase ϕ is a consequence of the geometry of the resulting interference pattern. The lattice geometry for different phases β at balanced field strengths is shown in Fig. 7.8.

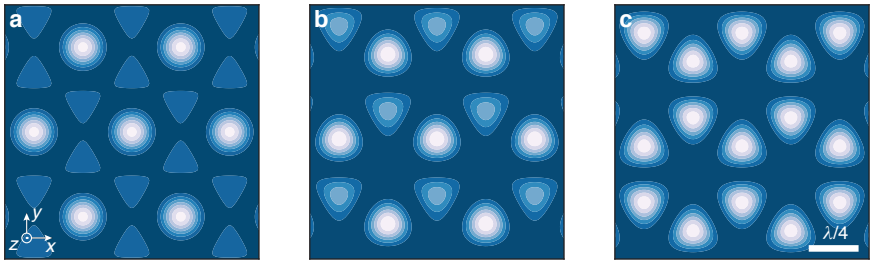

Figure 7.8: *Accessible lattice geometries for balanced field amplitudes.* The geometry of the attractive lattice potential from the interference of the standing waves of the transverse pump and the cavities depends on their relative positions. The color plots show the lattice potential for different phase displacement of β. **a,** For $\beta = 0$, the lattice potential shows a triangular geometry. Between the lattice sites, a shallow honeycomb pattern is visible. **b,** Two sites of the honeycomb structure merge into one with increased depth for $0 < \beta < \pi/2$, resulting in a staggered honeycomb lattice. **c,** At $\beta = \pi/2$, the interference pattern has a symmetric honeycomb geometry. The process is reversed for $\beta > \pi/2$ until the initial lattice is recovered at $\beta = \pi$.

- For $\beta = \pi/2$, the lattice geometry is regular hexagonal and the unit cell hosts two minima at equal energy. This configuration was discussed in the previous section, and we have seen that neigbouring layers move in opposite direction when the ratio of the cavity fields is changed. The regular hexagon is only obtained for balanced amplitudes of all three light fields.
- A triangular lattice geometry appears when choosing the phase $\beta = 0$. The triangular symmetry is symmetric for all beam ratios, while the potential wells between the lattice sites have only equal hight for balanced field amplitudes. Additionally, a second layer appears at half the lattice constant whenever one field amplitude is superior to the others.
- For $0 < \beta < \pi/2$, the geometry is a staggered hexagonal lattice. We can see how between the lattice sites a second layer appears that is congruent with the hexagonal pattern, yet does not have the same potential depth.

We have access to all three lattice geometries by adjusting the spatial phase β of the transverse pump standing wave with a piezoelectric actuator at the retroreflecting mirror. The interference potentials as a function of β have also been studied for our cavity geometry [292].

7.3 REALIZATION OF A SUPERSOLID

We now turn to the experimental studies on the continuous symmetry breaking. The situation of symmetrically coupled cavities is presented, including a verification of the ground-state degeneracy for the continuous symmetry. Additionally, the independent control over both couplings allows us to introduce an asymmetry and to study the crossover region to a discrete symmetry.

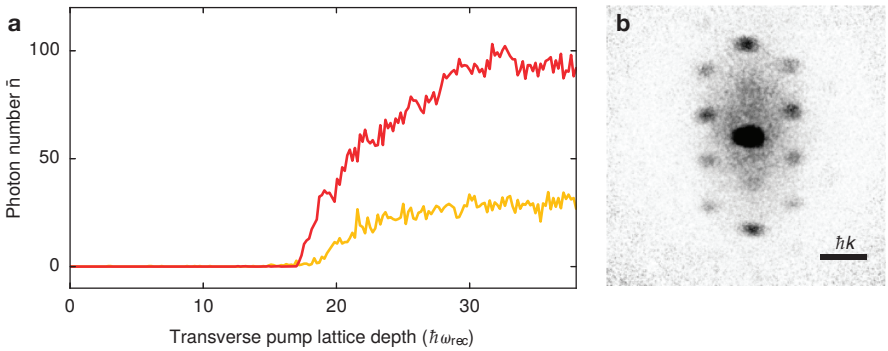

Figure 7.9: *Observation of a supersolid.* **a,** Traces of the mean photon numbers in cavity 1 (red) and 2 (yellow) as a function of transverse pump lattice depth for a ramp time of 100 ms at constant $\Delta_1 = -2.1$ MHz and $\Delta_2 = -2.0$ MHz. The ramp corresponds to a single scan diagonal in the phase diagram of Fig. 6.9. The traces are binned in intervalls of 0.5 ms. **b,** Absorption image of the atomic momentum distribution, recorded along the z–axis after 25 ms ballistic expansion. Black areas show high atomic densities. The eight atomic momentum modes associated to the scattering of photons from the pump to the cavities are visible.

7.3.1 Symmetric coupling to both cavities

We can investigate the situation, where the coupling to both cavities is symmetric by adequately adjusting the pump-cavity detunings Δ_1 and Δ_2 at constant coupling λ set by the pump power. The decay rates of the two cavities are not the same, resulting in $\Delta_1 \approx \Delta_2$ without being strictly equal (cf. Sec. 5.3.1).

We set the detunings to constant values $\Delta_1/2\pi = -2.1$ MHz and $\Delta_2/2\pi = -2.0$ MHz and increase the transverse pump power in a linear ramp up to $38(1)\,\hbar\omega_{\mathrm{rec}}$. This corresponds to a diagonal ramp in the phase diagram for competing order with two cavities (cf. Fig. 6.9). The result is shown in Fig. 7.9. Past the critical point at a lattice depth of around $17\,\hbar\omega_{\mathrm{rec}}$ we observe finite intracavity photon numbers in both cavities, providing evidence for a new type of self-organized phase. This is in contrast to the results in Fig. 6.8, where the two self-organized phases exclude each other. The presence of a doubly-organized phase is the result of fine-tuned coupling strengths to reach the symmetry-enhanced line in the phase diagram.

Observing the supersolid phase transition

We record the atomic momentum distribution by performing absorption imaging of the cloud after ballistic expansion. Interference maxima at momenta associated with scattering processes for both cavities are visible. They correspond to the momentum modes displayed in Fig. 7.4, apart from two momenta at $\pm 2\hbar k$, which stem from the standing wave potential of the transverse pump lattice.

We use the connection between crystal position and intracavity fields to characterize the ground state symmetry of the supersolid phase. To this end, we repeat the measurement shown in Fig. 7.9a many times and extract the mean intracavity photon numbers averaged over 5 ms at the end of the ramp. The square root of the photon numbers, that is the absolute value of the cavity fields, are shown in Fig. 7.10. Their distribution falls on a quarter circle, revealing a high ground state degeneracy of the system. Whilst the U(1) symmetry includes the sign of the cavity field amplitudes, our photon detection only allows to measure their magnitude. Therefore the full circular symmetry is folded to the positive quadrant. As the combination of the

Characterization of the ground-state degeneracy

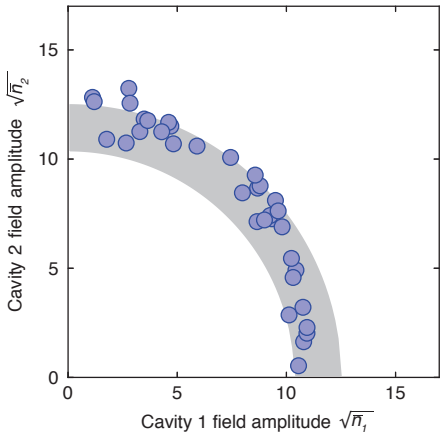

Figure 7.10: *Breaking continuous translational symmetry.* Field amplitudes for 35 different experimental realizations of the ramp in Fig. 7.9a, deduced from the intracavity photon numbers averaged over 5 ms at the end of the ramp. The data reveal the continuous translational symmetry which is broken in the supersolid. The grey shaded area contains the systematic uncertainty from the calibration of the intracavity photon numbers.

intracavity field amplitudes determines the position of the atomic density modulation along the x–axis, we conclude that in each realization the superfluid crystallizes to a different position. This provides evidence for the broken continuous translational symmetry of the supersolid.

7.3.2 Transition to a lattice supersolid

The transition between the supersolid and a lattice supersolid amounts to introducing an asymmetric coupling to both cavities (cf. 6.2.2). We study this transition by starting in the SO2 phase, hence realizing a lattice supersolid associated with cavity 2, and then approaching the situation of symmetric couplings. The measurement is shown in Fig. 7.11. We initialize the system at a pump lattice depth of $38(1)\,\hbar\omega_{\mathrm{rec}}$ and detunings $\Delta_1/2\pi = -2.8\,\mathrm{MHz}$ and $\Delta_2/2\pi = -2.2\,\mathrm{MHz}$. Here, the coupling to cavity 2 dominates and is strong enough for self-organization. We then approach the symmetric situation by slowly ramping Δ_1 until the phase boundary is reached. There we keep the detunings fixed and monitor the evolution of both cavity light fields.

Anticorrelated photon numbers

We observe finite mean intracavity photon numbers in both cavities over the entire duration of the measurement at symmetric coupling. During the measurement the light fields evolve and show anticorrelations in the cavity light fields predominantly on the ms time scale. We quantify this evolution by calculating the Pearson correlation coefficient for fourteen realizations of the same experiment to $-0.82(9)$, providing evidence for anticorrelated behaviour. The mean photon number in cavity 2 immediately turns to zero when further reducing Δ_1, while the mean photon number in cavity 1 increases further, because the smaller detuning increases the coupling strength.

Effective potential

We interpret the phase transition between the lattice supersolid and the supersolid in terms of the mean-field energy as a function of the cavity field amplitudes α_1 and α_2, as illustrated in Fig. 7.11c. We start in region (I) with cavity 2 slightly stronger coupled than cavity 1. Due to the asymmet-

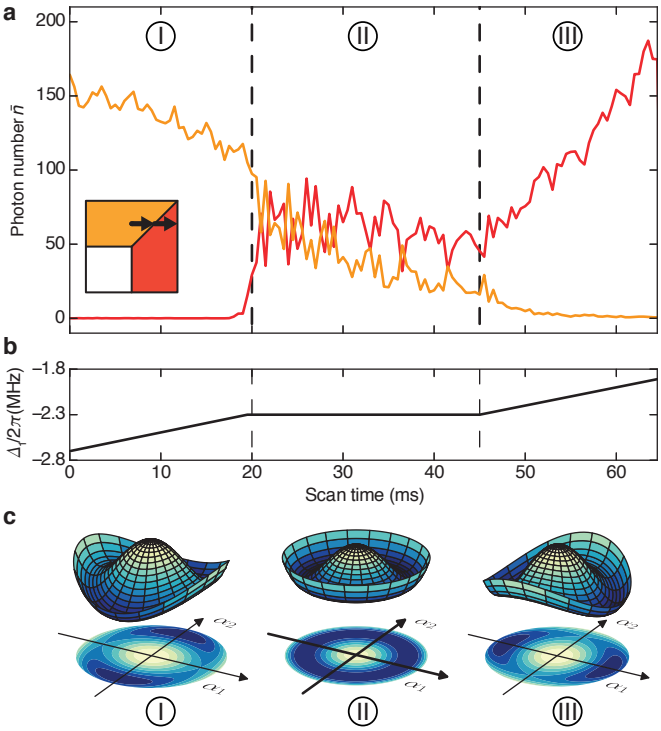

Figure 7.11: *Emergence of a doubly self-organized phase.* **a,** Mean intracavity photon numbers (binned in intervalls of 0.5 ms) for the frequency ramp shown in **(b)** for cavity 1 (red) and 2 (yellow) at constant transverse pump lattice depth $38(1)\,\hbar\omega_{\mathrm{rec}}$. The simultaneous presence of photons in both cavities signals the transition to a doubly self-organized phase. **b,** Detuning ramp through the phase diagram. At constant $\Delta_2/2\pi = -2.2\,\mathrm{MHz}$, Δ_1 is ramped from far-detuned to reaching the phase boundary, held there for 25 ms and subsequently ramped closer to resonance. **c,** The mean-field energy as a function of cavity field amplitudes α_1 and α_2 is qualitatively displayed for three different regions in the phase diagram: inside the self-organized phase to cavity 2 (I) and 1 (III), and on the phase boundary in between (II).

ric coupling the continuous symmetry is only approximate and the ground state manifold exhibits two minima on the α_2 axis at equal distance from the origin. In terms of the phase diagram explored in Chapter 6, this corresponds to the SO2 phase with self-organization only to cavity 2 with a broken $\mathbb{Z}_2$ symmetry. These minima are rotated to the α_1 axis when the coupling to cavity 1 is dominant (region III). This situation corresponds to the SO1 phase with self-organizaion to cavity 1 only. Despite the jump in the order parameter, the boundary presents a continuous phase transition, since no latent heat is involved, see Chap. 6.

Only at the point in between, the ground state manifold extends to a circle that connects both axes (region II), thereby realizing a U(1) symmetry. A low-energy evolution on the ground state manifold results in the observed anticorrelated signals in the mean intracavity photon numbers $\overline{n}_i = |\alpha_i|^2$, corresponding to a spatial displacement of the density modulation along the x–axis.

7.3.3 *Crossover of discrete and continuous symmetries*

The transverse width of the supersolid, that is, the precision of Δ_1 and Δ_2 over which the supersolid phase extends, can be characterized by the region

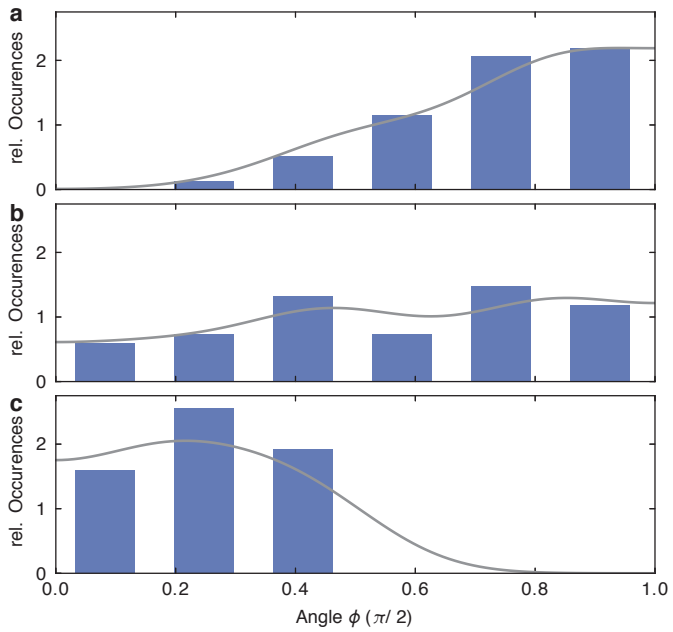

Figure 7.12: *Transition between discrete and continuous symmetries.* Histograms (normalized to unity area) of the angles θ describing the position of the crystal lattice, measured in the same way as the data in Fig. 7.10, but at $\Delta_1/2\pi = -2.1\,\mathrm{MHz}$ **(a)**, $\Delta_1/2\pi = -2.2\,\mathrm{MHz}$ **(b)** and $\Delta_1/2\pi = -2.3\,\mathrm{MHz}$ **(c)**. The grey lines show kernel density estimation analyses with a Gaussian kernel whose bandwidth of $0.13 \times \pi/2$ was determined from a cross-validation maximum likelihood reconstruction. The histograms consist of 19-49 realizations each.

where both cavities are populated. Although the supersolid phase theoretically extends only over a line in the phase diagram, we experimentally observe a finite width of around 100 kHz where light fields appear in both cavities if we keep the couplings and detunings constant for several ms. We attribute this to two reasons. First, our experimental preparation of a point in the phase diagram has a finite resolution due to the stability of the transverse pump frequency and the cavity resonance frequency of around $30 - 50\,\mathrm{kHz}$ each. Second, the chemical potential of the cloud limits the resolution with which we can probe the ground state of the system. Close to the U(1)-symmetric line, the two minima of the parity symmetry are only very weakly pronounced. As the chemical potential increases compared to the depth of the minima, the ground-state manifold approaches a U(1) symmetry.

Angular distribution for asymmetric coupling

We can further quantify the extension of the supersolid phase by studying the homogeneity of the U(1) symmetry. We repeat the measurement shown in Fig. 7.10 for different pairs of (Δ_1, Δ_2) that correspond to deviations from the situation of symmetric coupling. The extracted angular distribution of the symmetry breaking is shown in Fig. 7.12 for three different points across the supersolid phase. Despite of the limited sample sizes, a qualitative difference between the histograms is visible. While the data taken in the center of the supersolid phase show an almost homogeneous distribution, a clear trend towards the effectively more strongly coupled cavity is visible for a positive or negative change in the detuning Δ_1.

The centre of the distribution changes with the detuning and follows the more strongly coupled cavity. This is in accordance with the picture of a rotated minimum in the effective potential from the axis of one cavity to

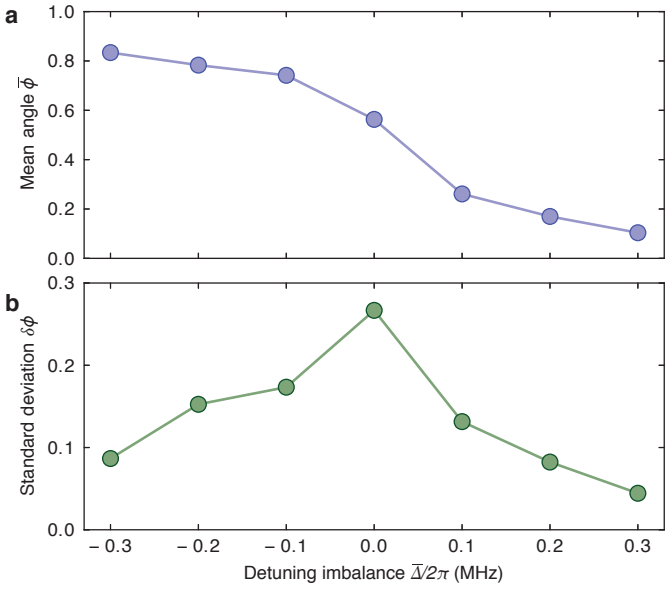

Figure 7.13: *Statistical analysis of the angular distribution.* **a,** We record histograms of the position distribution similar to the ones shown in Fig. 7.12 for more detunings $\Delta_1/2\pi$ around the symmetrically coupled point of $\Delta_1/2\pi = -2.1\,\mathrm{MHz}$ and extract the mean angle $\bar{\theta}$. Across the supersolid phase, the expectation value changes from close to $\pi/2$ (cavity 2 axis in the effective potential) to 0 (cavity 1 axis). **b,** The corresponding standard deviation $\delta\theta$ shows maximal scattering at the symmetric coupling and decreases rapidly with increasing distance.

the other, as illustrated in Fig. 7.11. We can extract this rotation from the histograms by computing the mean value $\bar{\theta}$ of the angular distribution. The result is shown in Fig. 7.13. The mean angle is close to $\pi/2$ for negative asymmetries in the couplings, i.e. a more strongly coupled cavity 2, and close to zero for positive asymmetries. The majority of the rotation takes place in the window between $-0.1\,\mathrm{MHz}$ and $0.1\,\mathrm{MHz}$. This is also visible from the standard deviation of the histograms, which shows a maximum at symmetric coupling. The displayed mean angles and standard deviations are lower bounds, since the lacking sign of the detected cavity field inhibits a full reconstruction of the circular distribution.

Part III

EXCITATIONS AND FLUCTUATIONS

8

ROTON MODE SOFTENING IN A RECTANGULAR LATTICE

In this chapter we present studies on the collective excitations across the self-organization phase transition for a BEC coupled to an optical cavity. The coupling is obtained with a transverse pump beam at 60° with respect to the cavity axis, which results in a rectangular geometry of the self-ordered lattice. We start with a theoretical description of the underlying excitation spectrum and then present different detection methods that give a complementary view on their nature.

CHAPTER CONTENTS

Structural phase transitions of many-body systems are driven by a displacement of the constituents. The structural character of the phase transition is inherited by the underlying collective excitations across the critical point, therefore the modes driving the phase transition are identical with the phonon modes that describe the lattice dynamics [293]. This is a remarkable insight, as it connects the high-energetic motion at phonon frequencies with the low-energetic critical behaviour at phase transitions.

Mode-softening at a phase transition

The consequence is a *mode softening*, where the frequency of the phonon mode decreases as the critical point is approached until reaching zero at the phase transition. At this point, the phonon is frozen, i.e. it is no longer dynamical. Conceptually, it has transformed into a static displacement pattern, which gives rise to the phase transition. In momentum space, the dispersion relation close to the phase transition shows a characteristic roton-maxon spectrum [294], see Fig. 8.1. It shows a parabolic dispersion relation in the long-wavelength regime, where the phonons remain non-interacting. Close to the wave vector of the reciprocal lattice associated to the structural transition, the phonon frequency decreases and the dispersion relation shows roton minimum. The term roton stems from Landau, whose initial interpretation to attribute the effect with a localized quantized vortex is still inconclusive [295–298].

After first indications for a mode softening in quartz crystals [300], the subject attracted attention when it was observed for superfluid helium [295, 299]. The roton minimum occurs at momenta corresponding to a wavelength of 3 Å, close to the interparticle distance of 3.7 Å. This points towards an

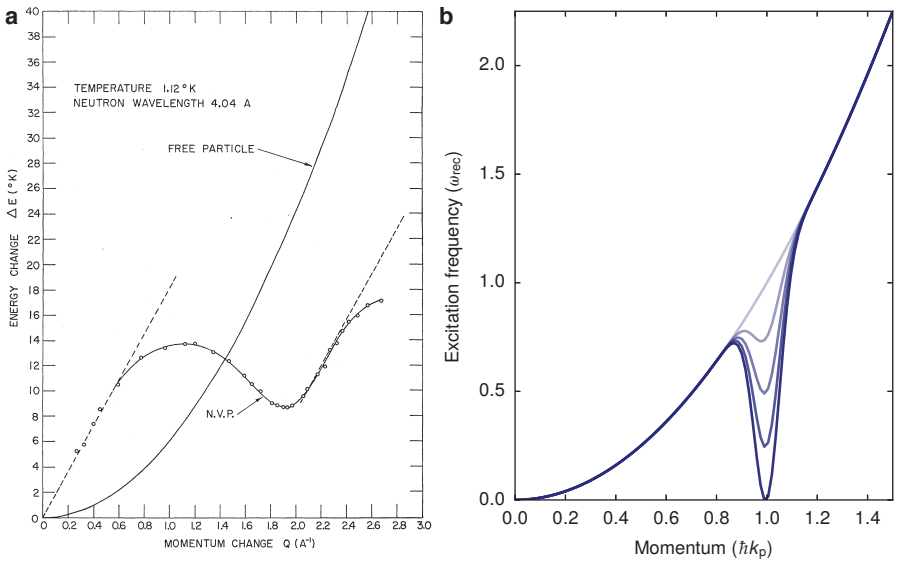

Figure 8.1: *Momentum dispersion of the soft mode frequency.* **a,** Dispersion relation in liquid helium. For small momenta, the phonon dispersion relation shows the parabolic shape of noninteracting particles. Close to the lattice vector $\mathbf{k}_L$, the phonon frequency decreases again, giving rise to the characteristic roton minimum. Adapted from [299]. **b,** Dispersion relation for a BEC coupled to an optical cavity. For increasing color depth, the solid lines show the roton minimum in the absence of cavity coupling and for $0.5\,\lambda_{cr}$, $0.7\,\lambda_{cr}$, $0.9\,\lambda_{cr}$ and $1\,\lambda_{cr}$. The width of the minimum is determined by the resolution in momentum space due to the finite system size.

origin at the density correlations of the liquid, which are induced by van-der-Waals interactions among adjacent atoms in the liquid. When the first dipolar BECs were created, the presence of a roton minimum was predicted in analogy to helium [57, 74, 294, 301–303], but experimental evidence has proven challenging. A different approach are spin-orbit coupled BECs [304–307], where band-structure engineering can create an analogous minimum [308–310].

Roton mode in a cavity

A roton mode softening also occurs when a BEC is dispersively coupled to an optical cavity with a transverse pump field. The associated structural phase transition breaks a spatial $\mathbb{Z}_2$ symmetry (cf. Chap. 5). For the case of a chequerboard lattice structure, the mode-softening has been studied theoretically [311] and experimentally [312–314]. Here we consider the situation of coupling with a non-orthogonal pump field, which gives rise to a structural phase transition with rectangular lattice geometry.

Parts of this chapter are based on the publication:

> J. Léonard, A. Morales, P. Zupancic, T. Donner and T. Esslinger:
> *Monitoring and manipulating Higgs and Goldstone modes in a supersolid quantum gas*
> *Science* **358**, 1415-1418 (2017)

8.1 EXCITATIONS AT A CONTINUOUS PHASE TRANSITION

In this section we give a conceptual introduction to the mode softening at a continuous phase transition. In mean-field approximation, the excitation energy can be derived from the effective potential. We then turn to the specific scenario of self-organization in a cavity. The associated phase transition

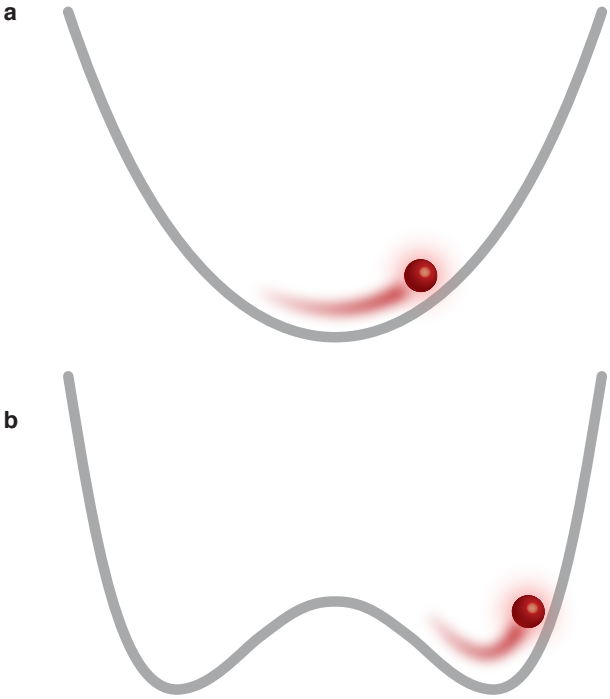

Figure 8.2: *Mode-softening and effective potential.* **a,** In the normal phase, the elementary excitations correspond to oscillations of the order parameter around zero. The parabolic contribution vanishes when approaching the phase transition and the oscillation frequency softens. **b,** Within the ordered phase, the order parameter becomes more and more localized at a nonzero value. The elementary excitations are now described by an oscillation around a finite order parameter. The curvature of the effective potential, and hence the excitation energy, rises with increasing distance from the critical point.

from a superfluid to a self-ordered state constitutes a structural phase transition, where a special type of mode-softening occurs: the *roton minimum*. Finally, the roton dispersion relation is derived from a microscopic description of the involved two-photon scattering processes, confirming the results from the effective potential.

8.1.1 *Effective potential*

Mean-field expansion

A mode softening is a necessary but not sufficient condition for a continuous phase transition. We can understand the mode softening in terms of the Landau expansion (see Eq. 5.1):

$$\mathcal{H}_\lambda(\Theta) = \frac{r}{2}\Theta^2 + \frac{g}{4}\Theta^4 + \mathcal{O}(\Theta^6), \tag{8.1}$$

where Θ is an order parameter with $\mathbb{Z}_2$ symmetry and r and g depend on the coupling strength λ. The curvature of the effective potential with respect to the order parameter gives access to the lowest excitation frequency [293]:

$$\omega^2 \propto \left.\frac{\partial^2\mathcal{H}}{\partial\Theta^2}\right|_{\Theta=\Theta_0} = \begin{cases} r, & \text{if } \lambda < \lambda_{cr} \\ -2r, & \text{if } \lambda > \lambda_{cr} \end{cases}. \tag{8.2}$$

Here Θ_0 is the potential minimum for the order parameter in equilibrium, which is $\Theta_0 = 0$ for $\lambda < \lambda_{cr}$ in the normal phase and $\lambda > \lambda_{cr}$ for constant $\lambda >$

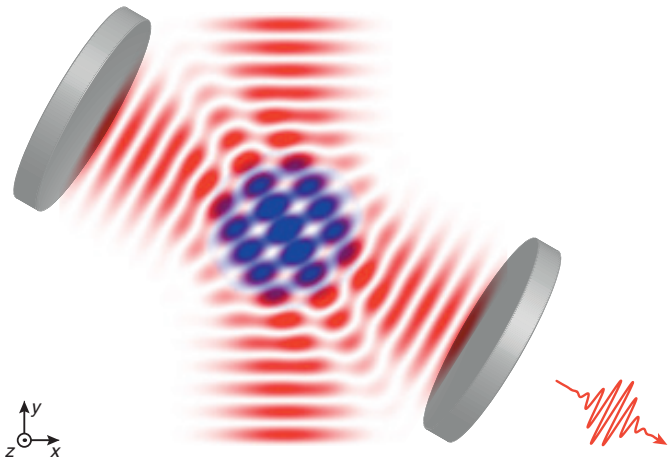

Figure 8.3: *Illustration of the experiment.* A BEC (blue stripes) cut into slices by a transverse pump lattice potential (red stripes) enters a supersolid state and breaks translational symmetry along x by symmetrically coupling it to two optical cavity modes α_1 (red) and α_2 (yellow) with a transverse pump lattice along y. The emerging Higgs and Goldstone excitations correspond to fluctuations of the strength and position of the density modulation, as shown in the zoom-in for one slice. They can be excited and read out with probe pulses on each cavity.

λ_{cr}. The proportionality factor is generally determined by the time evolution of the Hamiltonian and can be deduced from the condition

$$\omega(\lambda = 0) = \omega_0, \tag{8.3}$$

Curvature of the effective potential

assuming that the time evolution is independent of λ over the considered range. The curvature at the minimum of the effective potential is illustrated in Fig. 8.2. In the normal phase, the elementary excitations correspond to an oscillation of the order parameter around zero. Upon approaching the phase transition, r vanishes and the excitation frequency accordingly tends to zero, before rising again in the ordered phase as an oscillation around a nonzero order parameter.

In order to connect the coefficient r with the coupling strength λ, we use the condition that r vanishes at the critical point and employ the Landau ansatz $r \propto (\lambda^2 - \lambda_{cr}^2)$. The linear relation presents the first term of an expansion of r in odd powers around the critical point. The quadratic scaling of the coupling strength is chosen without loss of generality to be in line with the definition applied in Chapters 5-7. Combining Eqs. 8.2 and 8.3, we find the dispersion relation for the soft mode in the normal phase

Elementary excitations across the critical point

$$\omega(\lambda) = \omega_- \sqrt{1 - \frac{\lambda^2}{\lambda_{cr}^2}}. \tag{8.4}$$

Within the ordered phase, we obtain a similar relationship:

$$\omega(\lambda) = \sqrt{2}\omega_- \sqrt{\frac{\lambda^2}{\lambda_{cr}^2} - 1} \tag{8.5}$$

The factor of $\sqrt{2}$ between the frequency in the normal and the ordered phase presents a characteristic scaling relation around the phase transition with general relevance for amplitude excitations [315].

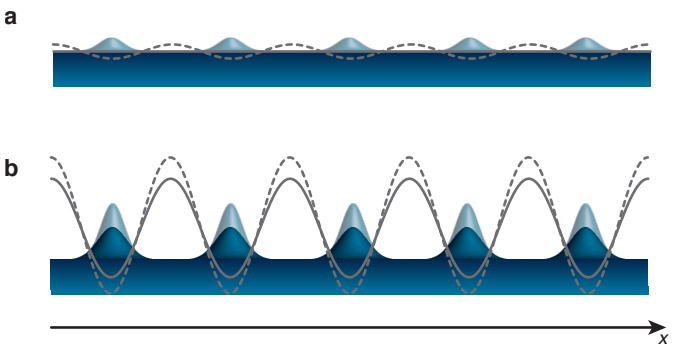

Figure 8.4: *Spatial character of the roton mode.* Shown are the steady state density distribution (blue) and the light-induced interaction potential (solid lines), together with the fluctuations of the density (shaded blue) and the potential (dashed lines) at the maximum displacement of the oscillation. **a,** Below the critical point, the elementary excitations are roton excitations, which describe fluctuations of a homogeneous density distribution at a specific wavelength. The position of the nodes and the antinodes of the oscillation is determined by the cavity mode. **b,** Above the critical point, the excitations correspond to fluctuations of the strength of the density modulation around a finite steady state value. Depending on when the structural phase transition was crossed, the roton was "frozen" either at the maxima or the minima of the roton oscillation, corresponding to a broken $\mathbb{Z}_2$ symmetry.

8.1.2 Roton mode softening and self-organization

Roton mode and cavities

Let us turn to the system under consideration, namely self-organization with a single cavity mode, as illustrated in Fig. 8.3. A BEC is coupled to the cavity mode by a 1D attractive optical lattice, the transverse pump. Its frequency is far red-detuned from the atomic resonance, but closely red-detuned from the cavity mode. At a critical coupling strength, which is set by the transverse pump power and the pump-cavity detuning, the superfluid BEC develops a density modulation. Its periodicity is determined by the transverse pump frequency and its position (see Chap. 5).

Roton mode as oscillating density modulation

The atom-cavity coupling alters the dispersion relation of the free particles at momenta corresponding to a two-photon process. Upon approaching the critical point, the excitation energy decreases and a roton minimum in the dispersion relation develops. The roton mode corresponds to a periodic oscillation of the homogeneous density around its expectation value, see Fig. 8.4a. Its periodicity is given by the inverse of the roton minimum momentum. Two properties of the cavity-induced roton mode are different from roton modes in most condensed matter systems:

- Discrete position: Since the cavity mode has a standing wave shape, the density oscillation can only be induced at the position of an antinode in the cavity field. The roton oscillation includes two antinodes per period, thus the position of the oscillation extrema is pinned to the cavity mode and neighboring antinodes are oscillating out of phase.
- Global coupling: All atoms couple identically to the cavity mode, therefore the roton mode also oscillates with the same amplitude and phase at any point in space. This inhibites the roton mode from having its own dispersion relation and only allows for a global oscillation without a finite wavelength.

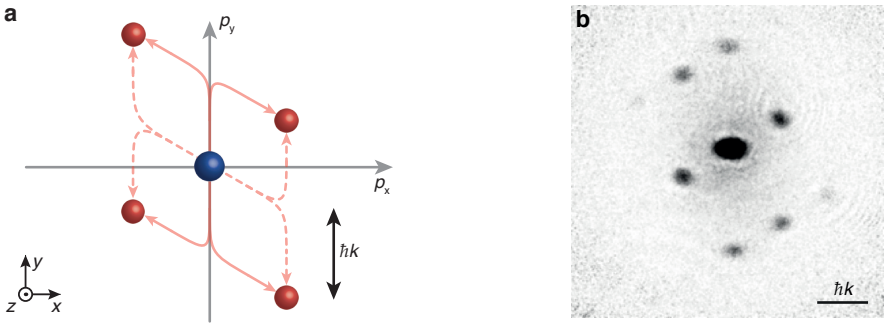

Figure 8.5: *Setup and mode expansion.* **a,** Schematic view of the setup. A BEC is loaded into a transverse lattice potential along y, which cuts the cloud into slices in the x-z plane. The transverse pump lattice also acts as a reservoir for photon scattering among the atoms. **b,** The momentum modes from two-photon scattering processes. The two excitation paths shown as solid and dashed lines correspond to the creation and annihilation of a cavity photon, respectively.

When the excitation energy approaches zero, the homogeneous density distribution becomes unstable and a roton instability occurs, a precursor of a structural phase transition. The roton mode 'freezes' with the density maxima either on the even or on the odd antinodes of the cavity mode. This sets corresponds to a $\mathbb{Z}_2$ symmetry breaking of the translational invariance. Past the critical point, the elementary excitations describe an oscillation around the steady-state value of the periodic density distribution, see Fig. 8.4b.

8.1.3 *Momentum mode expansion*

Microscopic origin of the roton mode softening

On a microscopic level, the roton mode softening stems from a coupling between the momentum ground state at $|\mathbf{k}\rangle = |0\rangle$ and a superposition state of the higher momenta $|\mathbf{k}\rangle = |\pm\mathbf{k}_p \pm \mathbf{k}_i\rangle$, where $\mathbf{k}_p$ and $\mathbf{k}_i$ denote the wavevectors of the transverse pump and cavity i, respectively. The coupling is achieved by Raman scattering processes between the pump and the cavity fields. The excited momentum states define a reciprocal lattice, and increasing the coupling leads to a softening of the dispersion relation at these momenta. The states fall into two groups with energy either $\hbar\omega_- = \hbar\omega_{rec}$ or $\hbar\omega_+ = 3\hbar\omega_{rec}$ (Fig. 8.5).

In the following we derive the soft mode frequency across the self-organization phase transition. We start with the microscopic Hamiltonian from Eq. 5.22, which was derived in Chap. 5:

$$\hat{\mathcal{H}} = -\hbar\tilde{\Delta}_c\hat{a}^\dagger\hat{a} + \hbar\omega_+\hat{c}_+^\dagger\hat{c}_+ + \hbar\omega_-\hat{c}_-^\dagger\hat{c}_- \tag{8.6}$$

$$+\hbar\frac{\lambda}{\sqrt{N}}(\hat{c}_+^\dagger\hat{c}_0 + \hat{c}_-^\dagger\hat{c}_0 + \text{h.c.}). \tag{8.7}$$

The first term describes the cavity field in the frame rotating with the transverse pump, where $\hat{a}^\dagger$ ($\hat{a}$) creates (annihilates) a photon with frequency $\tilde{\Delta}_c$. The excited momentum modes have kinetic energy $\hbar\omega_+$ and $\hbar\omega_-$ and are described by the creation (annihilation) operators $\hat{c}_+^\dagger$ ($\hat{c}_+$) and $\hat{c}_-^\dagger$ ($\hat{c}_-$), respectively. The last term captures the atom-light interaction with a coupling strength λ.

Whilst the exact eigenenergies of this Hamiltonian can only be computed numerically, we obtain an approximate analytical description by neglecting the coupling to the high-energy momentum state $\hbar\omega_+$, thereby recover-

Analytical connection to the effective potential

ing a Hamiltonian similar to self-organization for an orthogonal pump (cf. Sec. 5.1.4). This does not affect the symmetry properties of the Hamiltonian, nor does it modify the scaling relations. A comparison with the numerical results shows that the separation $\omega_+ = 3\omega_-$ for a pump-cavity angle of 60° is sufficient to yield differences below 10% in the energy spectrum. The position of the phase boundaries remains unaffected.

We use this reduced Hamiltonian in the limit $\omega_- \ll |\Delta_c|$ and adiabatically eliminate the light field with the condition $\partial\hat{a}/\partial t \approx$ to restrict the description to the atomic excitations:

$$\hat{\mathcal{H}} = \hbar\omega_-\hat{c}_-^\dagger\hat{c}_- + \hbar\frac{\lambda^2}{N\Delta_c}(\hat{c}_-^\dagger\hat{c}_0 + \hat{c}_0^\dagger\hat{c}_-)^2. \tag{8.8}$$

The corresponding effective potential follows from a mean-field approximation with:

$$\langle\hat{a}\rangle = \sqrt{N}\alpha \tag{8.9}$$

$$\langle\hat{c}_-\rangle = \sqrt{N}\psi_- \tag{8.10}$$

$$\langle\hat{c}_0\rangle = \sqrt{N - \sum_{i=1,2}\hat{c}_-^\dagger\hat{c}_-}, \tag{8.11}$$

and we obtain

$$\mathcal{H} = \hbar\omega_-\left[\psi_-^2\left(1 - \frac{\lambda^2}{\lambda_{cr}^2}\right) + \psi_-^4\frac{\lambda^2}{\lambda_{cr}^2}\right] \tag{8.12}$$

with the critical coupling $\lambda_{cr} = \sqrt{-\tilde{\Delta}_c\omega_-/4}$. The minima of the effective potential are determined from the condition $\partial\mathcal{H}/\partial\psi = 0$:

$$\psi_- = \begin{cases} 0, & \text{if } \lambda < \lambda_{cr} \\ \sqrt{\frac{1}{2}\left(1 - \frac{\lambda_{cr}^2}{\lambda^2}\right)}, & \text{if } \lambda > \lambda_{cr} \end{cases} \tag{8.13}$$

The eigenfrequency follows from the relation $\omega(\lambda) \propto \partial^2\mathcal{H}/\partial\psi^2\big|_\lambda$ and the condition $\omega(\lambda = 0) = \omega_-$ to:

$$\omega(\lambda) = \begin{cases} \omega_-\sqrt{1 - \frac{\lambda^2}{\lambda_{cr}^2}}, & \text{if } \lambda < \lambda_{cr} \\ \sqrt{2}\omega_-\sqrt{\frac{\lambda^2}{\lambda_{cr}^2} - 1}, & \text{if } \lambda > \lambda_{cr} \end{cases}. \tag{8.14}$$

Additionally, we obtain the excitation spectrum in a quantized description with a Bogoliubov transformation. All atoms occupy the zero momentum state within the normal phase and we can set $\langle\hat{c}_0\rangle = \sqrt{N}$ in Eq. 8.8. The creation and annihilation operators for the momentum excitations are replaced by the superposition:

$$\hat{b} = \mu\hat{c}_- + \nu\hat{c}_-^\dagger \tag{8.15}$$

$$\hat{b}^\dagger = \mu\hat{c}_-^\dagger + \nu\hat{c}_-. \tag{8.16}$$

We assume $\mu, \nu \in \mathbb{R}$, since the order parameter can only acquire real values. The Hamiltonian then takes the form $\hat{\mathcal{H}} = \hbar\omega(\lambda)\hat{b}^\dagger\hat{b}$ with the solution from Eq. 8.14. In the ordered phase, we have to expand the Hamiltonian around the expectation value [235]:

$$\begin{aligned} \hat{c}_- &= \sqrt{N}\psi_- + \delta\hat{c}_- \\ \hat{c}_0 &= \sqrt{N - \hat{c}_-^\dagger\hat{c}_-} \end{aligned} \tag{8.17}$$

and then perform the same Bogoliubov transformation to obtain the result from Eq. 8.14.

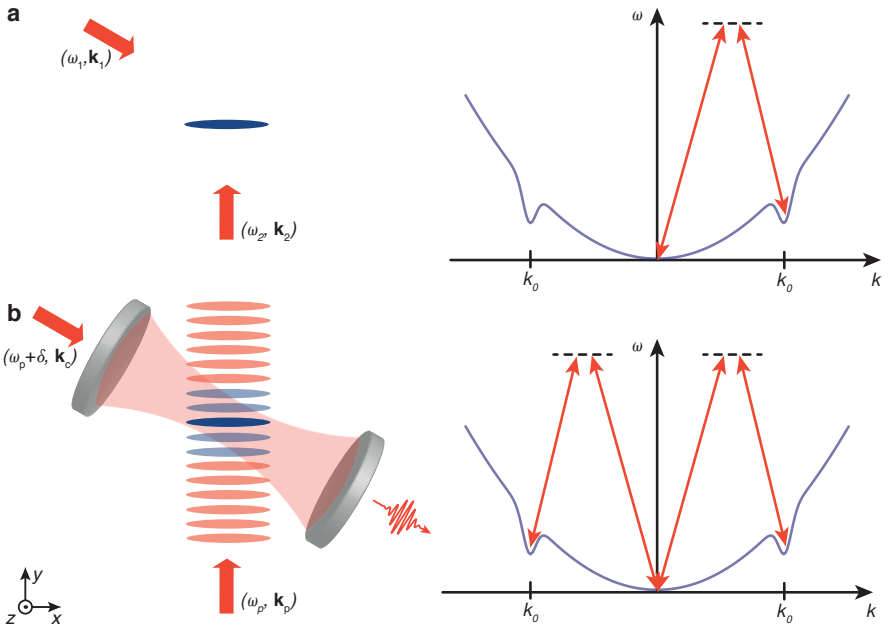

Figure 8.6: *Principle of Bragg spectroscopy.* **a,** In free space, an atomic cloud is exposed to two Bragg beams with frequencies ω_1, ω_2. and wave vectors $\mathbf{k}_1$, $\mathbf{k}_2$. A stimulated emission of a photon from the first into the second laser beam is resonantly enhanced if the energy difference $\hbar\omega_2 - \hbar\omega_1$ and the momentum difference $\hbar\mathbf{k}_2 - \hbar\mathbf{k}_1$ match the energy and the momentum of a quasi-particle. The dispersion relation is probed along the $\hbar\mathbf{k}_2 - \hbar\mathbf{k}_1$ direction. **b,** In a cavity, the two Bragg beams are replaced by two standing waves, the cavity mode and the transverse pump, probing the dispersion relation symmetrically around zero momentum $\pm(\hbar\mathbf{k}_2 - \hbar\mathbf{k}_1)$, as well as at $\pm(\hbar\mathbf{k}_2 + \hbar\mathbf{k}_1)$ (not shown).

8.2 CAVITY-ENHANCED BRAGG SPECTROSCOPY

A standard method to probe the dispersion relation of collective excitations is Bragg spectroscopy. In most condensed matter systems Bragg spectroscopy is performed inelastically with neutrons [316] or photons [317–320]. For ultracold atoms, Bragg spectroscopy is typically used as a coherent process, which enhances resolution and sensitivity [321, 322].

Principle of Bragg spectrocopy

The measurement principle is shown in Fig. 8.6a. The atomic cloud is exposed to two non-parallel laser beams with wave vectors $(\mathbf{k}_1, \mathbf{k}_2)$ and frequencies (ω_1, ω_2). A stimulated emission of a photon from the first into the second laser beam involves a recoil momentum of $\hbar\Delta\mathbf{k} = \hbar\mathbf{k}_2 - \hbar\mathbf{k}_1$. The process is usually suppressed if the laser beams are absent, since the recoil is mostly associated to a change in kinetic energy. The momentum state at $\hbar\Delta\mathbf{k}$ is resonantly excited only if the energy difference between the two photons $\hbar\omega_2 - \hbar\omega_1$ equals the energy of a quasi-particle. In a real-space picture, the two laser beams create a running wave at wavelength $2\pi/|\Delta\mathbf{k}|$ that oscillates in time with frequency $\Delta\omega$. This modulation can resonantly excite a phonon when the oscillation frequency matches the phonon frequency for this wavelength.

Bragg spectrocopy in a cavity

We apply this technique to a BEC that is coupled to an optical cavity with a transverse pump at constant intensity. A schematic of the principle is shown in Fig. 8.6. We send a probe field along the cavity axis with a frequency difference δ from the transverse pump at frequency ω_p. Compared

to standard Bragg spectroscopy with quantum gases, this method is characterized by two key differences:

- The transverse pump does not only induce the photon coupling, but also provides one of the two laser beams involved in the Bragg spectroscopy.
- Both Bragg beams, the transverse pump and the probe pulse on the cavity axis, are standing waves instead of running waves. This increases the number of probed momentum states to four, namely $\pm\hbar k_p \pm \hbar k_c$. For our system this is rather advantageous, since the phonon that drives the structural phase transition is a superposition of these very momentum states.

We use three different variants of cavity-enhanced Bragg spectroscopy, among which the former two have been developed previously [312]. The theoretical framework for the dynamical description during the Bragg pulse is an extension of the work in [312, 323].

8.2.1 Atomic dynamics

Driving Hamiltonian

We probe the cavity by applying a weak field with amplitude $\eta_{pr}(t)$ and frequency $\omega_{pr} = \omega_p + \delta$. This is described by the following driving Hamiltonian in the frame rotating with the pump frequency:

$$\hat{\mathcal{H}} = -\hbar\eta_{pr}(t)\left(\hat{a}e^{i(\delta t+\varphi)} + \hat{a}^\dagger e^{i(\delta t+\varphi)}\right) \tag{8.18}$$

Here φ is the relative phase between probe and pump beam. It depends on the optical path lengths of the probe beam and the transverse pump and can vary over several experimental realizations. The probe field gives rise to the intracavity field amplitude

$$\alpha_{pr}(t) = -\frac{\eta_{pr}(t)e^{-i(\delta t+\varphi)}}{\tilde{\Delta}_c + i\kappa} \tag{8.19}$$

The probe field can interfere with the transverse pump field and (in the self-organized phase) with the steady state intracavity field α_0. This results in a lattice potential that is modulated in time with frequency δ. The perturbation of the probe field on the atomic state is given by

$$\hat{\mathcal{H}}_{pr} = \hbar\xi(t)\delta\hat{\Theta}\cos(\delta t + \varphi) \tag{8.20}$$

The perturbation is proportional to the amplitude $\xi(t) = 2\eta_{pr}\sqrt{n_{pr}(t)}$, where $n_{pr} = \frac{\eta_{pr}^2(t)}{\tilde{\Delta}_c^2+\kappa^2}$ is the mean intracavity photon number. For simplicity, we neglect again the higher momentum state and write the Hamiltonian in terms of the atomic mode operators $\hat{c}_-$

$$\hat{\mathcal{H}}_{pr} = \hbar\xi(t)\sqrt{N}\left(\hat{c}_-^\dagger + \hat{c}_-\right)\cos(\delta t + \varphi) \tag{8.21}$$

Equation of motion for the atomic field

The equation of motion for the operator $\hat{c}_-$ under the presence of $\hat{\mathcal{H}}_{exc} + \hat{\mathcal{H}}_{pr}$ is:

$$i\hbar\frac{\partial\hat{c}_-}{\partial t} = E_1\hat{c}_- + 2NV\left(\hat{c}_- + \hat{c}_-^\dagger\right) + \hbar\xi(t)\sqrt{N}\cos(\delta t + \varphi) - i\hbar\gamma\hat{c}_- \tag{8.22}$$

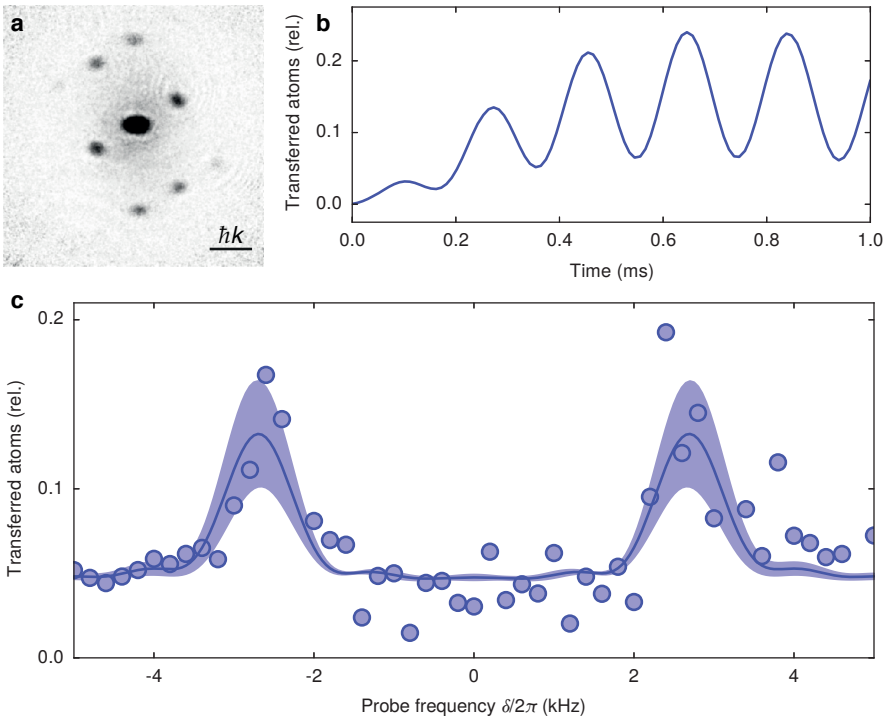

Figure 8.7: *Probing excitations with atoms* We prepare the quantum gas in the normal phase at $\Delta_1/2\pi = -2.0\,\mathrm{MHz}$ and at a transverse pump lattice depth of $12.8(3)\,\hbar\omega_{\mathrm{rec}}$. **a,,** Atom picture after pulse. **b,** Evolution of the atom number in the excited state during the probe pulse. **c,** We extract the population in the excited atomic state from pictures taken after 25 ms ballistic expansion of the atoms after releasing them from the trap. The pictures are taken together with the data in **(B)**. The solid line is a fit of Eq. 8.26 to the data, resulting in a resonance frequency of $2.7(7)\,\mathrm{kHz}$. The dashed lines show the deduced photon number from Bragg scattering off the created excitations. Shaded areas denote the standard deviation of the fit function from the average over the phase φ.

Here we have included a phenomenological damping term. The damping rate γ accounts for incoherent processes like s-wave scattering with other momentum modes, trap loss or finite-size dephasing. The solution to the Heisenberg equation is

$$\hat{c}_1(t) = 2\eta\sqrt{n n_{\mathrm{pr,o}}}\left(\frac{\omega_-}{\omega_s}\mathfrak{I}(y(t)) + i\mathfrak{R}(y(t))\right) \tag{8.23}$$

with the soft mode frequency ω_s. $y(t)$ is given by the integral:

$$y(t) = e^{(i\omega_s-\gamma)t}\int_0^t dt' e^{-(i\omega_s-\gamma)t'}\cos(\delta t' + \varphi) \tag{8.24}$$

Excited state population

The population of the excited momentum state is then

$$\langle \hat{c}_-^\dagger \hat{c}_- \rangle = 4\eta^2 n_{\mathrm{pr.o}} N\left[\left(\frac{\omega_-}{\omega_s}\right)^2 \mathfrak{I}(y(t)) + \mathfrak{R}(y(t))^2\right] \tag{8.25}$$

We can numerically evaluate this quantity and calculate the excited state population $\langle \hat{c}_-^\dagger \hat{c}_- \rangle$ during a probe pulse. The result is shown in Fig. 8.7. The population shows an oscillatory behaviour around a mean value that increases during the probe pulse. The phase of the oscillation is determined by φ.

Probing the atomic distribution

We can measure the atomic population in the excited state by ballistic expansion and absorption imaging after the probe pulse. This projects the atoms in the collective modes $\hat{c}_-$ and $\hat{c}_+$ onto free-particle states with one of the four momenta $\pm\mathbf{k}_p \pm \mathbf{k}_c$. We sum up the number of atoms in all four states after probe pulses for different detunings. We observe two resonances symmetrically positioned from zero detuning to the transverse pump. The resonance at $\delta > 0$ corresponds to the creation of a collective excitation by stimulated scattering of transverse pump photons into the cavity, and *vice versa* for $\delta < 0$. The resonance widths are Fourier limited by the duration of the probe pulse of 1 ms.

We can compare the expected population of the excited momentum states after the probe pulse with the theoretical prediction based on Eq. 8.25. The average population is expected largest for the resonance condition $\delta \approx \pm\omega_s$, but the oscillatory behaviour causes the atom number at the pulse end to vary with φ, causing intrinsic fluctuations of the population. We can incorporate this effect by calculating the phase average of Eq. 8.25:

$$\langle \hat{c}_-^\dagger \hat{c}_- \rangle_\varphi = \frac{1}{2\pi} \int_0^{2\pi} d\varphi \langle \hat{c}_-^\dagger \hat{c}_- \rangle \tag{8.26}$$

Fit function for the measured atomic spectrum

We use this expression to extract the resonance frequency from the data by performing a fit with free amplitude and resonance frequency. Additionally we allow for an overall offset that accounts for the detection background on the absorption imaging pictures. The phase average also allows to capture the intrinsic fluctuations with the standard deviation

$$\Delta\langle \hat{c}_-^\dagger \hat{c}_- \rangle_\varphi = \sqrt{\frac{1}{2\pi} \int_0^{2\pi} d\varphi \left(\langle \hat{c}_-^\dagger \hat{c}_- \rangle - \langle \hat{c}_-^\dagger \hat{c}_- \rangle_\varphi \right)^2} \tag{8.27}$$

which we use as weight for the fitting.

8.2.2 Cavity light field dynamics

The mean intracavity photon number during the probe pulse is [312]:

$$n_{ph}(t) = \left| \alpha_0 - \frac{4\eta^2 \sqrt{n_{pr}} N}{\Delta_i + i\kappa} \left(\frac{\omega_-}{\omega_s} \right) \mathcal{I}(y(t)) + \sqrt{n_{pr}(t)} e^{-i(\delta t + \varphi)} \right|^2 . \tag{8.28}$$

The expression contains the interference between the probe pulse, the scattered field and the steady-state light field, which is nonzero in the self-organized phase only. An exemplary curve is shown in Fig. 8.8a. The intracavity photon number oscillates with increasing amplitude over the entire duration of the pulse. We can observe this behaviour by determining the intracavity photon number during the probe pulse from detected photons that leak from the cavity. A typical trace is shown in Fig. 8.8b.

Fluctuating phase of the probe field

As for the atoms, the phase of the oscillation of the photon number is determined by φ and therefore fluctuates over different experimental realizations. The oscillation amplitude, and therefore the total photon number during the probe pulse, is expected to be maximal at the resonance condition $\delta \approx \pm\omega_s$ show much smaller fluctuations for pulse lengths longer than the period of the oscillation. We therefore use the mean intracavity photon number during the probe pulse as an observable for Bragg spectroscopy:

$$\langle n_{ph} \rangle = \frac{1}{\tau} \int_0^\tau dt n_{ph}(t) \tag{8.29}$$

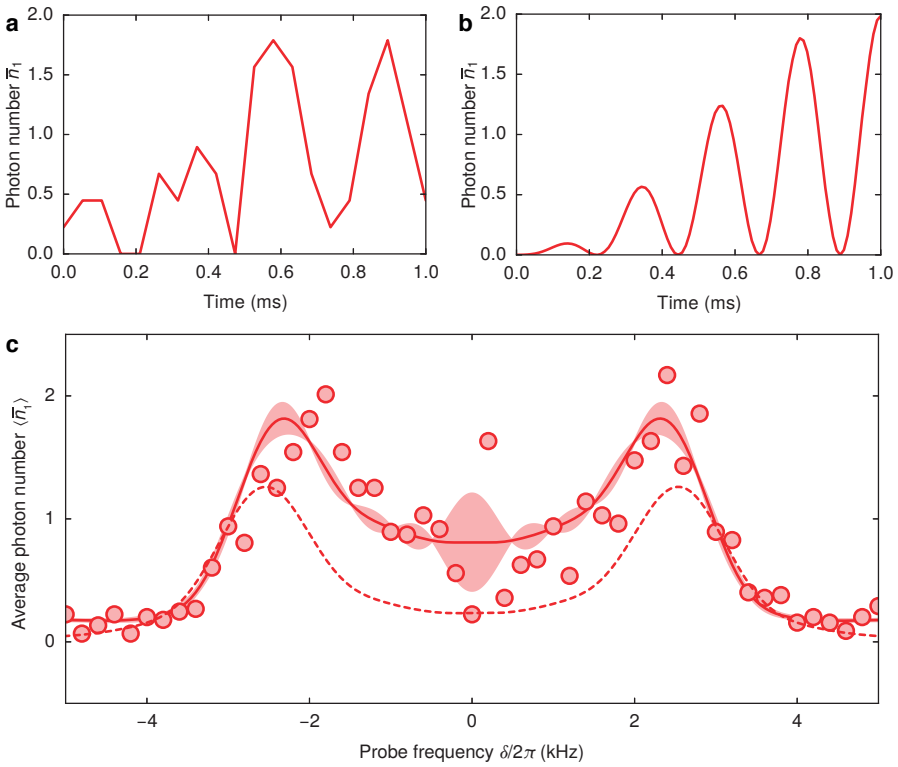

Figure 8.8: *Probing excitations with photons.* We prepare the quantum gas in the normal phase at $\Delta_c = -2.0\,\mathrm{MHz}$ and at a transverse pump lattice depth of $12.8(3)\,\hbar\omega_{\mathrm{rec}}$. **a,** Single photon trace at $\delta = 3\,\mathrm{kHz}$. An oscillation with the beat frequency is visible in the mean intracavity photon number. **b,** We can compare the recorded photon traces with the simulated time evolution during the pulse. **c,** Each data point corresponds to the mean photon number during a probe pulse of 1 ms length at constant detuning δ with mean photon number $\bar{n}_1 = 0.07(1)$ in cavity 1. The solid line shows the fit with Eq. 8.28, resulting in a resonance frequency of $2.92(5)\,\mathrm{kHz}$. The data were taken together with the pictures in Fig. 8.7. The dashed lines show the deduced photon number from Bragg scattering off the created excitations. Shaded areas denote the standard deviation of the fit function from the average over the phase φ.

with the probe pulse length τ. A measurement of $\langle n_{\mathrm{ph}} \rangle$ for different detunings δ is shown in Fig. 8.8c. Similarly to the atomic measurement, we observe two resonances symmetrically positioned from zero detuning to the transverse pump. The behaviour around $\delta = 0$ is different, however, since even a resonant probe pulse gives rise to a finite intracavity photon number.

Fit function for the photon spectrum

We fit the data with the phase-averaged photon number $\langle n_{\mathrm{ph}} \rangle_\varphi$, leaving amplitude and resonance frequency as free parameters, and use the standard deviation $\Delta\langle n_{\mathrm{ph}} \rangle_\varphi$ as weight:

$$\begin{aligned} \langle n_{\mathrm{ph}} \rangle_\varphi &= \frac{1}{2\pi} \int_0^{2\pi} \mathrm{d}\varphi \langle n_{\mathrm{ph}} \rangle, \\ \Delta\langle n_{\mathrm{ph}} \rangle_\varphi &= \sqrt{\frac{1}{2\pi} \int_0^{2\pi} \mathrm{d}\varphi (\langle n_{\mathrm{ph}} \rangle - \langle n_{\mathrm{ph}} \rangle_\varphi)^2} \end{aligned} \tag{8.30}$$

8.2.3 *Time-dependent probe frequency*

The previous two methods require a number of realizations to extract the resonance frequency for a single transverse pump coupling strength λ. We

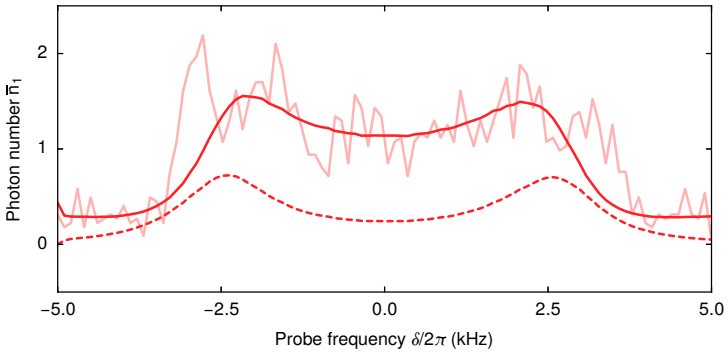

Figure 8.9: *Probing excitations with photons in real-time.* We prepare the quantum gas in the normal phase at $\Delta_c/2\pi = -2.0\,\mathrm{MHz}$ and at a transverse pump lattice depth of $12.8(3)\,\hbar\omega_{\mathrm{rec}}$. Frequency ramp at a rate of $0.5\,\mathrm{kHz/ms}$ with mean photon number $n = 0.03(1)$ in cavity 1. We extract a resonance frequency of $2.97(10)\,\mathrm{kHz}$ from a fit with Eq. 8.31 with time-dependent detuning $\delta(t)$. The dashed lines show the deduced photon number from Bragg scattering off the created excitations. Shaded areas denote the standard deviation of the fit function from the average over the phase φ.

can instead take advantage from the real-time access to the intracavity light field and apply a probe pulse with time-dependent detuning $\delta(t)$ relative to the transverse pump frequency. The detuning is scanned linearly in time, i. e. $\delta(t) = \delta_0 + \delta' t$ with start value δ_0 and scan rate δ'.

Fit function for the frequency scan

We can describe the intracavity light field by adapting Eq. 8.28 for time-dependent δ:

$$n_{\mathrm{ph}}(t) = \left| \alpha_0 - \frac{4\eta^2\sqrt{n_{\mathrm{pr}}}N}{\Delta_i + i\kappa} \left(\frac{\omega_-}{\omega_s}\right) \mathcal{I}(\mathcal{Y}(t)) + \sqrt{n_{\mathrm{pr}}(t)}e^{-i(\delta_0 t + \delta' t^2 + \varphi)} \right|^2, \tag{8.31}$$

with the integral $\mathcal{Y}(t)$ now:

$$\mathcal{Y}(t) = e^{(i\omega_s - \gamma)t} \int_0^t dt' e^{-(i\omega_s - \gamma)t'} \cos(\delta_0 t' + \delta' t'^2 + \varphi) \tag{8.32}$$

The resulting time evolution is more complex than for constant δ, because of the interplay between oscillations from interference of the scattered light with the probe field and the frequency-dependent scattering amplitude. An exemplary photon trace is shown in Fig. 8.9. Essentially it combines the behaviour of the photon number during a pulse at constant δ (see Fig. 8.8b) and its frequency dependence (see Fig. 8.8c): the photon number oscillates with frequency $|\delta(t)|$ and acquires an amplitude that itself depends on $\delta(t)$ with maximum. The trace shows an asymmetric shape, which originates from the decay rate γ.

Dynamical Bragg spectroscopy

An average over several measurements is shown in Fig. 8.9. We observe two resonances at positive and negative δ symmetrically around zero. The mean and the standard deviation over φ can be used again for a weighted fit to the data with free resonance frequency and response amplitude. We attribute the additional sharp resonance at around $\delta = -2.5\,\mathrm{kHz}$ to a mechanical resonance of the lock and exclude the region of $[-3.2, -2.5]\,\mathrm{kHz}$ from the fit.

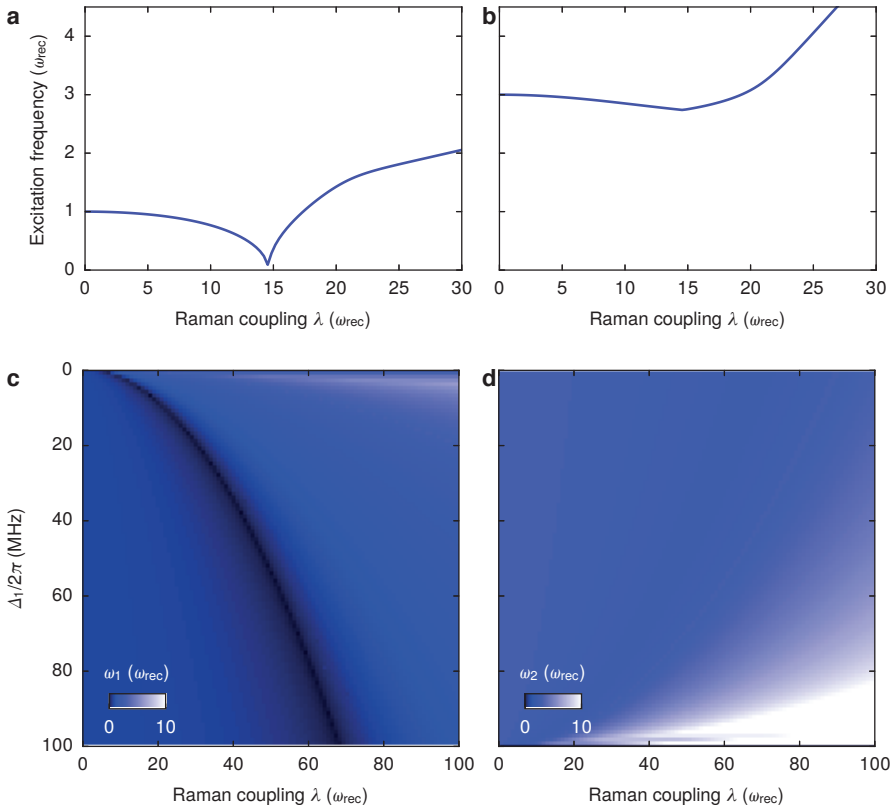

Figure 8.10: *Numerical simulation of the soft mode.* **a, b,** Lowest two collective excitations as a function of λ for fixed cavity detuning $\tilde{\Delta}_c/2\pi = 60\,\mathrm{MHz}$. The soft mode starts at ω_- and decreases in frequency upon approaching the critical point. **c, d,** Frequency of the lowest two excitations in the phase diagram of the $(\lambda, \tilde{\Delta}_c)$-plane.

8.3 MODE SOFTENING AT THE SELF-ORGANIZATION PHASE TRANSITION

We study the collective excitations of the quantum gas across the phase transition by probing it with cavity-enhanced Bragg spectroscopy, where probe photons are scattered off collective excitations into the transverse pump and *vice versa*.

8.3.1 Numerical mean–field solution

Diagonalization of the Hessian matrix

We can numerically obtain the eigenfrequencies of the full Hamiltonian in Eq. 8.8 (including the excited state at energy $\hbar\omega_+$) by expanding each operator around its expectation value and diagonalizing the Hessian matrix of the resulting mean–field Hamiltonian. We then inforce the relation

$$\omega_i^2 \propto (\mathbf{H}_d(\mathcal{H}))_{ii}\,, \tag{8.33}$$

where $\mathbf{H}_d$ is the diagonalized Hessian matrix. This allows to extract the excitation frequencies ω_i. The result for the lowest two excitations is shown in Fig. 8.10. Cavity decay and atom–atom contact interactions are taken into account.

For the lowest mode, we observe a characteristic softening upon approaching the phase transition, which persists over the entire range of detuning Δ_c.

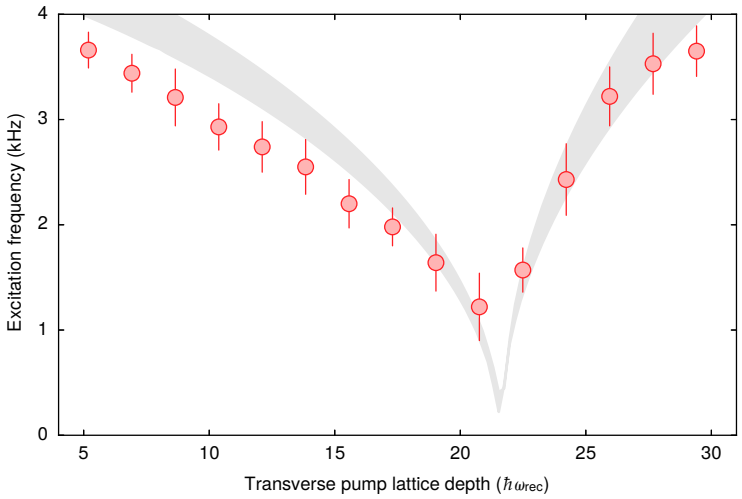

Figure 8.11: *Excitation spectrum across the self-organization phase transition.* Shown are the resonance frequencies extracted from the measured photon traces. Gray shading shows the theoretical prediction based on numerical solution of the Bogoliubov analysis. The detuning of the cavity resonance from the transverse pump is $\Delta_c = -2.0\,\mathrm{MHz}$ for all data points.

8.3.2 *Excitation frequencies across the phase transition*

We vary the coupling strength λ by preparing the system at different transverse pump lattice depths and study the collective excitations of the quantum gas. The lattice depth is reached in a linear ramp over 50 ms. We use the method with time-dependent probe detuning as described in Sec. 8.2.3 throughout the range covered by our measurements. The speed of the frequency ramp for the probe field is 0.5 kHz/ms. For each coupling strength, we extract the resonance from a fit to the data. Over the entire coupling range covered by our measurements, we prepare the system in a weakly driven situation by adjusting the resulting mean intracavity photon numbers within a range of $\bar{n}_1 = 0.03(1) - 0.9(1)$.

Observing the roton mode softening

The result is shown in Fig. 8.11. We observe a softening of the excitation frequency for increasing coupling strength λ. The excitation frequency tends to zero at the critical point for the self-organization phase transition. Here the soft mode energy is identical with the ground-state energy of the system. Within the self-organized phase the excitation frequency rises again.

We compare the experimental data to the numerical solution of the Bogoliubov theory. The expected frequency range is shown by the grey-shaded area. The uncertainties of these experimental parameters are determined from independent measurements and taken into account by the range of the shaded area. We find good agreement with the theoretical prediction over the entire range covered by the measurements.

8.3.3 *Response*

Studying the susceptibility

The amplitude of the intracavity light field contains a measure of the excited density modulation from the perturbation of the probe pulse. We can use this connection to study the susceptibility of the system across the phase transition.

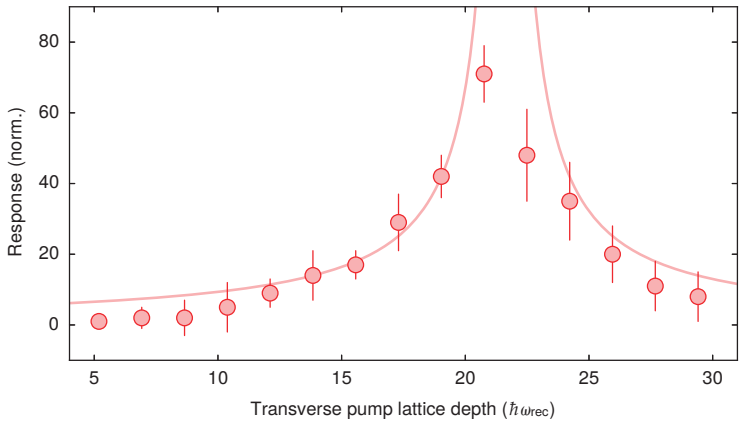

Figure 8.12: *System response across the phase transition.* The data points show the density response in the normal and the self-organized phase. We observe an increased response close to the phase boundary by around two orders of magnitude. The solid lines shows the prediction from Feynman's relation.

We consider the linear expansion of the density operator $\hat{\rho} = \hat{\Psi}^\dagger(\mathbf{r})\hat{\Psi}(\mathbf{r})$ around its expectation value $\rho_0 = \langle\hat{\rho}\rangle$:

$$\hat{\rho} = \rho_0 + \delta\hat{\rho} = N|\psi_0|^2 + \sqrt{N}\psi_0(\delta\hat{\psi}^\dagger + \delta\hat{\psi}). \tag{8.34}$$

In Fourier space the fluctuations $\delta\hat{\Theta}$ of the order parameter are

$$\delta\hat{\Theta} = \frac{1}{4}\sum_{\mathbf{k}\in\pm\mathbf{k}_p\pm\mathbf{k}_c} \delta\hat{\rho}_{\mathbf{k}} \tag{8.35}$$

In analogy to [312], this allows to write the intracavity light field fluctuations as:

$$\delta\hat{a} = \frac{\eta}{4(\Delta_c + i\kappa)}\sum_{\mathbf{k}\in\pm\mathbf{k}_p\pm\mathbf{k}_c} \delta\hat{\rho}_{\mathbf{k}} \tag{8.36}$$

We determine the total number of scattered photons by integrating over the entire photon trace. The response is then given by the scattered photon number normalized to the number of probe photons:

$$\mathcal{R} = \frac{1}{\int_0^\tau dt n_{pr}(t)}\int_0^\tau dt \frac{|\langle\delta\hat{a}\rangle|^2}{\left|\eta/(4\tilde{\Delta}_c + i\kappa)\right|^2} \tag{8.37}$$

Diverging response at the phase transition

The result is shown in Fig. 8.12. We observe a divergence of the density response when approaching the critical point, which extends over almost two orders of magnitude. This points towards increasing density fluctuations with wave vectors $\pm\mathbf{k}_p \pm \mathbf{k}_c$ triggering the phase transition. Inside the self-organized phase, the response decreases again.

Generally, the density response of a system is described by the static structure factor $S(k)$. For a homogeneous system with dispersion relation $S(k)$, the static structure is predicted by *Feynman's relation* [324]:

$$S(k) = \frac{\hbar k^2/2m}{\omega(k)} \tag{8.38}$$

The relation can be verified by dividing the excitation frequency in the limit $\lambda/\lambda_{cr} \ll 1$ by its renormalized value. The result is shown in Fig. 8.12 and shows good agreement with the data.

9 MONITORING HIGGS AND GOLDSTONE MODES

Higgs and Goldstone modes are amplitude and phase excitations of a complex order parameter. In this chapter, we present studies on these modes across the superfluid-supersolid phase transition. Monitoring the cavity fields in real time allows us to observe the dynamics of the associated Higgs and Goldstone modes and reveal their amplitude and phase nature. We use a spectroscopic method to measure their frequencies and give a tunable mass to the Goldstone mode by exploring the crossover between continuous and discrete symmetry. Our experiments link spectroscopic measurements to the theoretical concept of Higgs and Goldstone modes.

CHAPTER CONTENTS

Collective excitations provide a unifying concept across different subfields of physics, from condensed matter [315] to particle physics [325] to cosmology [291]. The symmetry of the underlying effective Hamiltonian determines the character of the excitations, which changes in a fundamental way when a continuous symmetry is broken at a phase transition. Major advances in the description of phase transitions that break continuous symmetries originated from the concept of massless and massive excitations, as introduced by Goldstone in [326, 327].

Higgs and Goldstone modes at continuous symmetry breaking

In the paradigmatic case of models with U(1)-symmetry breaking, the system can be described by a complex scalar order parameter in an effective potential as illustrated in Fig. 9.2(a–b) [1]. In the normal phase, the potential is bowl-shaped with a single minimum at vanishing order parameter, and correspondingly two orthogonal amplitude excitations. Within the ordered phase, the potential shape changes to a 'sombrero' with an infinite number of minima on a circle. Here, fluctuations of the order parameter reveal two different excitations: a Higgs (or amplitude) mode, which stems from amplitude fluctuations of the order parameter and shows a finite excitation energy, and a Goldstone (or phase) mode, which stems from phase fluctuations of the order parameter and has zero excitation energy. The former should yield correlated fluctuations in the two squared quadratures of the order parameter, whereas the latter should show anticorrelated behavior.

Despite their conceptual relevance, Higgs and Goldstone modes are extremely challenging to detect as amplitude and phase excitations, since this requires time-resolved access to both the amplitude and the phase of the order parameter. Instead, spectroscopic measurements in different systems have shown excitations that were interpreted as Higgs or Goldstone modes because of their resonance frequencies. Examples include experiments on the Higgs mode in solid-state systems [328–331] and with cold atoms in 2D optical lattices [332, 333]. Experiments on the Goldstone mode have been carried out, for example, in superfluid helium [334] and BECs [335]. Time-resolved studies have been limited to relaxation measurements of the amplitude of the order parameter in high-temperature superconductors [336], but without access to the phase of the order parameter.

Parts of this chapter have been published in:

> J. Léonard, A. Morales, P. Zupancic, T. Donner and T. Esslinger:
> *Monitoring and manipulating Higgs and Goldstone modes in a supersolid quantum gas*
> *Science* **358**, 1415-1418 (2017)

9.1 THEORETICAL DESCRIPTION

In general, a 'sombrero' shaped effective potential is not sufficient to support independent amplitude and phase oscillations. Whether a system with continuous symmetry breaking actually supports both a Higgs and a Goldstone mode additionally depends on the time dynamics of the effective action. In brief, both modes only exist for neutral particles that follow a Lorentz-invariant time evolution in the vicinity of the phase transition for the low-energy limit. We will discuss this topic first for the general effective action, and then consider the excitations that are present across the superfluid-supersolid phase transition for self-organization in the two-cavity setup.

9.1.1 Effective action

We consider the Landau expansion for two competing order parameters each with an underlying $\mathbb{Z}_2$ symmetry, as introduced in Eq. 7.4:

$$\mathcal{H}(\Theta_1,\Theta_2) = \frac{r}{2}(|\Theta_1|^2+|\Theta_2|^2) + \frac{g}{4}(|\Theta_1|^2+|\Theta_2|^2)^2 + \chi\,|\Theta_1|^2\,|\Theta_2|^2\,. \quad (9.1)$$

The Hamiltonian is invariant under $\Theta_i \to -\Theta_i$ and $\Theta_1 \to \Theta_2$. In the following we restrict ourselves to the situation $\chi = 0$, when the ground-state has an infinite number of minima (cf. Chap. 7). Let us switch to a parametrization in polar coordinates with $\Theta_1 = \cos(\theta)\,|\Theta|$ and $\Theta_2 = \sin(\theta)\,|\Theta|$ for $\theta \in [0, 2\pi]$ and $|\Theta| = \sqrt{|\Theta_1|^2+|\Theta_2|^2}$. The Hamiltonian then takes the simpler form:

Landau theory for a complex order parameter

$$\mathcal{H}(\theta,|\Theta|) = \frac{r}{2}\,|\Theta|^2 + \frac{g}{4}\,|\Theta|^4\,. \quad (9.2)$$

The Hamiltonian is independent of θ and therefore shows an SO(2) symmetry, or alternatively, a U(1) symmetry with the parametrization $\Theta = \Theta_1 + i\Theta_2$. The shape of the effective potential is shown in Fig. 9.1. It exhibits a 'bowl' shape with a single minimum at $|\Theta| = 0$ in the normal phase, but acquires a 'sombrero' shape in the ordered phase with minima on a circle with radius $|\Theta|$.

Action density

We can describe the elementary excitations of the system by allowing the

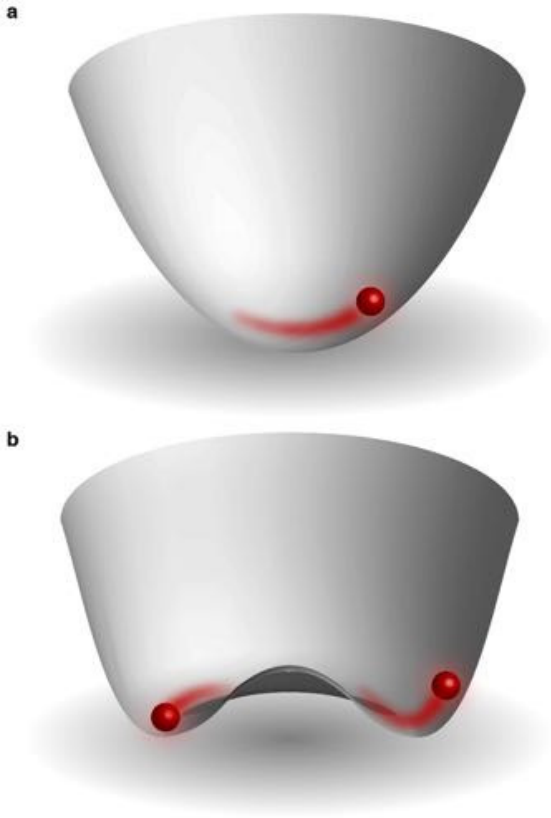

Figure 9.1: *Collective excitations for continuous symmetry breaking.* Effective potential across the phase transition as a function of the order parameter $\Theta = |\Theta| e^{i\phi}$. **a,** In the normal phase, the effective potential has a 'bowl' shape and the order parameter can fluctuate along any direction. The oscillation is gapped and decreases in energy when approaching the critical point, since the curvature of the effective potential reduces. **b,**. In the ordered phase, the effective potential acquires a 'sombrero' shape with an infinite number of minima on a circle. Higgs and Goldstone modes describe amplitude ($\delta|\Theta|$) and phase ($\delta\phi$) fluctuations around the finite expectation value of the order parameter.

order parameter to change in space and in time, i.e. $\Theta \equiv \Theta(\mathbf{r}, t)$. This extends the description by a spatial derivative $(\nabla\Theta^*)(\nabla\Theta)$ and the time evolution up to second order, yielding the action density $\mathcal{S}$:

$$\begin{aligned}\mathcal{S}(\Theta, t) =& iK_1\Theta^*\partial_t\Theta - K_2\,(\partial_t\Theta^*)\,(\partial_t\Theta) \\ &+ \frac{r}{2}\,|\Theta|^2 + \frac{g}{4}\,|\Theta|^4 + \xi^2(\nabla\Theta^*)(\nabla\Theta).\end{aligned} \tag{9.3}$$

Here, the constants K_1 and K_2 govern the first and second order time evolution, respectively, and ξ is the characteristic length scale of the system that determines the spread of correlations. Formally, the action density is related to the Lagrange density $\mathcal{L}$ by the condition $\mathcal{S} = \int \mathcal{L}\,dt$, where the integral follows the minimal action trajectory. The equations of motion for the fluctuations of $\Theta(\mathbf{r}, t)$ are determined by the conditions

$$\frac{\partial\mathcal{S}}{\partial\Theta} = 0 \tag{9.4}$$

$$\frac{\partial\mathcal{S}}{\partial\Theta^*} = 0 \tag{9.5}$$

Fluctuations of the order parameter

In order to obtain the eigenfrequencies of the elementary excitations, we linearize these equations by expanding the order parameter around its equilibrium value:

$$\begin{aligned}\Theta(\mathbf{r}, t) &= \Theta_0 + \delta\,|\Theta(\mathbf{r}, t)| + i\Theta_0\theta(\mathbf{r}, t) + \ldots \\ &= \Theta_0 + \delta_a + i\delta_{ph}\theta(\mathbf{r}, t) + \ldots\end{aligned} \tag{9.6}$$

with the amplitude and phase oscillations δ_a and δ_{ph}, respectively. Transforming to the Fourier space representation in terms of q and ω, we obtain the following linear equations:

$$\begin{pmatrix} 2r + \xi^2 q^2 - K_2\omega^2 & iK_1\omega \\ -iK_1\omega & \xi^2 q^2 - K_2\omega^2 \end{pmatrix} \begin{pmatrix} \delta_a \\ \delta_{ph} \end{pmatrix} = 0 \tag{9.7}$$

First and second order time dynamics

The dispersion relation is governed by this system of equations. We find that K_2 is diagonal in δ_a and δ_{ph}, whereas K_1 couples them. Let us consider the some important cases for the parameters K_1 and K_2:

- $K_1 \neq 0$, $K_2 \approx 0$: This scenario occurs, for instance, in superfluid helium or BECs, whose dynamics are governed by the Gross-Pitaevskii equation with a first order derivative only [2]. Amplitude and phase oscillations are coupled, so that no distinct amplitude and phase fluctuations exist. Only one solution exists:

  $$\omega^2 = \frac{1}{K_1^2}\left(2r + \xi^2 q^2\right)\xi^2 q^2 \tag{9.8}$$

  These are the Bogoliubov modes with a linear dispersion in the long-wavelength limit. The excitation spectrum is gapless, as expected from Goldstone's theorem [326, 327].

- $K_1 \approx 0$, $K_2 \neq 0$: In case the system has particle-hole symmetry, the action must be invariant under $\Theta \to \Theta^*$. As a consequence, the first term of the action density in Eq. 9.16 vanishes, leaving a second order time evolution only. We find that both space and time derivatives are of

second order, making the action density Lorentz-invariant. We obtain two distinct excitation branches:

$$\omega^2 = \frac{1}{K_2}\left(2r + \xi^2 q^2\right) \tag{9.9}$$

$$\omega^2 = \frac{1}{K_2}\xi^2 q^2 \tag{9.10}$$

The first one describes pure amplitude fluctuations and is called *Higgs* mode. Throughout the ordered phase the Higgs mode remains gapped by $\Delta_0 = \sqrt{2r/K_2}$. The second branch corresponds to the phase fluctuations and remains gapless, since $\omega = 0$ for $q = 0$.

- $K_1 \ll K_2$: A small coupling between amplitude and phase modes pushes the Higgs-like mode to higher frequenciest:

$$\omega_{q=0} = \frac{1}{K_2}\sqrt{2r + K_1^2} \tag{9.11}$$

Even at the transition point, where $r = 0$, the Higgs-like mode remains gapped by $\Delta_0 = K_1/K_2$.

We conclude that a sombrero potential is not sufficient to obtain both a Higgs and a Goldstone mode. In particle physics, the Lorentz invariance naturally imposes $K_1 = 0$. In most condensed matter systems, for instance superfluids and metals, amplitude and phase fluctuations are coupled and $K_1 \neq 0$. Some systems, however, exhibit a particle-hole symmetry, including dimer-antiferromagnets and superconductors. For bosons in optical lattices, a particle-hole symmetry is present as an enhanced symmetry along certain lines in the chemical potential–interaction phase diagram.

Particle-hole-like symmetry

A particle-hole-like symmetry, that is, a symmetry $\Theta \to \Theta^*$, generally enforces a Lorentz-invariant evolution, as can be seen by explicitly calculating the dynamic terms of the effective action density:

$$\mathcal{S}_{\text{dynamic}} = K_1(\Theta^*\partial_t\Theta - \Theta\partial_t\Theta^*) + K_2\partial_t\Theta^*\partial_t\Theta. \tag{9.12}$$

With $\Theta = \Theta_1 + i\Theta_2$ we get

$$\mathcal{S}_{\text{dynamic}} = 2iK_1(\Theta_1\partial_t\Theta_2 - \Theta_2\partial_t\Theta_1) + K_2\left[(\partial_t\Theta_1)^2 + (\partial_t\Theta_2)^2\right]. \tag{9.13}$$

A particle-hole symmetry requires the action to be invariant under the transformation $\Theta_1 \to \Theta_2$, yielding $K_1 = 0$ [315].

A particular situation arises for a charged-matter field obeying Lorentz invariance, as in superconductivity or high-energy physics. Here, we have to include the electromagnetic field and its interaction with $\Theta(\mathbf{r}, t)$ in a gauge-invariant way by the substitution $\nabla \to \nabla - ie\mathbf{A}/c$, where $\mathbf{A}(\mathbf{r}, t)$ is the vector potential, e is the elementary charge and c the speed of light. This corresponds to the gauge transformation:

$$\Theta \to \Theta e^{ie\theta A/c} \tag{9.14}$$

$$\boldsymbol{A} \to \mathbf{A} + \nabla\theta \tag{9.15}$$

The effective action then reads

$$\begin{aligned}\mathcal{S}(\Theta, t) = &-K_2\,(\partial_t\Theta^*)\,(\partial_t\Theta) \\ &+ \frac{r}{2}|\Theta|^2 + \frac{g}{4}|\Theta|^4 + \xi^2\left(\left[\nabla + i\frac{e}{c}\mathbf{A}\right]\Theta^*\right)\left(\left[\nabla - i\frac{e}{c}\mathbf{A}\right]\Theta\right).\end{aligned} \tag{9.16}$$

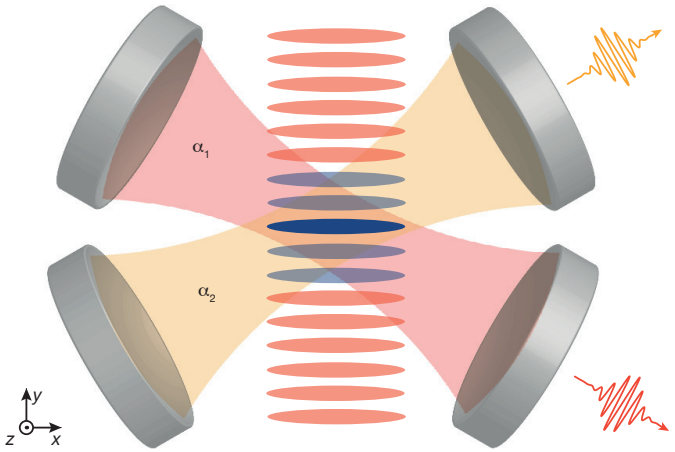

Figure 9.2: *Illustration of the experiment.* A Bose-Einstein condensate (blue stripes) cut into slices by a transverse pump lattice potential (red stripes) enters a supersolid state and breaks translational symmetry along x by symmetrically coupling it to two optical cavity modes α_1 (red) and α_2 (yellow) with a transverse pump lattice along y. The emerging Higgs and Goldstone excitations correspond to fluctuations of the strength and position of the density modulation, as shown in the zoom-in for one slice. They can be excited and read out with probe pulses on each cavity.

The coupling to the vector potential introduces off-diagonal terms to the system of linear equations for the amplitude and phase fluctuations. Analogously to the uncharged situation, we obtain the resonance frequencies and find that the Goldstone mode has acquired a finite frequency:

$$\omega^2 = \xi^2 \left(\frac{e^2}{K_2} + q^2 \right), \tag{9.17}$$

which is always nonzero and bound by the plasma frequency $\omega_p^2 = \xi^2 e^2 / K_2$ in the limit $q_- \to 0$. The gapless mode has vanished at the expense of reducing the global gauge symmetry to a local one. This phenomenon is called the *Anderson-Higgs mechanism*. The gauge symmetry is abelian, namely U(1), in superconductors, but in general the underlying symmetry group can also be non-abelian, as is the case for weak interactions.

9.1.2 Collective excitations across the critical point

Self-organization with two cavities

Let us turn to the system under consideration, namely self-organization with two cavity modes. The experimental situation is illustrated in Fig. 9.2. A spatial U(1)-symmetry breaking is induced in a setting in which a BEC is off-resonantly driven by a transverse optical standing wave and degenerately coupled to the modes of two optical cavities [337]. Both cavity modes overlap with the BEC and are oriented in a 60° angle with respect to the transverse pump lattice, which also provides an attractive 1D standing wave potential for the atoms. Coherent transitions, induced by a transverse pump photon plus a cavity photon, couple two states with and without a density-modulation of the condensate. For small two-photon couplings the system remains in the normal phase. As soon as the coupling strength exceeds a critical value, the kinetic energy associated with the density-modulation of the atomic wave function is overcome and the system enters a self-organized phase, which is periodically ordered perpendicular to the transverse pump

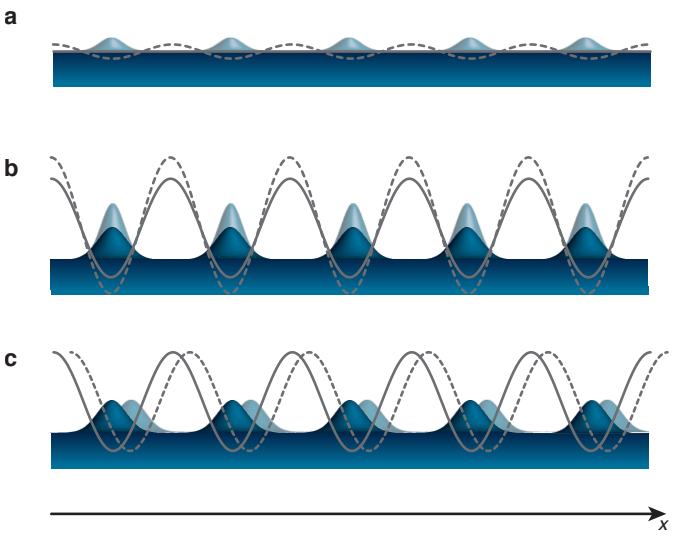

Figure 9.3: *Spatial character of the collective excitations.* Shown are the steady state density distribution (blue) and the light-induced interaction potential (solid lines), together with the fluctuations of the density (shaded blue) and the potential (dashed lines) at the maximum displacement of the oscillation. **a,** Below the critical point, the elementary excitations are roton excitations, which describe fluctuations of a homogeneous density distribution at a specific wavelength. The position of the nodes and the antinodes of the oscillation is determined by the contribution of the two cavity modes. **b,** Above the critical point, Higgs excitations appear, which correspond to fluctuations of the strength of the density modulation. c, Additionally, a second type of excitations exists, the Goldstone excitations, which describe oscillations around the position of the density modulation.

lattice. Due to the symmetric coupling to both cavities, this phase transition breaks the continuous translational symmetry along the x-axis and a supersolid phase emerges.

Since the density ordering is driven by light scattering between the transverse pump lattice and the cavities, the phase transition is accompanied by the appearance of non-zero real-valued field amplitudes in cavity 1 (α_1) and 2 (α_2). Together they form an order parameter $\alpha = \alpha_1 + i\alpha_2 = |\alpha| e^{i\phi}$ whose amplitude and phase directly map to the strength and the position of the density modulation. By detecting the photons leaking from the cavities we can continuously monitor the order parameter along both quadratures.

Order parameter in the cavity fields

Rewriting the order parameter as $\Theta = |\Theta| e^{i\phi}$ with an amplitude $|\Theta|$ and a phase ϕ allows for an interpretation without falling back to the individual cavity modes. The amplitude $|\Theta|$ determines the overall strength of the density modulation, that is, the localization of the atoms on the emergent lattice sites. It is set by the total mean photon number $\overline{n}$ in the two cavity modes. The phase ϕ corresponds to the position of the lattice sites and is determined by the ratio of the mean photon numbers in the two cavities.

With this interpretation we obtain an intuitive picture of the spatial nature of the collective excitations in the system, as illustrated in Fig. 9.3. In the normal phase, the excitations correspond to a modulation with the periodicity of the lattice constant around the equilibrium flat density. Oscillations at any other wave vector are suppressed, because they form a Bragg grating that is incommensurate with the cavity geometry and the scattering amplitudes interfere destructively. The position ϕ of the lattice positions of the oscilla-

Spatial nature of the excitations

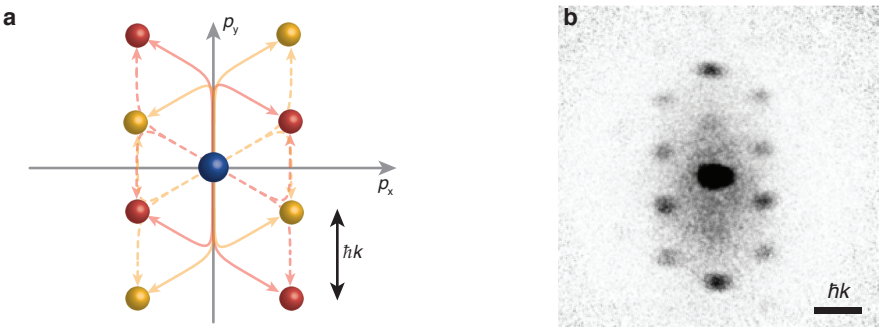

Figure 9.4: *Photon scattering and momentum states.* **a,** Coherent scattering processes of pump photons into cavity 1 (red) or cavity 2 (orange) and back give rise to atomic momentum states at energies $\hbar\omega_- = \hbar\omega_{\mathrm{rec}}$ and $\hbar\omega_+ = 3\hbar\omega_{\mathrm{rec}}$. The coordinate system is with respect to momentum space. **b,** Absorption image of the atoms in the supersolid phase after 25 ms ballistic expansion. All momentum states highlighted in (**a**) are populated. The additional momentum states at $p_y = \pm 2\hbar k$ stem from pump-pump scattering processes.

tions can take any value, leading to correlated fluctuations of the two cavity light fields with the contributions depending on ϕ.

The situation is different in the supersolid phase, where the oscillations occur around a finite expectation value. An oscillation of the amplitude corresponds to a modulation of the strength of the density modulation. Within one oscillation, the many-body wave function is first more strongly localized at the lattice sites, and then more weakly. Correspondingly, the total mean photon number first increases and then decreases. A phase oscillation modulates the position of the lattice sites without changing the strength of the density modulation, thus alternating between a movement to the right and the left direction. This corresponds to an increasing mean photon number in one cavity at the expense of the mean photon number in the other cavity, while the total mean photon number remains constant. The center of mass of the atomic ensemble remains constant during the entire oscillation period, solely the underlying lattice structure is displaced.

9.1.3 *Microscopic model*

Raman scattering between the pump and cavity fields via the atoms couples the atomic momentum state at $|\mathbf{k}\rangle = |\mathbf{0}\rangle$ to a superposition state of the higher momenta $|\mathbf{k}\rangle = |\pm\mathbf{k}_p \pm \mathbf{k}_i\rangle$, where $\mathbf{k}_p$ and $\mathbf{k}_i$ denote the wave-vectors of the transverse pump and cavity i, respectively. These states fall into two groups with energy either $\hbar\omega_- = \hbar\omega_{\mathrm{rec}}$ or $\hbar\omega_+ = 3\hbar\omega_{\mathrm{rec}}$ (Fig. 9.4). Our system is described by the effective Hamiltonian

$$\begin{aligned}\hat{\mathcal{H}} = \sum_{i=1,2}\Big[&-\hbar\Delta_i\hat{a}_i^\dagger\hat{a}_i + \hbar\omega_+\hat{c}_{i+}^\dagger\hat{c}_{i+} + \hbar\omega_-\hat{c}_{i-}^\dagger\hat{c}_{i-} \\ &+ \frac{\hbar\lambda_i}{\sqrt{N}}\left(\hat{a}_i^\dagger + \hat{a}_i\right)\left(\hat{c}_{i+}^\dagger\hat{c}_0 + \hat{c}_{i-}^\dagger\hat{c}_0 + \mathrm{h.c.}\right)\Big].\end{aligned} \tag{9.18}$$

$\hat{a}_i^\dagger$ ($\hat{a}_i$) are the creation (annihilation) operators for a photon in cavity i, $\hat{c}_{i\pm}^\dagger$ ($\hat{c}_{i\pm}$) and $\hat{c}_0^\dagger$ ($\hat{c}_0$) create (annihilate) an atomic momentum excitation at energy $\hbar\omega_\pm$ associated with cavity i and in the atomic ground state, respectively, N is the atom number and $\lambda_i = \frac{\eta_i\sqrt{N}}{2\sqrt{2}}$ the Raman coupling

which can be controlled via $\eta_i = -\frac{\Omega_p g_i}{\Delta_a}$ with the transverse pump Rabi frequency Ω_p. The dispersive shift $Ng_i^2/(2\Delta_a) \ll \Delta_i$ is similar for both cavities and can be absorbed into Δ_i. Other optomechanical terms can be discarded for our experimental parameters. As the vacuum Rabi coupling g_i of both cavities are very similar, we use a single coupling $\lambda = \lambda_i$.

When coupling symmetrically to both cavities, i. e. $\Delta_c = \Delta_1 = \Delta_2$, the Hamiltonian is symmetric under a simultaneous rotation in the basis of the light fields and the atomic fields. This can be captured by the generator

$$\hat{C} = -i\Big[\hat{a}_1^\dagger \hat{a}_2 - \hat{a}_2^\dagger \hat{a}_1 + \sum_{s=\pm}\Big(\hat{c}_{1s}^\dagger \hat{c}_{2s} - \hat{c}_{2s}^\dagger \hat{c}_{1s}\Big)\Big]. \tag{9.19}$$

It satisfies $[\hat{C}, \hat{\mathcal{H}}] = 0$, and, consequently, the Hamiltonian $\hat{\mathcal{H}}$ stays unchanged under the transformation $\hat{U} = e^{i\theta\hat{C}}$ for any $\theta \in [0, 2\pi]$, i. e. $\hat{U}\hat{\mathcal{H}}\hat{U}^\dagger = \hat{\mathcal{H}}$. This U(1)–symmetry is broken at the phase transition. For arbitrary values of λ, Δ_1 and Δ_2, Eq. 9.18 is instead $\mathbb{Z}_2$–symmetric under the operations $(a_i, c_{i+}, c_{i-}) \to -(a_i, c_{i+}, c_{i-})$ for each individual cavity $i \in 1, 2$.

The Hamiltonian in Eq. 9.18 can be solved numerically. We find that for cavity i, the state for the lowest eigenvalue has largest contribution from $\hat{c}_{i-}$, and the admixture of the $\hat{c}_{i+}$ mode is maximally 15% in the explored parameter range, leading to a relative shift of the eigenfrequencies of $< 10\%$ compared to including only the lowest mode. In order to derive an approximate analytic expression for the Higgs and Goldstone modes, we neglect the high-energy mode at ω_+ in the following and consider the reduced Hamiltonian:

Low-energy Hamitlonian

$$\begin{aligned}\hat{\mathcal{H}} = \sum_{i=1,2}\Big[&-\hbar\Delta_i \hat{a}_i^\dagger \hat{a}_i + \hbar\omega_- \hat{c}_{i-}^\dagger \hat{c}_{i-} \\ &+ \frac{\hbar\lambda}{\sqrt{N}}\Big(\hat{a}_i^\dagger + \hat{a}_i\Big)\Big(\hat{c}_{i-}^\dagger \hat{c}_0 + \hat{c}_0^\dagger \hat{c}_{i-}\Big)\Big].\end{aligned} \tag{9.20}$$

We describe the behaviour of the atomic and the light modes by means of the Holstein-Primakoff transformations [235]:

Holstein-Primakoff transformation

$$\begin{aligned}\hat{a}_i &= \sqrt{N}\alpha_i + \delta\hat{a}_i \\ \hat{c}_{i-} &= \sqrt{N}\psi_{i-} + \delta\hat{c}_{i-} \\ \hat{c}_0 &= \sqrt{N - \sum_{i=1,2}\hat{c}_{i-}^\dagger \hat{c}_{i-}}\end{aligned} \tag{9.21}$$

where $\delta\hat{a}_i$ ($\delta\hat{c}_{i-}$) describe the photonic (atomic) fluctuations of the system around its mean-field values α_i (ψ_{i-}). We expand the Hamiltonian in Eq. 9.20 up to quadratic order in the excitations and use the quadratic part $\hat{h}^{(2)} = \hat{h}^{(2)}(\delta\hat{a}_i, \delta\hat{c}_{i-})$ to determine the excitation spectra of the system. In the normal phase ($\alpha_i = \psi_{i-} = 0$), we obtain two orthogonal massive modes for the atomic excitations (see Fig. 1A)

$$\omega_i = \omega_- \sqrt{1 - \frac{\lambda^2}{\lambda_{cr}^2}} \tag{9.22}$$

in the limit $\omega_- \ll |\Delta_c|$ with $\Delta_c = \Delta_1 = \Delta_2$. Within the supersolid phase we have $\alpha_i, \psi_i \neq 0$. Performing a rotation in the space of the excitations,

$$\begin{aligned}\delta\hat{a}_1 &= \cos\theta\ \delta\hat{a}_H + \sin\theta\ \delta\hat{a}_G \\ \delta\hat{a}_2 &= -\sin\theta\ \delta\hat{a}_H + \cos\theta\ \delta\hat{a}_G \\ \delta\hat{c}_{1-} &= \cos\theta\ \delta\hat{c}_H + \sin\theta\ \delta\hat{c}_G \\ \delta\hat{c}_{2-} &= -\sin\theta\ \delta\hat{c}_H + \cos\theta\ \delta\hat{c}_G,\end{aligned} \tag{9.23}$$

the quadratic part of the Hamiltonian separates into two contributions from the new modes $(\delta\hat{a}_G, \delta\hat{a}_H, \delta\hat{c}_G, \delta\hat{c}_H)$,

$$\begin{aligned}&\hat{h}^{(2)}(\delta\hat{a}_G, \delta\hat{a}_H, \delta\hat{c}_G, \delta\hat{c}_H) = \\ &\hat{h}^{(2)}(\delta\hat{a}_G, \delta\hat{c}_G) \;+\; \hat{h}^{(2)}(\delta\hat{a}_H, \delta\hat{c}_H).\end{aligned} \tag{9.24}$$

where

$$\begin{aligned}\hat{h}^{(2)}(\delta\hat{a}_G, \delta\hat{c}_G) &= -\Delta_c \delta\hat{a}_G^\dagger \delta\hat{a}_G + \tilde{\omega}_- \delta\hat{c}_G^\dagger \delta\hat{c}_G \\ &+ \lambda\sqrt{\frac{1+\mu}{2}}\left(\delta\hat{a}_G^\dagger + \delta\hat{a}_G\right)\left(\delta\hat{c}_G^\dagger + \delta\hat{c}_G\right),\end{aligned} \tag{9.25}$$

and

$$\begin{aligned}\hat{h}^{(2)}(\delta\hat{a}_H, \delta\hat{c}_H) =& -\Delta\delta\hat{a}_H^\dagger \delta\hat{a}_H + \tilde{\omega}_- \delta\hat{c}_H^\dagger \delta\hat{c}_H \\ &+ \frac{\omega_-(1-\mu)(3+\mu)}{4\mu(1+\mu)}\left(\delta\hat{c}_H^\dagger + \delta\hat{c}_H\right)^2 \\ &+ \lambda\mu\sqrt{\frac{2}{1+\mu}}(\delta\hat{a}_H^\dagger + \delta\hat{a}_H)\left(\delta\hat{c}_H^\dagger + \delta\hat{c}_H\right)\end{aligned} \tag{9.26}$$

with $\mu = (\lambda_{cr}/\lambda)^2$ and $\tilde{\omega}_- = \omega_-(1+\mu)/(2\mu)$. $\hat{h}^{(2)}(\delta\hat{a}_G, \delta\hat{c}_G)$ is of the form of the Hamiltonian in the normal phase ($\alpha_i = \psi_i = 0$) where $(\tilde{\omega}_-^2 - \Delta_c^2)^2 + 16\lambda^2\left[(1+\mu)/2\right]\Delta_c\tilde{\omega}_- = (\omega_-^2 + \Delta_c^2)^2$. From this condition it directly follows that the excitation energy of this branch is zero [236]. On the other hand, $\hat{h}^{(2)}(\delta\hat{a}_H, \delta\hat{c}_H)$ is of the form of the Hamiltonian that describes fluctuations around a superradiant phase with nonzero α_i, ψ_i and therefore a non–zero excitation energy. From this analysis we have shown that the excitation spectra in the supersolid phase separate into a gapped (Higgs) branch and a gapless (Goldstone) branch.

Effective potential

Connect to effective potential

We can connect to the discussion in the previous section by deriving an effective potential from the microscopic Hamiltonian in Eq. 9.20. We start by inserting the mean-field ansatz $\langle\hat{a}_i\rangle = \sqrt{N}\alpha_i$, $\langle\hat{c}_{i-}\rangle = \sqrt{N}\psi_i$ and $\langle\hat{c}_0\rangle = \sqrt{N\left(1-\psi_1^2-\psi_2^2\right)} = \sqrt{N}\psi_0$ into the reduced Hamiltonian in Eq. 9.20, with $\alpha_i, \psi_i \in \mathbb{R}$. This results in the effective potential

$$\mathcal{H}(\alpha_i, \psi_i) = \sum_{i=1,2}\left[-\hbar\Delta_i\alpha_i^2 + \hbar\omega_-\psi_i^2 + 4\hbar\lambda\alpha_i\psi_i\psi_0\right]. \tag{9.27}$$

As $\Delta_i \gg \omega_-$, the photon fields reach their steady state quasi-instantaneously with respect to the atomic fields. We can hence adiabatically eliminate the light fields enforcing the condition $\frac{\partial\mathcal{H}}{\partial\alpha_i} = 0$ and obtain

$$\mathcal{H}(\psi_1, \psi_2) = \hbar\omega_-(\psi_1^2 + \psi_2^2) + 4\hbar\lambda^2\psi_0^2\left(\frac{\psi_1^2}{\Delta_1} + \frac{\psi_2^2}{\Delta_2}\right). \tag{9.28}$$

For the U(1)–symmetric case with $\Delta_C = \Delta_1 = \Delta_2$, this simplifies to

$$\mathcal{H}(\psi) = \hbar\omega_-\left[|\psi|^2\left(1 - \frac{\lambda^2}{\lambda_{cr}^2}\right) + |\psi|^4\frac{\lambda^2}{\lambda_{cr}^2}\right], \tag{9.29}$$

where $\psi = \psi_1 + i\psi_2$ is a complex atomic order parameter and the critical coupling strength is $\lambda_{cr} = \sqrt{-\Delta_c\omega_-/4}$. For $\lambda < \lambda_{cr}$, the potential has a 'bowl' shape as displayed in Fig. 9.5. For $\lambda > \lambda_{cr}$, it acquires a 'sombrero' shape with a circular manifold of minima at

$$|\psi_0| = \sqrt{\frac{1}{2}\left(1 - \frac{\lambda_{cr}^2}{\lambda^2}\right)} \tag{9.30}$$

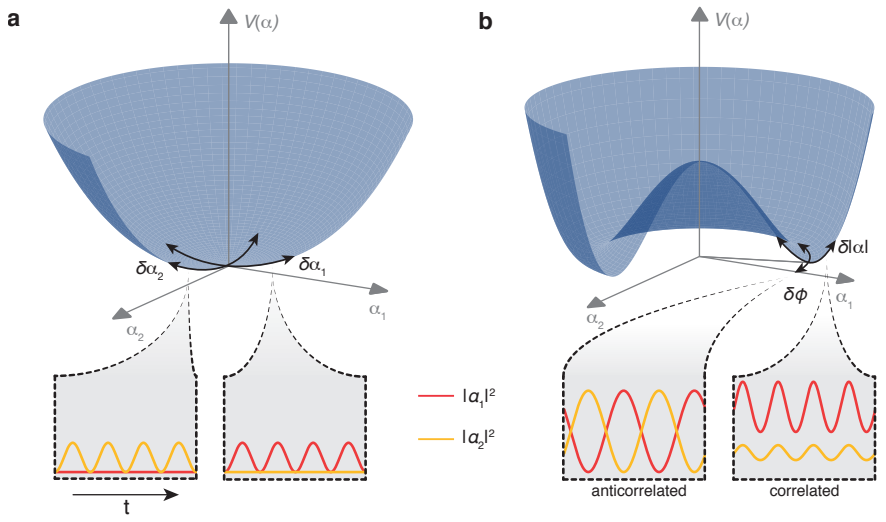

Figure 9.5: *Higgs and Goldstone modes for a U(1) symmetry.* Effective potential across the phase transition as a function of the order parameter $\alpha = \alpha_1 + i\alpha_2 = |\alpha|e^{i\phi}$. **a,** In the normal phase, two excitations, $\delta\alpha_1$ and $\delta\alpha_2$, correspond to fluctuations of the order parameter along each quadrature. Both excitations have an amplitude character involving one quadrature of the order parameter. **b,**. In the ordered phase, Higgs and Goldstone modes describe amplitude ($\delta|\alpha|$) and phase ($\delta\phi$) fluctuations around a finite expectation value of the order parameter. The squares of the quadratures show either correlations (Higgs) or anticorrelations (Goldstone).

This potential can be probed along ψ_1 and ψ_2 independently thanks to the expression $\alpha_i = 2\lambda\psi_i\psi_0/\Delta_c$, obtained from the condition $\frac{\partial\mathcal{H}}{\partial\alpha_i} = 0$. The combined cavity field $\alpha = \alpha_1 + i\alpha_2$ therefore constitutes an equivalent order parameter.

The cavity light field amplitudes $\alpha_i = \langle a_i \rangle$ are order parameters describing the different phases of the system. A phase transition from the superfluid phase (SF, $\alpha_1 = \alpha_2 = 0$) to a self-organized phase in cavity i (SO1 with $\alpha_1 \neq 0 = \alpha_2$ and SO2 with $\alpha_2 \neq 0 = \alpha_1$) occurs when the coupling λ crosses the critical coupling $\lambda_i^{cr} = \sqrt{-\Delta_i\overline{\omega}/4}$, with $\overline{\omega}^{-1} = \omega_+^{-1} + \omega_-^{-1}$. This crossing is obtained by either changing λ or Δ_i. The supersolid phase ($\alpha_1, \alpha_2 \neq 0$) on the phase boundary between the SO1 and the SO2 phase is identified by the condition $\lambda_1^{cr} = \lambda_2^{cr}$, where the coupling to both cavities is symmetric.

9.2 MEASURING THE EXCITATION SPECTRUM

9.2.1 Numerical mean–field solution

We numerically obtain the eigenfrequencies of the Hamiltonian in Eq. 9.18 (including $\hat{c}_{i+}$) by expanding each operator around its expectation value and diagonalizing the Hessian matrix of the resulting mean–field Hamiltonian. The result for the lowest two excitations is shown in Fig. 9.6. Cavity decay, atom–atom contact interactions and the transverse pump potential are taken into account.

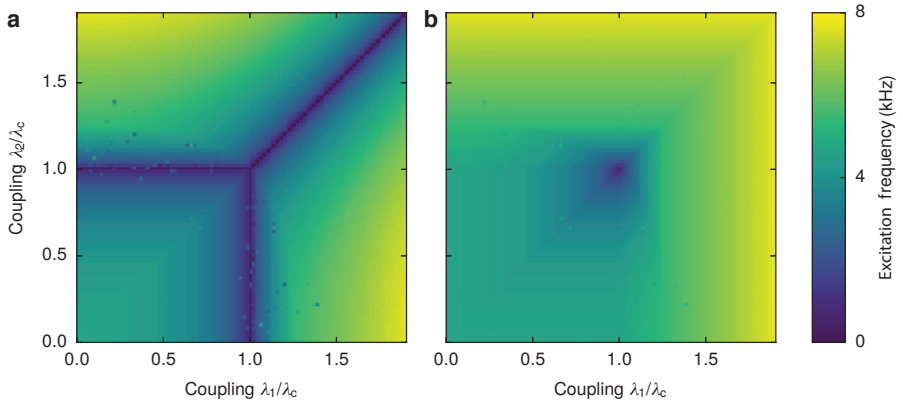

Figure 9.6: *Numerical mean-field results.* Mean-field results for the lowest **(a)** and the second lowest **(b)** eigenmode. The couplings to each cavity are normalized by the critical coupling $\lambda_{cr} = \sqrt{-\Delta_c \bar{\omega}/4}$. In Fig. 2, we probe the system on the diagonal for $\lambda_1 = \lambda_2$. The calculation includes all terms of the Hamiltonian in Eq. 9.18 and additionally atomic contact interaction, the lattice potential and cavity decay.

9.2.2 *Time evolution of the excitations*

The Hamiltonian in Eq. 9.20 separates into two parts that each describe one atomic mode coupled to a light mode. We can adiabatically eliminate the light fields and obtain the following effective Hamiltonian for each mode $\hat{c}_M$:

$$\hat{\mathcal{H}}_{exc} = \sum_{M\in A,B} \hbar\omega_- \hat{c}_M^\dagger \hat{c}_M + \frac{\hbar\lambda^2}{N\Delta}\left(\hat{c}_M^\dagger \hat{c}_0 + \hat{c}_M \hat{c}_0^\dagger\right)^2. \tag{9.31}$$

The operators $\hat{c}_M$ coincide with $\hat{c}_{i-}$ in the normal phase and are rotated in the ordered phase according to the outcome θ of the broken symmetry. In this section we explicitly include the decay rates κ_i of the cavity fields into the calculation. A probe field on cavity $i \in \{1, 2\}$ can be captured by

$$\hat{\mathcal{H}}_{pr} = \hbar\xi(t)\sqrt{N}\left(\hat{c}_i^\dagger + \hat{c}_i\right)\cos(\delta t + \phi). \tag{9.32}$$

Here, $\xi(t) = 2\eta n_{pr}(t)$ is the probe field amplitude with mean intracavity photon number $n_{pr}(t) = \frac{\eta_{pr}^2}{\Delta_c^2+\kappa_i^2}$ for a cavity decay rate κ_i. The operator $\hat{c}_i^\dagger$ ($\hat{c}_i$) creates (annihilates) an atom in the excited state for cavity i. It can be decomposed in the excitation basis $\{\hat{c}_A, \hat{c}_B\}$. Similarly to the derivation in Chap. 8, this results in the time-dependent population of the excited state

$$\langle \hat{c}_-^\dagger \hat{c}_- \rangle(t) = 4\eta^2 n_{pr} N \xi \left[\left(\frac{\omega_-}{\omega_s}\right)^2 \mathfrak{I}(y(t))^2 + \mathfrak{R}(y(t)^2)\right] \tag{9.33}$$

with mode frequency ω_s, $\hat{c}_- = \hat{c}_{1-} + i\hat{c}_{2-}$, and

$$y(t) = e^{(i\omega_s-\gamma)t}\int_0^t dt' e^{-(i\omega_s-\gamma)t'}\cos(\delta t' + \varphi). \tag{9.34}$$

The damping rate γ is phenomenologically introduced to account for atomic decay. The corresponding photon field is

$$n_{ph}(t) = \left|\alpha - \frac{4\eta^2\sqrt{n_{pr}}N}{\Delta_i + i\kappa}\left(\frac{\omega_-}{\omega_s}\right)\mathfrak{I}(y(t)) + \sqrt{n_{pr}(t)}e^{-i(\delta t+\varphi)}\right|^2. \tag{9.35}$$

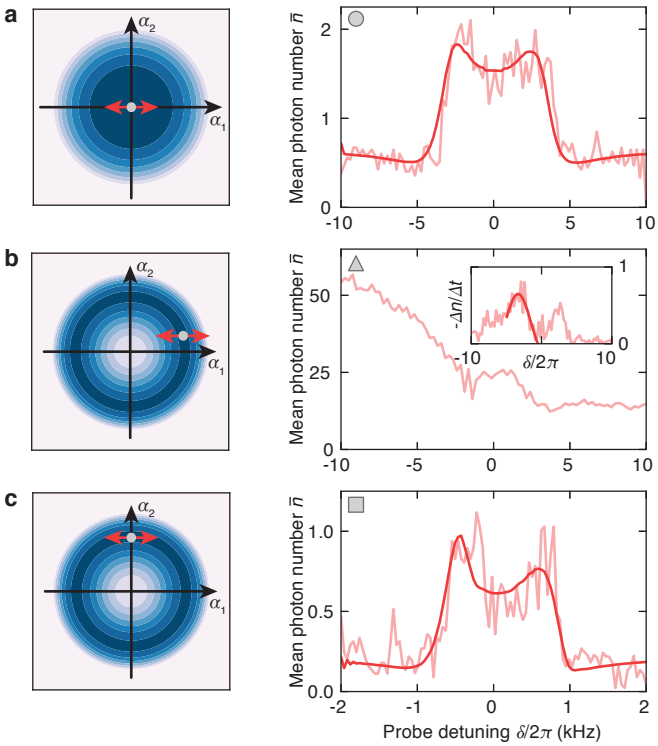

Figure 9.7: *Measuring the excitation spectrum across the phase transition.* **(a-c)** Response of the intracavity photon number to the probe field. Shaded red lines show the mean photon numbers for cavity 1, binned in intervalls of 0.2 ms and averaged over at least ten realizations. Solid lines show fits from a theoretical model. **a,** Response to a probe field of $\bar{n}_1 = 3.4(2)$ in cavity 1 whose frequency is ramped by 1 kHz/ms, measured at $16.7(4)\,\hbar\omega_{\mathrm{rec}}$ lattice depth. **b,** Response to a probe field of $\bar{n}_2 = 3.4(1)$ in cavity 2 whose frequency is ramped by 1 kHz/ms, measured at $35.9(8)\,\hbar\omega_{\mathrm{rec}}$ lattice depth. The inset displays the inferred negative derivative, representing the response as a function of δ with symmetric resonances at positive and negative detunings. The fit takes into account the negative resonance only to limit influence from the decaying order parameter. **c,** Response to a probe field of $\bar{n}_1 = 0.06(1)$ in cavity 1 whose frequency is ramped by 0.2 kHz/ms, measured at $35.9(8)\,\hbar\omega_{\mathrm{rec}}$ lattice depth.

Since the relative phase φ varies between realizations of the experiment, we perform an average $\langle n_{\mathrm{ph}}(t)\rangle_\varphi$ over $\varphi \in [0, 2\pi]$ and use the result as fit function for the response to a probe field with frequency δ relative to the transverse pump. We sweep $\delta = \delta(t) = \delta_0 + \delta' t$ over time with rate δ'.

Eq. 9.25 implies that the time evolution for probing the Goldstone mode on a previously empty cavity is equivalent to probing the system in the normal phase. We therefore use $\langle n_{\mathrm{ph}}(t)\rangle_\varphi$ as fit function to extract the resonance freqencies ω_s for the measurements in the normal phase and for the Goldstone mode in. The fit parameters are ω_s, $\sqrt{n_{\mathrm{pr}}}$, η and γ. For the Higgs mode measurements, we use a Gaussian ansatz with free frequency, width, amplitude and offset.

9.2.3 *Extracting the excitation frequencies*

The starting point of the experiment is an optically trapped, almost pure BEC of $2.02(6) \times 10^5$ ^{87}Rb atoms that we expose to the transverse pump with wavelength 785.3 nm and variable lattice depth. We study the collective excitations of the quantum gas across the phase transition by probing

Probing method

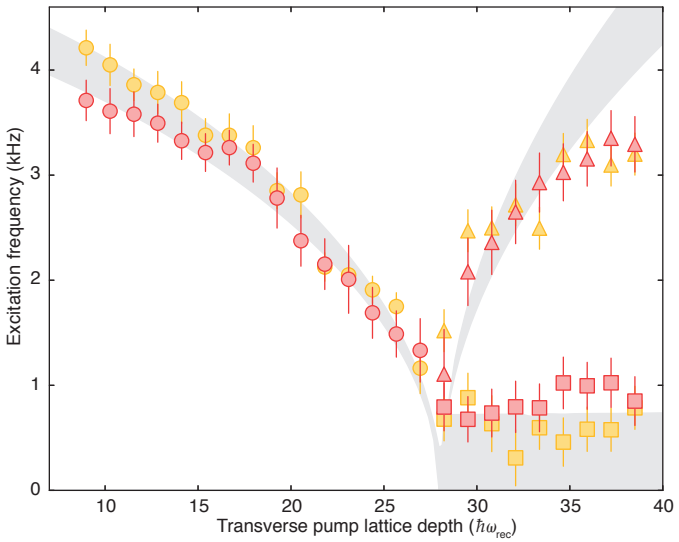

Figure 9.8: *Excitation spectrum across the phase transition.*Resonance frequencies for the normal phase (circles) and the ordered phase at high (triangles) and low (squares) frequencies extracted from the response to probe pulses in cavity 1 (red) and 2 (yellow). The gray-shaded area shows the *ab initio* prediction including experimental uncertainties. Errorbars combine fit errors and the uncertainty of the probe frequency.

it with cavity-enhanced Bragg spectroscopy, where probe photons are scattered off collective excitations into the transverse pump and vice versa. Our technique takes advantage of two key properties of optical cavities: enhancement of Bragg scattering and real-time access to the intracavity fields from leaking photons. The energy scale of the excitations is determined by the corresponding atomic recoil frequency $\omega_{\mathrm{rec}}/2\pi = 3.7\,\mathrm{kHz}$ for a transverse pump photon [223]. We prepare the system at a fixed transverse pump lattice depth and subsequently excite one of the two cavities with a probe field with time-varying detuning δ relative to the transverse pump frequency. In terms of the effective potential, this perturbs the order parameter along the quadrature of the probed cavity field (Fig. 9.7). We scan δ linearly in time from negative to positive detunings and record the intracavity photon numbers. Our technique can be regarded as a frequency-dependent extension of the method presented in [312].

Probing situation in the normal and the ordered phase

The probing situation qualitatively changes between the two phases. In the normal phase, we probe the system on initially empty cavities and observe symmetric resonances at positive and negative δ. These correspond to two-photon processes of probe and pump photons that involve the creation or annihilation of a density excitation in the system (Fig. 9.7a). The circumstances are different in the ordered phase, in which the probe is applied on top of a finite order parameter and we observe a decay of the photon numbers in both cavities at a specific detuning δ (Fig. 9.7b). We interpret this signal as a result of heating from an increased number of decaying excitations. The loss rate shows a symmetric resonance feature at positive and negative detunings. In addition, when probing weakly at detunings $\delta \ll \omega_{\mathrm{rec}}$, a second resonance pair appears, see Fig. 9.7c. Its visibility is highest when probing on an initially empty cavity. We therefore first enter the ordered phase in the presence of a symmetry breaking field along one quadrature and then ramp it down to zero before applying the probe field. Over the entire coupling range covered by our measurements, we prepare

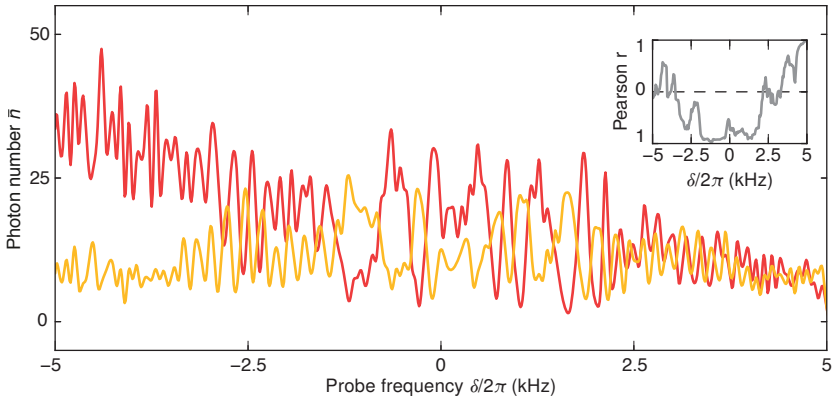

Figure 9.9: *Establishing amplitude and phase character.* Response of the system at lattice depth 38.5(8) $\hbar\omega_{\mathrm{rec}}$ to a probe field on cavity 1. The insets show the Pearson correlation coefficient, deduced from a moving window of 2 ms width of the mean photon numbers for cavity 1 (red) and 2 (yellow). All data are binned in intervals of 0.1 ms.

the system in a weakly driven situation by adjusting the resulting mean intracavity photon numbers within a range of $\bar{n}_{1,2} = 0.06(1) - 3.4(2)$.

Excitation frequencies across the phase transition

We record excitation spectra for different transverse pump lattice depths in the normal and the ordered phase. The signals can be obtained by probing either of the cavities. The resonance frequencies of the excitations are extracted from the spectra by fitting the data with a theoretical model. The combined result is shown in Fig. 9.8. In the normal phase we observe decreasing resonance frequencies on approach to the critical point. When entering the ordered phase, two branches appear, one resonance remaining at frequencies small compared to ω_{rec}, and a second one with rising frequencies. We find good agreement among the measurements for the two cavities over the entire covered range. The excitation frequencies can be well-described with a microscopic model, which is related to previous theoretical work on spin systems with continuous symmetries [280, 281, 338]. The theoretical prediction is obtained from the calculation in Sec. 9.2.1, where uncertainties in the experimental parameters lead to the shaded gray area. We consider a 20% systematic error in the atom numbers, fluctuations of the cavity resonance and the transverse pump laser frequency of 30 kHz each, as well as a density uncertainty from the trapping frequency measurements.

For the measurements in the superfluid phase and for the Higgs mode, we fix the detunings at $(\Delta_1^{\mathrm{eq}}, \Delta_2^{\mathrm{eq}})$ and prepare the system at a given coupling strength by linearly increasing the transverse pump intensity within 50 ms to lattice depths up to 38.5(8) $\hbar\omega_{\mathrm{rec}}$, with ω_{rec} being the recoil frequency for a transverse pump photon. The measurements for the Goldstone mode were taken by first ramping up the transverse pump lattice within 30 ms at an imbalanced detuning of $(\Delta_1/2\pi, \Delta_2^{\mathrm{eq}}/2\pi) = (-4.0, -2.9)$ MHz for the case of probing cavity 1 or $(\Delta_1^{\mathrm{eq}}/2\pi, \Delta_2/2\pi) = (-3.2, -3.7)$ MHz for probing cavity 2, and then approaching the balanced situation at $(\Delta_1^{\mathrm{eq}}/2\pi, \Delta_2^{\mathrm{eq}}/2\pi)$ in a linear ramp of 20 ms length. This effectively creates a symmetry breaking field during the preparation that sets the order parameter in the supersolid phase to have only one cavity populated. This way an empty cavity can be probed, which increases the signal quality. In some realizations the order parameter evolves during probing, and we post-select for zero order parameter in the probed cavity. The speed of the frequency ramp for the probe

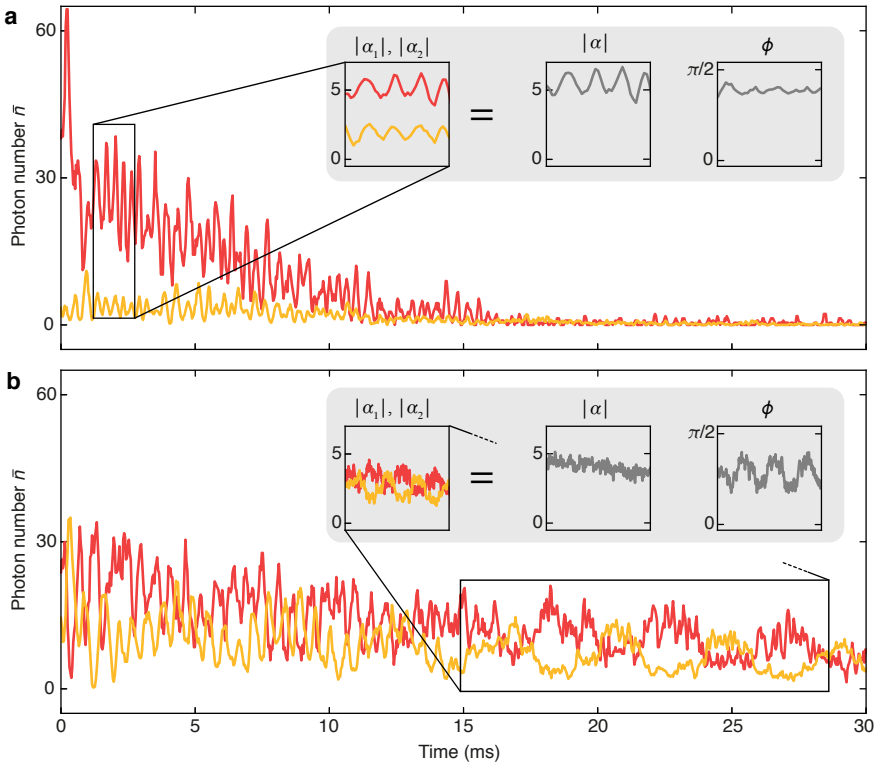

Figure 9.10: *Dynamics of Higgs and Goldstone excitations.* Response of the system at lattice depth $38.5(8)\,\hbar\omega_{rec}$ after a probe pulse of 1 ms length with mean photon number $\bar{n}_1 = 2.4(2)$ in cavity 1. **a,** Evolution following a pulse at $\delta/2\pi = 2.5\,\text{kHz}$. From the photon traces we extract the real and imaginary part of the order parameter via $|\alpha_i| = \sqrt{\bar{n}_i}$ (inset). Transforming the order parameter into polar coordinates, $\alpha = \alpha_1 + \alpha_2 = |\alpha|\, e^{i\phi}$, reveals an oscillation of the amplitude $|\alpha|$ at nearly constant phase ϕ. The order parameter decreases over $\sim$ 15 ms. **b,** Evolution after a pulse at $\delta/2\pi = 0.5\,\text{kHz}$. The coordinate transform in the inset shows phase oscillations of the order parameter without significant appreciable change of its amplitude. All data are averaged over an interval of 0.1 ms.

field is 0.2 kHz/ms for the Goldstone mode measurements and 1 kHz/ms for the other measurements.

9.3 REAL-TIME OBSERVATION OF HIGGS AND GOLDSTONE MODES

9.3.1 Establishing amplitude and phase character

The separation of the excitation frequencies inside the ordered phase into a high and a low frequency branch suggests an interpretation in terms of a Higgs and a Goldstone mode. In order to carry out a direct test of the distinctive amplitude and phase character of the modes, we exploit the fact that the two cavity fields form the real and the imaginary part of the order parameter, thereby providing access to both quadratures. We prepare the system within the ordered phase at $38.5\,\hbar\omega_{rec}$ transverse pump lattice depth and apply a frequency-ramped probe field weak enough not to influence the lifetime of the system. The recorded evolution of the intracavity photon numbers is shown in Fig. 9.9. We observe correlated signals for $|\delta|/2\pi \gtrsim 2.5\,\text{kHz}$ and anticorrelated signals at smaller probe detunings, consistent

with the resonance frequencies shown in Fig. 9.8. From their amplitude and phase character, we identify the excitations as Higgs and Goldstone modes.

Correlated and anticorrelated light fields

With regard to the atomic part of the excitations, these correspond to fluctuations in the strength and the position of the density modulation, as illustrated in Fig. 9.3. The atomic coupling to delocalized cavity photons is equivalent to an effective atom–atom interaction of global range [81, 237]. As a consequence, Higgs and Goldstone excitations are not inhibited, as it is the case in short-range interacting low-dimensional systems without long-range order [1]. The global nature of the interaction furthermore results in a rigid crystal structure that inhibits the presence of excitations at non-zero wavenumbers, in contrast to theoretical studies on supersolid helium [247]. The presence of a Higgs mode is ensured by the invariance of the system under an exchange of α_1 and α_2, which enforces a Lorentz-invariant time evolution analogous to the particle-hole symmetry in e. g. superconductors and optical lattices at half-filling [315]. Finite-temperature effects are not expected to overdamp the Goldstone mode [241].

9.3.2 *Dynamics after a pulse*

Using the direct access to both quadratures of the order parameter we study the excitation dynamics induced by a strong probe pulse with constant detuning. We first ramp up the transverse pump within 50 ms to a lattice depth of $38.5(8)\,\hbar\omega_{\mathrm{rec}}$ at $(\Delta_1^{\mathrm{eq}}, \Delta_2^{\mathrm{eq}})$. Following a pulse of 1 ms length at $\delta/2\pi = 2.5\,\mathrm{kHz}$, we observe correlated intracavity photon numbers signaling Higgs excitations, see Fig. 9.10a. The evolution of the light fields shows a damping of the Higgs modes over $\sim 15\,\mathrm{ms}$, accompanied by a decreasing order parameter. When applying a pulse at $\delta/2\pi = 0.5\,\mathrm{kHz}$ anticorrelated intracavity photon numbers are visible, showing the presence of Goldstone excitations, see Fig. 9.10b. We transform the cavity fields to polar coordinates, according to $(\alpha_1, \alpha_2) \to (|\alpha|, \phi)$ to reveal the Higgs and Goldstone modes as amplitude and phase excitations. The persisting low-frequency Goldstone mode is overlayed by a second fast-oscillating phase mode that decays within $\sim 15\,\mathrm{ms}$.

9.4 ENGINEERING A MASSIVE GOLDSTONE MODE

Sensitivity of the Goldstone mode to symmetry breaking fields

A hallmark of the Goldstone mode is its sensitivity to deviations from the continuous symmetry. Goldstone modes only show a vanishing excitation frequency for perfect symmetries in the absence of symmetry breaking fields or further interactions. An analogous behavior is known e. g. in the context of chiral symmetry breaking, approximate symmetries, extra dimensions and the mass hierarchy problem [339, 340]. The continuous symmetry that is broken in our system is the result of balanced coupling to two cavities, which each exhibit parity symmetry only. We can generate an adjustable symmetry breaking field along each quadrature of the order parameter individually by controlling the coupling to each cavity mode through its detuning from the transverse pump frequency. For an imbalance Δ in the detunings, this results in an asymmetric effective potential with only two ground states on the axis of the more strongly coupled cavity field. The evolution of the resonance frequency of the Goldstone mode for various Δ around the balanced situation is shown in Fig. 9.11. While it tends to zero for vanishing Δ, we observe an increased resonance frequency for larger $|\Delta|$, approaching

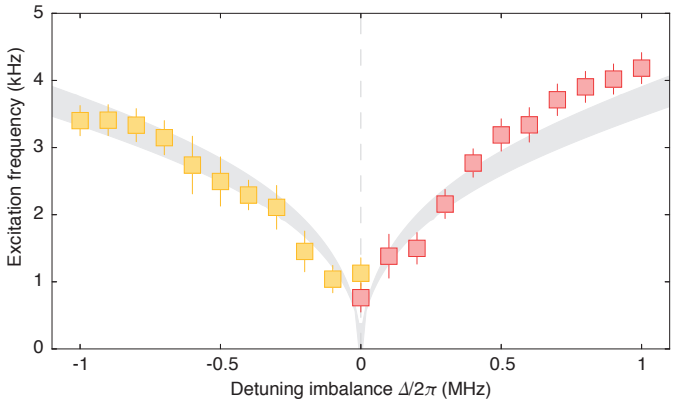

Figure 9.11: *Tunable mass of the Goldstone mode.* Resonance frequency as a function of the detuning imbalance Δ. For positive (negative) Δ, the mode couples to a probe field in cavity 1 (2) and its resonance frequency is shown in red (yellow). The resonance frequencies are derived from photon traces similar to Fig. 9.7c, averaged over at least ten realizations. The gray-shaded area shows the theoretical prediction including experimental uncertainties. The dashed line illustrates the situation of balanced coupling to both cavities. Error bars combine fit errors and the uncertainty of the probe frequency.

the soft mode associated to self-organization with a single cavity. The data are in agreement with our microscopic model.

A measurement for detuning imbalance Δ corresponds to the cavity detunings $(\Delta_1/2\pi, \Delta_2/2\pi) = (\Delta_1^{\mathrm{eq}} + \Delta/\sqrt{2}, \Delta_2^{\mathrm{eq}} - \Delta/\sqrt{2})$. To prepare this measurement point, we first ramp up the transverse pump lattice within 30 ms at a far-imbalanced detuning of $(\Delta_1/2\pi, \Delta_2/2\pi) = (\Delta_1^{\mathrm{eq}} + 0.7\,\mathrm{MHz}, \Delta_2^{\mathrm{eq}} - 0.7\,\mathrm{MHz})$ for $\Delta > 0$ and $(\Delta_1/2\pi, \Delta_2/2\pi) = (\Delta_1^{\mathrm{eq}} - 0.7\,\mathrm{MHz}, \Delta_2^{\mathrm{eq}} + 0.7\,\mathrm{MHz})$ for $\Delta < 0$. We then approach the point for the measurement in a linear ramp. Afterwards, the probe frequency is ramped at a rate of 0.5 kHz/ms from -5 kHz to 5 kHz.

Thanks to the control over the effective potential landscape, our approach introduces a model system for studies on discrete and continuous symmetries. The unique real-time access to the system dynamics offers exciting prospects to examine the decay channels and coupling of Higgs and Goldstone modes [341].

Summary of the spectroscopic measurements

The spectrocopic measurements in all four phases are summarized in Fig. 9.12. The phase boundaries as a function of the transverse pump lattice depth and the detuning imbalance Δ are shown on the bottom plane in Fig. 9.12. The spectra observed in Fig. 9.8 and 9.11 can be interpreted as the excitations for the supersolid phase and the SO1 and SO2 phases, respectively.

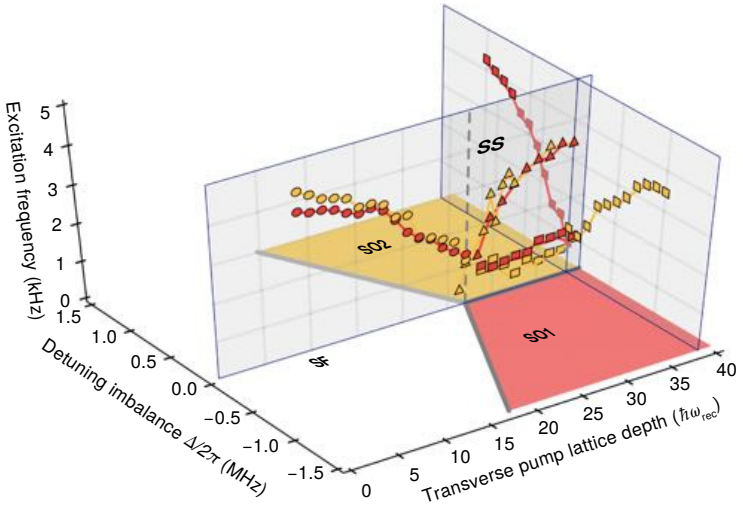

Figure 9.12: *Full phase diagram with excitation spectrum.* This figure shows the spectroscopic results of the paper in the context of the phase diagram of the system (bottom plane). For $\Delta = 0$, an increasing transverse pump field leads to a phase transition from superfluid (SF) to supersolid (SS). The broken U(1) symmetry supports the massless Goldstone mode (lower branch) and massive Higgs mode (upper branch). Leaving the $\Delta = 0$ line beyond critical coupling, self-organisation is limited to only cavity 1 (SO1, $\Delta < 0$) or cavity 2 (SO1, $\Delta > 0$), accompanied by a crossover from continuous to discrete symmetry and a rise of the mass of the lower branch.

10 CRITICAL BEHAVIOUR

At the critical point between two states of matter, the relevant time and length scales show a universal behaviour, independent from the microscopic details of the phase transition. An active field of research is the influence of dissipation on the critical behaviour, as well as the multicritical behaviour arising when the critical points of two phase transitions fall together. In this chapter, we first describe the framework of critical phenomena in general and then present measurements of the density fluctuations close to critical and multicritical points in a driven-dissipative system. In particular, we extract the critical exponent of the superfluid-supersolid phase transition.

CHAPTER CONTENTS

Phase transitions

A phase of a thermodynamic system has uniform physical properties that can change during a phase transition as a result of a varying external condition. The change can occur in a continuous or discontinuous manner. While the specific property that changes depends on the studied system, many thermodynamic quantities show a similar behaviour at a phase transition.

First order and continuous phase transitions

Phase transitions are classified based on the behaviour of the free energy as a function of the external parameter that is adjusted during the transition [342, 343]. First-order phase transitions involve a latent heat. The system has to release or add energy when crossing the transition. In contrast, continuous phase transitions show a vanishing first order derivative of the free energy during the transition. They exhibit a divergence of the susceptibility and the characteristic length and time scales.

Critical behaviour

The first observation of a critical phenomenon was made in a vessel filled with carbon dioxide as critical opalescence [344], see Fig. 10.1. Below the boiling temperature, a liquid and a gaseous state is visible. However, when approaching the critical point fluctuations are enhanced and increase their length scale, causing gas bubbles of increasing size. When the size of the fluctuations becomes comparable to optical wavelengths, the light is Rayleigh scattered and the mixture turns opaque. At the critical point, the distinction between gas and liquid vanishes and both phases coexist.

This was a first indication for the absence of a length scale. If the correlation length exceeds the system size, critical fluctuations on all length scales can occur. Similar behaviour has also been observed for other physical quantities, for example the susceptibility and the elementary excitations.

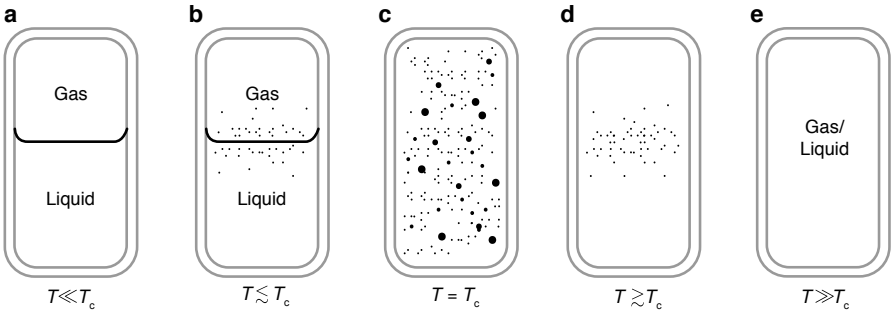

Figure 10.1: *Critical opalescence.* **a,** Two different phases, for instance a fluid and a gas, are spatially separated. **b,** As the critical point is approached, the extensions of the phases begin to fluctuate over increasingly large length scales. **c,** As the density fluctuations become of size comparable to optical wavelengths, the light is Rayleigh scattered and causes the transparent liquid to appear opaque. At the critical point, the length scale of the diverges and density fluctuations of any size appear. **d,** Above the critical point, the length scale of the fluctuations decreases and the two phases remain separates. **e,** At temperatures far above the critical point the two phases are well separated and fluctuations are suppressed.

10.1 CRITICAL BEHAVIOUR AT A PHASE TRANSITION

Critical phenomena occur at a continuous phase transition, but are absent at first order phase transitions. Their theoretical description has been one of the most challenging open questions in physics during the last century. In this section, we develop a quantitative description of the critical behaviour based on a mean-field expansion, both for classical and quantum phase transitions. Finally, we discuss the influence of global interactions to the system, which are present in our experiment.

10.1.1 Classical critical points

Scaling of the correlation length

We consider a classical phase transition from a normal to the ordered phase that is driven by thermal fluctuations. The system is brought from one phase to the other by changing the temperature T across the critical point at T_c. The two phases are distinguished by a local order parameter $\Theta(\mathbf{r})$ that is only nonzero in the ordered phase. Correlations of the order parameter between different parts of the system usually decay exponentially with distance r, described by $C(r) \propto e^{-r/\xi}$, where ξ is the correlation length. The correlation length is determined by the microscopic properties of the system and is usually small compared to the system size.

When approaching the critical point, the correlation length shows a divergence according to a power-law scaling

$$\xi \propto |T - T_c|^{-\nu}, \tag{10.1}$$

where ν is called the critical exponent. The diverging correlation length modifies the exponential decay to a power law decay of the correlations with $C(r) \propto r^{-\eta}$ with the critical exponent η. The correlations are not determined by the correlation length any more and the system is scale-free.

The absence of a characteristic length scale is an unusual property for a system. It indicates that its microscopic properties are irrelevant for the macroscopic description. As a consequence, critical exponents are not only

valid for the specific system but are universal quantities that only depend on few general properties [342]:

- Symmetry relations: most phase transitions are associated with the breaking of a symmetry. The order parameter is then a representation of the underlying symmetry group. The type of symmetry that is broken affects the number of accessible ground states across the phase transition, which in turn influences the scaling behaviour.
- Dimensionality of space: it is intuitive that the fluctuations of a system are reduced when the number of nearest neighbours of the constituents increases. For instance, the XY model shows a phase transition in 3D with a finite magnetization, whereas fluctuations inhibit long-range order in 1D and allow for quasi-long-range order in 2D only [345, 346].
- Interaction range: alternatively, the range of the interaction can change the critical behaviour. It acts in a similar way as the coordination number, since an interaction of longer range effectively increases the number of relevant neighbours.

Universality hypothesis

The so-called *universality hypothesis* assumes that the critical exponent is determined by exactly these three properties. It is motivated and supported by experimental measurements of systems in very different contexts. It allows to sort all possible phase transitions in a limited number of universality classes.

Landau theory

Critical scalings go beyond a scaling of the spatial correlations. In the following, we derive the mean-field critical exponents in Landau theory, based on the free energy potential

$$\mathcal{F}(\Theta) = \frac{r}{2}\Theta^2 + \frac{g}{4}\Theta^4. \tag{10.2}$$

The coefficients r and g are real values with $r \propto |T - T_c| = |t|$. Analogously to the discussion in Sec. 5.1.1, we use the condition $\partial\mathcal{F}/\partial\Theta|_{T=\text{const}} = 0$ to obtain the order parameter $\Theta = \pm\sqrt{-r/g}$ below the critical temperature. We find the universal relation $\Theta \propto |t|^\beta$ with the critical exponent $\beta = 1/2$, while the amplitude is system dependent. The heat capacity is given by the relation $C = -1/T\partial^2\mathcal{F}/\partial T^2$. It vanishes in the normal phase and acquires a constant value in the ordered phase, yielding a critical exponent $\alpha = 0$. The susceptibility is inversely proportional to the curvature of the effective potential, $\chi^{-1} \propto \partial^2\mathcal{F}/\partial\Theta^2 \propto |t|$. Rewriting this expression to $\chi \propto |t|^{-\gamma}$ we obtain $\gamma = 1$. Finally, the exponent δ is associated to the behaviour in the presence of a symmetry breaking field, captured by an additional term $-h\Theta$ in the free energy potential. It is defined as $\Theta \propto h^{1/\delta}$ and describes the behaviour of the order parameter discontinuity across the coexistence line, also called the *critical isotherm*. We minimize the free energy potential at $t = 0$, including the symmetry breaking field, and obtain $\Theta \propto h^{1/3}$, yielding the exponent $\delta = 3$.

Scaling relations

General scaling arguments as well as experiments suggest that various critical exponents are not independent but obey certain constraints [347]. One relation involving the first three critical exponents is the *Rushbrooke identity*:

$$\alpha + 2\beta + \gamma = 2 \tag{10.3}$$

Soon thereafter, the *Widom identity* was found, including also the exponent for the critical isotherm [348]:

$$\gamma = \beta(\delta - 1) \tag{10.4}$$

There is also the *hyperscaling relation*, which additionally involves the dimension d:

$$2 - \alpha = \nu d \tag{10.5}$$

Finally, we can connect the critical exponents of the susceptibility with the correlation length via:

$$\gamma = \nu(2 - \eta) \tag{10.6}$$

These four constraints reduce the number of independent critical exponents to only two. Although the scaling relations in Eqs. 10.3-10.6 are derived within the renormalization group approach, the critical exponents predicted by Landau theory also fulfill the relations.

Conformal field theories

In a broader context, the scaling relations are the result of certain symmetries that the system exhibits at the critical point, which correspond to translations, rotations and dilations. They are described by the following transformations

$$\begin{aligned} &\mathbf{r} \to \mathbf{r} + \mathbf{a} \quad \text{for } \mathbf{a} \in \mathbb{R}^d \\ &\mathbf{r} \to \alpha\mathbf{r} \quad \text{for } \alpha \in \mathbb{R} \\ &\mathbf{r} \to M\mathbf{r} \quad \text{for } M \in SO(d) \end{aligned} \tag{10.7}$$

These transformations form a symmetry group called the *conformal group*. Studies on the underlying field theory that describes the system and inherits these symmetries led to the theoretical development of conformal field theories [349].

10.1.2 Quantum critical points

The scaling behaviour at a critical point is not limited to classical phase transitions. Very similar scaling is also observed for quantum critical phenomena, which occur at $T = 0$. However, the exponents are expected to change, since the critical behaviour is governed by quantum fluctuations instead of thermal fluctuations. Many systems lacking a microscopic theory benefit from the scaling relations to make predictions about the critical behaviour and the localion of critical points.

Landau theory at $T = 0$ does provide a framework to describe the quantum critical behaviour on a mean-field level, i.e. in the limit of infinite coordination number. This is in good approximation to our system, since the photon-mediated interactions are of global range. In fact, we have already encountered some critical exponents in the previous chapters. Let us consider the situation of a single order parameter Θ and the Landau expansion as introduced in Eq. 5.1

$$\mathcal{H}_\lambda(\Theta) = \frac{r}{2}\Theta^2 + \frac{g}{4}\Theta^4 + \mathcal{O}(\Theta^6), \tag{10.8}$$

Critical exponents

with r, g functions of λ. The expectation value of Θ in equilibrium is given by the minimum of $\mathcal{H}_\lambda(\Theta)$ and we obtain $\Theta_0 = (-r/g)^{1/2}$. The critical exponents are typically labelled with Greek letters. We expand the coefficient

r linearly in $r \propto (1 - \lambda^2/\lambda_{cr}^2)$ and obtain the critical exponent $\beta = 1/2$ for the order parameter. This is in accordance with the analytical solution for self-organization with orthogonal transverse pump [234, 236].

We already came across a second critical exponent when discussing the susceptibility in Chapter 8. It is related to the curvature of the effective potential:

$$\chi^{-1} \propto \frac{\partial^2 \mathcal{H}}{\partial \Theta^2} \propto \left(1 - \frac{\lambda^2}{\lambda_{cr}^2}\right) \tag{10.9}$$

This gives a critical exponent $\gamma = -1$ for the susceptibility. Since the soft mode frequency $\omega^2 \propto \chi^{-1}$, it shows the same critical behaviour as the order parameter with $\beta = 1/2$.

10.1.3 Globally interacting systems

Global correlations

The self-organization phase transitions studied in the context of this thesis can be described as a globally interacting system (see Sec. 5.1.3 and 7.1.3). The distance between two atoms does not affect the interaction strength (up to a periodicity set by the wavelength of the cavity mode) and density modulations triggered by atom-cavity coupling are always global. We can consider the system in the limit where the correlation length exceeds the system size. The absence of a finite correlation length is an unusual property in condensed matter systems. In the following we describe some qualitative differences compared to phase transitions that are driven by short-range interactions.

Absence of domains and defects

The global nature of the interactions forces the density modulation to have the same strength at each point in space. All variations of the density modulation happen in a perfectly homogeneous way. This property suppresses the presence of local structures such as defects or finite size domains. The value of the order parameter Θ is spatially independent, yielding a perfectly correlated system with all atoms in the same single particle state.

Only global excitations

The elementary excitations are restricted to the zero momentum limit, that is, the dispersion relation has only a single point at $k = 0$ (see Chap. 8 and 9). We can interpret this behaviour as an extremely stiff solid with a high sound velocity c_s at which correlations spread. The dispersion relation $\omega = c_s k$ diverges for $k \neq 0$, shifting the associated frequencies to an unreachable level.

Critical exponents

In general, computing critical exponents for long-range interacting systems is a challenging task. Yet, for global interactions the critical exponents can be calculated according to Landau theory. The critical exponents β for the order parameter and γ for the susceptibility remain intact, as does the exponent δ for the critical isotherm. However, since the correlation length is always divergent, the critical exponents ν and η become obsolete. With that, the previously discussed scaling relations are not relevant any more, since they rely on a finite exponent ν. Similarly, the connection with conformal field theories relies on short-range interactions and becomes invalid [350].

Effectively infinite dimensions

Global interactions are equivalent to an infinite dimensionality, since the effective coordination number (number of nearest neighbours) is infinite in both cases. In this limit, the mean-field expansion in Landau theory becomes exact again and ceases to be an approximation. The effectively infinite dimensions also make the actual dimensionality of the system irrelevant. Whether the atoms are confined in one, two or three dimensions does not

affect the critical behaviour since the effective coordination number remains the same.

Diverging time scale

The correlation length ξ in the vicinity of the critical point is usually connected to a diverging time scale τ by the speed of sound, $\xi \sim c_s\tau$. While ξ is infinite for global interactions, the characteristic time scale τ retains its divergence properties. The reason is that τ is set by the energy of the elementary excitations, which soften at the phase transition (see Chap. 8 and 9).

10.2 DISSIPATIVE CRITICAL BEHAVIOUR

Equilibrium phase transistions...

The concept of phase transitions stems from equilibrium thermodynamics, which is based on the principle that a system is in its stationary state. We have seen that a phase transition in an equilibrium system is characterized by an abrupt change in the ground state, accompanied by a non-analyticity in certain thermodynamic quantities.

...vs. non-equilibrium phase transitions

However, the concept of phase transitions can be generalized to non-equilibrium systems, which are brought far from both the ground state and equilibrium conditions. This can be realized either by a sudden change in the system's parameters, or by coupling it to an external drive. The existence of out-of-equilibrium phase transitions has raised the questions whether these systems also exhibit critical behaviour, and in which way its properties differ from equilibrium critical behaviour.

10.2.1 Non-equilibrium phase transitions

Phase transitions with unitary dynamics

Non-equilibrium phase transitions are classified into two categories. One type of non-equilibrium phase transitions occurs in systems that are described by a hermitian Hamiltonian [351]. Such phase transitions occur in systems that are initially prepared far from the stationary state and then approach equilibrium state under unitary dynamics. In the thermodynamic limit, the time scale to approach equilibrium state can diverge and may never reach a stationary state. Examples for such phase transitions include ordering systems, glasses and spin glasses.

Non-unitary dynamics

In contrast, for the second class of non-equilibrium phase transitions the underlying Hamiltonian is not hermitian. Even for a finite size, such systems may not have a stationary state, for instance, when combining different dynamics in reaction-diffusion models or epidemics [351]. These systems are not related to equilibrium models and are sometimes referred to as *genuine non-equilibrium systems*.

We are instead interested in *driven-dissipative phase transitions*, which occur in a non-hermitian environment but can reach a stationary state. Such models can be created by generating external currents with a drive. The stationary state corresponds then to a situation where drive and dissipation are balanced. In a dissipative phase transition the steady state abruptly changes as a system parameter is varied [352]. By tailoring the coupling to the environment and the driving it is possible to prepare a desirable steady state in the non-equilibrium system that behaves reminiscent of a continuous phase transition.

10.2.2 Dissipative phase transitions

Analogy of driven-dissipative and equilibrium phase transitions

Driven-dissipative phase transitions can be described in an analogous way

to quantum phase transitions in closed systems. The ground state $|\psi_0(\lambda)\rangle$ of a closed system that is described by a Hamiltonian $\mathcal{H}(\lambda)$ fulfills the condition $\mathcal{H}(\lambda)\,|\psi_0(\lambda)\rangle = E_0(\lambda)\,|\psi_0(\lambda)\rangle$, where $E_0(\lambda)$ is the ground state energy and λ is a system parameter. As long as $\mathcal{H}(\lambda)$ is gapped, that is, the energy difference between $E_0(\lambda)$ and the first excited state is finite, any small change in λ alters the physical properties of $|\psi_0(\lambda)\rangle$ smoothly. Only if the energy gap closes at a given $\lambda = \lambda_c$, the properties may change abruptly and a phase transition occurs.

A driven-dissipative system that obeys Markovian dynamics can be described by a Lindblad master equation [352]

$$\frac{d\rho}{dt} = \mathcal{L}\rho \tag{10.10}$$

where ρ is the density matrix and $\mathcal{L}$ is the Liouvillian superoperator [353]. The steady state ρ_0 is then a zero eigenvector to the Liouville superoperator, i. e. $\mathcal{L}(\lambda)\rho_0(\lambda) = 0$. We find that this description is analogous to the quantum phase transition if one replaces $\mathcal{H}(\lambda) - E_0(\lambda) \to \mathcal{L}(\lambda)$. Although the Hamiltonian and the Liouvillian are different mathematical objects (hermitian operator vs. hermiticity-preserving superoperator), the critical point is identified by a closing gap in their respective spectrum. Although driven-dissipative systems in general cannot be mapped onto an effective closed system, the stationary state of a driven-dissipative system may even share the same mean-field properties as the ground state of an effective Hamiltonian [233]. This approach has been applied in the previous chapters.

One active field of research tries to generalize the concept of critical behaviour to non-equilibrium quantum phase transitions [354]. Such phase transitions can occur in driven-dissipative systems at zero temperature. It remains an open question how vacuum fluctuations from the environment influence the critical behaviour at a phase transition. The generalization to driven-dissipative systems requires to introduce new universality classes with an even larger number than for the equilibrium systems, since time becomes an extra degree of freedom [352, 355–357].

Influence of dissipation on the critical behaviour

In general, the coupling to the environment by the drive and the dissipation channel implies additional fluctuations in the system. Dissipation acts as an effective temperature and typically shifts the critical point to higher values of the relevant system parameter [358]. In addition, the critical exponents and even properties of the phases may be altered by the environment [354]. Near the critical point, a scale-independent effective temperature emerges and dominates the critical dynamics [359]. Accordingly, the coherent dynamics at a quantum phase transition is significantly affected by the decoherent thermalization. The decoherence exponent cannot be captured by any equilibrium model and places the driven-dissipative system in a new universality class beyond the equilibrium classification. It has been found that the low-frequency spectral properties of the bath are crucial for the critical dynamics [360]. However, the precise interplay of dissipation, interactions, dimensionality and symmetry breaking remains currently elusive and further theoretical and experimental effort is required to develop a classification scheme for universal critical behaviour in driven-dissipative systems.

10.2.3 Self-organization and dissipation

Self-organization as a driven-dissipative phase transition

The self-organization phase transition in an atom-cavity system constitutes

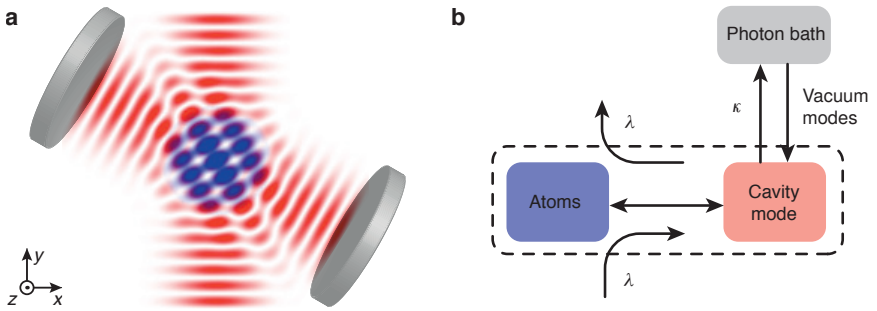

Figure 10.2: *Driven-dissipative atom-cavity system* **a,** Experimental scheme. A transverse pump field (red) couples a BEC in the ground state to an excited momentum state. The induced phase transition to a self-ordered state is of driven-dissipative character and can be monitoring in real-time by recording the output photons. **b,** Open-system description of the coupled atom-cavity system. The atomic and the photonic mode are coupled via the transverse pump with strength λ. The decay of the cavity mode can be described as a dissipative coupling to a zero-temperature bath of electromagnetic vacuum field modes.

a driven-dissipative phase transition. A schematic illustration of the setup is shown in Fig. 10.2. A BEC is subject to a coherent drive in form of the transverse pump. The coupling of the condensate to the cavity lead to an exchange of cavity photons and atomic excitations. Eventually the photons leave the cavity by leaking through the mirrors, thereby introducing the dissipative character to the system. The photon decay can be interpreted as a coupling of the system to a photon bath with zero temperature.

Real-time access to density fluctuations

The driven-dissipative character leads to an additional advantage when it comes to observables of the system, since the photon dissipation provides a tool to measure the intracavity photon number in real time. We use this access to measure the incoherent field in the vicinity of the phase transition.

The critical behaviour of the system has been theoretically described with a quantum Langevin equation [313], and observed in terms of the critical photon fluctuations as well as the spectrum of the cavity field [314]. The measured critical exponents of $0.9(1)$ and $0.7(1)$, respectively, are to be compared with the theoretical prediction of 1 [361], or possibly lower due to collisional interactions [360]. Our experimental setup includes two optical cavities whose photon decay rates differ by around a factor of five (see Chap. 4). This allows us to study the influence of dissipation for two strengths and benchmark the results with previous measurements.

We start with a measurement of the density fluctuations when approaching the self-organization phase transition with cavity 1. We prepare a BEC of ^{87}Rb in the two-cavity setup and set the detuning to cavity 2 to $\Delta_2/2\pi = -10.0\,\mathrm{MHz}$, far below the critical point for the employed transverse pump powers. In contrast, the resonance frequency of cavity 1 has a detuning of $\Delta_1/2\pi = -2.5\,\mathrm{MHz}$ from the transverse pump frequency. We increase the transverse pump power over 170 ms to its final value corresponding to $\sim 1.1\lambda^2/\lambda_c^2$ and measure the intracavity photon number through the photons leaking from the cavity.

The result for an average over 328 realizations is shown in Fig. 10.3a. We observe a progressively increasing mean intracavity photon number with increasing transverse pump power until an abrupt rise marks the transition to the self-ordered phase. The exact transition point depends on the total atom number, which changes by around 5 % between different experimental

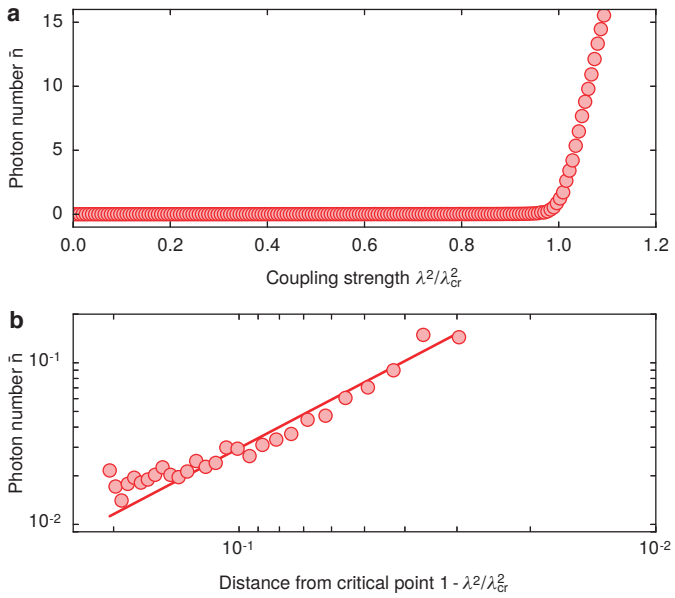

Figure 10.3: *Fluctuations at the phase boundary in cavity 1.* **a,** Mean intracavity photon number $\overline{n}_1$ in cavity 1 during a ramp of 170 ms length up to a transverse pump lattice depth of $26(1)\,\hbar\omega_{rec}$ at a pump-cavity detuning of $\Delta_1/2\pi = -2.5$ MHz. The data are binned in intervalls of 1 ms. **b,** The data between $85-97\,\%$ are shown on a double logarithmic scale. We extract a critical exponent of 1.32(3) from a fit to the data.

realizations. We therefore first extract the critical point separately in each realization, convert the time axis to increasing coupling and finally average over all realizations.

The same data is displayed in Fig. 10.3b on a double logarithmic scale for the range of $85-97\,\%$ of the critical coupling. The data at lower coupling strengths has been excluded because of significant background noise. A power-law fit to the data reveals a critical exponent of $\beta = 1.32(3)$, significantly higher than in previous measurements [313, 314].

We repeat the measurement for cavity 2 by adjusting the resonance frequency for the other cavity far enough from the transverse pump to suppress the coupling. Again, we linearly increase the transverse pump lattice depth, but this time with the detunings $\Delta_1/2\pi = -10$ MHz and $\Delta_2/2\pi = -2.4$ MHz, thereby suppressing the coupling to cavity 1. The result is shown in Fig. 10.4. The power-law fit to the same data range yields a critical exponent of 1.36(7), consistent with the measurement of cavity 1.

We conclude that we do not find evidence for a change in the critical behaviour when the dissipation rate changes. A possible explanation is that in both cases the dissipation rate was above the other relevant time scales.

10.3 MULTI-CRITICAL BEHAVIOUR

Research on driven-dissipative phase transitions is an active field of research, but theoretical and experimental studies have focussed on systems with a single order parameter [313, 362–365]. The interplay of two order parameters has been studied extensively in the classical limit for equilibrium phase transitions, where the simultaneous criticality of two order parameters at a multicritical point is expected to cause a change from one universality class to another [255]. However, extensions of these concepts to quantum

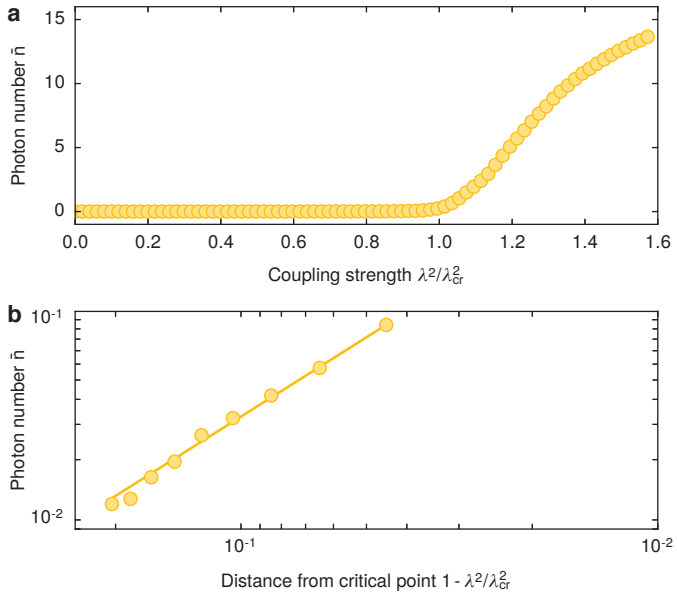

Figure 10.4: *Fluctuations at the phase boundary in cavity 2.* **a,** Mean intracavity photon number $\overline{n}_2$ during a ramp of 100 ms length up to a transverse pump lattice depth of $38(1)\,\hbar\omega_{\mathrm{rec}}$ at a pump-cavity detuning of $\Delta_2/2\pi = -2.5$ MHz. The data are binned in intervalls of 1 ms. **b,** The data between $85-97$ % are shown on a double logarithmic scale. We extract a critical exponent of 1.36(7) from a fit to the data.

systems or driven-dissipative systems have proven to be challenging [366, 367]. Experimental evidence has remained elusive, since investigations of a critical point require both a fine-tuning of the Hamiltonian parameters and the access to suitable observables to detect the critical dynamics.

10.3.1 Multicritical points

A systematic mean-field analysis of multicritical points was triggered by the quest for supersolid helium [247], and soon after analyzed in detail for anisotropic antiferromagnetic systems [260, 368–371]. The presence of multicritical points can be explained in the canonical example of two competing order parameters. Here the phase boundaries separating the normal and the two ordered phases intersect for one particular choice of control parameters. At this point, both order parameters become critical simultaneously, and the system is called *multicritical*.

Classes of multicritical points

Multicritical points are classified according to the total number of intersecting boundaries with continuous phase transitions. We distinguish three different scenarios, as illustrated in Fig. 10.5. If the two ordered phases are separated by a first order phase transition, the phase boundaries separating the normal and the two ordered phases are the only critical ones and a *bicritical* point is present. A *tricritical* point emerges if the two ordered phases are separated by a continuous phase transition. Finally, in case a mixed phase with intertwined order is present, we find four intersecting phase boundaries and the system is called *tetracritical*. Higher order critical points require the presence of additional order parameters.

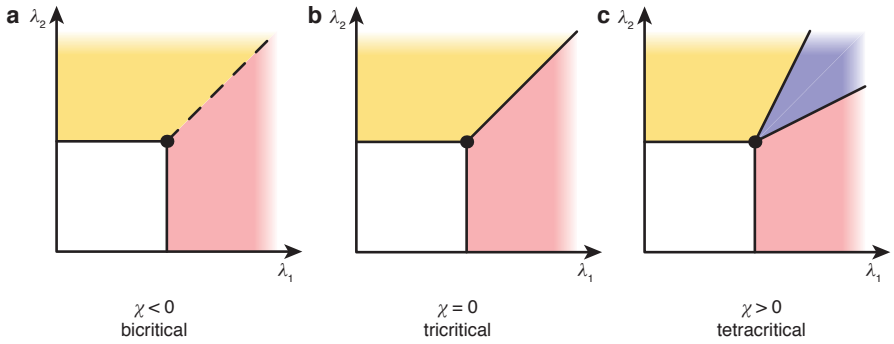

Figure 10.5: *Orders of multicritical points.* Multicritical points (black dots) are classified in terms of the number of intersecting phase boundaries of continuous phase transitions. In the canonical situation of two competing order parameters, the order of the multicritical point depends on the coupling between the two orders, quantified by the determinant χ (see Eq. 10.11). **a,** A *bicritical* point ($\chi < 0$) occurs, if the two ordered phases are separated by a first order phase transition. **b,** The point turns into a *tricritical* point ($\chi = 0$), if the ordered phases are separated by a continuous phase transition. **c,** In case a mixed phase with the simultaneous presence of both orders, the point becomes a *tetracritical* point ($\chi > 0$).

We can analyze the different scenarios in a mean-field approximation around the multicritical point. Let us recall the Landau expansion for two competing order parameters Θ_1 and Θ_2 from Eq. 6.1:

$$\begin{aligned}\mathcal{H}(\Theta_1,\Theta_2) =& \frac{r_1}{2}\Theta_1^2 + \frac{r_2}{2}\Theta_2^2 \\ &+ \frac{g_1}{4}\Theta_1^4 + \frac{g_2}{4}\Theta_2^4 + \frac{g_{12}}{4}\Theta_1^2\Theta_2^2\end{aligned} \tag{10.11}$$

with the coefficients r_1, r_2, g_1, g_2 and g_{12} being functions of λ_1 and λ_2. Whether a multicritical point is bicritical, tricritical or tetracritical depends on the sign of the determinant $\chi = g_1 g_2 - g_{12}^2/4$ (see Chap. 6). A bicritical point occurs for $\chi < 0$, a tricritical point for $\chi = 0$ and a tetracritical point for $\chi > 0$. Reaching a multicritical point in a 2D phase diagram requires fine-tuning of two control parameters instead of one. In addition, the presence of a tricritical point requires fine-tuning of the determinant to $\chi = 0$, see Fig. 10.6.

The concept of multicritical points can be extended to higher dimensions. Consider a system with d control parameters, where each is associated to a continuous phase transition. The phases are separated by phase boundaries of dimension $d-1$. The union of all points in parameter space for which the system is critical is called the critical manifold. The intersection points of different phase boundaries can be of order up to 2^n.

Symmetries at a multicritical point

Conceptually, multicritical points are of interest from a group theoretical point of view. If two order parameters are representations of the groups G and H, the multicritical point is a representation of $G \oplus H$. This enhances the symmetry of the group, which affects the critical behaviour of the system. The universality class can therefore change at a multicritical point. When measuring the critical exponents of a system, we generally expect a change upon approaching the multicritical point. Again, this change does not depend on the microscopic details of the system, but is solely governed by the general principles mentioned earlier.

Independently of the determinant $\chi = g_1 g_2 - g_{12}^2/4$, the symmetry is enhanced at the multicritical point, since all quantities $\propto (1 - \lambda^2/\lambda_{cr})$ disappear. The fact that for $\chi = 0$ the symmetry-enhanced region extends over a

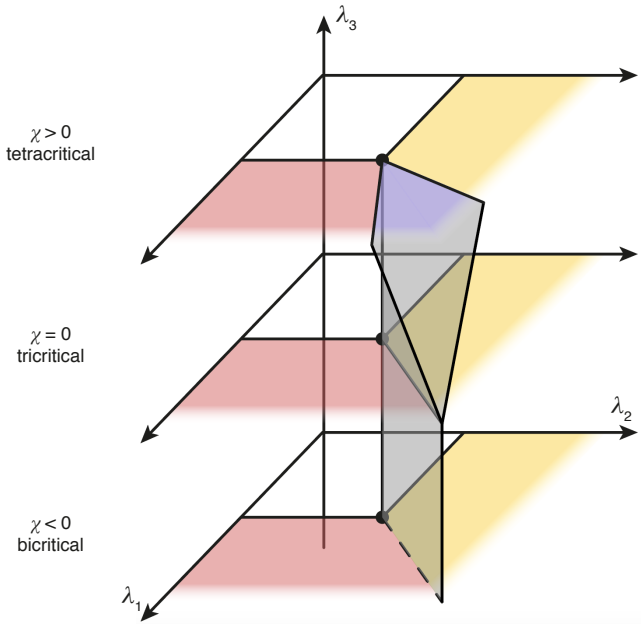

Figure 10.6: *Multicritical points in three dimensions.* The transition from a bicritical, to a tricritical and eventually a tetracritical point can be illustrated in a 3D phase diagram. Each plane shows the phase diagram spanned by the control parameters λ_1 and λ_2. The third parameter, λ_3, controls the order of the critical point from *bicritical*, to *tricritical* and *tetracritical*. The presence of a tricritical point requires a fine-tuning of the parameters to $\lambda_3 = 0$, or $\chi = 0$.

line in the phase diagram points towards a higher-dimensional multicritical point. Indeed, we can interpret χ as a third control parameter and find that the continuous symmetry marks the crossing point of two phase boundaries at $\chi > 0$ that separate the phase with intertwined order from the SO_1 and the SO_2 phases. For $\chi < 0$, the boundary persists as a first order phase transition. The continuous symmetry therefore can be interpreted as the end point of a first order phase transition and the merging point of two second order phase transitions.

Some phase diagrams show more than four phases and multicritical points beyond fourth order, despite the presence of only two control parameters. Such behaviour is only possible if the control parameters are not orthogonal, that is, they simultaneously couple to several order parameters. The 2D phase diagram can then be interpreted as a (not necessarily flat) plane in the d-dimensional space spanned by the (potentially unknown) orthogonal control parameters. An example is the phase diagram of high-temperature superconductors, where temperature and doping are sufficient to explore superfluidity, antiferromagnetism and charge order [372, 373].

10.3.2 Fluctuations at a tricritical point

Critical exponent of the superfluid-supersolid transition

The phase diagram associated with self-organization to two cavities corresponds to the illustration Fig. 10.5. It exhibits a multicritical point at the intersection of the two phase boundaries for self-organization to each cavity. For the transverse pump wavelength chosen in the context of this thesis, $\chi = 0$ and the multicritical point is tricritical. This allows us to study the critical dynamics in the vicinity of the multicritical point in a driven-dissipative

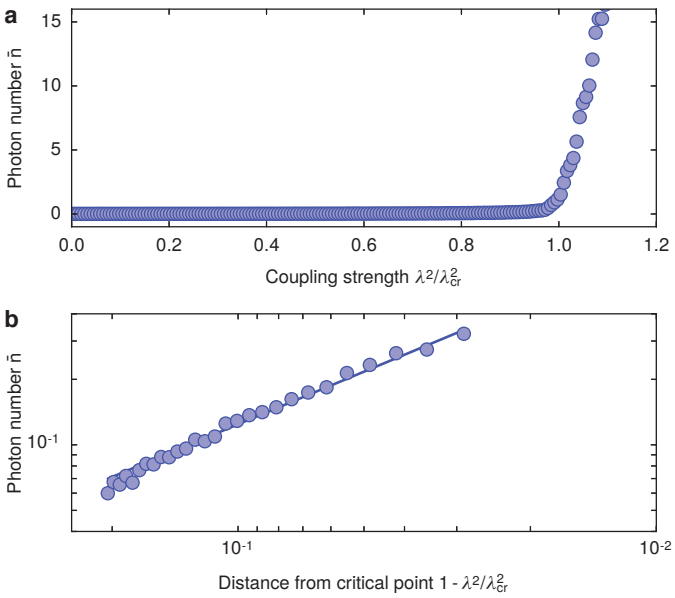

Figure 10.7: *Fluctuations at the supersolid phase transition.* **a,** Total mean intracavity photon number $\overline{n}$ as a sum of the mean photon numbers $\overline{n}_1$ in cavity 1 and $\overline{n}_2$ in cavity 2 during a ramp of 170 ms length up to a transverse pump lattice depth of $26(1)\,\hbar\omega_{\mathrm{rec}}$ at a pump-cavity detuning of $\Delta_c/2\pi = -2.5$ MHz. The data are binned in intervalls of 1 ms. **b,** The data between $85-97\,\%$ are shown on a double logarithmic scale. We extract a critical exponent of 0.80(2) from a fit to the data.

system, or, equivalently, the critical exponent of the superfluid-supersolid phase transition.

We use the same method as in Sec. 10.2 to study critical fluctuations and monitor the density fluctuations of the quantum gas in the normal phase while increasing the coupling strength to approach the phase transition. In contrast to the previous section, we choose the couplings to both cavities to be equal in order to position ourselves along the diagonal in the phase diagram. This is achieved with pump-cavity detunings of $\Delta_1/2\pi = -2.5$ MHz and $\Delta_2/2\pi = -2.4$ MHz. We then linearly increase the transverse pump power over an acquisition time of 170 ms to a maximum value of $26(1)\,\hbar\omega_{\mathrm{rec}}$.

Measuring the critical exponent

During a single experimental realization we record a full photon trace across the critical point, which shows fluctuations in the photon number when approaching the critical point, which are distinct from the coherent onset of a light field inside the self-organized phase. From the photon count rate we induce the intracavity photon number by calibrating the intracavity lattice depth (cf. Sec. 4.3.3). The exact position of the phase transition depends on the total number of atoms, which fluctuates by a few percent between repeated experimental runs. We therefore determine the critical point of the phase transition from a fit to the data and convert the time axis into an increasing coupling strength.

The result is shown in Fig. 10.7 as an average over 528 realizations of the experiment. As for the single-cavity fluctuations in Sec. 10.2, we use the data between 85 % and 97 % of the critical point to extract the critical exponent of the order parameter when approaching the phase transition. A fit to the data reveals an exponent of $\beta = 0.80(2)$.

The critical exponent differs significantly from both measurements at the single cavity self-organization phase transition. Since the measurements are performed under similar conditions, possible systematic errors are expected

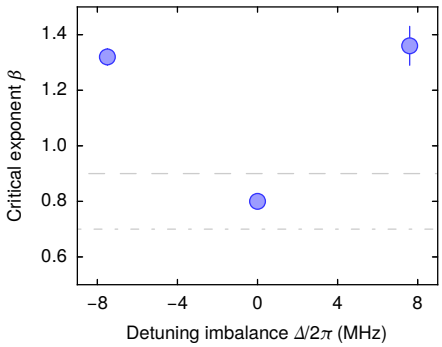

Figure 10.8: *Critical exponent across a tricritical point.* Summary of the extracted critical exponents for different detuning imbalances $\Delta/2\pi = \Delta_1/2\pi - \Delta_2/2\pi$. We find a significantly lower critical exponent at the tricritical point, compared to the critical point for single-cavity self-organization. The results from [313] and [314] for a single cavity (equivalent to the condition $|\Delta| \gg \min\{|\Delta_1|, |\Delta_2|\}$) are shown as grey dashed and dotted-dashed lines, respectively.

to be present in all three measurement. Our results suggest a change in the universality class of the driven-dissipative phase transition when the order parameter turns from $\mathbb{Z}_2$ to $\mathrm{U}(1)$. The measurements constitute the first step to further studies on the multicritical behaviour. For instance, investigating the effective extent of the multicritical point by performing measurements of the critical exponents at smaller detuning imbalances. The autocorrelation functions of the two photon fields at the multicritical point could reveal the diverging time scales and decay rates of the density fluctuations, and the cross-correlation function between the two fields would shed light on the interplay between the two cavity fields, which are expected to be correlated, or possibly entangled. A particularly promising research line would be to investigate the critical behaviour over the transition from a tricritical point to a tetracritical point by changing the coupling between the two order parameters.

11 OUTLOOK

Versatile platform for many-body phenomena

The principal motivation of our experiment is to provide a versatile platform to engineer atom-light interactions that give rise to new many-body phenomena. The work presented in this thesis marks the first step in this direction by constructing interactions that are free from any boundary conditions of the cavity mirrors. We have shown that the coupling to photons induces a structural phase transition that breaks continuous translational symmetry, yet, the interaction potential remains sufficiently simple to understand the physics with only few modes in momentum space. This contrasts with most solids, where interaction potentials show a broad momentum distribution whose precise shape often remains unknown, rendering exact theoretical calculations unfeasible. Our vision is to extract the essence of interaction-induced many-body phenomena by recovering the same effect with a more simple interaction potential. The supersolid presents an basic example for such a simulation.

More complex atom-light interactions

In future experiments, the extension to more complex atom-light interactions will lead to more phenomena that may or may not have a counterpart in solid state physics. Concepts for new types of couplings based on different cavity geometries can be readily implemented, since the setup is exchangeable. This establishes our experiment as a flexible quantum simulator to study a wide range of Hamiltonians. The engineered interactions follow a bottom-up approach: the interaction potential is constructed from momentum modes, which in turn are determined by the initial momentum distribution of the atomic cloud, the wave vector of the cavity mode(s) and of the transverse pump. The interaction range is set by the extension of the mode profiles of the photon fields, i.e cavities and transverse pumps.

These tools permit the creation of advanced interaction potentials already for the existing setup. In the following we give some examples for possible future experiments. First, we discuss some appealing studies of the supersolid state, which further our understanding of the unique interplay of two continuous symmetries. We then demonstrate how the interactions can be adapted to give rise to new phases by changing the frequency of the photons that mediate the interactions. This is followed by some ideas how the control over the mode profiles can be used to adjust the range of the interactions. Ultimately, we present a few prospects in a more general context, proposing candidates for possible future cavity setups.

FURTHER STUDIES ON SUPERSOLIDITY

Decay channels of Higgs and Goldstone modes

Thanks to the control, our experiments offer promising prospects for further studies on the properties of the supersolid state. For instance, the real-time access to the intracavity light fields allows us to characterize the decay channels of Higgs and Goldstone modes. The connection between the Goldstone modes associated to the two broken continuous symmetries has triggered theoretical research and remains an open question. Here we have the opportunity to study this connection with a simple interaction potential. In addition, the access to incoherent fluctuations close to the critical point offers a

tool to investigate the multicritical behaviour associated to competing order from self-organization to the two cavities. Multicritical points play a key role in our understanding of systems with competing order, since they present a singularity with enhanced symmetry in the phase diagram [253]. For a discrete symmetry breaking in a single optical cavity, the fluctuations have shown to reveal a critical slowdown visible in the autocorrelation function [313]. Finally, extending the detection tools by a heterodyne setup permits to measure the phases of the light fields [314], hence to reconstruct the entire ground-state manifold and study the angular distribution functions.

Melting the supersolid

This thesis presents a characterization of the supersolid phase at zero temperature. By preparing a cold gas at finite temperature, we can access the interplay of crystalline order and phase coherence, which give rise to four distinct phases: fluid, superfluid, solid and supersolid. The measurements at finite temperature presented in Chap. 5 have already shown finite temperature effects for self-organization with a single cavity. Theoretical simulations for the $\mathbb{Z}_2$ crystalline order suggest the two order parameters to influence each other, to give rise to first and second order phase transitions, changes in the critical behaviour and the elementary excitations and a restored coherence by the crystalline order [241]. The situation for a continuous symmetry remains theoretically and experimentally unexplored.

ADDING INTERCAVITY INTERACTIONS

The relative strengths of photon scattering between the pump and each cavity, and intercavity photon scattering is set by the pump Rabi frequency and the vacuum Rabi frequency of the cavities. This becomes clear by considering the scaling

$$\frac{\lambda_i}{\lambda_{cr}} \propto \frac{\Omega_p g_i}{\Delta_a} \tag{11.1}$$

$$\frac{\lambda_{12}}{\lambda_{cr}} \propto \frac{\sqrt{N} g_1 g_2}{\Delta_a} \tag{11.2}$$

We cannot adjust the vacuum Rabi frequencies g_i of the cavities, since they are set by the cavity mode volume. The detuning Δ_a from the atomic resonance in contrast can be set on a wide range by changing the frequency of the transverse pump. Upon approaching the atomic resonance, both λ_i/λ_{cr} and $\lambda_{12}/\lambda_{cr}$ increase simultaneously, but the critical point can be reached at much lower transverse pump Rabi frequency Ω_p. As a result, our experimental parameters permit to adjust the intercavity coupling over a range of $10^{-3} - 1$ compared to the pump-cavity couplings.

Coupling two order parameters

Whilst for the work in this thesis the pump frequency was chosen such that intercavity coupling can be neglected, it is conceivable to increase it for future experiments. As discussed in Chap. 6 this gives rise to a new phase with intertwined order and simultaneous self-organization to both cavities, breaking two $\mathbb{Z}_2$ symmetries simultaneously. An exciting extension is a predicted additional phase close to the intertwined phase, where no coherent light fields are present yet, but vestigial order in terms of correlated light fields [374]. It is characterized by vanishing expectation values of the two light fields, whereas their combination does not vanish.

Chaotic behaviour for attractive atom-light interactions

Going further, the pump frequency can also be set to a positive detuning from the atomic resonance. In this regime, the dipole potential created by the photons is repulsive and the photon-mediated interactions have a positive sign. The result is a chaotic behaviour, where bifuractions and vortices are

predicted [239]. A similar situation is also achieved at a pump frequency that is positive detuned from both the atomic and the cavity resonances [323]. Proper choice of the cavity and transverse pump frequencies should allow to enter an intermediate regime with opposite sign for the pump-cavity and the intercavity interactions. The resulting phase diagram is equivalent to the Coleman-Weinberg mechanism for a mass generation of gauge bosons beyond the standard model based on higher order quantum corrections [257, 258].

CHANGING THE INTERACTION RANGE

While the potential of the photon-mediated interactions distinguishes itself by its simplicity, the global range inhibits a number of phenomena that require a broader momentum distribution, for instance a momentum dispersion of elementary excitations, defect formation, and sound propagation. Such an interaction requires to reach length scales below to extension of the cloud, which could be realized in our setup with an aspheric lens that is integrated into the cavity setup (cf. Chap. 4).

Increasing the number of involved momentum state

One approach is to enhance the number of involved momentum modes that contribute to the interaction. This could be achieved already with a single cavity by confining the cloud in a one-dimensional potential that is oriented at an angle with respect to both the pump and the cavity axes. Such a potential could be projected through the aspheric lens with a dipole laser beam. At potential depths in the Lamb-Dicke regime the transferred momentum is projected on the potential axis [109]. For angles incommensurate with the pump-cavity angle, multiple momentum modes also below a single recoil momentum are involved and coupled via higher-order scattering processes.

Local transverse pumps

A different route is based on a reduction of the interaction volume to a subset of the atoms. This can be achieved by reducing the size of either the transverse pump or the cavity mode below the diameter of the BEC. In our setup, this could be realized with a local transverse pump beam that is focussed into the BEC through the aspheric lens. The illuminated atoms scatter photons between the pump beam and the cavity mode, whereas the remaining atoms are insensitive to photon scattering due to a lacking pump. If the pump beam diameter is comparable to the optical wavelength, the shape of the interaction potential becomes broader in momentum space and approaches a Lennard-Jones-type potential. Introducing several local pump beams results in a situation of an interacting few-body system with tunable interactions and real-time access through the leaking photons.

INTERACTIONS WITH ADVANCED SCIENCE SETUPS

The flexible approach allows for a plethora of opportunities to engineer atom-light interactions with a cavity setup that is tailored for the corresponding application. One attractive system is a BEC coupled with a multimode cavity, where many transverse modes are degenerate. For such a system, many-body phenomena like dislocations, frustration and glassiness are predicted to appear [79, 375]. Whilst coupling to few transverse cavity modes has been observed with thermal gases in the electronic [376] and with a BEC in the motional degree of freedom [225], an extension to a sufficient number of modes to show genuinely new many-body phenomena is within reach.

Multimode cavities

Rydberg atoms

An exciting direction are Rydberg atoms, which present an interaction

range in between the collisional contact interactions and the global photon-mediated interaction. The combination of the Rydberg blockade effect and cavity quantum electrodynamics has been investigated theoretically and is expected to retrieve an effective Jaynes-Cummings model [82]. Choosing the blockade radius below the cloud diameter allows to increase the number of excitations in the system and form cavity-coupled Rydberg crystals, whose dynamics can be monitored with the optical cavity [377].

Self-organization with a fermionic quantum gas

Coupling a fermionic quantum gas with an optical cavity would constitute a further experimental path for novel interaction phenomena. Such systems increase the number of accessible momentum modes not by the scattering processes but by the initial momentum distribution, which forms a sphere that is filled up to the Fermi surface because of Pauli blocking [378]. Self-organization of the atoms strongly depends on the geometry of the Fermi surface and can already appear at essentially arbitrarily small threshold thanks to resonant umklapp processes [379]. Proper choice of the cavity detuning is expected to give rise to topological states from atom-cavity coupling [380–382].

A

OPTICAL CAVITIES

The setup that was studied in the context of this thesis consists of two crossed optical cavities. In order to provide a theoretical basis for the understanding of the properties of optical cavities, we introduce in the following the basic resonator properties that are relevant to describe and understand the performed experiments. We derive the quantized eigenmodes of an optical cavity, describe their shape and stability conditions, and finish the discussion by including mirror loss to the formalism.

CHAPTER CONTENTS

In this introduction, we focus on the shape and spectral properties of the modes in an optical cavity. For a more detailed discussion on optical cavities we refer the reader to the literature, e. g. [167, 202, 383, 384].

A.1 SOLUTIONS OF THE PARAXIAL WAVE EQUATION

Strictly speaking, a Fabry-Pérot cavity consists of two parallel mirrors with a plane surface. Since this would result in an unstable mode, cavities are mostly built with curved mirror substrates. The cavities used in the context of this thesis are in the quasi-planar regime, where the mirror curvature is large compared to the cavity length. We can therefore calculate the electric field within the paraxial approximation, as is described in the following.

Wave equation

The electric field $E(\mathbf{r})$ in an optical cavity follows the wave equation:

$$\nabla^2 E(\mathbf{r}) + k^2 E(\mathbf{r}) = 0 \tag{A.1}$$

with wavenumber $k = 2\pi/\lambda_p$ and wavelength λ_p. We start with the ansatz

$$E(\mathbf{r}) = \psi(\mathbf{r}) e^{-ikz} \tag{A.2}$$

with $\psi(\mathbf{r})$ the envelope of the electric field. The envelope captures the finite extent of the beam and distinguishes the mode from a plane wave. We assume that $\psi(\mathbf{r})$ varies so slowly along z that we can neglect its second derivative $\frac{\partial^2\psi}{\partial z^2}$ and obtain:

Paraxial approximation

$$\frac{\partial^2\psi}{\partial x^2} + \frac{\partial^2\psi}{\partial y^2} - 2ik\frac{\partial\psi}{\partial z} = 0 \tag{A.3}$$

One solution to this equation is of the form:

$$\psi(r, z) = u(z) \exp i\frac{kr^2}{2q(z)} \tag{A.4}$$

where we have switched to cylindrical coordinates with $r^2 = x^2 + y^2$. The two complex-valued functions $u(z)$ and $q(z)$ capture the varying amplitude,

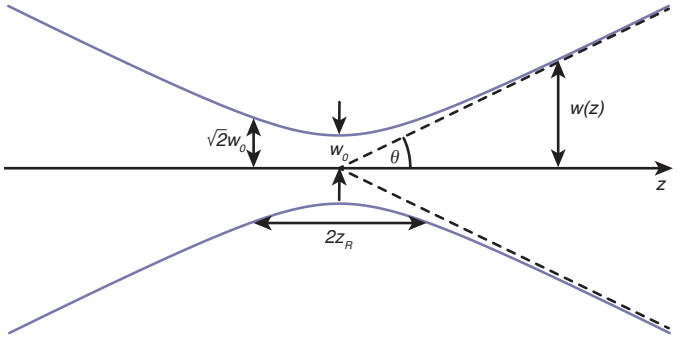

Figure A.1: *Propagation of the fundamental Gaussian mode.* The mode diameter $w(z)$ is minimal at the position $z = 0$ with a diameter w_0. The mode diverges symmetrically around the origin with a divergence $\tan\theta = w_0/z_R$. The Rayleigh length z_R determines the distance from the origin where the mode diameter has increased by a factor $\sqrt{2}$.

width and phase of the mode during the propagation. Inserting this ansatz into Eq. A.3 yields two differential equations:

$$\begin{aligned} \frac{\partial q}{\partial z} &= 1 \\ \frac{\partial u}{\partial z} + \frac{u}{q} &= 1 \end{aligned} \tag{A.5}$$

Field distribution of a Gaussian mode

The equations have the solutions $q(z) = z + z_0 + iz_R$ and $u = iz_R\tilde{E}_0/q$ with the constants $\tilde{E}_0, z_R \in \mathbb{R}$. We can set $z_0 \equiv 0$ by choosing the origin of the coordinate system appropriately. The resulting expression for $\psi(r,z)$ reads:

$$\psi(r,z) = \tilde{E}_0(z)\frac{w_0}{w(z)}e^{-i\left(\Phi(z)+\frac{k}{2R(z)}r^2\right)-\frac{r^2}{w(z)^2}}. \tag{A.6}$$

Here we have used the beam radius

$$w(z) = w_0\sqrt{1+\frac{z^2}{z_R^2}} \tag{A.7}$$

with the Rayleigh length $z_R = \pi w_0^2/\lambda_p$. In the limit $|z|/z_R \gg 1$, the beam radius becomes $w(z) \approx \lambda_p z/\pi w_0$. The Gouy phase $\phi(z)$ is given by

$$\tan\phi(z) = \frac{z}{z_R} \tag{A.8}$$

and the curvature of the wave front is:

$$R(z) = \frac{z_R^2}{z} + z. \tag{A.9}$$

The wave front curvature is maximal at a distance $\pm z_R$ from the origin, and it vanishes at the origin and for $|z| \gg z_R$. The time dependence of the electric field can be included by $\psi(r,z,t) = \psi(r,z)\exp i(kz - \omega t)$.

Solutions of paraxial wave equation

The expression in Eq. A.6 presents one solution of Eq. A.3 with the property that its field profile is the same in every beam cross section, namely a Gaussian distribution. It is called the fundamental Gaussian mode, and describes the electric field of many laser beams (see Fig. A.1). There are other

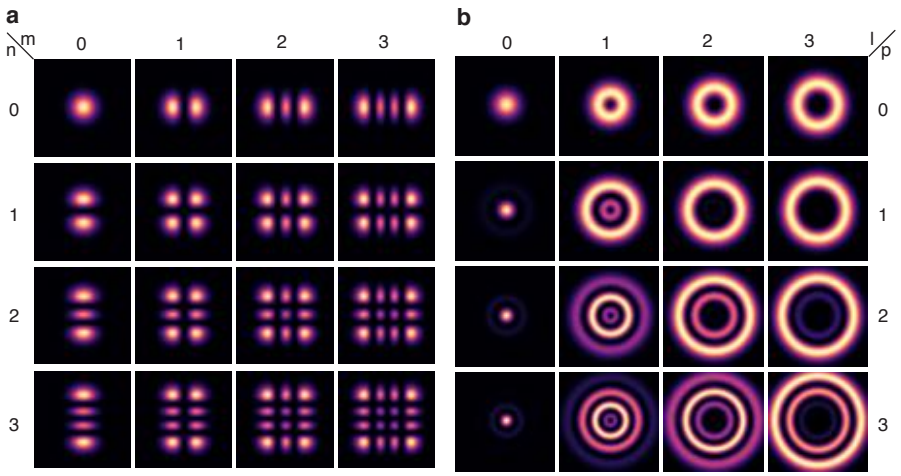

Figure A.2: *Transverse cavity modes.* Intensity distribution $I(x,y) = |E(x,y)|^2$ for the lowest eigenmodes of an optical cavity. **a,** Hermite-Gauss modes ψ_{mn} emerge in a cavity with rectangular boundary conditions. They exhibit m (n) nodes in the intensity distribution along the horizontal (vertical) direction. **b,** Laguerre-Gauss are present in cavities with circular boundary conditions. The radial field distribution is determined by p, whereas l labels the number of phase windings.

solutions with more complex field distributions, for instance the Laguerre-Gauss modes with cylindric symmetry, and the Hermite-Gauss with cartesian symmetry. Both families form a complete and orthogonal set of solutions to Eq. A.3. Their intensity distributions are shown in Fig. A.2.

The Hermite-Gauss modes are

Hermite-Gauss modes

$$\psi_{mn}(x,y,z) = H_m\left(\sqrt{2}\frac{x}{w}\right) H_n\left(\sqrt{2}\frac{y}{w}\right) \tilde{E}_0(z)\frac{w_0}{w(z)} e^{-i\left(\phi_{mn}(z)+\frac{k}{2R(z)}r^2\right)-\frac{r^2}{w(z)^2}}. \tag{A.10}$$

The Hermite polynomials H_m, $m \in \mathbb{N}$ are real-valued functions that are determined by

$$\begin{aligned} H_0(x) &= 1 \\ H_1(x) &= 2x \\ H_{m+1} &= 2xH_m(x) - 2mH_{m-1}(x), \end{aligned} \tag{A.11}$$

and equivalently for $H_n(y)$, $n \in \mathbb{N}$. The Gouy phase $\phi_{mn}(z)$ is now given by

$$\tan\left(\frac{\phi_{mn}(z)}{m+n+1}\right) = \frac{z}{z_R} \tag{A.12}$$

The radius of curvature $R(z)$ is independent of m and n. The Hermite-Gauss mode $\psi_{mn}(x,y,z)$ is characterized by $m+1$ ($n+1$) field antinodes and m (n) field nodes along the vertical (horizontal) direction. For $m = n = 0$, we recover the fundamental Gaussian mode that we discussed previously. The intensity for the lowest Hermite-Gauss modes is shown in Fig. A.2a.

The Laguerre-Gauss modes are

Laguerre-Gauss modes

$$\psi(r,\varphi,z) = \left(\sqrt{2}\frac{r}{w}\right)^l L_p^l\left(2\frac{r^2}{w^2}\right) \tilde{E}_0(z)\frac{w_0}{w(z)} e^{-il\varphi} e^{-i\left(\phi(z)+\frac{k}{2R(z)}r^2\right)-\frac{r^2}{w(z)^2}}. \tag{A.13}$$

The Laguerre polynomials L_p are axially symmetric functions and can be iteratively calculated according to:

$$\begin{aligned} L_0(r) &= 1 \\ L_1(r) &= -r + 1 \\ L_{p+1}(r) &= \frac{2p+1-r}{p+1} L_p(r) - \frac{p}{p+1} L_{p-1}(r), \end{aligned} \tag{A.14}$$

Gouy phase

The Gouy phase $\phi_{pl}(z)$ is now given by

$$\tan\left(\frac{\phi_{pl}(z)}{2p+l+1}\right) = \frac{z}{z_R} \tag{A.15}$$

Modes with orbital angular momentum

The effect of the rotational mode number l is mainly contained in the phase factor $e^{-il\varphi}$, which describes a phase winding of l complete 2π phases in one rotation around the beam. This is the result of orbital angular momentum of the light in that mode, and presents an example of an optical vortex with the topological charge l.

Further families of modes can be equally considered, depending on the choice of boundary conditions for Eq. A.3, for instance Ince-Gaussian modes, Bessel modes or Hypergeometric-Gaussian modes. Their treatment goes beyond the scope of this introduction and we refer the reader to [384].

A.2 STABILITY AND UNSTABLE CAVITY GEOMETRIES

Wavefront and mirror curvatures

The choice of the mirror curvatures and of the cavity length determines whether the resonator supports stable cavity modes or remains unstable. In the following we consider a linear cavity with two mirrors at positions z_1, z_2 and curvature R_1 and R_2. By convention, the radii are positive if the reflective surface inside the cavity is concave. The mirror curvatures are required to equal the curvature of the wavefront at the mirror position, yielding:

$$\begin{aligned} R(z_1) &= -R_1 = z_1 + \frac{z_R^2}{z_1} \\ R(z_2) &= R_2 = z_2 + \frac{z_R^2}{z_2} \end{aligned} \tag{A.16}$$

The wavefront curvature can be calculated according to Eq. A.9. We define the cavity length $d = z_2 - z_1$, and the mirror parameters $g_1 = 1 - d/R_1$ and $g_2 = 1 - d/R_2$ and obtain:

$$z_R^2 = \frac{g_1 g_2 (1 - g_1 g_2) d^2}{(g_1 + g_2 - 2 g_1 g_2)^2} \tag{A.17}$$

$$z_1 = -\frac{g_2 (1 - g_1) d}{g_1 + g_2 - 2 g_1 g_2} \tag{A.18}$$

$$z_2 = \frac{g_1 (1 - g_2) d}{g_1 + g_2 - 2 g_1 g_2} \tag{A.19}$$

We see that z_R is not defined if

$$\begin{aligned} (1 - g_1 g_2) < 0 \quad &\text{and} \quad g_1 g_2 > 0 \\ (1 - g_1 g_2) < 0 \quad &\text{and} \quad g_1 g_2 > 0 \\ g_1 + g_2 - 2 g_1 g_2 &= 0 \end{aligned} \tag{A.20}$$

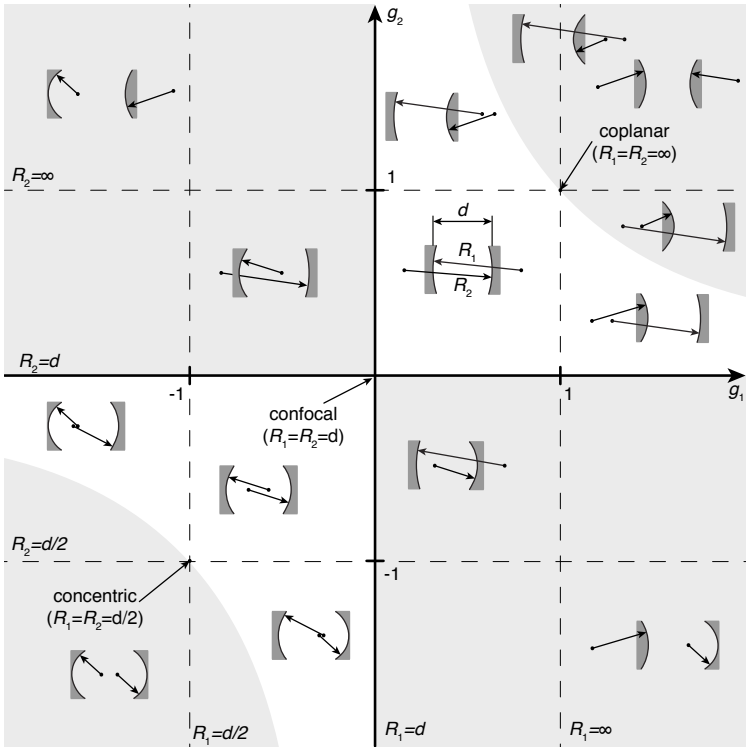

Figure A.3: *Stability diagram for linear cavities.* The existence of a stable cavity mode depends on the mirror parameters $g_1 = 1 - d/R_1$ and $g_2 = 1 - d/R_2$, where d is the cavity length and R_1 and R_2 are the radii of curvature for the cavity mirrors. The stable (unstable) regions are shaded in white (gray). The coplanar, confocal and concentric cavity geometries are at the stability edge.

or, equivalently, the cavity is only stable if:

Condition for a stable cavity mode

$$0 < g_1 g_2 < 1 \tag{A.21}$$

A diagram with the stable regions in the g_1-g_2 plane and the corresponding cavity geometries are illustrated in Fig. A.3.

A.3 LONGITUDINAL AND TRANSVERSE MODES OF AN OPTICAL CAVITY

A cavity mode defines a self-consistent field configuration. In a wave beam picture, a resonator mode can be represented as a wave beam whose parameters must be the same after one round trip. This condition is used to calculate the mode parameters. We distinguish two types of resonators: *linear cavities*, where the beam that presents the mode travels in both directions between the mirrors, and *ring cavities*, where the mode round-trip does not involve retro-reflection of the beam.

We focus in the following on a linear cavity, formed by two mirrors at z_1 and z_2 at a distance $d = z_2 - z_1$. For a mode to be stable we require the phase over one round-trip to be a multiple of 2π, or, a multiple of π over the cavity length. The phase shift is determined by the Gouy phase in Eq. A.8.

$$kd + \phi(z_1) - \phi(z_2) = kd + \arctan z_1/z_R - \arctan z_2/z_R = p\pi \tag{A.22}$$

with $p \in \mathbb{N}$. The phase over one round-trip is then $2\pi p$. With $\omega = ck$ we obtain the resonance frequencies

$$\omega_{pmn} = 2\pi\nu_{pmn} = 2\pi \times \nu_{FSR}\,[p + (m + n + 1)\epsilon]\,. \tag{A.23}$$

Here, the frequency splitting between two successive longitudinal modes is given by the free spectral range

$$\omega_{FSR} = 2\pi \times \nu_{FSR} = \frac{c}{2d} \tag{A.24}$$

and the transverse mode splitting between two families with $m+n = const$ is

$$\omega_{TEM} = 2\pi \times \nu_{TEM} = 2\pi \times \epsilon\nu_{FSR} = \frac{c}{d} \arccos\left(\sqrt{g_1 g_2}\right). \tag{A.25}$$

Linear cavity geometries

Let us consider some specific cavity geometries:

- **Coplanar cavity:** If both mirror curvatures are large compared to the cavity length d, the Gouy phase vanishes throughout the mode, because $d/2 \ll z_R$. All transverse modes are almost degenerate since $\epsilon \ll 1$. A strictly coplanar cavity with degenerate modes does not fulfill the stability criterion in Eq. A.21, since $g_1 g_2 = 1$
- **Concentric cavity:** If both mirror curvatures lie on a circle, i. e. each curvature equals $d/2$, the Gouy phase is maximum with $\phi(d/2) = \pi/2$, because $d/2 \gg z_R$. A concentric cavity exhibits degenerate transverse modes, but it is also at the stability limit with $g_1 g_2 = 1$.
- **Confocal:** If the mirror curvatures equal the cavity length, the Gouy phase equals $\phi(d/2) = \pi/4$, because $z_R = d/2$. As a consequence, the free spectral range twice as large as the transverse mode spacing, $\Delta\nu_{TEM} = \frac{c}{4d}$. The transverse modes group into two families of degenerate modes, one with $n+m$ even and one with $n+m$ odd.

Our cavities are built in the quasi-coplanar regime, where $R/L \ll 1$ and accordingly $\Delta\nu_{TEM} \ll \nu_{FSR}$. Additionnally, we work at detunings $\Delta_c = \omega_p - \omega_c$ of the pump from one fundamental mode that are small compared to $\Delta\nu_{TEM}$. We can therefore neglect the coupling to any other mode than the fundamental mode.

A.4 OPTICAL CAVITIES INCLUDING MIRROR LOSS

So far we have dealt with the idealized situation of lossless cavity mirrors that invoke perfect boundary conditions. We will now discuss how photon losses at the mirrors affect the cavity mode structure. The cavity mirrors are characterized by their reflectivity R, their transmissivity T and the losses L, where $R+T+L = 1$. Let us consider an incoming beam with field amplitude E_{in} that is partially transmitted by the first cavity mirror. The transmitted field amplitude is then:

$$E_0 = \sqrt{T_1} E_{in} \tag{A.26}$$

Amplitude loss over one round-trip

During each round trip, the amplitude is further reduced by the factor

$$g_{rt} = \sqrt{R_1 R_2} \tag{A.27}$$

Phase shift over one round-trip

Also the phase of the electric field is modified after one round-trip, depending on the propagation length. It reads:

$$\delta\phi = \phi_c - \phi_{in} = \Delta_c \frac{2d}{c} \tag{A.28}$$

with the frequency detuning $\Delta_c = \omega - \omega_c$ of the incoming beam frequency ω from the resonance frequency ω_c. In summary, the electric field changes over one round trip by:

$$E_{j+1} = g_{rt} e^{-i\delta\phi} E_j \tag{A.29}$$

Intracavity field

The cumulative field amplitude circulating in the cavity is then given by

$$E_c = \sum_{j=0}^{\infty} E_j = \sum_{j=0}^{\infty} \left(g_{rt} e^{-i\delta\phi} \right)^j E_0 = \frac{E_0}{1 - g_{rt} e^{-i\delta\phi}} \tag{A.30}$$

The intracavity power is then given by

$$\begin{aligned} P_c &= \frac{|E_0|^2}{(1 - g_{rt})^2 + 4 g_{rt} \sin^2(2\pi\Delta_c d/c)} \\ &= \frac{P_{max}}{1 + (2\mathcal{F}/\pi)^2 \sin^2(2\pi\Delta_c d/c)}, \end{aligned} \tag{A.31}$$

Cavity finesse

where we have defined the maximum power $P_{max} = \epsilon_0 c/2$ and the finesse

$$\mathcal{F} = \pi\sqrt{g_{rt}}/(1 - g_{rt}). \tag{A.32}$$

A photon will be reflected $\mathcal{F}/\pi$ times on average before it leaves the cavity. In the limit of $T, L \ll 1$, the finesse takes the form $\mathcal{F} = \pi/(T + L)$.

Around the cavity resonance for $\Delta_c \ll c/d$, the intracavity power approximates a Lorentzian line shape. We can obtain the FWHM $\Delta\nu$ of the resonance by the condition $P_c = P_{max}/2$, yielding

$$\Delta\nu = \frac{2}{\pi} \sin^{-1}\left(\frac{\pi}{2\mathcal{F}}\right) \nu_{FSR} \approx \frac{\nu_{FSR}}{\mathcal{F}} \tag{A.33}$$

The linewidth of the cavity resonance is directly related to the lifetime of the cavity field. We consider the situation where an intracavity power $P(t = 0) = P_0$ starts to decay due to mirror loss. The loss rate during one round trip is given by

$$\frac{dP(t)}{dt} = -P(t)(2 - R_1 - R_2)\nu_{FSR} \tag{A.34}$$

Cavity ringdown time

This differential equation has the solution $P(t) = P_0 e^{-t/\tau_c}$ with the cavity ringdown time

$$\tau_c = \frac{1}{(2 - R_1 - R_2)\,\nu_{FSR}} \tag{A.35}$$

The photon decay rate κ then follows with $\kappa = 2\pi/\tau_c = 2\pi \times \Delta\nu/2$.

B

ATOM-LIGHT INTERACTIONS

In the following we derive the Hamiltonian that is at the basis of all collective phenomena discussed throughout this thesis. We start with a single atom that is coupled to a single cavity mode and step by step extend this model until we arrive at a description of the dispersive interactions of many atoms with two cavity modes. .

CHAPTER CONTENTS

Parts of the description are based on [207]. An instructive description with emphasis on a semi-classical view on atom-light interactions is given in [385].

B.1 A SINGLE ATOM IN AN OPTICAL CAVITY

A two-level system that is coupled to the quantized light field of a cavity can be described by the Hamiltonian

$$\hat{\mathcal{H}} = \hat{\mathcal{H}}_a + \hat{\mathcal{H}}_a + \hat{\mathcal{H}}_{int} \tag{B.1}$$

$\hat{\mathcal{H}}_a$ describes the atomic evolution, $\hat{\mathcal{H}}_c$ the evolution of the cavity field and $\hat{\mathcal{H}}_{int}$ the atom-light interactions. Let us consider each term individually.

Atom as a two-level system

We start with a description of the atom, which we model as a two-level system of the ground state $|g\rangle$ and the electronically excited state $|e\rangle$. Transitions between the states are described in terms of the operators

$$\begin{aligned} \hat{\sigma}_z &= \frac{1}{2}\left(|e\rangle\langle e| - |g\rangle\langle g|\right) \\ \hat{\sigma}_+ &= |e\rangle\langle g| \\ \hat{\sigma}_- &= |g\rangle\langle e| \end{aligned} \tag{B.2}$$

The operators are Pauli matrices that obey a spin algebra with commutators $[\hat{\sigma}_-, \hat{\sigma}_+] = -2\hat{\sigma_z}$ and $[\hat{\sigma}_-, \hat{\sigma}_z] = \hat{\sigma_-}$. Setting the transition energy to $E_e - E_g = \hbar\omega_0$ and $\hat{\mathcal{H}}_a|g\rangle = 0$, we obtain the Hamiltonian

$$\hat{\mathcal{H}}_a = E_g\langle g|g\rangle + E_e\langle e|e\rangle = \hbar\omega_0\hat{\sigma}_+\hat{\sigma}_- \tag{B.3}$$

Quantized light field as harmonic oscillator

The light field of a cavity mode with frequency $\hbar\omega$ can be described in quantized form by the creation and annihilation operators $\hat{a}^\dagger$ and $\hat{a}$ obeying $\left[\hat{a}, \hat{a}^\dagger\right] = 1$. This results in the Hamiltonian

$$\hat{\mathcal{H}}_c = \hbar\omega_c\hat{a}^\dagger\hat{a} \tag{B.4}$$

in analogy to a harmonic oscillator with eigenfrequencies $E_n = \hbar\omega_c\,(n + 1/2)$ separated by the photon energy $\hbar\omega_c$.

Interaction between the atom and the light field

The remaining term describes the interaction between the atom and the cavity field. The coupling can be caught in terms of the dipole moment $\hat{d}$ with

$$\hat{d} = -e\hat{r} = -\sum_{i,j\in\{e,g\}} e\,|i\rangle\langle i|\,\hat{r}\,|j\rangle\langle j| = -\sum_{i,j} \mathcal{D}\,|i\rangle\langle j| = -\mathcal{D}\left(\hat{\sigma}_+ + \hat{\sigma}_-\right) \quad \text{(B.5)}$$

With $\hat{E} = \mathcal{E}_{max}\left(\hat{a}^\dagger + \hat{a}\right)$ and the single-atom coupling strength $g_0 = \mathcal{D}\mathcal{E}_{max}/\hbar$ we obtain the interaction Hamiltonian

$$\hat{\mathcal{H}}_{int} = -\hat{d}\hat{E} = \hbar g_0\left(\hat{\sigma}_+ + \hat{\sigma}_-\right)\left(\hat{a}^\dagger + \hat{a}\right) \quad \text{(B.6)}$$

The resulting Hamiltonian for the description of the entire atom-light system is

$$\hat{\mathcal{H}} = \hbar\omega_0\hat{\sigma} + \hat{\sigma}_- + \hbar\omega_c\hat{a}^\dagger\hat{a} + \hbar g_0\left(\hat{\sigma}_+ + \hat{\sigma}_-\right)\left(\hat{a} + \hat{a}^\dagger\right). \quad \text{(B.7)}$$

B.2 THE JAYNES-CUMMINGS MODEL

Rotating wave approximation

The Jaynes-Cummings Hamiltonian is obtained from Eq. B.7 with the rotating wave approximation for the limit $\omega - \omega_0, g_0 \ll \omega, \omega_0$. We start by introducing the unitary transformation

$$\begin{aligned}\hat{U}(t) &= e^{\left(i\hat{\mathcal{H}}_a/\hbar + i\hat{\mathcal{H}}_c/\hbar\right)}\\ &= e^{\left(i\omega_0 t\hat{\sigma}_+\hat{\sigma}_- + i\omega t\hat{a}^\dagger\hat{a}\right)}\\ &= e^{\left(i\omega_0 t\hat{\sigma}_+\hat{\sigma}_-\right)}e^{\left(-i\omega t\hat{a}^\dagger\hat{a}\right)}\\ &= \hat{U}_1(t)\hat{U}_2(t)\end{aligned} \quad \text{(B.8)}$$

Interaction picture

Since the commutator $\left[\hat{U}_1, \hat{U}_2\right] = 0$ vanishes, we can separately consider the transformation of the Hamiltonian for the photon and the atom operators. An operator in the Schrödinger picture $\hat{\mathcal{A}}_S$ is transformed to the interaction picture as $\hat{\mathcal{A}}_I = \hat{U}\hat{\mathcal{A}}_S\hat{U}^\dagger$, and correspondingly a ket via $|\psi_I\rangle = \hat{U}\,|\psi_S\rangle$. The transformation of the raising operator reads:

$$\begin{aligned}\hat{\sigma}_+ \to \hat{U}\hat{\sigma}_+\hat{U}^\dagger = \hat{U}_1\hat{\sigma}_+\hat{U}_1 &= e^{i\omega_a\hat{\sigma}_+\hat{\sigma}_-}\hat{\sigma}_+e^{-i\omega_a\hat{\sigma}_+\hat{\sigma}_-}\\ &= \sum_{n,m=0}^{\infty}\frac{(i\omega_a)^n(\hat{\sigma}_+\hat{\sigma}_-)^n}{n!}\hat{\sigma}_+\frac{(i\omega_a t)^m(\hat{\sigma}_+\hat{\sigma}_-)^m}{m!}\\ &= \sum_{n=0}^{\infty}\frac{(i\omega_a t)^n}{n!}\hat{\sigma}_+\hat{\sigma}_-^n\hat{\sigma}_+ = e^{i\omega_a t}\hat{\sigma}_+\end{aligned} \quad \text{(B.9)}$$

Analogously, we obtain the transformation $\hat{\sigma}_- \to e^{-i\omega_a t}\hat{\sigma}_-$. The transformation for the photonic annihilation operator $\hat{a}$ can be computed with the relation $e^{\hat{X}}\hat{Y}e^{-\hat{X}} = \hat{Y} + \left[\hat{X},\hat{Y}\right] + \left[\hat{X},\left[\hat{X},\hat{Y}\right]\right]/2! + \ldots$, yielding

$$\begin{aligned}\hat{a} \to \hat{U}\hat{a}\hat{U}^\dagger = \hat{U}_2\hat{a}\hat{U}_2^\dagger &= e^{i\omega_c t\hat{a}^\dagger\hat{a}}\hat{a}e^{-i\omega_c t\hat{a}^\dagger\hat{a}}\\ &= \hat{a} + \left[i\omega_c t\hat{a}^\dagger\hat{a},\hat{a}\right] + \frac{1}{2!}\left[i\omega_c t\hat{a}^\dagger\hat{a},\left[i\omega_c t\hat{a}^\dagger\hat{a},\hat{a}\right]\right]\\ &= \hat{a} + (-i\omega_c t)\,\hat{a} + \frac{1}{2!}(-i\omega_c t)^2\,\hat{a} + \ldots = e^{-i\omega_c t}\hat{a}\end{aligned} \quad \text{(B.10)}$$

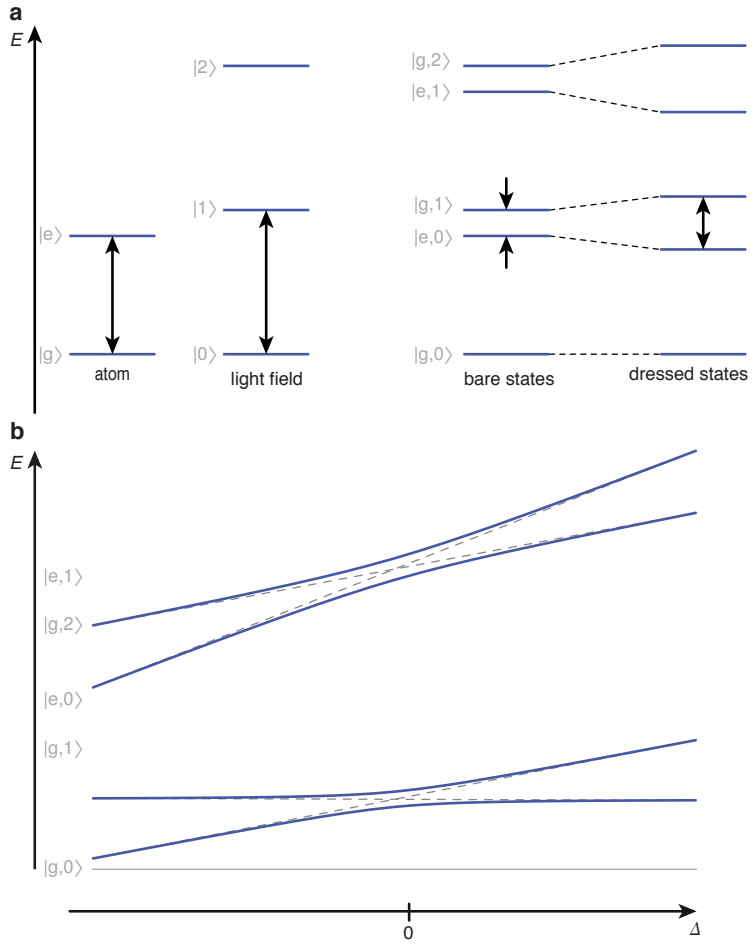

Figure B.1: *Jaynes-Cummings model.* **a,** The atom is modeled as a two-level system with ground state $|g\rangle$ and excited state $|e\rangle$. The light field consists of a ladder of equally spaced energy levels labelled with the photon number $|n\rangle$. The photon energy and the atomic transition energy are close to each other. Atom-light coupling induces a repulsion between adjacent levels with dressed states as new eigenstates of the system. **b,** Energy of the dressed states as a function of detuning of the photon energy and the atomic transition energy. We find an avoided crossing when two energies approach one another.

And analogously $\hat{a}^\dagger \rightarrow \hat{U}_2 \hat{a}^\dagger \hat{U}_2^\dagger = e^{i\omega_c t}\hat{a}^\dagger$. The transformation of the Hamiltonian to the interaction picture

$$\begin{aligned} i\hbar\frac{\partial}{\partial t}|\psi_I\rangle &= i\hbar\frac{\partial}{\partial t}\left(\hat{U}|\psi_S\rangle\right) = -\hat{\mathcal{H}}_0\hat{U}\psi_S + i\hbar\hat{U}\frac{\partial}{\partial t}|\psi_S\rangle \\ &= -\hat{\mathcal{H}}_0\psi_I + \hat{U}\hat{\mathcal{H}}_S|\psi_S\rangle \\ &= -\hat{\mathcal{H}}_0\psi_I + \hat{U}\hat{\mathcal{H}}_S\hat{U}^\dagger\hat{U}|\psi_S\rangle \\ &= -\hat{\mathcal{H}}_0\psi_I + \hat{\mathcal{H}}_I|\psi_I\rangle = \hat{\mathcal{H}} * |\psi_I\rangle\,. \end{aligned} \tag{B.11}$$

with the transformed Hamiltonian

$$\begin{aligned} \hat{\mathcal{H}}^* =& \hbar g_0 \Big[\hat{\sigma}_-\hat{a}^\dagger e^{-i(\omega_0-\omega)t} + \hat{\sigma}_+\hat{a}e^{i(\omega_0-\omega)t} + \\ & \hat{\sigma}_+\hat{a}^\dagger e^{i(\omega_0+\omega)t} + \hat{\sigma}_-\hat{a}e^{-i(\omega_0+\omega)t}\Big] \end{aligned} \tag{B.12}$$

The relevant timescale is set by g_0, which is typically orders of magnitude below ω_a and ω_c. For instance, in our experiment $g_0/w\pi \approx 10^6$ Hz and $\omega_a/2\pi, \omega_c/2\pi \approx 4\times10^{14}$ Hz. The first two terms, which oscillate at a frequency of $\omega_a + \omega_c$ will average on a timescale set by g_0 and can be neglected, but the last two terms remain relevant. After transforming back to the Schrödinger picture we obtain the Jaynes-Cummings Hamiltonian

Jaynes-Cummings Hamiltonian

$$\hat{\mathcal{H}} = \hbar\omega_0\hat{\sigma}_+\hat{\sigma}_- + \hbar\omega\hat{a}^\dagger\hat{a} + \hbar g_0\left(\hat{\sigma}_+\hat{a} + \hat{\sigma}_-\hat{a}^\dagger\right). \tag{B.13}$$

The Jaynes-Cummings model is a fundamental model in quantum optics. It presents the most simple non-trivial model to describe the interaction of an atom with an electromagnetic wave on a quantum mechanical level. A canonical basis for the first two terms of the Hamiltonian for each photon number n is given the bare states $|e,n\rangle$ and $|g,n+1\rangle$, labeling the ground (g) or excited (e) state of the atom. The coupling term introduces a coherent mixture of these two states, resulting in the eigenenergies $E_\pm(n)$

$$E_\pm(n) = \hbar\omega_c\left(n+\frac{1}{2}\right) \pm \frac{\hbar\Omega_n}{2}, \tag{B.14}$$

with the Rabi frequency $\Omega_n = \sqrt{4(n+1)g_0^2+\Delta^2}$ and the detuning $\Delta = \omega_c - \omega_a$. For resonant light, we obtain an energy splitting $E_+ - E_- = \hbar\sqrt{2}(n+1)g_0$ between each pair of eigenstates, which increases with n. For large detuning $|\Delta| \gg 2(n+1)g_0$, the eigenstates approach the bare states and the eigenenergies show a characteristic avoided crossing behaviour. The mixing angle is given by

Mixing angle

$$\theta = \arctan\left(\frac{2g_0\sqrt{n+1}}{\Delta}\right) \tag{B.15}$$

The experiments that were carried out in the context of this thesis are within the limit of small mixing angle, since the transverse pump is far detuned from the atomic resonance. The atoms are subject to the energy shift from the cavity field, while the fraction in the excited state can be neglected. This will be taken into account in Sec. B.4.

B.3 MOTIONAL DEGREE OF FREEDOM

We have so far assumed that the position of the atom was fixed with respect to the cavity mode. This assumption is now dropped and we include atomic

motion in terms of a trapping potential $V(\mathbf{r})$ and the kinetic energy $\hat{\mathbf{p}}^2/2m$. We also add a transverse pump field that is described by a classical Rabi frequency $h(\mathbf{r}) = \Omega_p h_t(\mathbf{r})$ with mode profile $h_t\mathbf{r}$ and maximum Rabi frequency Ω_p. A driving field along the cavity axis can be taken into account in a similar fashion with $\hbar\eta\left(\hat{a}e^{i\omega_p t} + \hat{a}^\dagger e^{-i\omega_p t}\right)$. An on-axis driving field is used in Chapters 8 and 9, but dropped here for simplicity. The Hamiltonian including the atomic motion reads then:

Transverse pump field

Hamiltonian including atomic motion

$$\begin{aligned}\hat{\mathcal{H}} = &\frac{\hat{\mathbf{p}}^2}{2m} + V_e(\mathbf{r})\hat{\sigma}_+\hat{\sigma}_- + V_g\hat{\sigma}_-\hat{\sigma_+} + \hbar\omega_0\hbar\hat{\sigma}_+\hat{\sigma}_- \\ &+ \hbar h(\mathbf{r})\left(\hat{\sigma}_+ e^{i\omega_p t} + \hat{\sigma}_- e^{-i\omega_p t}\right) \\ &+ \hbar\omega\hat{a}^\dagger\hat{a} + \hbar\Omega_c\left(\hat{a}e^{i\omega_p t} + \hat{a}^\dagger e{-}i\omega_p t\right) \\ &+ \hbar g(\mathbf{r})\left(\hat{\sigma}_+\hat{a} + \hat{\sigma}_-\hat{a}^\dagger\right)\end{aligned} \tag{B.16}$$

The explicit time dependency can be eliminated by moving to the frame rotating with the transverse pump frequency. Analogously to the description in Sec. B.2, this can be achieved with the unitary transformation

Transformation to the rotating frame

$$\hat{U}(t) = \exp\left[i\omega_p t\left(\hat{\sigma}_+\hat{\sigma}_- + \hat{a}^\dagger\hat{a}\right)\right] \tag{B.17}$$

yielding the transformed Hamiltonian

$$\begin{aligned}\hat{\mathcal{H}} = &\frac{\hat{\mathbf{p}}^2}{2m} + V_e(\mathbf{r})\hat{\sigma}_+\hat{\sigma}_- + V_g\hat{\sigma}_-\hat{\sigma_+} - \hbar\Delta_a\hbar\hat{\sigma}_+\hat{\sigma}_- \\ &+ \hbar h(\mathbf{r})\left(\hat{\sigma}_+ + \hat{\sigma}_-\right) \\ &- \hbar\Delta_c\hat{a}^\dagger\hat{a} + \hbar\Omega_c\left(\hat{a} + \hat{a}^\dagger\right) \\ &+ \hbar g(\mathbf{r})\left(\hat{\sigma}_+\hat{a} + \hat{\sigma}_-\hat{a}^\dagger\right)\end{aligned} \tag{B.18}$$

with $\Delta_c = \omega_p - \omega_c$ and $\Delta_a = \omega_p - \omega_a$.

B.4 DISPERSIVE ATOM-LIGHT INTERACTIONS

In the next step, we extend the description to N atoms and move to the limit of dispersive interaction. Let us introduce the atomic field operators $\hat{\Psi}_g^\dagger(\mathbf{r})$ ($\hat{\Psi}_g(\mathbf{r})$) and $\hat{\Psi}_e^\dagger(\mathbf{r})$ ($\hat{\Psi}_e(\mathbf{r})$), which create (annihilate) an atom at position $\mathbf{r} = (x, y)$ in the ground and excited state, respectively. We drop the z coordinate since none of the light fields has a wave vector that points out of the x-y plane and we can assume the motion being frozen along this direction. The operators follow the bosonic commutation relations

Atomic field operators

$$\begin{aligned}\left[\hat{\Psi}_i(\mathbf{r}), \hat{\Psi}_j^\dagger(\mathbf{r'})\right] &= \delta^2(\mathbf{r} - \mathbf{r'})\delta_{ij} \\ \left[\hat{\Psi}_i(\mathbf{r}), \hat{\Psi}_j(\mathbf{r'})\right] &= 0\end{aligned} \tag{B.19}$$

We rewrite the Hamiltonian in Eq. B.18 in terms of the atomic field operators, yielding

Many-body Hamiltonian

$$\begin{aligned}\hat{\mathcal{H}} = &-\hbar\Delta_c\hat{a}^\dagger\hat{a} + \hbar\Omega_c(\hat{a}^\dagger + \hat{a}) \\ &+ \int_{\mathcal{A}} dr \left[\hat{\Psi}_g^\dagger(r)\left(-\frac{\hbar^2}{2m}\nabla^2 + V_g(r)\right)\hat{\Psi}_g(r)\right. \\ &\qquad \left. + \hat{\Psi}_e^\dagger(r)\left(-\frac{\hbar^2}{2m}\nabla^2 - \hbar\Delta_a + V_e(r)\right)\hat{\Psi}_e(r)\right] \\ &+ \int_{\mathcal{A}} dr \left[\hat{\Psi}_g^\dagger(r)g(r)\hat{a}^\dagger\hat{\Psi}_e(r) + \hat{\Psi}_e^\dagger(r)g(r)\hat{a}^\dagger\hat{\Psi}_g(r)\right] \\ &+ \int_{\mathcal{A}} dr \left[\hat{\Psi}_g^\dagger(r)h(r)\hat{\Psi}_e(r) + \hat{\Psi}_e^\dagger(r)h(r)\hat{\Psi}_g(r)\right]\end{aligned} \tag{B.20}$$

Here, $\mathcal{A}$ is the size of the unit cell (see Sec. 5.7). This Hamiltonian describes the interaction of an arbitrary number of atoms with a cavity, which is subject to a transverse pump field. Since we have included the kinetic energy of the atoms, our model captures the interplay of the potential generated by the light fields and the position of the atoms.

In the present thesis, we have explored the regime of dispersive coupling, which is realized by a large detuning Δ_a of the light fields from the atomic resonance frequency. The evolution of the excited state population is determined by the Heisenberg equation

$$\frac{\partial\hat{\Psi}_e(r)}{\partial t} = i\left(\frac{\hbar}{2m}\nabla^2 + \Delta_a\right)\hat{\Psi}_e(r) - (g(r)\hat{a} + h(r))\,\hat{\Psi}_g(r). \tag{B.21}$$

Time scales for the ground and the excited state

We find that the phase of $\hat{\Psi}_e$ essentially evolves at a rate Δ_a, much faster than the other relevant time scales. Accordingly, the time average $\langle\frac{\partial\hat{\Psi}_e(r)}{\partial t}\rangle = 0$ vanishes on all experimentally accessible time scales. The average excited state population $\langle\hat{\Psi}_e\rangle_t$, however, does not vanish, in agreement with the non-zero mixing angle in Eq. B.15, and can be obtained from Eq. B.21

$$\langle\hat{\Psi}_e(r)\rangle_t = \frac{i}{\Delta_a}\left(h(r) + g(r)\hat{a}(t)\right)\hat{\Psi}_g(r) \tag{B.22}$$

Adiabatic elimination of the excited state

We use this result to replace $\hat{\Psi}_e$ in Eq. B.20. This procedure is called *adiabatic elimination of the excited state*. It is equivalent to the Born-Oppenheimer approximation for atoms in a solid, where the slow and the fast time scales are set by the ionic and the electronic dynamics, rather than the atomic ground and excited states. Inserting the result into Eq. B.20 gives the effective Hamiltonian:

$$\begin{aligned}\hat{\mathcal{H}}_{mb} = &-\hbar\Delta_c\hat{a}^\dagger\hat{a} \\ &+ \int_{\mathcal{A}} dr\hat{\psi}^\dagger(r)\left[\frac{\hat{p}^2}{2m} + V(r) + \hbar\frac{h(r)g(r)}{\Delta_a}(\hat{a}^\dagger + \hat{a})\right. \\ &\qquad \left. + \hbar\frac{g^2(r)}{\Delta_a}\hat{a}^\dagger\hat{a} + \hbar\frac{h^2(r)}{\Delta_a}\right]\hat{\psi}(r) \\ &+ \frac{U}{2}\int_{\mathcal{A}} dr dr'\hat{\psi}^\dagger(r)\hat{\psi}^\dagger(r')\hat{\psi}(r')\hat{\psi}(r)\end{aligned} \tag{B.23}$$

This is the many-body Hamiltonian in Eq. 5.11, with which we start in Chap. 5.

B.5 ATOM-LIGHT INTERACTIONS WITH TWO CAVITY MODES

An extension of Eq. B.23 to two cavity modes requires a number of additional terms in the Hamiltonian. As previously, we work in the frame rotating with the transverse pump. The two light fields evolve differently according to their detuning from the transverse pump frequency with

Quantized cavity fields

$$\hat{\mathcal{H}}_{c,i} = -\hbar\Delta_i \hat{a}_i^\dagger \hat{a}_i \tag{B.24}$$

The index $i \in \{1,2\}$ labels the two cavities, $\hat{a}_i^\dagger$ ($\hat{a}_i$) is the creation (annihilation) operator for a photon in cavity i and $\Delta_i = \omega_i - \omega_p$ is the detuning of cavity i at frequency ω_i from the transverse pump. The interaction of the atoms with each mode is captured by

Interaction of the atoms with each cavity mode

$$\hat{\mathcal{H}}_{\text{int},i} = \int_{\mathcal{A}} \hat{\psi}^\dagger(\mathbf{r}) \left[\hbar \frac{h(\mathbf{r}) g_i(\mathbf{r})}{\Delta_a} (\hat{a}_i^\dagger + \hat{a}_i) + \hbar \frac{g_i^2(\mathbf{r})}{\Delta_a} \hat{a}_i^\dagger \hat{a}\right] \hat{\psi}(\mathbf{r})\, d\mathbf{r} \tag{B.25}$$

Here Δ_a is the detuning from the atomic resonance, $g_i(\mathbf{r})$ is the mode profile of cavity i and $\mathbf{r} = (x, y)$ and $\mathbf{r'} = (x', y')$ are the spatial coordinates that are integrated over the unit cell with area A. The field operator $\hat{\psi}^\dagger$ ($\hat{\psi}$) creates (annihilates) an atom at position $\mathbf{r}$ with mass m. In addition, we have to take into account the effective interaction between the two cavities:

Cavity-cavity interaction

$$\hat{\mathcal{H}}_{\text{int},12} = \int_{\mathcal{A}} \hat{\psi}^\dagger(\mathbf{r}) \left[\hbar \frac{g_1(\mathbf{r}) g_2(\mathbf{r})}{\Delta_a} (\hat{a}_1^\dagger \hat{a}_2 + \hat{a}_2^\dagger \hat{a}_1) + \hbar \frac{h^2(\mathbf{r})}{\Delta_a}\right] \hat{\psi}(\mathbf{r})\, d\mathbf{r} \tag{B.26}$$

Including atomic motion and the contact interaction, we obtain the many-body Hamiltonian used in Eq. 6.12:

Many-body Hamiltonian for two cavities

$$\begin{aligned}
\hat{\mathcal{H}}_{\text{mb}} = &- \sum_{i=1,2} \hbar\Delta_i \hat{a}_i^\dagger \hat{a}_i \\
&+ \int_{\mathcal{A}} \hat{\psi}^\dagger(\mathbf{r}) \left[\frac{\hat{\mathbf{p}}^2}{2m} + V(\mathbf{r})\right. \\
&+ \sum_{i=1,2} \left(\hbar \frac{h(\mathbf{r}) g_i(\mathbf{r})}{\Delta_a} (\hat{a}_i^\dagger + \hat{a}_i) + \hbar \frac{g_i^2(\mathbf{r})}{\Delta_a} \hat{a}_i^\dagger \hat{a}_i\right) \\
&\left. + \hbar \frac{g_1(\mathbf{r}) g_2(\mathbf{r})}{\Delta_a} (\hat{a}_1^\dagger \hat{a}_2 + \hat{a}_2^\dagger \hat{a}_1) + \hbar \frac{h^2(\mathbf{r})}{\Delta_a}\right] \hat{\psi}(\mathbf{r})\, d\mathbf{r} \\
&+ \frac{U_{2D}}{2} \int_{\mathcal{A}} d\mathbf{r} d\mathbf{r'} \hat{\psi}^\dagger(\mathbf{r}) \hat{\psi}^\dagger(\mathbf{r'}) \hat{\psi}(\mathbf{r'}) \hat{\psi}(\mathbf{r}).
\end{aligned} \tag{B.27}$$

The bare atomic dynamics is captured with the momentum operator $\hat{\mathbf{p}}$, the harmonic trapping potential $V(\mathbf{r})$ and collisions with the 2D contact interaction $U_{2D} = A\bar{n}U$, rescaled from the 3D interaction $U = 4\pi\hbar^2 a/m$ with the s-wave scattering length a and the 3D atomic density $\bar{n}$ [2].

LIST OF FIGURES

LIST OF TABLES

ACRONYMS

1D one-dimensional 54, 55, 141, 158, 175
2D two-dimensional 80, 100, 104, 113, 125, 154, 175, 183, 184, 205
2DMOT two-dimensional magneto-optical trap 14–19, 22, 29, 31, 32, 34, 38–40
3D three-dimensional 43, 59, 80, 104, 175, 184, 205
3DMOT three-dimensional magneto-optical trap 14, 15, 18–23, 31–35, 38–41, 43, 50, 51

AC alternating current 36–38, 43
AOI angle of incidence 55, 56, 58
AOM acousto-optic modulator 36–38, 40, 44, 50, 65, 67, 68
AR anti-reflection 16, 19, 20, 39, 40, 58
AWG american wire gauge 27

BCS Bardeen-Cooper-Schrieffer 1
BEC Bose-Einstein condensate 5, 12, 31–33, 42, 48, 53, 60, 69, 70, 76, 77, 80, 81, 84, 86, 88, 92, 97–99, 109, 111, 117, 118, 121, 137, 138, 140–142, 144, 154, 156, 158, 165, 180, 189

CAD computer-aided design 16, 19, 25
CCD charge-coupled device 34, 44, 45, 49, 89
CEM channel electron multiplier 15
CERN Conseil européen pour la recherche nucléaire 21
CF ConFlat 17

DC direct current 65, 68
DDS direct digital synthesizer 36–38, 43, 63, 65
DN Durchgangsnorm 17–19, 23, 24, 56

ENVICO environment control 34, 41
EOM electro-optic modulator 63–65, 67

FALC Fast Analog Linewidth Control 62, 63
FEOM fiber-coupled electro-optic modulator 62–65, 67
FIB focussed ion beam 60
FM frequency modulation 36–38, 62
FSR free spectral range 64, 65, 68, 69
FWHM full width at half maximum 197

GPS global positioning system 34, 36, 63, 65
GSI Gesellschaft für Schwerionenforschung 21
GUI graphical user interface 34

HR high-reflection 25, 56
HT high transmission 66
HV high voltage 20, 26

LAN local area network 34, 63
LMG Lipkin-Meshkov-Glick 113–115
LO local oscillator 36, 37

MBE molecular-beam epitaxy 12, 13, 24
MCP micro-channel plate 15
MW microwave 11, 37, 63
MySQL My structured query language 34

NA numerical aperture 19, 25, 60
Nd:YAG neodymium-doped yttrium aluminum garnet 43
NEG non-evaporable getter 21, 23, 29
NPBS non-polarizing beam splitter 63, 66, 68

OFHC oxygen-free high thermal conductivity 25, 27, 29

PBS polarizing beam splitter 38, 39, 44, 66, 67
PC personal computer 38, 41
PCF photonic crystal fiber 44, 45
PD photodiode 36–40, 44, 45, 63–68
PDH Pound–Drever–Hall 61–65
PEEK polyether ether ketone 25–27
PID proportional-integral-derivative 36, 37, 40, 62, 65, 66
PM polarization-maintaining 33, 38
PSF point spread function 60
PVC polyvinyl chloride 41

QED quantum electrodynamics 53

RF radio frequency 5, 14, 15, 20, 32, 33, 42, 43, 46, 63
RGA residual gas analyser 29

SMA SubMiniature version A 15, 20, 26, 27
SPCM single photon counting module 34, 66–68, 70, 88

TA tapered amplifier 37, 38
TEM transverse electromagnetic 61, 69
TMP turbomolecular pump 23, 24, 29
TTL transistor-transistor logic 34, 43, 67

UHV ultra-high vacuum 11–13, 15, 17, 20, 23, 24, 26, 27, 58, 59

VCO voltage-controlled oscillator 37

XML extensible markup language 34

BIBLIOGRAPHY

1. Sachdev, S. *Quantum phase transitions* (Cambridge University Press, Cambridge, 2011) (cit. on pp. 1, 6, 77, 153, 169).
2. Pitaevskii, L. P. & Stringari, S. *Bose-Einstein condensation* (Oxford University Press, Oxford, 2003) (cit. on pp. 1, 80, 104, 156, 205).
3. Kapitza, P. Viscosity of Liquid Helium below the λ-Point. *Nature* **141,** 74 (1938) (cit. on p. 1).
4. Allen, J. F. & Misener, A. D. Flow Phenomena in Liquid Helium II. *Nature* **142,** 643–644 (1938) (cit. on p. 1).
5. London, F. The λ-Phenomenon of Liquid Helium and the Bose-Einstein Degeneracy. *Nature* **141,** 643–644 (1938) (cit. on p. 1).
6. Tisza, L. Transport Phenomena in Helium II. *Nature* **141,** 913 (1938) (cit. on p. 1).
7. Bardeen, J., Cooper, L. & Schrieffer, J. Theory of Superconductivity. *Phys. Rev.* **108,** 1175 (1957) (cit. on p. 1).
8. Van Delft, D. & Kes, P. The discovery of superconductivity. *Phys. Today* **63,** 38–43 (2010) (cit. on p. 1).
9. Anderson, M. H., Ensher, J. R., Matthews, M. R., Wieman, C. E. & Cornell, E. a. Observation of Bose-Einstein Condensation in a Dilute Atomic Vapor. *Science* **269,** 198–201 (1995) (cit. on pp. 2, 3).
10. Davis, K. B., Mewes, M.-O., Andrews, M. R., van Druten, N. J., Durfee, D. S., Kurn, D. M. & Ketterle, W. Bose-Einstein Condensation in a Gas of Sodium Atoms. *Phys. Rev. Lett* **75,** 3969–3974 (1995) (cit. on pp. 2, 3).
11. Thouless, D. J. The Flow of a Dense Superfluid. *Ann. Phys. (N. Y.)* **52,** 403–427 (1969) (cit. on p. 2).
12. Andreev, A. F. & Lifshitz, I. M. Quantum Theory of Defects in Crystals. *Soviet Physics JETP* **29,** 1107–1113 (1969) (cit. on p. 2).
13. Penrose, O. & Onsager, L. Bose-Einstein Condensation and Liquid Helium. *Phys. Rev.* **104,** 576–584 (1956) (cit. on p. 2).
14. Chester, G. V. Speculations on Bose-Einstein Condensation and Quantum Crystals. *Phys. Rev. A* **2,** 256–258 (1970) (cit. on p. 2).
15. Meisel, M. W. Superspolid ^{4}He: an overview of past searches and future possibilities. *Physica B* **178,** 121–128 (1992) (cit. on pp. 2, 3).
16. De Boer, J. Quantum theory of condensed permanent gases I: the law of corresponding states. *Physica* **14,** 139–148 (1948) (cit. on p. 3).
17. De Boer, J. *Progress in Low Temperature Physics, Vol. 2* (ed Gorter, J.) (North-Holland, Amsterdam, 1957) (cit. on p. 3).
18. Bernardes, N. Quantum Mechanical Law of Corresponding states for Van der Waals Solids at 0°K. *Phys. Rev.* **120,** 807–813 (1960) (cit. on p. 3).
19. Varma, C. M. *The physics of liquid and solid helium* (eds Bennemann, K. H. & Ketterson, J. B.) (John Wiley & Sons, New York, 1976) (cit. on p. 3).

20. Andreev, A. F. in *Prog. Low. Temp. Phys.* (ed Brewer, D. F.) (North-Holland Publishing Company, Amsterdam, 1982) (cit. on p. 3).
21. Henriksen, P. N., Panczyk, M. F., Trickey, S. B. & Adams, E. D. Temperature dependence of Debye theta's for bcc ^{3}He and hcp ^{4}He. *Phys. Rev. Lett.* **23,** 518–520 (1969) (cit. on p. 3).
22. Straty, G. C. & Adams, E. D. Highly Sensitive Capacitive Pressure Gauge. *Rev. Sci. Instrum.* **40,** 1393–1397 (1969) (cit. on p. 3).
23. Trickey, S. B., Kirk, W. P. & Adams, E. D. Thermodynamic, Elastic, and Magnetic Properties of Solid Helium. *Rev. Mod. Phys.* **44,** 668–715 (1972) (cit. on p. 3).
24. Griffioen, W. & Frossati, G. Small sensitive pressure transducer for use at low temperatures. *Rev. Sci. Instrum.* **56,** 1236 (1985) (cit. on p. 3).
25. Van de Haar, P. G., van Woerkens, C. M.C. M., Meisel, M. W. & Frossati, G. An Experiment to Detect Vacancies and Their Possible Bose-Einstein Condensation in Solid ^{4}He. *J. Low Temp. Phys.* **86,** 349–362 (1992) (cit. on p. 3).
26. Lengua, G. A. & Goodkind, J. M. Elementary Excitations and a Collective Mode in hcp ^{4}He. *J. Low Temp. Phys.* **79,** 251–287 (1990) (cit. on p. 3).
27. Ho, P.-C., Bindloss, I. P. & Goodkind, J. M. A New Anomaly in Solid ^{4}He. *J. Low Temp. Phys.* **109,** 409–421 (1997) (cit. on p. 3).
28. Goodkind, J. M. Interaction of First and Second Sound in Solid ^{4}He: Properties of a Possible Bose Condensate. *Phys. Rev. Lett.* **89,** 095301 (2002) (cit. on p. 3).
29. Andreev, A., Keshishev, K., Mezhov-Deglin, L. & Shal'nikov, A. Attempt at observing vacancions in He^4 crystals. *JETP Lett.* **9,** 306–308 (1969) (cit. on p. 3).
30. Suzuki, H. Plastic Flow in Solid Helium. *J. Phys. Soc. Jpn.* **35,** 1472–1479 (1973) (cit. on p. 3).
31. Tsymbalenko, V. L. Plastic flow of crystalline He^4. *JETP Lett.* **23,** 653–656 (1976) (cit. on p. 3).
32. Greywall, D. S. Search for superfluidity in solid ^{4}He. *Phys. Rev. B* **16,** 1291–1292 (1977) (cit. on p. 3).
33. Leggett, A. J. Can a Solid be "Superfluid"? *Phys. Rev. Lett.* **25,** 1543–1546 (1970) (cit. on p. 3).
34. Bishop, D. J. & Paalanen, M. A. Search for superfluidity in hcp ^{4}He. *Phys. Rev. B* **24,** 2844–2845 (1981) (cit. on p. 3).
35. Brewer, D. F., Liezhao, C., Girit, C. & Reppy, J. D. Helium-four transition in a restricted geometry below and above the bulk solidification pressure. *Physica B* **107,** 583–584 (1981) (cit. on p. 3).
36. Lie-zhao, C., Brewer, D. F., Girit, C., Smith, E. N. & Reppy, J. D. Flow and torsional oscillator measurements on liquid helium in restricted geometries under pressure. *Phys. Rev. B* **33,** 106–117 (1986) (cit. on p. 3).
37. Kim, E. & Chan, M. H. W. Probable observation of a supersolid helium phase. *Nature* **427,** 225–227 (2004) (cit. on p. 3).

38. Kim, E. & Chan, M. H. W. Observation of Superflow in Solid Helium. *Science* **305,** 1941–1945 (2004) (cit. on p. 3).
39. Rittner, A. S. C. & Reppy, J. D. Observation of Classical Rotational Inertia and Nonclassical Supersolid Signals in Solid ^{4}He below 250 mK. *Phys. Rev. Lett.* **97,** 165301 (2006) (cit. on p. 3).
40. Aoki, Y., Graves, J. C. & Kojima, H. Oscillation Frequency Dependence of Nonclassical Rotation Inertia of Solid ^{4}He. *Phys. Rev. Lett.* **99,** 0145301 (2007) (cit. on p. 3).
41. Kondo, M., Takada, S., Shibayama, Y. & Shirahama, K. Observation of Non-Classical Rotational Inertia in Bulk Solid ^{4}He. *J. Low Temp. Phys.* **158,** 695–699 (2007) (cit. on p. 3).
42. Penzev, A., Yasuta, Y. & Kubota, M. Annealing Effect for Supersolid Fraction in ^{4}He. *J. Low Temp. Phys.* **148,** 677–681 (2007) (cit. on p. 3).
43. Rittner, A. S. C. & Reppy, J. D. Disorder and the Supersolid State of Solid ^{4}He. *Phys. Rev. Lett.* **98,** 175302 (2007) (cit. on p. 3).
44. Lin, X., Clark, A. C. & Chan, M. H. W. Probable heat capacity signature of the supersolid transition. *Nature* **449,** 1025–1028 (2007) (cit. on p. 3).
45. Lin, X., Clark, A. C., Cheng, Z. G. & Chan, M. H. W. Heat Capacity Peak in Solid ^{4}He: Effects of Disorder and ^{3}He Impurities. *Phys. Rev. Lett.* **102,** 125302 (2009) (cit. on p. 3).
46. Sasaki, S., Ishiguro, R., Maris, H. J. & Balibar, S. Superfluidity of Grain Boundaries and. *Science* **313,** 1098–1100 (2006) (cit. on p. 3).
47. Sasaki, S., Caupin, F. & Balibar, S. Wetting Properties of Grain Boundaries in Solid ^{4}He. *Phys. Rev. Lett.* **99,** 205302 (2007) (cit. on p. 3).
48. Balibar, S. & Caupin, F. Supersolidity and disorder. *J. Phys. Condens. Matter* **20,** 173201 (2008) (cit. on p. 3).
49. Kuklov, A., Prokof'ev, N. & Svistunov, B. How Solid is Supersolid? *Physics* **4,** 109 (2011) (cit. on p. 3).
50. Boninsegni, M. & Prokof'ev, N. V. Supersolids: What and where are they? *Rev. Mod. Phys.* **84,** 759–776 (2012) (cit. on p. 3).
51. Day, J. & Beamish, J. Low-temperature shear modulus changes in solid ^{4}He and connection to supersolidity. *Nature* **450,** 853–856 (2007) (cit. on p. 3).
52. Kim, D. Y. & Chan, M. H. W. Absence of Supersolidity in Solid Helium in Porous Vycor Glass. *Phys. Rev. Lett.* **109,** 155301 (2012) (cit. on p. 3).
53. Chin, C., Grimm, R., Julienne, P. & Tiesinga, E. Feshbach resonances in ultracold gases. *Rev. Mod. Phys.* **82,** 1225–1286 (2010) (cit. on pp. 3, 14).
54. Griesmaier, A., Werner, J., Hensler, S., Stuhler, J. & Pfau, T. Bose-Einstein Condensation of Chromium. *Phys. Rev. Lett.* **94,** 160401 (2005) (cit. on pp. 3, 118).
55. Lu, M., Burdick, N. Q., Youn, S. H. & Lev, B. L. Strongly Dipolar Bose-Einstein Condensate of Dysprosium. *Phys. Rev. Lett.* **107,** 190401 (2011) (cit. on pp. 3, 118).
56. Aikawa, K., Frisch, A., Mark, M., Baier, S., Rietzler, A., Grimm, R. & Ferlaino, F. Bose-Einstein Condensation of Erbium. *Phys. Rev. Lett.* **108,** 210401 (2012) (cit. on pp. 3, 118).

57. Lahaye, T., Menotti, C., Santos, L., Lewenstein, M. & Pfau, T. The physics of dipolar bosonic quantum gases. *Rep. Prog. Phys.* **72,** 126401 (2009) (cit. on pp. 4, 118, 138).
58. Baier, S., Mark, M. J., Petter, D., Aikawa, K., Chomaz, L., Cai, Z., Baranov, M., Zoller, P. & Ferlaino, F. Extended Bose-Hubbard models with ultracold magnetic atoms. *Science* **352,** 201–205 (2016) (cit. on pp. 4, 118).
59. Kadau, H., Schmitt, M., Wenzel, M., Wink, C., Maier, T., Ferrier-Barbut, I. & Pfau, T. Observing the Rosensweig instability of a quantum ferrofluid. *Nature* **530,** 194–197 (2016) (cit. on p. 4).
60. Ferrier-Barbut, I., Kadau, H., Schmitt, M., Wenzel, M. & Pfau, T. Observation of Quantum Droplets in a Strongly Dipolar Bose Gas. *Phys. Rev. Lett.* **116,** 215301 (2016) (cit. on p. 4).
61. Chomaz, L., Baier, S., Petter, D., Mark, M. J., Santos, L. & Ferlaino, F. Quantum-fluctuation-driven crossover from a dilute Bose-Einstein condensate to a macro-droplet in a dipolar quantum fluid. *Phys. Rev. X* **6,** 041039 (2016) (cit. on p. 4).
62. Moses, S. A., Covey, J. P., Miecnikowski, M. T., Jin, D. S. & Ye, J. New frontiers for quantum gases of polar molecules. *Nat. Phys.* **13,** 13–20 (2017) (cit. on pp. 4, 118).
63. Takekoshi, T., Reichsöllner, L., Schindewolf, A., Hutson, J. M., Le Sueur, C. R., Dulieu, O., Ferlaino, F., Grimm, R. & Nägerl, H.-C. Ultracold Dense Samples of Dipolar RbCs Molecules in the Rovibrational and Hyperfine Ground State. *Phys. Rev. Lett.* **113,** 205301 (2014) (cit. on pp. 4, 118).
64. Molony, P. K., Gregory, P. D., Ji, Z., Lu, B., Köppinger, M. P., Sueur, C. R. L., Blackley, C. L., Hutson, J. M. & Cornish, S. L. Creation of Ultracold Molecules in the Rovibrational Ground State. *Phys. Rev. Lett.* **113,** 255301 (2014) (cit. on pp. 4, 118).
65. Guo, M., Zhu, B., Lu, B., Ye, X., Wang, F., Vexiau, R., Bouloufa-maafa, N., Quéméner, G., Dulieu, O. & Wang, D. Creation of an Ultracold Gas of Ground-State Dipolar Molecules. *Phys. Rev. Lett.* **116,** 205303 (2016) (cit. on pp. 4, 118).
66. Ni, K.-K., Ospelkaus, S., de Miranda, M. H. G., Pe, A., Neyenhuis, B., Zirbel, J. J., Kotochigova, S., Julienne, P. S., Jin, D. S. & Ye, J. A High Phase-Space-Density Gas of Polar Molecules. *Science* **322,** 231–235 (2008) (cit. on pp. 4, 118).
67. Park, J. W., Will, S. A. & Zwierlein, M. W. Ultracold Dipolar Gas of Fermionic $^{23}Na^{40}K$ Molecules in Their Absolute Ground State. *Phys. Rev. Lett.* **114,** 1–5 (2015) (cit. on pp. 4, 118).
68. Moses, S. A., Covey, J. P., Miecnikowski, M. T., Miecnikowski, B. Y., Gadway, B., Ye, J. & Jin, D. S. Creation of a low-entropy quantum gas of polar molecules in an optical lattice. *Science* **350,** 659–662 (2015) (cit. on pp. 4, 118).
69. Löw, R., Weimer, H., Nipper, J., Balewski, J. B., Butscher, B., Büchler, H. P. & Pfau, T. An experimental and theoretical guide to strongly interacting Rydberg gases. *J. Phys. B* **45,** 113001 (2012) (cit. on pp. 4, 118).

70. Schauß, P., Cheneau, M., Endres, M., Fukuhara, T., Hild, S., Omran, A., Pohl, T., Gross, C., Kuhr, S. & Bloch, I. Observation of spatially ordered structures in a two-dimensional Rydberg gas. *Nature* **490,** 87–91 (2012) (cit. on pp. 4, 118).

71. Schauß, P., Zeiher, J., Fukuhara, T., Hild, S., Cheneau, M., Macri, T, Pohl, T., Bloch, I. & Gross, C. Crystallization in Ising quantum magnets. *Science* **347,** 1455–1458 (2015) (cit. on pp. 4, 118).

72. Pupillo, G., Micheli, A., Boninsegni, M., Lesanovsky, I. & Zoller, P. Strongly Correlated Gases of Rydberg-Dressed Atoms: Quantum and Classical Dynamics. *Phys. Rev. Lett.* **104,** 223002 (2010) (cit. on pp. 4, 118).

73. Zeiher, J., van Bijnen, R., Schauß, P., Hild, S., Choi, J.-y., Pohl, T., Bloch, I. & Gross, C. Many-body interferometry of a Rydberg-dressed spin lattice. *Nat. Phys.* **12,** 1095–1099 (2016) (cit. on pp. 4, 118).

74. O'Dell, D. H. J., Giovanazzi, S. & Kurizki, G. Rotons in Gaseous Bose-Einstein Condensates Irradiated by a Laser. *Phys. Rev. Lett.* **90,** 110402 (2003) (cit. on pp. 4, 138).

75. Baumann, K., Guerlin, C., Brennecke, F. & Esslinger, T. Dicke quantum phase transition with a superfluid gas in an optical cavity. *Nature* **464,** 1301–1306 (2010) (cit. on pp. 4, 12, 75, 76, 86, 118).

76. Büchler, H. & Blatter, G. Supersolid versus Phase Separation in Atomic Bose-Fermi Mixtures. *Phys. Rev. Lett.* **91,** 130404 (2003) (cit. on p. 4).

77. Labeyrie, G., Tesio, E., Gomes, P. M., Oppo, G.-L., Firth, W. J., Robb, G. R. M., Arnold, A. S., Kaiser, R. & Ackemann, T. Optomechanical self-structuring in a cold atomic gas. *Nat. Photonics* **8,** 321–325 (2014) (cit. on pp. 4, 76, 118).

78. Ostermann, S., Piazza, F. & Ritsch, H. Spontaneous Crystallization of Light and Ultracold Atoms. *Physical Review X* **6,** 021026 (2016) (cit. on p. 4).

79. Gopalakrishnan, S., Lev, B. L. & Goldbart, P. M. Emergent crystallinity and frustration with Bose–Einstein condensates in multimode cavities. *Nat. Phys.* **5,** 845–850 (2009) (cit. on pp. 4, 76, 189).

80. Léonard, J., Lee, M., Morales, A., Karg, T. M., Esslinger, T. & Donner, T. Optical transport of ultracold atoms using focus-tunable lenses. *New J. of Phys.* **16,** 093028 (2014) (cit. on p. 5).

81. Ritsch, H., Domokos, P., Brennecke, F. & Esslinger, T. Cold atoms in cavity-generated dynamical optical potentials. *Rev. Mod. Phys.* **85,** 553–601 (2013) (cit. on pp. 5, 12, 53, 75, 80, 86, 107, 118, 169).

82. Guerlin, C., Brion, E., Esslinger, T. & Mølmer, K. Cavity quantum electrodynamics with a Rydberg-blocked atomic ensemble. *Phys. Rev. A* **82,** 053832 (2010) (cit. on pp. 7, 190).

83. Wolke, M., Klinner, J., Keßler, H. & Hemmerich, A. Cavity cooling below the recoil limit. *Science* **337,** 75–78 (2012) (cit. on pp. 7, 11, 61).

84. Wallquist, M., Hammerer, K., Rabl, P, Lukin, M. D. & Zoller, P. Hybrid quantum devices and quantum engineering. *Phys. Scr.* **T137,** 014001 (2009) (cit. on p. 11).

85. Daniilidis, N. & Häffner, H. Quantum Interfaces Between Atomic and Solid-State Systems. *Annu. Rev. Condens. Matter Phys.* **4,** 83–112 (2013) (cit. on p. 11).

86. Kurizki, G., Bertet, P., Kubo, Y., Mølmer, K., Petrosyan, D. & Rabl, P. Quantum technologies with hybrid systems. *Proc. Natl. Acad. Sci. USA* **112,** 3866–3873 (2015) (cit. on p. 11).

87. Raimond, J. M., Brune, M. & Haroche, S. Colloquium: Manipulating quantum entanglement with atoms and photons in a cavity. *Rev. Mod. Phys.* **73,** 565–582 (2001) (cit. on p. 11).

88. Reiserer, A. & Rempe, G. Cavity-based quantum networks with single atoms and optical photons. *Rev. Mod. Phys.* **87,** 1379–1418 (2015) (cit. on p. 11).

89. Lodahl, P., Mahmoodian, S., Stobbe, S., Rauschenbeutel, A., Schneeweiss, P., Volz, J., Pichler, H. & Zoller, P. Chiral quantum optics. *Nature* **541,** 473–480 (2017) (cit. on p. 11).

90. Devoret, M. H. & Schoelkopf, R. J. Superconducting Circuits for Quantum Information: An Outloook. *Science* **339,** 1169 (2013) (cit. on p. 11).

91. Teufel, J. D., Donner, T, Li, D., Harlow, J. W., Allman, M. S., Cicak, K, Sirois, A. J., Whittaker, J. D., Lehnert, K. W. & Simmonds, R. W. Sideband cooling of micromechanical motion to the quantum ground state. *Nature* **475,** 359–363 (2011) (cit. on p. 11).

92. Jöckel, A., Faber, A., Kampschulte, T., Korppi, M., Rakher, M. T. & Treutlein, P. Sympathetic cooling of a membrane oscillator in a hybrid mechanical – atomic system. *Nat. Nanotechnol.* **10,** 55–59 (2015) (cit. on p. 11).

93. Hosseini, M., Duan, Y., Beck, K. M. & Chen, Y.-T. Cavity cooling of many atoms. *Phys. Rev. Lett.* **118,** 183601 (2017) (cit. on p. 11).

94. Cho, A. Y. & Arthur, J. R. Molecolar beam epitaxy. *Prog. Solid State Chem.* **10,** 157–191 (1975) (cit. on p. 12).

95. Frigeri, P., Seravalli, L., Trevisi, G. & Franchi, S. in *Comprehensive Semiconductor Science and Technology* 3, 480–522 (Elsevier, Amsterdam, 2011) (cit. on p. 12).

96. Colombe, Y., Steinmetz, T., Dubois, G., Linke, F., Hunger, D. & Reichel, J. Strong atom–field coupling for Bose–Einstein condensates in an optical cavity on a chip. *Nature* **450,** 272–276 (2007) (cit. on p. 12).

97. Brennecke, F., Donner, T., Ritter, S., Bourdel, T., Köhl, M. & Esslinger, T. Cavity QED with a Bose-Einstein condensate. *Nature* **450,** 268–271 (2007) (cit. on p. 12).

98. Gupta, S., Moore, K. L., Murch, K. W. & Stamper-Kurn, D. M. Cavity Nonlinear Optics at Low Photon Numbers from Collective Atomic Motion. *Phys. Rev. Lett.* **99,** 213601 (2007) (cit. on p. 12).

99. Brennecke, F., Ritter, S., Donner, T. & Esslinger, T. Cavity Optomechanics with a Bose-Einstein condensate. *Science* **322,** 235–238 (2008) (cit. on p. 12).

100. DeMarco, B. & Jin, D. S. Onset of Fermi Degeneracy in a Trapped Atomic Gas. *Science* **285,** 1703–1706 (1999) (cit. on p. 12).

101. Greiner, M., Regal, C. A. & Jin, D. S. Emergence of a molecular Bose–Einstein condensate from a Fermi gas. *Nature* **34,** 665–668 (2003) (cit. on p. 12).

102. Jochim, S., Bartenstein, M., Altmeyer, A., Hendl, G., Riedl, S., Chin, C., Denschlag, J. H. & Grimm, R. Bose-Einstein Condensation of Molecules. *Science* **302,** 2101–2103 (2003) (cit. on p. 12).

103. Wutz, M., Adam, H., Walcher, W. & Jousten, K. *Handbuch Vakuumtechnik* (Vieweg Verlag, Braunschweig, 2000) (cit. on pp. 13, 17, 21, 22, 26).

104. *According to the ampule datasheet.* (cit. on p. 13).

105. Ferlaino, F., Errico, C. D., Roati, G., Zaccanti, M., Inguscio, M., Modugno, G. & Simoni, A. Feshbach spectroscopy of a K-Rb atomic mixture. *Phys. Rev. A* **73,** 040702 (2006) (cit. on p. 13).

106. Ferlaino, F., Errico, C. D., Roati, G., Zaccanti, M., Inguscio, M., Modugno, G. & Simoni, A. Erratum: Feshbach spectroscopy of a K-Rb atomic mixture. *Phys. Rev. A* **74,** 039903 (2006) (cit. on p. 13).

107. Steck, D. A. *Rubidium 87 D Line Data* tech. rep. (2010). http://steck.us/alkalidata/rubidium87numbers.1.6.pdf (cit. on pp. 13, 49).

108. Tiecke, T. G. *Properties of Potassium* tech. rep. (2011), 1–14. http://tobiastiecke.nl/archive/PotassiumProperties.pdf (cit. on p. 13).

109. Bloch, I., Dalibard, J. & Zwerger, W. Many-body physics with ultracold gases. *Rev. Mod. Phys.* **80,** 885–964 (2008) (cit. on pp. 14, 111, 117, 189).

110. Inouye, S, Andrews, M. R., Stenger, J, Miesner, H & Ketterle, W. Observation of Feshbach resonances in a Bose–Einstein condensate. *Nature* **392,** 151–154 (1998) (cit. on p. 14).

111. Roati, G., Riboli, F., Modugno, G. & Inguscio, M. Fermi-Bose Quantum Degenerate ^{40}K-^{87}Rb Mixture with Attractive Interaction. *Phys. Rev. Lett.* **89,** 150403 (2002) (cit. on p. 14).

112. Bendkowsky, V., Butscher, B., Nipper, J., Shaffer, J. P., Löw, R. & Pfau, T. Observation of ultralong-range Rydberg molecules. *Nature* **458,** 1005–1008 (2009) (cit. on p. 14).

113. Okano, M. *et al.* Vibration isolation for scanning tunneling microscopy Vibration isolation for scanning tunneling microscopy. *J. Vac. Sci. Techn. A* **5,** 3313–3320 (1987) (cit. on pp. 15, 27, 59).

114. Phillips, W. D. & Metcalf, H. Laser Deceleration of an Atomic Beam. *Phys. Rev. Lett.* **48,** 596–599 (1982) (cit. on p. 15).

115. Myatt, C. J., Newbury, N. R., Ghrist, R. W., Loutzenhiser, S & Wieman, C. E. Multiply loaded magneto-optical trap. *Opt. Lett.* **21,** 290–292 (1996) (cit. on p. 15).

116. Dieckmann, K., Spreeuw, R. J. C., Weidemüller, M. & Walraven, J. T. M. Two-dimensional magneto-optical trap as a source of slow atoms. *Phys. Rev. A* **58,** 3891–3895 (1998) (cit. on pp. 15, 16, 18, 35).

117. Gehr, R. *Towards a two-dimensional magneto-optical trap for potassium atoms Diploma thesis* Diploma thesis (ETH Zürich, 2006) (cit. on p. 16).

118. Leitz, D. *Realisierung einer zweidimensionalen magneto-optischen Falle für Kalium* Diploma thesis (ETH Zürich, 2006) (cit. on p. 16).

119. Uehlinger, T. *A 2D Magneto-Optical Trap as a High-Flux Source of Cold Potassium Atoms* Diploma thesis (ETH Zürich, 2008) (cit. on p. 16).

120. Catani, J., Maioli, P., De Sarlo, L., Minardi, F. & Inguscio, M. Intense slow beams of bosonic potassium isotopes. *Phys. Rev. A* **73,** 033415 (2006) (cit. on pp. 17, 18, 35).

121. Ridinger, A., Chaudhuri, S., Salez, T., Eismann, U., Fernandes, D. R., Magalhães, K., Wilkowski, D., Salomon, C. & Chevy, F. Large atom number dual-species magneto-optical trap for fermionic ^{6}Li and ^{40}K atoms. *Eur. Phys. J. D* **65,** 223–242 (2011) (cit. on pp. 18, 35).

122. Chaudhuri, S., Roy, S. & Unnikrishnan, C. Realization of an intense cold Rb atomic beam based on a two-dimensional magneto-optical trap: Experiments and comparison with simulations. *Phys. Rev. A* **74,** 1–11 (2006) (cit. on pp. 18, 35).

123. Conroy, R., Xiao, Y., Vengalattore, M., Rooijakkers, W. & Prentiss, M. Compact, robust source of cold atoms for efficient loading of a magnetic guide. *Opt. Commun.* **226,** 259–266 (2003) (cit. on pp. 18, 35).

124. Gokhroo, V., Rajalakshmi, G, Easwaran, R. K. & Unnikrishnan, C. S. Sub-Doppler deep-cooled bosonic and fermionic isotopes of potassium in a compact 2D^{+}–3DMOT set-up. *Journ. Phys. B* **44,** 115307 (2011) (cit. on pp. 18, 35).

125. Herrmann, A. *Permanent Magnets for a 2D Magneto-Optical Trap* Semester thesis (ETH Zürich, 2010), 1–22 (cit. on p. 18).

126. Ketterle, W, Durfee, S, Stamper, M, The, I. & Fermi, E. *Making, probing and understanding Bose-Einstein condensates* in *Proceedings of the 1998 Enrico Fermi summer school on Bose-Einstein condensation in Varenna, Italy* (1999) (cit. on pp. 19, 40, 42, 43, 49, 95).

127. Benvenuti, C. *Non-Evaporable Getters: From Pumping Strips to Thin Film Coatings* in *Proc. EPAC* (Stockholm, 1998), 200–204 (cit. on p. 21).

128. Benvenuti, C. & Chiggiato, P. Pumping characteristics of the St707 nonevaporable getter. *J. Vac. Sci. Technol.* **14,** 3278–3282 (2000) (cit. on p. 21).

129. Chiggiato, P. & Costa Pinto, P. Ti–Zr–V non-evaporable getter films: From development to large scale production for the Large Hadron Collider. *Thin Solid Films* **515,** 382–388 (2006) (cit. on p. 21).

130. Benvenuti, C., Bojon, J. P., Chiggiato, P. & Losch, G. Ultimate pressures of the large electron positron collider (LEP) vacuum system. *Vacuum* **44,** 507–509 (1993) (cit. on p. 21).

131. Benvenuti, C & Chiggiato, P. Obtention of pressures in the 10^{-14} torr range by means of a Zr-V-Fe non evaporable getter. *Vacuum* **44,** 511–513 (1993) (cit. on p. 21).

132. Benvenuti, C., Chiggiato, P., Costa Pinto, P., Santana, A. E., Hedley, T., Mongelluzzo, A., Ruzinov, V. & Wevers, I. Vacuum properties of TiZrV non-evaporable getter films. *Vacuum* **60,** 57–65 (2001) (cit. on p. 21).

133. Bellachioma, M. C., Kurdal, J., Krämer, A. & Savino, G. Evaluation of the Vacuum Performance of NEG Coated Chambers in the SIS18*. *GSI Sc. Rep.* **15,** 118 (2008) (cit. on p. 21).

134. NASA. *Outgassing Data for Selecting Spacecraft Materials* `http://outgassing.nasa.gov` (cit. on p. 21).

135. O'Hanlon, J. F. *A user's guide to vacuum technology* (Wiley & Sons, New York, 1989) (cit. on p. 21).

136. Davis, D. H. Monte Carlo Calculation of Molecular Flow Rates through a Cylindrical Elbow and Pipes of Other Shapes. *J. Appl. Phys.* **31,** 1169–1176 (1960) (cit. on p. 22).

137. Tingwei, X. & Kaiping, W. The relation between the cunductance of an elbow and the angle between the tubes. *Vacuum* **32,** 655–659 (1982) (cit. on p. 22).

138. Regal, C. A. & Jin, D. S. Measurement of Positive and Negative Scattering Lengths in a Fermi Gas of Atoms. *Phys. Rev. Lett.* **90,** 230404 (2003) (cit. on p. 22).

139. Regal, C. A., Greiner, M & Jin, D. S. Observation of Resonance Condensation of Fermionic Atom Pairs. *Phys. Rev. Lett.* **4,** 040403 (2004) (cit. on p. 22).

140. Inouye, S., Goldwin, J., Olsen, M. L., Ticknor, C., Bohn, J. L. & Jin, D. S. Observation of Heteronuclear Feshbach Resonances in a Mixture of Bosons and Fermions. *Phys. Rev. Lett.* **18,** 183201 (2004) (cit. on p. 22).

141. Moore, J. H., Davis, C. C. & Coplan, M. A. *Building scientific apparatus* (Perseus Books Publishing, Cambridge, MA, 1991) (cit. on pp. 23, 26).

142. Park, C. D., Chung, S. M. & Manini, P. Combination of compact nonevaporable getter and small ion pumps for ultrahigh vacuum systems. *J. Vac. Sci. Techn. A* **29,** 011012 (2011) (cit. on p. 23).

143. Karg, T. M. *Production and Optical Transport of an Ultracold Gas of Rubidium Atoms* Master thesis (ETH Zürich, 2014) (cit. on pp. 32, 42, 43).

144. Vogelbacher, F. & Frank, A. *Control and Logging of Environmental Parameters via Ethernet* Semester thesis (ETH Zürich, 2012) (cit. on p. 34).

145. Stöferle, T. *Exploring Atomic Quantum Gases in Optical Lattices* PhD thesis (ETH Zürich, 2005) (cit. on p. 34).

146. Phillips, W. D. Laser cooling and trapping of neutral atoms. *Rev. Mod. Phys.* **70,** 721–741 (1998) (cit. on p. 34).

147. Metcalf, H. & van der Straten, P. *Laser cooling and trapping* **4,** 242–249 (Springer, New York, 1999) (cit. on p. 34).

148. Schoser, J., Batär, A., Löw, R., Schweikhard, V., Grabowski, A., Ovchinnikov, Y. & Pfau, T. Intense source of cold Rb atoms from a pure two-dimensional magneto-optical trap. *Phys. Rev. A* **66,** 1–10 (2002) (cit. on p. 35).

149. Lu, Z., Corwin, K., Renn, M., Anderson, M., Cornell, E. & Wieman, C. Low-Velocity Intense Source of Atoms from a Magneto-optical Trap. *Phys. Rev. Lett.* **77,** 3331–3334 (1996) (cit. on p. 35).

150. Wohlleben, W., Chevy, F., Madison, K. W. & Dalibard, J. An atom faucet. *Eur. Phys. J. D* **15,** 237–244 (2001) (cit. on p. 35).

151. Müller, T., Wendrich, T., Gilowski, M., Jentsch, C., Rasel, E. & Ertmer, W. Versatile compact atomic source for high-resolution dual atom interferometry. *Phys. Rev. A* **76,** 063611 (2007) (cit. on p. 35).

152. Tiecke, T., Gensemer, S., Ludewig, A. & Walraven, J. High-flux two-dimensional magneto-optical-trap source for cold lithium atoms. *Phys. Rev. A* **80,** 013409 (2009) (cit. on p. 35).

153. Lett, P. D., Watts, R. N., Westbrook, C. I. & Phillips, W. D. Observation of Atoms Laser Cooled below the Doppler Limit. *Phys. Rev. Lett.* **61,** 169–172 (1988) (cit. on p. 35).

154. Dalibard, J. & Cohen-Tannoudji, C. Laser cooling below the Doppler limit by polarization gradients: simple theoretical models. *J. Opt. Soc. Am. B* **6,** 2023 (1989) (cit. on p. 35).

155. Monroe, C., Swann, W., Robinson, H. & Wieman, C. Very Cold Trapped Atoms in a Vapor Cell. *Phys. Rev. Lett.* **65,** 1571–1575 (1990) (cit. on p. 35).

156. Corman, L. *Towards a novel ultracold Rubidium experiment* Master thesis (ETH Zürich) (cit. on p. 35).

157. Wieman, C. E. & Hollberg, L. Using diode lasers for atomic physics. *Rev. Sci. Instrum.* **62,** 1–20 (1991) (cit. on p. 35).

158. Wieman, C. E., Flower, G. & Gilbert, S. Inexpensive laser cooling and trapping experiment for undergraduate laboratories. *Am. J. Phys.* **63,** 317–330 (1995) (cit. on p. 35).

159. Bjorklund, G. C., Levenson, M. D., Lenth, W. & Ortiz, C. Frequency Modulation (FM) Spectroscopy. *Appl. Phys. B* **43,** 145–152 (1983) (cit. on p. 37).

160. Preston, D. W. Doppler-free saturated absorption: Laser spectroscopy. *Am. J. Phys.* **64,** 1432–1436 (1996) (cit. on p. 37).

161. Schünemann, U., Engler, H., Grimm, R. & Weidemüller, M. Simple scheme for tunable frequency offset locking of two lasers. *Rev. Sci. Instrum.* **70,** 242–243 (1999) (cit. on p. 37).

162. Young, E. H. & Yao, S.-K. Design Considerations for Acousto-Optic Devices. *Proc. IEEE* **69,** 54–64 (1981) (cit. on p. 38).

163. Migdall, A. L., Prodan, J. V., Phillips, W. D., Bergeman, T. H. & Metcalf, H. J. First Observation of Magnetically Trapped Neutral Atoms. *Phys. Rev. Lett.* **54,** 2596–2599 (1985) (cit. on p. 40).

164. Wipfli, O. *A Radio Frequency Setup for the Evaporative Cooling of Ultracold Atoms* Semester thesis (ETH Zürich, 2013) (cit. on pp. 42, 43).

165. Masuhara, N., Doyle, J. M., Sandberg, J. C., Kleppner, D., Greytak, T. J., Hess, H. F. & Kochanski, G. P. Evaporative Cooling of Spin-Polarized Atomic hydrogen. *Phys. Rev. Lett.* **61,** 935–938 (1988) (cit. on p. 42).

166. Ketterle, W. & van Druten, N. J. Evaporative cooling of trapped atoms. *Adv. At., Mol., Opt. Phys.* **37,** 181–236 (1996) (cit. on p. 42).

167. Grimm, R. & Weidemüller, M. Optical Dipole Traps. *Adv. At., Mol., Opt. Phys.* **42,** 95–170 (2000) (cit. on pp. 43, 191).

168. Zosel, C. *A novel transport scheme for ultracold atoms* Master thesis (ETH Zürich, 2013) (cit. on p. 43).

169. Berger, E. *Towards a high-resolution imaging system for ultracold atoms in two crossed cavities* Master thesis (2017) (cit. on p. 43).

170. Lin, Y.-J., Perry, A., Compton, R., Spielman, I. & Porto, J. V. Rapid production of ^{87}Rb Bose-Einstein condensates in a combined magnetic and optical potential. *Phys. Rev. A* **79,** 1–8 (2009) (cit. on p. 45).

171. Pinkse, P. W. H., Mosk, A., Weidemüller, M., Reynolds, M. W., Hijmans, T. W. & Walraven, J. T. M. Adiabatically Changing the Phase-Space Density of a Trapped Bose Gas. *Phys. Rev. Lett.* **78,** 990–993 (1997) (cit. on p. 45).

172. Stamper-Kurn, D. M., Miesner, H.-J., Chikkatur, A. P., Inouye, S, Stenger, J & Ketterle, W. Reversible Formation of a Bose-Einstein Condensate. *Phys. Rev. Lett.* **81,** 2194–2197 (1998) (cit. on p. 45).

173. Greiner, M., Bloch, I., Hänsch, T. & Esslinger, T. Magnetic transport of trapped cold atoms over a large distance. *Phys. Rev. A* **63,** 031401 (2001) (cit. on p. 45).

174. Goldwin, J., Inouye, S., Olsen, M., Newman, B., DePaola, B. & Jin, D. Measurement of the interaction strength in a Bose-Fermi mixture with ^{87}Rb and ^{40}K. *Phys. Rev. A* **70,** 021601 (2004) (cit. on p. 45).

175. Gustavson, T., Chikkatur, A., Leanhardt, A., Görlitz, A., Gupta, S., Pritchard, D. & Ketterle, W. Transport of Bose-Einstein Condensates with Optical Tweezers. *Phys. Rev. Lett.* **88,** 020401 (2002) (cit. on p. 45).

176. Sauer, J. A., Fortier, K. M., Chang, M. S., Hamley, C. D. & Chapman, M. S. Cavity QED with optically transported atoms. *Phys. Rev. A* **69,** 051804 (2004) (cit. on p. 45).

177. Schmid, S., Thalhammer, G., Winkler, K., Lang, F. & Denschlag, J. H. Long distance transport of ultracold atoms using a 1D optical lattice. *New J. Phys.* 159–159 (2006) (cit. on p. 45).

178. Eberle, G., Chiron, V. & Wegener, K. Simulation and Realization of a Focus Shifting Unit using a Tunable Lens for 3D Laser Material Processing. *Phys. Procedia* **41,** 441–447 (2013) (cit. on p. 45).

179. Savidis, N., Peyman, G., Peyghambarian, N. & Schwiegerling, J. Non-mechanical zoom system through pressure-controlled tunable fluidic lenses. *Appl. Opt.* **52,** 2858–2865 (2013) (cit. on p. 45).

180. Tanaka, Y. 3D multiple optical tweezers based on time-shared scanning with a fast focus tunable lens. *J. Opt.* **15,** 025708 (2013) (cit. on p. 45).

181. Grewe, B. F., Voigt, F. F., van 't Hoff, M. & Helmchen, F. Fast two-layer two-photon imaging of neuronal cell populations using an electrically tunable lens. *Biomed. Opt. Express* **2,** 2035–46 (2011) (cit. on p. 45).

182. *EL-10-30 Datasheet* https://www.optotune.com/images/products/OptotuneEL-10-30.pdf (cit. on p. 47).

183. Weber, T., Weber, T., Herbig, J., Mark, M., Nägerl, H.-C. & Grimm, R. Bose-Einstein Condensation of Cesium. *Science* **299,** 232–235 (2003) (cit. on p. 48).

184. Kinoshita, T., Wenger, T. & Weiss, D. All-optical Bose-Einstein condensation using a compressible crossed dipole trap. *Phys. Rev. A* **71,** 1–4 (2005) (cit. on p. 48).

185. Hung, C. L., Zhang, X., Gemelke, N. & Chin, C. Accelerating evaporative cooling of atoms into Bose-Einstein condensation in optical traps. *Phys. Rev. A* **78,** 1–4 (2008) (cit. on p. 48).

186. Miller, R., Northup, T. E., Birnbaum, K. M., Boca, A., Boozer, A. D. & Kimble, H. J. Trapped atoms in cavity QED: coupling quantized light and matter. *J. Phys. B* **38,** 551–565 (2005) (cit. on p. 53).

187. Öttl, A., Ritter, S., Köhl, M., Esslinger, T., Öttl, A., Ritter, S., Köhl, M. & Esslinger, T. Hybrid apparatus for Bose-Einstein condensation and cavity quantum electrodynamics: Single atom detection in quantum degenerate gases. *Rev. Mod. Phys.* **77,** 063118 (2006) (cit. on p. 56).

188. Ritter, S. *Probing Coherence During Bose-Einstein Condensation* PhD thesis (ETH Zürich, 2007) (cit. on pp. 56, 61).

189. Lee, M., Kim, J., Seo, W., Hong, H.-g., Song, Y., Dasari, R. R. & An, K. Three-dimensional imaging of cavity vacuum with single atoms localized by nanohole array. *Nat. Commun.* **5,** 1–6 (2014) (cit. on p. 56).

190. Trupke, M., Hinds, E. A., Eriksson, S., Curtis, E. A., Moktadir, Z., Kukharenka, E. & Kraft, M. Microfabricated high-finesse optical cavity with open access and small volume. *Appl. Phys. Lett.* **87,** 211106 (2005) (cit. on p. 56).

191. Hunger, D., Steinmetz, T., Colombe, Y., Deutsch, C., Hänsch, T. W. & Reichel, J. A fiber Fabry-Perot cavity with high finesse. *New J. Phys.* **12,** 065038 (2010) (cit. on p. 56).

192. Born, M. & Wolf, E. *Principles of Optics* (Cambridge University Press, Cambridge, 1999) (cit. on pp. 60, 75).

193. Drever, R. W. P., Hall, J. L., Kowalski, F. V., Hough, J., Ford, G. M., Munley, a. J. & Ward, H. Laser phase and frequency stabilization using an optical resonator. *Appl. Phys. B* **31,** 97–105 (1983) (cit. on p. 61).

194. Black, E. D. An introduction to Pound–Drever–Hall laser frequency stabilization. *Am. J. Phys.* **69,** 79–87 (2001) (cit. on p. 61).

195. Bux, S., Krenz, G., Slama, S., Zimmermann, C. & Courteille, P. W. Ultra-cold atoms in an optical cavity: two-mode laser locking to the cavity avoiding radiation pressure. *Appl Phys. B* **89,** 181–186 (2007) (cit. on p. 61).

196. Kollár, A. J., Papageorge, A. T., Baumann, K., Armen, M. A. & Lev, B. L. An adjustable-length cavity and Bose-Einstein condensate apparatus for multimode cavity QED. *New J. Phys.* **17,** 43012 (2015) (cit. on p. 61).

197. Öttl, A. *Correlations and counting statistics of an atom laser.* PhD thesis (ETH Zürich, 2006) (cit. on p. 61).

198. Burghardt, B., Jitschin, W. & Meisel, G. Precise rf Tuning for cw Dye Lasers. *Appl. Phys.* **20,** 141–146 (1979) (cit. on p. 61).

199. Mabuchi, H., Ye, J. & Kimble, H. J. Full observation of single-atom dynamics in cavity QED. *Appl. Phys. B* **68,** 1095–1108 (1999) (cit. on p. 61).

200. Bohlouli-Zanjani, P., Afrousheh, K. & Martin, J. D. D. Optical transfer cavity stabilization using current-modulated injection-locked diode lasers. *Rev. Sci. Instrum.* **77,** 093105 (2006) (cit. on p. 61).

201. Kelly, J. F. & Gallagher, A. Efficient electro-optic modulator for optical pumping of Na beams. *Rev. Sci. Instrum.* **58,** 563–566 (1987) (cit. on p. 63).

202. Hruby, L. *Towards a 3D optical lattice potential inside an optical high-finesse cavity* Diploma thesis (ETH Zürich, 2013) (cit. on pp. 64, 191).

203. NIST. *Vacuum Wavelength and Ambient Conditions* `http://emtoolbox.nist.gov/Wavelength/ciddor.asp` (cit. on p. 64).

204. Sandholzer, K. *A stabilised in-vacuum transfer cavity system* Master thesis (ETH Zürich, 2016) (cit. on p. 64).

205. Donley, E. A., Heavner, T. P., Levi, F., Tataw, M. O. & Jefferts, S. R. Double-pass acousto-optic modulator system. *Rev. Sci. Instrum.* **76,** 063112 (2005) (cit. on p. 65).

206. Sallen, R. P. & Key, E. L. A Practical Method of Designing RC Active Filters. *IRE Trans. Circuit Theory* **2,** 74–85 (1955) (cit. on p. 65).

207. Baumann, K. G. *Experimental Realization of the Dicke Quantum Phase Transition presented by* PhD thesis (ETH Zürich, 2011) (cit. on pp. 67, 86, 199).

208. Hood, C. J., Kimble, H. J. & Ye, J. Characterization of high-finesse mirrors: Loss, phase shifts, and mode structure in an optical cavity. *Phys. Rev. A* **64,** 033804 (2001) (cit. on p. 68).

209. Poirson, J., Bretenaker, F., Vallet, M. & Le Floch, A. Analytical and experimental study of ringing effects in a Fabry–Perot cavity. Application to the measurement of high finesses. *Journ. Opt. Soc. Am. B* **14,** 2811–2817 (1997) (cit. on p. 68).

210. Morsch, O. & Oberthaler, M. Dynamics of Bose-Einstein condensates in optical lattices. *Rev. Mod. Phys.* **78,** 179–215 (2006) (cit. on p. 70).

211. Gould, P. L., Ruff, G. A. & Pritchard, D. E. Diffraction of Atoms by Light: The Near-Resonant Kapitza-Dirac Effect. *Phys. Rev. Lett.* **56,** 827–830 (1986) (cit. on p. 70).

212. Black, A., Chan, H. & Vuletić, V. Observation of Collective Friction Forces due to Spatial Self-Organization of Atoms: From Rayleigh to Bragg Scattering. *Phys. Rev. Lett.* **91,** 203001 (2003) (cit. on pp. 75, 76, 118).

213. Mandel, L. & Wolf, E. *Optical coherence and quantum optics* (Cambridge University Press, Cambridge, 1995) (cit. on pp. 75, 125).

214. Inouye, S., Chikkatur, A. P., Stamper-Kurn, D. M., Stenger, J., Pritchard, D. E. & Ketterle, W. Superradiant Rayleigh Scattering from a Bose-Einstein Condensate. *Science* **285,** 571–574 (1999) (cit. on p. 76).

215. Birkl, G, Gatzke, M, Deutsch, I. H., Rolston, S. L. & Phillips, W. D. Bragg Scattering from Atoms in Optical Lattices. *Phys. Rev. Lett.* **75,** 2823–2826 (1995) (cit. on p. 76).

216. Weidemüller, M., Hemmerich, A., Gorlitz, A., Esslinger, T. & Hänsch, T. W. Bragg Diffraction in an Atomic Lattice Bound by Light. *Phys. Rev. Lett.* **75,** 4583–4586 (1995) (cit. on p. 76).

217. Westbrook, C. I., Jurczak, C., Birkl, G., Desruelle, B., Phillips, W. D. & Aspect, A. A study of atom localization in an optical lattice by analysis of the scattered light. *J. Mod. Opt.* **44,** 1837–1851 (1997) (cit. on p. 76).

218. Raithel, G., Birkl, G., Kastberg, A., Philipps, W. D. & Rolston, S. L. Cooling and Localization Dynamics in Optical Lattices. *Phys. Rev. Lett.* **78,** 630–633 (2005) (cit. on p. 76).

219. Weidemüller, M., Görlitz, A., Hänsch, T. W. & Hemmerich, A. Local and global properties of light-bound atomic lattices investigated by Bragg diffraction. *Phys. Rev. A* **58,** 4647–4661 (1998) (cit. on p. 76).

220. Weitenberg, C., Schauß, P., Fukuhara, T., Cheneau, M., Endres, M., Bloch, I. & Kuhr, S. Coherent Light Scattering from a Two-Dimensional Mott Insulator. *Phys. Rev. Lett.* **106,** 2–5 (2011) (cit. on p. 76).

221. Purcell, E. M. Spontaneous Emission Probabilities at Radio Frequencies. *Phys. Rev.* **69,** 681 (1946) (cit. on p. 76).

222. Domokos, P. & Ritsch, H. Collective Cooling and Self-Organization of Atoms in a Cavity. *Phys. Rev. Lett.* **89,** 253003 (2002) (cit. on p. 76).

223. Nagy, D., Szirmai, G. & Domokos, P. Self-organization of a Bose-Einstein condensate in an optical cavity. *Eur. Phys. J. D.* **48,** 127–137 (2008) (cit. on pp. 76, 166).

224. Klinder, J., Keßler, H., Wolke, M., Mathey, L. & Hemmerich, A. Dynamical phase transition in the open Dicke model. *Proc. Natl. Acad. Sci. USA* **112,** 3290–3295 (2015) (cit. on p. 76).

225. Kollár, A. J., Papageorge, A. T., Vaidya, V. D., Guo, Y., Keeling, J. & Lev, B. L. Supermode-density-wave-polariton condensation with a Bose–Einstein condensate in a multimode cavity. *Nat. Commun.* **8,** 14386 (2017) (cit. on pp. 76, 189).

226. Landau, L. D. On the theory of phase transitions. *Zh. Eksp. Teor. Fiz.* **7,** 19–32 (1937) (cit. on p. 77).

227. Ginzburg, V. & Landau, L. On the theory of superconductivity. *Zh. Eksp. Teor. Fiz.* **20,** 1064–1082 (1950) (cit. on p. 77).

228. Wilson, K. G. Renormalization Group and Critical Phenomena. I. Renormalization Group and the Kadanoff Scaling Picture. *Phys. Rev. B* **4,** 3174–3183 (1971) (cit. on p. 77).

229. Wilson, K. G. Renormalization Group and Critical Phenomena. II. Phase-Space Cell Analysis of Critical Behavior. *Phys. Rev. B* **4,** 3184–3205 (1971) (cit. on p. 77).

230. Sakhnenko, V. P. & Chechin, G. M. Symmetry methods and space group representations in the theory of phase transitions. *Comput. Math. Applic.* **16,** 453–464 (1988) (cit. on pp. 77, 99, 119).

231. Langer, J. S. Theory of the Condensation Point. *Ann. Phys. (N. Y.)* **41,** 108–157 (1967) (cit. on p. 78).

232. Baumann, K., Mottl, R., Brennecke, F. & Esslinger, T. Exploring Symmetry Breaking at the Dicke Quantum Phase Transition. *Phys. Rev. Lett.* **107,** 140402 (2011) (cit. on p. 79).

233. Nagy, D., Kónya, G., Szirmai, G. & Domokos, P. Dicke-Model Phase Transition in the Quantum Motion of a Bose-Einstein Condensate in an Optical Cavity. *Phys. Rev. Lett.* **104,** 1–4 (2010) (cit. on pp. 82, 86, 179).

234. Emary, C. & Brandes, T. Quantum Chaos Triggered by Precursors of a Quantum Phase Transition: the Dicke Model. *Phys. Rev. Lett.* **90,** 044101 (2003) (cit. on pp. 83, 84, 86, 87, 177).

235. Hayn, M., Emary, C. & Brandes, T. Phase transitions and dark-state physics in two-color superradiance. *Phys. Rev. A* **84,** 053856 (2011) (cit. on pp. 83, 143, 161).

236. Emary, C. & Brandes, T. Chaos and the quantum phase transition in the Dicke model. *Phys. Rev. E* **67,** 066203 (2003) (cit. on pp. 84, 87, 162, 177).

237. Asboth, J. K., Domokos, P. & Ritsch, H. Correlated motion of two atoms trapped in a single-mode cavity field. *Phys. Rev. A* **70,** 013414 (2004) (cit. on pp. 84, 118, 169).

238. Dicke, R. H. Coherence in Spontaneous Radiation Processes. *Phys. Rev.* **93,** 99–110 (1954) (cit. on p. 86).

239. Piazza, F. & Ritsch, H. Self-Ordered Limit Cycles, Chaos, and Phase Slippage with a Superfluid inside an Optical Resonator. *Phys. Rev. Lett.* **115,** 163601 (2015) (cit. on pp. 87, 189).

240. Carmichael, H. J., Gardiner, C. W. & Walls, D. F. Higher order corrections to the Dicke superradiant phase transition. *Phys. Lett.* **46,** 47–48 (1973) (cit. on p. 92).

241. Piazza, F., Strack, P. & Zwerger, W. Bose–Einstein condensation versus Dicke–Hepp–Lieb transition in an optical cavity. *Ann. Phys. (N. Y.)* **339,** 135–159 (2013) (cit. on pp. 92, 169, 188).

242. Keßler, H., Klinder, J., Wolke, M. & Hemmerich, A. Steering matter wave superradiance with an ultranarrow-band optical cavity. *Phys. Rev. Lett.* **113,** 070404 (2014) (cit. on p. 95).

243. Dimer, F., Estienne, B., Parkins, A. & Carmichael, H. Proposed realization of the Dicke-model quantum phase transition in an optical cavity QED system. *Phys. Rev. A* **75,** 013804 (2007) (cit. on p. 95).

244. Baden, M. P., Arnold, K. J., Grimsmo, A. L., Parkins, S. & Barrett, M. D. Realization of the Dicke Model Using Cavity-Assisted Raman Transitions. *Phys. Rev. Lett.* **113,** 020408 (2014) (cit. on p. 95).

245. Zhiqiang, Z., Lee, C. H., Kumar, R., Arnold, K. J., Masson, S. J., Parkins, A. S. & Barrett, M. D. Nonequilibrium phase transition in a spin-1 Dicke model. *Optica* **4,** 424–429 (2017) (cit. on p. 95).

246. Fradkin, E., Kivelson, S. A. & Tranquada, J. M. Colloquium: Theory of intertwined orders in high temperature superconductors. *Rev. Mod. Phys.* **87,** 457–482 (2015) (cit. on pp. 97, 98, 112).

247. Liu, K.-S. & Fisher, M. E. Quantum Lattice Gas and the Existence of a Supersolid. *J. Low Temp. Phys.. Low Temp. Phys.* **10,** 655–683 (1973) (cit. on pp. 98, 169, 182).

248. Senthil, T., Vishwanath, A., Balents, L., Sachdev, S. & Fisher, M. P. A. Deconfined Quantum Critical Points. *Science* **303,** 1490–1493 (2004) (cit. on pp. 98, 112, 113).

249. Gegenwart, P., Si, Q. & Steglich, F. Quantum criticality in heavy-fermion metals. *Nat. Phys.* **4,** 186–197 (2008) (cit. on p. 98).

250. Dutta, A. & Bhattacharjee, J. K. Competing order parameters and a tricritical point with a difference. *Physica B* **407,** 3722–3726 (2012) (cit. on p. 98).

251. Eichhorn, A., Mesterhàzy, D. & Scherer, M. M. Multicritical behavior in models with two competing order parameters. *Phys. Rev. E* **88,** 042141 (2013) (cit. on pp. 98, 100, 121).

252. Moon, E.-G. Competing Orders and Anomalies. *Sci. Rep.* **6,** 31051 (2016) (cit. on p. 98).

253. Demler, E., Hanke, W. & Zhang, S. C. SO(5) theory of antiferromagnetism and superconductivity. *Rev. Mod. Phys.* **76,** 909–974 (2004) (cit. on pp. 98, 112, 121, 188).

254. Onodera, A., Cynshi, O. & Shiozaki, Y. Landau theory of the ferrielectric phase transition with two order parameters. *J. Phys. Chem. Solid* **18,** 2831 (1985) (cit. on p. 99).

255. Stokes, H. T. & Hatch, D. M. Coupled order parameters in the Landau theory of phase transitions in solids. *Phase transitions* **34** (1991) (cit. on pp. 99, 181).

256. Guhr, T., Müller-Groeling, A. & Weidenmüller, H. A. Random-matrix theories in quantum physics: common concepts. *Phys. Rep.* **299,** 189–425 (1998) (cit. on p. 100).

257. Coleman, S. & Weinberg, E. Radiative corrections as the Origin of Spontaneous Symmetry Breaking. *Phys. Rev. D.* **7,** 1888–1910 (1973) (cit. on pp. 102, 189).

258. Bornholdt, S., Tetradis, N. & Wetterich, C. Coleman-Weinberg phase transition in two-scalar models. *Phys. Lett. B* **348,** 89–99 (1995) (cit. on pp. 102, 119, 121, 189).

259. Henley, C. L. Exact Realization of SO(5) Symmetry in Extended Hubbard Models. *Phys. Rev. Lett.* **80,** 3590–3593 (1998) (cit. on p. 112).

260. Kosterlitz, J. M., Nelson, D. R. & Fishert, E. Bicritical and tetracritical points in anisotropic antiferromagnetic systems. *Phys. Rev. B* **13,** 412–432 (1976) (cit. on pp. 112, 182).

261. Balents, L., Fisher, M. P. A. & Nayak, C. Nodal liquid theory of the pseudo-gap phase of high-T_c superconductors. *Int. J. Mod. Phys. B* **12,** 1033–1068 (1998) (cit. on p. 113).

262. Lee, D. H. & Kivelson, S. A. Two classes of Mott insulator. *Phys. Rev. B* **67,** 024506 (2003) (cit. on p. 113).

263. Lipkin, H., Meshkov, N. & Glick, A. Validity of many-body approximation methods for a solvable model (I). Exact Solutions and Perturbation Theory. *Nucl. Phys. B* **62,** 188–198 (1965) (cit. on p. 113).

264. Garanin, D., Martínez Hidalgo, X. & Chudnovsky, E. Quantum-classical transition of the escape rate of a uniaxial spin system in an arbitrarily directed field. *Phys. Rev. B* **57,** 13639–13654 (1998) (cit. on p. 113).

265. Botet, R. & Jullien, R. Large-size critical behavior of infinitely coordinated systems. *Phys. Rev. B* **28,** 3955–3967 (1983) (cit. on p. 113).

266. Turbiner, A. V. Quasi-Exactly-Solvable Problems and $sl(2)$ Algebra. *Commun. Math. Phys.* **118,** 467–474 (1988) (cit. on p. 113).

267. Ulyanov, V. V. & Zaslavskii, O. B. New methods in the theory of quantum spin systems. *Phys. Rep.* **216,** 179–251 (1992) (cit. on p. 113).

268. Dusuel, S. & Vidal, J. Finite-Size Scaling Exponents of the Lipkin-Meshkov-Glick Model. *Phys. Rev. Lett.* **93,** 237204 (2004) (cit. on p. 113).

269. Vidal, J., Palacios, G. & Mosseri, R. Entanglement in a second-order quantum phase transition. *Phys. Rev. A* **69,** 022107 (2004) (cit. on p. 113).

270. Latorre, J. I., Orus, R., Rico, E. & Vidal, J. Entanglement entropy in the Lipkin-Meshkov-Glick model. *Phys. Rev. A* **71,** 064101 (2005) (cit. on p. 113).

271. Barthel, T., Dusuel, S. & Vidal, J. Entanglement Entropy beyond the Free Case. *Phys. Rev. Lett.* **97,** 220402 (2006) (cit. on p. 113).

272. Ma, J. & Wang, X. Fisher information and spin squeezing in the Lipkin-Meshkov-Glick model. *Phys. Rev. A* **80,** 012318 (2009) (cit. on p. 113).

273. Dziarmaga, J. Dynamics of a quantum phase transition and relaxation to a steady state. *Adv. Phys.* **59,** 1063–1189 (2010) (cit. on p. 113).

274. Kitagawa, M. & Ueda, M. Squeezed spin states. *Phys. Rev. A* **47,** 5138–5143 (1993) (cit. on p. 114).

275. Ma, J., Wang, X., Sun, C. P. & Nori, F. Quantum spin squeezing. *Phys. Rep.* **509,** 89–165 (2011) (cit. on p. 114).

276. Gross, C., Zibold, T., Nicklas, E., Esteve, J. & Oberthaler, M. K. Nonlinear atom interferometer surpasses classical precision limit. *Nature* **464,** 1165–1169 (2010) (cit. on p. 114).

277. Shore, B. W. & Knight, P. L. The Jaynes–Cummings model. *J. Mod. Opt.* **40,** 1195–1238 (1993) (cit. on p. 115).

278. Zou, X. & Mathis, W. Creating quantum entanglement between multiatom Dicke states and two cavity modes. *J. Mod. Optics* **52,** 2001–2011 (2005) (cit. on p. 115).

279. Yi-xiang, Y., Ye, J. & Liu, W.-M. Goldstone and Higgs modes of photons inside a cavity. *Sci. Rep.* **3,** 3476 (2013) (cit. on p. 115).

280. Baksic, A. & Ciuti, C. Controlling Discrete and Continuous Symmetries in "Superradiant" Phase Transitions with Circuit QED Systems. *Phys. Rev. Lett.* **112,** 173601 (2014) (cit. on pp. 115, 167).

281. Fan, J., Yang, Z., Zhang, Y., Ma, J., Chen, G. & Jia, S. Hidden continuous symmetry and Nambu-Goldstone mode in a two-mode Dicke model. *Phys. Rev. A* **89,** 023812 (2014) (cit. on pp. 115, 167).

282. Quezada, L. F. & Nahmad-Achar, E. Characterization of the quantum phase transition in a two-mode Dicke model for different cooperation numbers. *Phys. Rev. A* **95,** 013849 (2017) (cit. on p. 115).

283. Li, J., Huang, W., Shteynas, B., Burchesky, S., Top, F. C., Su, E., Lee, J., Jamison, A. O. & Ketterle, W. Spin-Orbit Coupling and Spin Textures in Optical Superlattices. *Phys. Rev. Lett.* **117,** 185301 (2016) (cit. on p. 118).

284. Schmitt, M., Wenzel, M., Böttcher, F., Ferrier-Barbut, I. & Pfau, T. Self-bound droplets of a dilute magnetic quantum liquid. *Nature* **539,** 259–262 (2016) (cit. on p. 118).

285. Andrews, M. R., Townsend, C. G., Miesner, H.-J., Durfee, D. S., Kurn, D. M. & Ketterle, W. Observation of Interference Between Two Bose Condensates. *Science* **275,** 637–641 (1997) (cit. on p. 118).

286. Raman, C., Köhl, M., Onofrio, R., Durfee, D. S., Kuklewicz, C. E., Hadzibabic, Z. & Ketterle, W. Evidence for a Critical Velocity in a Bose-Einstein Condensed Gas. *Phys. Rev. Lett.* **83,** 2502–2505 (1999) (cit. on p. 118).

287. Cariglia, M. Hidden symmetries of dynamics in classical and quantum physics. *Rev. Mod. Phys.* **86,** 1283–1336 (2014) (cit. on p. 121).

288. Hasenbusch, M., Pelissetto, A. & Vicari, E. Instability of O(5) multicritical behavior in SO(5) theory of high-T_c superconductors. *Phys. Rev. B* **72,** 1–9 (2005) (cit. on p. 121).

289. Silveira, V. & Zee, A. Scalar phantoms. *Phys. Lett.* **161B,** 136–140 (1985) (cit. on p. 121).

290. Cardoso, G. L., Lüst, D. & Mohaupt, T. Threshold corrections and symmetry enhancement in string compactifications. *Nuclear Physics B* **450,** 115–173 (1995) (cit. on p. 121).

291. *Inflationary Cosmology* (eds Lemoine, M., Martin, J. & Peter, P.) (Springer, Berlin Heidelberg, 2008) (cit. on pp. 121, 153).

292. Safaei, S., Miniatura, C. & Grémaud, B. Triangular and honeycomb lattices of cold atoms in optical cavities. *Phys. Rev. A* **92,** 043810 (2015) (cit. on p. 128).

293. Cochran, W. Crystal stability and the theory of ferroelectricity. *Adv. Phys.* **9,** 387–423 (1960) (cit. on pp. 137, 139).

294. Santos, L., Shlyapnikov, G. V. & Lewenstein, M. Roton-Maxon Spectrum and Stability of Trapped Dipolar Bose-Einstein Condensates. *Phys. Rev. Lett.* **90,** 250403 (2003) (cit. on pp. 137, 138).

295. Landau, L. The theory of superfluidity of helium II. *J. Phys. USSR* **5,** 71 (1941) (cit. on p. 137).

296. Landau, L. On the theory of superfluidity of helium II. *J. Phys. USSR* **11,** 91 (1947) (cit. on p. 137).

297. Wilson, R. M. *Manifestations of the Roton in Dipolar Bose-Einstein Condensates* PhD thesis (University of Colorado, 2011) (cit. on p. 137).

298. Zloshchastiev, K. G. Volume element structure and roton-maxon-phonon excitations in superfluid helium beyond the Gross-Pitaevskii approximation. *Eur. Phys. J. B* **85,** 273 (2012) (cit. on p. 137).

299. Henshaw, D. G. & Woods, A. D. B. Modes of Atomic Motions in Liquid Helium by Inelastic Scattering of Neutrons. *Phys. Rev.* **121,** 1266–1274 (1961) (cit. on pp. 137, 138).

300. Raman, C. V. & Nedungadi, T. M. K. The $\alpha - \beta$ Transformation of Quartz. *Nature,* 147 (1940) (cit. on p. 137).

301. Goral, K., Santos, L. & Lewenstein, M. Quantum Phases of Dipolar Bosons in Optical Lattices. *Phys. Rev. Lett.* **88,** 170406 (2002) (cit. on p. 138).

302. Wilson, R. M., Ronen, S., Bohn, J. L. & Pu, H. Manifestations of the Roton Mode in Dipolar Bose-Einstein Condensates. *Phys. Rev. Lett.* **100,** 245302 (2008) (cit. on p. 138).

303. Henkel, N., Nath, R. & Pohl, T. Three-Dimensional Roton Excitations and Supersolid Formation in Rydberg-Excited Bose-Einstein Condensates. *Phys. Rev. Lett.* **104,** 195302 (2010) (cit. on p. 138).

304. Higbie, J. & Stamper-Kurn, D. M. Periodically Dressed Bose-Einstein Condensate: A Superfluid with an Anisotropic and Variable Critical Velocity. *Phys. Rev. Lett.* **88,** 090401 (2002) (cit. on p. 138).

305. Zheng, W. & Li, Z. Collective modes of a spin-orbit-coupled Bose-Einstein condensate: A hydrodynamic approach. *Phys. Rev. A* **85,** 053607 (2012) (cit. on p. 138).

306. Martone, G. I., Li, Y., Pitaevskii, L. P. & Stringari, S. Anisotropic dynamics of a spin-orbit-coupled Bose-Einstein condensate. *Phys. Rev. A* **86,** 063621 (2012) (cit. on p. 138).

307. Zheng, W., Yu, Z.-Q., Cui, X. & Zhai, H. Properties of Bose gases with the Raman-induced spin–orbit coupling. *J. Phys. B* **46,** 134007 (2013) (cit. on p. 138).

308. Khamehchi, M. A., Zhang, Y., Hamner, C., Busch, T. & Engels, P. Measurement of collective excitations in a spin-orbit-coupled Bose-Einstein condensate. *Phys. Rev. A* **90,** 063624 (2014) (cit. on p. 138).

309. Ha, L. C., Clark, L. W., Parker, C. V., Anderson, B. M. & Chin, C. Roton-Maxon Excitation Spectrum of Bose Condensates in a Shaken Optical Lattice. *Phys. Rev. Lett.* **114,** 055301 (2015) (cit. on p. 138).

310. Ji, S. C., Zhang, L., Xu, X. T., Wu, Z., Deng, Y., Chen, S. & Pan, J. W. Softening of Roton and Phonon Modes in a Bose-Einstein Condensate with Spin-Orbit Coupling. *Phys. Rev. Lett.* **114,** 105301 (2015) (cit. on p. 138).

311. Kulkarni, M., Öztop, B. & Türeci, H. E. Cavity-Mediated Near-Critical Dissipative Dynamics of a Driven Condensate. *Phys. Rev. Lett.* **111,** 220408 (2013) (cit. on p. 138).

312. Mottl, R., Brennecke, F., Baumann, K., Landig, R., Donner, T. & Esslinger, T. Roton-Type Mode Softening in a Quantum Gas with Cavity-Mediated Long-Range Interactions. *Science* **336,** 1570–1573 (2012) (cit. on pp. 138, 145, 147, 152, 166).

313. Brennecke, F., Mottl, R., Baumann, K., Landig, R., Donner, T. & Esslinger, T. Real-time observation of fluctuations at the driven-dissipative Dicke phase transition. *Proc. Natl. Acad. Sci. USA* **110,** 11763–11767 (2013) (cit. on pp. 138, 180, 181, 186, 188).

314. Landig, R., Brennecke, F., Mottl, R., Donner, T. & Esslinger, T. Measuring the dynamic structure factor of a quantum gas undergoing a structural phase transition. *Nat. Commun.* **6,** 7046 (2015) (cit. on pp. 138, 180, 181, 186, 188).

315. Pekker, D. & Varma, C. M. Amplitude/Higgs Modes in Condensed Matter Physics. *Annu. Rev. Condens. Matter Phys.* **6,** 269–297 (2015) (cit. on pp. 140, 153, 157, 169).

316. Bramwell, S. T. & Keimer, B. Neutron scattering from quantum condensed matter. *Nat. Mater.* **13,** 763–767 (2014) (cit. on p. 144).

317. Javanainen, J. Spectrum of Light Scattered from a Degenerate Bose Gas. *Phys. Rev. Lett.* **75,** 1927–1930 (1995) (cit. on p. 144).

318. Graham, R. & Walls, D. Spectrum of Light Scattered from a Weakly Interacting Bose-Einstein Condensed Gas. *Phys. Rev. Lett.* **76,** 1774–1775 (1996) (cit. on p. 144).

319. Politzer, H. D. Bose-stimulated scattering off a cold atom trap. *Phys. Rev. A* **55,** 1140–1146 (1997) (cit. on p. 144).

320. Parkins, A. S. & Walls, D. The physics of trapped dilute-gas Bose–Einstein condensates. *Phys. Rep.* **303,** 1–80 (1998) (cit. on p. 144).

321. Stenger, J., Inouye, S., Chikkatur, A. P., Stamper-Kurn, D. M., Pritchard, D. E. & Ketterle, W. Bragg Spectroscopy of a Bose-Einstein Condensate. *Phys. Rev. Lett.* **82,** 4569–4573 (1998) (cit. on p. 144).

322. Steinhauer, J., Ozeri, R., Katz, N. & Davidson, N. Excitation Spectrum of a Bose-Einstein Condensate. *Phys. Rev. Lett.* **88,** 120407 (2002) (cit. on p. 144).

323. Mottl, R. *Roton-type mode softening in a dissipative quantum many-body system with cavity-mediated long-range interactions* PhD thesis (ETH Zürich, 2014) (cit. on pp. 145, 189).

324. Feynman, R. P. Atomic Theory of the Two-Fluid Model of Liquid Helium. *Phys. Rev.* **94,** 262–277 (1954) (cit. on p. 152).

325. Bernstein, J. Spontaneous symmetry breaking, gauge theories, the Higgs mechanism and all that. *Rev. Mod. Phys.* **1,** 7–48 (1974) (cit. on p. 153).

326. Goldstone, J. Field theories with "Superconductor" solutions. *Nuovo Cimento* **19,** 154–164 (1961) (cit. on pp. 153, 156).

327. Goldstone, J., Salam, A. & Weinberg, S. Broken Symmetries. *Phys. Rev.* **127,** 965 (1961) (cit. on pp. 153, 156).

328. Sooryakumar, R. & Klein, M. V. Raman Scattering by Superconducting-Gap Excitations and Their Coupling to Charge-Density Waves. *Phys. Rev. Lett.* **45,** 660–662 (1980) (cit. on p. 154).

329. Littlewood, P. B. & Varma, C. M. Gauge-Invariant Theory of the Dynamical Interaction of Charge Density Waves and Superconductiviy. *Phys. Rev. Lett.* **47,** 811–814 (1981) (cit. on p. 154).

330. Rüegg, C., Normand, B., Matsumoto, M., Furrer, A., McMorrow, D. F., Krämer, K. W., Güdel, H.-U., Gvasaliya, S. N., Mutka, H. & Boehm, M. Quantum Magnets under Pressure: Controlling Elementary Excitations in $TlCuCl_3$. *Phys. Rev. Lett.* **100,** 205701 (2008) (cit. on p. 154).

331. Méasson, M.-A., Gallais, Y., Cazayous, M., Clair, B., Rodière, P., Cario, L. & Sacuto, A. Amplitude Higgs mode in the 2H-$NbSe_2$ superconductor. *Phys. Rev. B* **89,** 060503 (2014) (cit. on p. 154).

332. Endres, M., Fukuhara, T., Pekker, D., Cheneau, M., Schau, P., Gross, C., Demler, E., Kuhr, S. & Bloch, I. The "Higgs" amplitude mode at the two-dimensional superfluid/Mott insulator transition. *Nature* **487,** 3–8 (2012) (cit. on p. 154).

333. Liu, L., Chen, K., Deng, Y., Endres, M., Pollet, L. & Prokof'ev, N. Massive Goldstone (Higgs) mode in two-dimensional ultracold atomic lattice systems. *Phys. Rev. B* **92,** 174521 (2015) (cit. on p. 154).

334. Yarnell, J. L., Arnold, G. P., Bendt, P. J. & Kerr, E. C. Energy vs. momentum relation for the excitations in liquid Helium. *Phys. Rev. Lett.* **1,** 9–11 (1958) (cit. on p. 154).

335. Stamper-Kurn, D. M., Chikkatur, A. P., Görlitz, A, Inouye, S, Gupta, S, Pritchard, D. E. & Ketterle, W. Excitation of Phonons in a Bose-Einstein Condensate by Light Scattering. *Phys. Rev. Lett.* **83,** 2876–2879 (1999) (cit. on p. 154).

336. Matsunaga, R., Hamada, Y. I., Makise, K., Uzawa, Y., Terai, H., Wang, Z. & Shimano, R. Higgs Amplitude Mode in the BCS Superconductors $Nb_{1-x}Ti_xN$ Induced by Terahertz Pulse Excitation. *Phys. Rev. Lett.* **111,** 057002 (2013) (cit. on p. 154).

337. Léonard, J., Morales, A., Zupancic, P., Esslinger, T. & Donner, T. Supersolid formation in a quantum gas breaking a continuous translational symmetry. *Nature* **543,** 87–90 (2017) (cit. on p. 158).

338. Morrison, S. & Parkins, A. S. Dynamical Quantum Phase Transitions in the dissipative Lipkin-Meshkov-Glick model with Proposed Realization in Optical Cavity QED. *Phys. Rev. Lett.* **100,** 1–4 (2008) (cit. on p. 167).

339. Peskin, M. & Schroeder, D. *An Introduction to Quantum Field Theory* (Westview Press, 1995) (cit. on p. 169).

340. Arkani-Hamed, N., Dimopoulos, S. & Dvali, G. The hierarchy problem and new dimensions at a millimeter. *Phys. Lett. B* **429,** 263–272 (1998) (cit. on p. 169).

341. Podolsky, D., Auerbach, A. & Arovas, D. P. Visibility of the amplitude (Higgs) mode in condensed matter. *Phys. Rev. B* **84,** 174522 (2011) (cit. on p. 170).

342. Binney, J., Dowrick, N., Fisher, A. & Newman, M. *The Theory of Critical Phenomena* (Clarendon Press, Oxford, 1992) (cit. on pp. 173, 175).

343. Jaeger, G. The Ehrenfest Classification of Phase Transitions: Introduction and Evolution. *Arch. Hist. Exact Sci.* **53,** 51–81 (1998) (cit. on p. 173).

344. Andrews, T., Trans, P. & Lond, R. S. The Bakerian Lecture: On the Continuity of the Gaseous and Liquid States of Matter. *Phil. Trans. R. Soc. Lond.* **159,** 575–590 (1869) (cit. on p. 173).

345. Mermin, D. & Wagner, H. Absence of Ferromagnetism or Antiferromagnetism in One-or Two-Dimensional Isotropic Heisenberg Models. *Phys. Rev. Lett.* **17,** 1133–1136 (1966) (cit. on p. 175).

346. Hohenberg, P. C. Existence of Long-Range Order in One and Two Dimensions. *Phys. Rev.* **158,** 383–386 (1967) (cit. on p. 175).

347. Domb, C. & Lebowith, J. L. *Phase transitions and critical phenomena* (Academic Press, London, 2001) (cit. on p. 175).

348. Widom, B. Equation of State in the Neighborhood of the Critical Point. *Journ. Chem. Phys.* **43,** 3898–3905 (1965) (cit. on p. 176).

349. Di Francesco, P., Mathieu, P. & Sénéchal, D. *Conformal Field Theory* (Springer Verlag, New York, 1997) (cit. on p. 176).

350. Polyakov, A. M. Conformal symmery of critical fluctuations. *JETP Letters* **12,** 381–383 (1970) (cit. on p. 177).

351. Ódor, G. Universality classes in nonequilibrium lattice systems. *Rev. Mod. Phys.* **76,** 663–724 (2004) (cit. on p. 178).

352. Kessler, E. M., Giedke, G., Imamoglu, A., Yelin, S. F., Lukin, M. D. & Cirac, J. I. Dissipative phase transition in a central spin system. *Phys. Rev. A* **86,** 012116 (2012) (cit. on pp. 178, 179).

353. Breuer, H.-P. & Petruccione, F. *The Theory of Open Quantum Systems* (Oxford University Press, New York, 2007) (cit. on p. 179).

354. Diehl, S., Micheli, A., Kantian, A., Kraus, B., Büchler, H. P. & Zoller, P. Quantum states and phases in driven open quantum systems with cold atoms. *Nat. Phys.* **4,** 878–883 (2008) (cit. on p. 179).

355. Mitra, A., Takei, S., Kim, Y. B. & Millis, A. J. Nonequilibrium Quantum Criticality in Open Electronic Systems. *Phys. Rev. Lett.* **97,** 236808 (2006) (cit. on p. 179).

356. Dalla Torre, E. G., Demler, E., Giamarchi, T. & Altman, E. Quantum critical states and phase transitions in the presence of non-equilibrium noise. *Nat. Phys.* **6,** 806–810 (2010) (cit. on p. 179).

357. Dalla Torre, E. G., Diehl, S., Lukin, M. D., Sachdev, S. & Strack, P. Keldysh approach for nonequilibrium phase transitions in quantum optics: Beyond the Dicke model in optical cavities. *Phys. Rev. A* **87,** 023831 (2013) (cit. on p. 179).

358. Hannukainen, J. & Larson, J. Dissipation driven quantum phase transitions and symmetry breaking. *arXiv:1703.010238* (2017) (cit. on p. 179).

359. Sieberer, L. M., Huber, S. D., Altman, E. & Diehl, S. Dynamical Critical Phenomena in Driven-Dissipative Systems. *Phys. Rev. Lett.* **110,** 195301 (2013) (cit. on p. 179).

360. Nagy, D. & Domokos, P. Nonequilibrium Quantum Criticality and Non-Markovian Environment: Critical Exponent of a Quantum Phase Transition. *Phys. Rev. Lett.* **115,** 043601 (2015) (cit. on pp. 179, 180).

361. Nagy, D., Szirmai, G. & Domokos, P. Critical exponent of a quantum-noise-driven phase transition: The open-system Dicke model. *Phys. Rev. A* **84,** 043637 (2011) (cit. on p. 180).

362. Mani, Ramesh, G, Smet, J. H., Klitzing, K. V., Narayanamurti, V., Johnson, W. B. & Umansky, V. Zero-resistance states induced by electromagnetic-wave excitation in GaAs/AlGaAs heterostructures. *Nature* **420,** 646–650 (2002) (cit. on p. 181).

363. Feldman, D. E. Nonequilibrium Quantum Phase Transition in Itinerant Electron Systems. *Phys. Rev. Lett.* **95,** 177201 (2005) (cit. on p. 181).

364. Roumpos, G., Lohse, M., Nitsche, W. H., Keeling, J. & Hanna, M. Power-law decay of the spatial correlation function in exciton-polariton condensates. *Proc. Natl. Acad. Sci. USA* **109** (2012) (cit. on p. 181).

365. Carusotto, I. & Ciuti, C. Quantum fluids of light. *Rev. Mod. Phys.* **85,** 299–366 (2013) (cit. on p. 181).

366. Patra, A., Divakaran, U. & Mukherjee, V. Non-equilibrium dynamics near a quantum multicritical point. *J. Phys.: Conf. Ser.* **297,** 012008 (2011) (cit. on p. 182).

367. Overbeck, V. R., Maghrebi, M. F., Gorshkov, A. V. & Weimer, H. Multicritical behavior in dissipative Ising models. *Phys. Rev. A* **95,** 042133 (2017) (cit. on p. 182).

368. Fisher, M. E. & Nelson, D. R. Spin Flop, Supersolids, and Bicritical and Tetracritical Points. *Phys. Rev. Lett.* **32,** 1350–1353 (1974) (cit. on p. 182).

369. Nelson, D. R., Kosterlitz, J. M. & Fisher, M. E. Renormalization-Group Analysis of Bicritical and Tetracritical Points. *Phys. Rev. Lett.* **33,** 813–817 (1974) (cit. on p. 182).

370. Fisher, M. E. Scaling Axes and the Spin-Flop Bicritical Phase Boundaries. *Phys. Rev. Lett.* **34,** 1634–1638 (1975) (cit. on p. 182).

371. Domany, E. & Fisher, M. E. Equations of state for bicritical points. III. Cubic anisotropy and tetracriticality. *Phys. Rev. B* **15,** 3510–3521 (1977) (cit. on p. 182).

372. Zachar, O., Kivelson, S. & Emery, V. Landau theory of stripe phases in cuprates and nickelates. *Phys. Rev. B* **57,** 1422–1426 (1998) (cit. on p. 184).

373. Kivelson, S. A., Aeppli, G. & Emery, V. J. Thermodynamics of the interplay between magnetism and high-temperature superconductivity. *Proc. Natl. Acad. Sci. USA* **98,** 11903–11907 (2001) (cit. on p. 184).

374. *Personal communication with E. Demler and Y. Shchadilova* (cit. on p. 188).

375. Gopalakrishnan, S., Lev, B. & Goldbart, P. Atom-light crystallization of Bose-Einstein condensates in multimode cavities: Nonequilibrium classical and quantum phase transitions, emergent lattices, supersolidity, and frustration. *Phys. Rev. A* **82,** 1–29 (2010) (cit. on p. 189).

376. Wickenbrock, A., Hemmerling, M., Robb, G. R. M., Emary, C. & Renzoni, F. Collective strong coupling in multimode cavity QED. *Phys. Rev. A* **87,** 043817 (2013) (cit. on p. 189).

377. Dogra, N. *Towards the single-photon nonlinearity in a Rydberg blocked BEC-cavity system* Master thesis (ETH Zürich, 2014) (cit. on p. 190).

378. Ketterle, W. & Zwierlein, M. W. Making, probing and understanding ultracold Fermi gases. *Rivista del Nuovo Cimento* **31,** 247–422 (2008) (cit. on p. 190).

379. Piazza, F. & Strack, P. Umklapp Superradiance with a Collisionless Quantum Degenerate Fermi Gas. *Phys. Rev. Lett.* **112,** 143003 (2014) (cit. on p. 190).

380. Sheikhan, A., Brennecke, F. & Kollath, C. Cavity-induced chiral states of fermionic quantum gases. *Phys. Rev. A* **93,** 043609 (2016) (cit. on p. 190).

381. Sheikhan, A., Brennecke, F. & Kollath, C. Cavity-induced generation of nontrivial topological states in a two-dimensional Fermi gas. *Phys. Rev. A* **94,** 061603 (2016) (cit. on p. 190).

382. Mivehvar, F., Piazza, F. & Ritsch, H. Disorder-Driven Density and Spin Self-Ordering of a Bose-Einstein Condensate in a Cavity. *Phys. Rev. Lett.* **119,** 063602 (2017) (cit. on p. 190).

383. Kogelnik, H. & Li, T. Laser Beams and Resonators. *Appl. Optics* **5,** 1550–1557 (1966) (cit. on p. 191).

384. Siegman, A. K. *Lasers* (Oxford University Press, Oxford, 1986) (cit. on pp. 191, 194).

385. Tanji-Suzuki, H., Leroux, I. D., Schleier-Smith, M. H., Cetina, M., Grier, A., Simon, J. & Vuletic, V. Interaction between Atomic Ensembles and Optical Resonators: Classical Description. *Adv. At., Mol., Opt. Phys.* **60,** 201–240 (2011) (cit. on p. 199).

ACKNOWLEDGEMENTS

The past years at Zurich have been a wonderful time with many happy memories. The great people and the unique atmosphere made it a privilege to live and study at this place, and coming to the lab remained a pleasure during my entire stay. I would like to reflect on the people who have supported and helped me so much throughout this period.

First, I would like to sincerely thank *Tilman Esslinger*. I am very grateful that he allowed me to join his group and work with him on such exciting research topics. His care to provide a pleasant and productive working atmosphere and his cheerful way to lead the group has inspired me to follow suit in my future. I have learned a lot from his ability to develop an intuitive picture for any physical phenomenon and to approach problems from an original perspective, and his seemingly playful and spontaneous way of taking decisions has always proven right in hindsight. I would also like to thank *Jonathan Home* for his enthusiasm for the experiment and for taking over the co-examination of this thesis.

I am equally grateful to *Tobias Donner* for putting great trust in me and allowing me to build the experiment with him. His friendly, encouraging and supportive nature are a great benefit for the team. Starting from the first day he gave me the freedom to bring my ideas and vision to the experiment, while providing the technical expertise to guarantee a fast progress. With the decision for a setup with two crossed cavities, he and Tilman brought a remarkable intuition for the right system at the right time. It was a fantastic experience to share the joy of the first vacuum, the disappointment of the leaks and the tension when we inserted the cavity setup. The speed at which he is able to locate a problem in the lab is unprecedented, as well as the short amount of time in which he proofread the lion's share of this manuscript.

During my graduate studies, I had the pleasure to work in a team of remarkable scientists. In the early days of the experiment, *Laura Corman* and *Matthias Bucher* became so much more than Master students, as they provided me with company, laughter and lots of cake. I am grateful to *Moonjoo Lee* for going through the buildup phase with me. His undaunted handling of cavity mirrors made an impression on everybody and led to the cavity setup in its current form. *Leigh Martin* was a great fellow in my second year, drastically increased my knowledge in electronics, and occasionally cheered me up when things went behind schedule. *Andrea Morales* brought a perfect mix of analytical precision, experimental pragmatism and sense of humour into the team. I will never forget the afternoon we shared in the lab, when the photon numbers started jumping and the supersolid was born. The team was completed with *Philip Zupancic*, whose eagerness to make the experiment more stable has been very valuable, and whose passion for chamber and orchestra music made for many unforgettable music hours. Both are brilliant physicists and became great friends, which made it an extraordinary experience to work with them. The experiment could not be left in better hands.

An essential contribution to the success of this work was the ease and implicitness with which members outside the team always provided knowledge, lab equipment and friendship. I would like to thank *Ferdinand Brennecke* for his insights on fundamental quantum optics and his enormous

amount of paper references, *Kristian Baumann*, whose knowledge on technical details of optical cavities has been of great help, *Rafael Mottl*, for his constant enthusiasm, motivation, and for leading us to the glorious Boltzmann cup victory, and *Renate Landig* for being my most faithful concert audience and a great on various hikes and ski trips. *Lorenz Hruby* has been a constant support and I am grateful for his patience to teach me the art of python and how to make a quantum gas experiment more professional. *Nishant Dogra* reminded me to continue asking (and running) whenever I would stop, *Manuele Landini* explored uncharted territory at Obergurgl with me, and *Kathrin Kröger* brought new laughter to the group and invented the post-midnight motivational meetings. I would like to acknowledge the enthusiastic discussions with *Leticia Tarruell* during the buildup phase, as well as with *Daniel Greif*, whose vast knowledge about lattice physics I plan to harvest even more in the near future. *Thomas Uehlinger* taught me lots about design and figure style, and kindly passed me his thesis template, and *Gregor Jotzu's* creative way of thinking has been an ongoing inspiration, in particular during all our common conferences. I share many coining experiences with *Michael Messer*, the first PhD that joined after me and my fellow YAO organizer and roadtrip buddy. My thank also goes to *Rémi Desbuquois* for bringing a more rigorous spirit into our discussions, *Frederik Görg*, who not only brought some 'Monnabauäh' to Zurich, but also learned about lattice physics in an admirable speed, and *Kilian Sandholzer*, whose sharp questions and fine sense of humour always made it a pleasure to be with him. *Jean-Philippe Brantut's* wisdom of both experiment and theory, *Jakob Meineke's* lakonic humour, *David Stadler's* enthusiasm on almost everything and *Charles Grenier's* patient explanations on quantum gases helped me through the buildup period. I will never forget the memorable journeys with *Sebastian Krinner*, including overheating at Grand Canyon, undercooling at Yosemite valley, bankruptcy at Las Vegas and undercover activities at Stanford university, as well as with *Dominik Husmann*, be it on Mount Fuji, at Niagara Falls or Chicago's finest jazz bars. *Martin Lebrat* was always good when it came to refreshing my french cursing vocabulary or mastering the exotic zoo of pythons, spyders and pandas, and *Samuel Häusler's* modest and efficient way of getting things done was an inspiration to all of us. I would also like to acknowledge all insightful discussions with scientists outside of our group, in particular the guest professors *Cheng Chin*, *Päivi Törmä*, *Eugene Demler* and *Wilhelm Zwerger*.

The work would not have been possible without *Veronica Bürgisser*, *Stephanie Ackermann* and *Eik Szee Goh Aschauer* in the administrative office, neither without *Alexander Frank's* custom-designed devices and muffin bakery. My special thanks go to *Marcel Bär*, *Walter Bachmann* and *Andreas Stuker* for their help during the construction of the vacuum system and the cavity setup, as well as *Hans-Jürg Gübeli*, *Isabelle Altdorfer*, *Sandro Tiegermann*, *Hansruedi Scherrer*, *Joakim Reuteler* and *Emilio Gini* for their technical assistance.

Finally, I would like to thank my friends for making Zurich my home, and for making it so hard for me to leave. My biggest gratitude goes to my family, in particular my parents *Oda* and *Patrick*, and my siblings *Sophia*, *Oliver* and *Charlotte*: for their constant support and appreciation for what I do, for always being there although we are mostly apart, and for reminding me of life beyond physics.

Zürich, May 2017

Julian Léonard

JULIAN LÉONARD — CURRICULUM VITÆ

PERSONAL

born January 15, 1989, in Viernheim, Germany
citizen of Germany

Hohlstrasse 9
8004 Zürich
Switzerland
E-mail: leonard@phys.ethz.ch

EDUCATION

2011 – 2017	Ph. D. thesis under the supervision of Prof. Dr. T. Esslinger: *A supersolid of matter and light*. ETH Zurich, Switzerland
2011	Master thesis under the supervision of Prof. Dr. J. Dalibard: *Création d'un défaut mobile dans un gaz de Bose bidimensionnel*. École normale supérieure/Laboratoire Kastler-Brossel, Paris, France
2010 – 2011	Graduate studies in Physics at Université Pierre et Marie Curie, Paris, France
2009 – 2010	Working student in the group of Prof. Dr. I. Bloch at Max-Planck Institute for Quantum Optics, Garching, Germany
2007 – 2010	Undergraduate and graduate studies in physics at TU Munich, Germany
2007	Abitur at Landesmusikgymnasium, Montabaur, Germany

PUBLICATIONS

1. J. Léonard, A. Morales, P. Zupancic, T. Donner, T. Esslinger
   Monitoring and manipulating Higgs and Goldstone modes in a supersolid quantum gas
   Science **358**, 1415-1418 (2017)

2. J. Léonard, A. Morales, P. Zupancic, T. Esslinger, T. Donner
   Supersolid formation in a quantum gas breaking a continuous translational symmetry
   Nature **543**, 87-90 (2017)

3. J. Léonard, A. Morales, P. Zupancic, T. Esslinger, T. Donner
   Optical transport and manipulation of ultracold atoms with focus-tunable lenses
   New J. Phys. **16**, 093028 (2014)

4. R. Desbuquois, L. Chomaz, T. Yefsah, J. Léonard, J. Beugnon, C. Weitenberg and J. Dalibard
   Superfluid behaviour of a two-dimensional Bose gas
   Nat. Phys. **8**, 645-648 (2012)

INVITED TALKS

1. Seminar talk, Max-Planck Institute of Quantum Optics, Garching, Germany
   A supersolid quantum gas and its Higgs and Goldstone modes, 2017
2. Seminar talk, Cambridge University, Cambridge, UK
   A supersolid quantum gas and its Higgs and Goldstone modes, 2017
3. Seminar talk, Collège de France, Paris, France
   A supersolid quantum gas and its Higgs and Goldstone modes, 2017
4. Seminar talk, Harvard University, Cambridge MA, USA
   A supersolid quantum gas and its Higgs and Goldstone modes, 2017
5. Seminar talk, IQOQI, Innsbruck, Austria
   Supersolid formation in a quantum gas – Breaking continuous translational symmetry with crossed cavities, 2016
6. Seminar talk, Harvard University, Cambridge MA, USA
   A novel experiment for coupling a Bose-Einstein condensate with two crossed cavity modes, 2015
7. Seminar talk, Goethe-Universität, Frankfurt am Main, Germany
   A novel experiment for coupling a Bose-Einstein condensate with two crossed cavity modes, 2014
8. Seminar talk, Laboratoire Kastler-Brossel, Paris, France
   A novel experiment for coupling quantum gases to optical cavities, 2013

COLOPHON

The design of this thesis is largely inspired by Robert Bringhurst's seminal book on typography *"The Elements of Typographic Style"*. It was typeset in XeLaTeX with a style that is partly based on `classicthesis.sty` by André Miede, `arsclassica.sty` by Lorenzo Pantieri and the dissertation of Thomas Uehlinger.